A FINITE ELEMENT HEAT TRANSFER MODEL OF FERROMAGNETIC THERMOSEEDS AND A PHYSIOLOGICALLY-BASED OBJECTIVE FUNCTION FOR PRETREATMENT PLANNING OF FERROMAGNETIC HYPERTHERMIA

by

DEAN THOMAS TOMPKINS

A thesis submitted in partial fulfillment of the

requirements for the degree of

Doctor of Philosophy

(Mechanical Engineering)

at the

UNIVERSITY OF WISCONSIN-MADISON

1992

ABSTRACT

Finite element heat transfer models of ferromagnetic thermoseeds and catheters were developed for computerized pretreatment planning of ferromagnetic hyperthermia. These models were implemented into a general purpose finite element program to solve the bioheat transfer equation. In simulations with a 4x4 array of thermoseeds in a two-dimensional tissue model, the heat transfer model predicted that fractions of tumor greater than 43°C were between 8 and 40% lower when thermoseed temperature depended on power versus models which assumed a constant thermoseed temperature. The modeling of catheters was found to be necessary since the fractions of tumor greater than 42°C in simulations using thermoseed and catheter models were between 1 and 45.3% lower than in simulations with bare thermoseeds.

An objective function was developed to aid in selecting optimal thermoseed temperatures and seed spacings *a priori*. The objective function has a physiological basis and considers increased cell killing at temperatures above 42 to 43°C (= $T_{min,\ thera.}$). There is a penalty term in the objective function to account for heating of normal tissues above $T_{min,\ thera.}$. The objective function is independent of the size and shape of normal tissues included in the model. There is a scalar weighting factor γ in the objective function that has treatment implications. In a simple tissue model, it was shown that the uncertainties associated with cell survival above $T_{min,\ thera.}$ had a small effect on the fraction of tumor killed and on the objective function. It was also shown that the objective function identifies optimal thermoseed spacings that maximize the fraction of tumor killed. In a model of a tumor in the human prostate, it was shown that if a compromise was sought between maximizing the minimum tumor temperature (= $T_{min,\ tumor}$) and minimizing the maximum temperature in normal tissues

(= $T_{max,\ normal}$), the objective function was an effective method to optimize the treatment plan. Additionally, it was shown in simulations that fractions of tumor above temperatures between 42 and 50°C were between 0 and 60% higher with a temperature-dependent versus a constant blood flow model.

ACKNOWLEDGEMENT

Several individuals need to be recognized for their contributions to this study. First and foremost, I would like to thank my major professor, Dr. Ray Vanderby, for providing the framework, in part, for this project which was in proposal form in 1988. Prof. Vanderby was a source of guidance throughout the project. His experience with finite element modeling of biological tissue systems and optimization techniques was quite helpful. Dr. Vanderby provided financial support early in this project and it was his efforts that 'started the ball rolling'.

Much appreciation goes to Professor Glen Myers for presenting the finite element method in a straightforward manner in his advanced heat conduction course. Professor Myers' lectures were tailored to facilitate maximum understanding and retention of the finite element method using the Galerkin approach. Professor Myers provided expert assistance during infrequent discussions on the finite element method and conduction heat transfer.

Clinical expertise and a lion's share of the funding for this project were provided by Professors Richard Steeves and Bhudatt Paliwal. Together, Drs. Steeves and Paliwal direct the local hyperthermia program at the University of Wisconsin-Madison Hospital. Dr. Steeves provided many clinical insights in the treatment of tumors with interstitial ferromagnetic hyperthermia. Prof. Paliwal was another early collaborator in this project and provided the opportunity to assist in the writing of several grant applications.

Heat transfer, optimization, and additional finite element expertise were provided by Professors Sanford Klein and William Beckman. During frequent advisory meetings, Drs. Klein and Beckman created an atmosphere of can-do and insight into interesting phenomena that arose during this study. The garnering of intermediary funding from the

UW Graduate School by Drs. Klein and Beckman during a critically low support period of this project is recognized and appreciated. Much gratitude is extended to Dr. Klein for several contributions. These contributions include timely (usually overnight) fixes of 'bugs' in FEHT and incorporating numerical algorithms into FEHT including the bioheat transfer solution routine, variable properties solution routine, and models of ferromagnetic thermoseeds and catheters.

Many thanks go to Drs. Beckman, Klein, Steeves and Vanderby for the hospitality, food and engaging discussions provided at picnics, house parties and/or conference sites. Experiences like these made my life more enjoyable during the last four years.

Lastly, the support from family and friends needs to be recognized. First, my father, mother, brothers and sister provided *food* money when it was nonexistent and moral support when it was needed. Gratitude is due to my extended family members who displayed sincere interest in the progress of my work at holiday and ceremonial gatherings. My colleagues including Jeff Thornton, Todd Jekel, Doug Reindl, Jeff Naber, Dave Ruch, Doug Frye, Matt Podgorsak and Sue Severson, among others, were good listeners and provided advice when sought. My wife, Mary, kept my mental balance through a major portion of this thesis by showing that the greatest forms of intellectual achievement are laughter and human compassion.

Madison, WI

October, 1992

TABLE OF CONTENTS

LIST OF FIGURES

Chapter 1

Chapter 2

Chapter 3

Chapter 4

Chapter 5

Chapter 7

Chapter 8

Appendix A

Appendix B

LIST OF TABLES

Chapter 3

Chapter 4

Chapter 5

Chapter 6

Chapter 7

Nomenclature

A compilation of all the symbols used in this study is provided below. Dimensions are in terms of mass (M), length (L), time (t), temperature (T), and energy (E). The location refers to the equation, section or figure in which the symbol is first used or thoroughly defined.

Symbol	Definition	Location	Dimension	SI Units
a	Radius of thermoseed	Sec. 3.2.3	L	m
a_1	Linear coefficient	Eq. 5.13	T	C
a_2	Linear coefficient	Eq. 5.13	T/L	C/m
a_3	Linear coefficient	Eq. 5.13	T/L	C/m
A	Cross-sectional area of tissue	Sec. 5.3	L^2	m^2
A_{cat}	Cross-sectional area of catheter model	Sec. 3.2.3	L^2	m^2
A_{ij}	Boundary-segment area of thermoseed i and finite element node j of seed	Sec. 3.2.3	L^2	m^2
A_s	Cross-sectional surface area of thermoseed	Eq. 3.3a	L^2	m^2
$A_{s,\ reg.\ hex}$	Cross-sectional surface area of hexagonal thermoseed model	Fig. 3.5a	L^2	m^2
$A_{s,\ dodec.}$	Cross-sectional surface area of dodecagonal thermoseed model	Fig. 3.5b	L^2	m^2
$A^{(e)}$	Area of finite element e	Eq. 5.11	L^2	m^2
b	Slope of cell-survival curves	Eq. 5.2b	1/T	1/C
b_{ijk}	Finite element area (= 2 $A^{(e)}$)	Eq. 5.12	L^2	m^2
b_i	Intercepts in linear equation approximation (i = 1, 2 and 3)	Fig. 5.4	L	m
$\mathbf{b}$	Column perfusion vector	Eq. 2.4	E/t-L	J/s-m
$\mathbf{b}^{(e)}$	Element perfusion vector	Eq. A.28	E/t-L	J/s-m
$\mathbf{B}$	Perfusion matrix	Eq. 2.4	E/t-L-T	J/s-m-C

$\mathbf{B}^{(e)}$	Element perfusion matrix	Eq. A.27	E/t-L-T	J/s-m-C
bei	Kelvin function	Eq. 4.2	–	–
ber	Kelvin function	Eq. 4.2	–	–
bei'	First derivative of Kelvin function	Eq. 4.2	–	–
ber'	First derivative of Kelvin function	Eq. 4.2	–	–
Bi	Biot number	Eq. 4.10	–	–
Bi_I	Implant-Biot number	Eq. 4.9	–	–
c_b	Specific heat of blood	Eq. 2.1	E/M-T	J/kg-C
c_t	Specific heat of tissue	Eq. 2.1	E/M-T	J/kg-C
$\mathbf{C}$	Capacitance matrix	Eq. 2.4	E/M-T	J/m-C
$\mathbf{C}^{(e)}$	Element capacitance matrix	Eq. A.24	E/M-T	J/m-C
dx	Infinitesimal length in x-direction of rectangular coordinate system	Eq. 2.3	L	m
dy	Infinitesimal length in y-direction of rectangular coordinate system	Eq. 2.3	L	m
e	Finite element e	Eq. 5.4	–	–
f	Weighting function	Eq. 2.3	–	–
f	Frequency of electromagnetic field	Eq. 4.2	1/t	Hz
$\mathbf{f}$	Vector of linear interpolating functions	Sec. A.2.1	–	–
$\mathbf{f}_x$	Vector of the x derivative of linear interpolating functions	Sec. A.2.1	–	–
$\mathbf{f}_y$	Vector of the y derivative of linear interpolating functions	Sec. A.2.1	–	–
F	Objective function	Eq. 5.6	–	–
g'''	Energy dissipation or absorption rate per unit volume	Sec. A.1	E/t-L^3	J/s-m^3
g_a'''	Energy absorption rate per unit volume of tissue	Eq. 2.1	E/t-L^3	J/s-m^3
g_m'''	Energy dissipation rate per unit volume due to metabolic processes	Eq. 2.1	E/t-L^3	J/s-m^3
g_s'''	Energy absorption rate per unit volume of thermoseed	Sec. 3.2.3	E/t-L^3	J/s-m^3

$\mathbf{g}$	Column energy dissipation or absorption rate vector	Eq. A.7	E/t-L	J/s-m
$\mathbf{g}^{(e)}$	Element energy dissipation or absorption rate vector	Eq. A.26	E/t-L	J/s-m
h	Convective heat transfer coefficient	Sec. 3.2.3	E/t-L^2-T	J/s-m^2-C
h_{ij}	Convective heat transfer coefficient between thermoseed i and finite element node j of seed i	Sec. 3.2.3	E/t-L^2-T	J/s-m^2-C
$\mathbf{h}$	Column convection vector	Eq. A.75	E/t-L	J/s-m
$\mathbf{h}^{(b_h)}$	Boundary-segment convection vector	Eq. A.75	E/t-L	J/s-m
H	Electromagnetic field strength	Eq. 4.1	M-L/t^3	A/m
H_o	Amplitude of magnetic field	Eq. 4.3	M-L/t^3	A/m
$\mathbf{H}$	Convection matrix	Eq. A.75	E/t-L-T	J/s-m-C
$\mathbf{H}^{(b_h)}$	Boundary-segment convection matrix	Eq. A.75	E/t-L-T	J/s-m-C
i	Unit length	Eq. 3.3a	L	m
I_0	Modified Bessel function of the First Kind of order 0	Eq. 3.4	–	–
I_1	Modified Bessel function of the First Kind of order 1	Eq. 3.4	–	–
k_{cat}	Thermal conductivity of catheter model	Sec. 3.2.3	E/t-L-T	J/s-m-C
k_N	Thermal conductivity of normal tissue	Sec. 5.2.3.1.1	E/t-L-T	J/s-m-C
k_s	Thermal conductivity of seed model	Sec. 3.2.3	E/t-L-T	J/s-m-C
k_t	Thermal conductivity of tissue	Eq. 2.1	E/t-L-T	J/s-m-C
k_T	Thermal conductivity of tumor	Sec. 5.2.3.1.1	E/t-L-T	J/s-m-C
$\mathbf{K}$	Conduction matrix	Eq. 2.4	E/t-L-T	J/s-m-C
$\mathbf{K}^{(e)}$	Element conduction matrix	Eq. A.25	E/t-L-T	J/s-m-C
K_0	Modified Bessel function of the Second Kind of order 0	Eq. 3.4	–	–
K_1	Modified Bessel function of the Second Kind of order 1	Eq. 3.4	–	–
l	Distance between thermoseeds	Sec. 4.2.1	L	m
l_{opt}	Optimum distance between thermoseeds	Table 6.2	L	m

L	Total length of tissue model	Sec. 5.3.2.1.1	L	m
L_N	Length of square normal tissue model	Sec. 4.2.1	L	m
L_{N_1}	Length of normal tissue model 1	Sec. 5.3.2.1.1	L	m
L_{N_2}	Length of normal tissue model 2	Sec. 5.3.2.1.1	L	m
L_T	Length of square tumor model	Sec. 4.2.1	L	m
L_{T_1}	Length of tumor model 1	Sec. 5.3.2.1.1	L	m
L_{T_2}	Length of tumor model 2	Sec. 5.3.2.1.1	L	m
m	Volumetric flow rate of blood per unit mass of tissue	Eq. 2.1	L^3/t-M	m^3/s-kg (l/min-kg)
m_n	Volumetric flow rate of blood in normal tissue	Sec. 4.3.2	L^3/t-M	m^3/s-kg (l/min-kg)
m_t	Volumetric flow rate of blood in tumor tissue	Sec. 4.3.2	L^3/t-M	m^3/s-kg (l/min-kg)
m_i	Slope of linear curve approximation (i = 1, 2, 3)	Fig. 5.4	–	–
M	Magnetization of thermoseed	Eq. 4.1	t/L^2	tesla
n	Energy flow parameter ($= \sqrt{w_b c_b / k_t}$)	Eq. 3.1	1/L	1/m
n	Normal direction to surface of tissue	Fig. 7.4	L	m
N	Number of equations in system	Sec. 2.2	–	–
N_n	Number of finite difference nodes in normal tissue model	Eq. 1.1	–	–
N_t	Number of finite difference nodes in tumor model	Eq. 1.1	–	–
P'	Energy absorption rate of thermoseed per unit length	Eq. 3.3a	E/t-L	J/s-m
$P'_{s,j}$	Energy absorption rate of thermoseed s and iteration j	Sec. 4.1.1.1	E/t-L	J/s-m
P'_{max}	Maximum energy absorption rate of thermoseed	Sec. 4.1.2	E/t-L	J/s-m
P^*	Nondimensional power of thermoseed s	Sec. 4.1.2	–	–
$P^*_{s,j}$	Nondimensional thermoseed power	Sec. 4.1.2.1	–	–

	and iteration j			
q	Scalar weighting factor	Eq. 1.1	–	–
q'	Heat transfer rate per unit length of thermoseed	Eq. 4.5d	E/t-L	J/s-m
q''	Heat flux	Eq. 3.3a	E/t-L^2	J/s-m^2
q_o''	Heat flux into tissue along boundary from outside the tissue	Eq. A.4	E/t-L^2	J/s-m^2
$\mathbf{q_o}$	Column heat flux vector	Eq. 2.4	E/t-L	J/s-m
$\mathbf{q}$	Column outer surface heat flux vector	A.75	E/t-L	J/s-m
$\mathbf{q}^{(bq)}$	Boundary-segment heat flux vector	A.75	E/t-L	J/s-m
r	Denotes radial direction	Eq. 3.1	L	m
r_i	Inner radius of tissue model	Eq. 3.3a	L	m
r_k	Inner radius of tissue model	Eq. 5.8	L	m
r_l	Outer radius of tissue model	Eq. 5.8	L	m
r_o	Outer radius of tissue model	Eq. 3.3b	L	m
r_s	Radius of thermoseed	Sec. 5.3.1	L	m
r_T	Radius of tumor model	Sec. 5.3.1	L	m
s	Number of thermoseeds	Sec. 4.1.1.1	–	–
s_{ij}	Boundary segment length between finite element nodes i and j	Eq. A.76	T	C
S	Surviving fraction of cells	Eq. 5.1	–	–
$S_{Tis.Type}$	Local surviving fraction of cells (*Tis. Type* = normal or tumor tissue)	Eq. 5.2	–	–
$S_{V,\ Ti.Ty.}$	Volumetric surviving fraction of cells (*Ti.Ty.* = normal or tumor tissue)	Eq. 5.3	–	–
$S_{V(e),\ Ti.Ty.}$	Volumetric surviving fraction of cells (*Ti.Ty.* = normal or tumor tissue in finite element *e*)	Eq. 5.4	–	–
t	Time	Eq. 2.1	t	s
t_{cat}	Thickness of catheter	Sec. 3.2.3	L	m
T	Tissue temperature	Eq. 2.1	T	C
T_{amb}	Ambient temperature	Fig. 7.4	T	C

$T_{ave,\ bound.}$	Average temperature on the boundary of the tumor and normal tissues	Sec. 6.3.2	T	C
T_b	Blood temperature	Eq. 2.1	T	C
$T_{max,\ normal}$	Maximum normal tissue temperature	Sec. 6.3.2	T	C
$T_{max,\ tumor}$	Maximum tumor temperature	Sec. 6.3.2	T	C
$T_{min,\ thera.}$	Minimum therapeutic temperature	Sec. 5.2.3.1	T	C
$T_{min,\ tumor}$	Minimum tumor temperature	Sec. 6.3.2	T	C
T_n	Temperature at normal tissue node	Eq. 1.1	T	C
$T_{n,\ set}$	Set temperature of normal tissue	Eq. 1.1	T	C
T_s	Thermoseed temperature	Sec. 4.1.1	T	C
$T_{s,\ c.p.}$	Curie temperature of thermoseed	Eq. 4.7	T	C
$T_{s,\ j\ Curve}$	Temperature of thermoseed s and iteration j computed with curve fit	Sec. 4.1.1.1	T	C
$T_{s,\ j\ FEHT}$	Temperature of thermoseed s and iteration j computed with FEHT	Sec. 4.1.1.1	T	C
$T_{s,\ lumped}$	Lumped thermoseed temperature	Sec. 3.2.3	T	C
$T_{s,\ surface}$	Thermoseed surface temperature	Sec. 3.2.3	T	C
T_t	Temperature at tumor node	Eq. 1.1	T	C
$T_{t,\ set}$	Set temperature of tumor tissue	Eq. 1.1	T	C
$T_{T1\ max}$	Maximum temperature in tumor 1	Sec. 5.2.3.1.1	T	C
$T_{T2\ max}$	Maximum temperature in tumor 2	Sec. 5.2.3.1.1	T	C
T_x	Derivative of temperature with respect to x	Eq. A.1	T/L	C/m
T_y	Derivative of temperature with respect to y	Eq. A.1	T/L	C/m
T_∞	Temperature at a large distance from surface of body	Eq. A.74	T	C
$T^{(e)}$	Temperature within finite element e	Eq. 5.4	T	C
$T_i^{(e)}$	Temperature at finite element node i	Eq. 5.10	T	C
$T_j^{(e)}$	Temperature at finite element node j	Eq. 5.10	T	C
$T_k^{(e)}$	Temperature at finite element node k	Eq. 5.10	T	C
T^*	Nondimensional temperature	Eq. 4.7	–	–

T^*_s	Nondimensional thermoseed temperature	Sec. 4.1.2	–	–
$T^*_{s,j\ Curve}$	Nondimensional temperature of thermoseed s and iteration j computed with curve fit	Sec. 4.1.2.1	–	–
$T^*_{s,j\ FEHT}$	Nondimensional temperature of thermoseed s and iteration j computed with FEHT	Sec. 4.1.2.1	–	–
T_{50}	Temperature at which 50% of all measured temperatures is above	Sec. 5.1	T	C
T_{90}	Temperature at which 90% of all measured temperatures is above	Sec. 5.1	T	C
$\mathbf{T}$	Column temperature vector	Eq. 2.4	T	C
$\dot{\mathbf{T}}$	Time derivative of column temperature vector	Eq. 2.4	T/t	C/s
V	Volume of tissue	Eq. 5.3	L^3	m^3
V_N	Volume of normal tissue	Sec. 5.2.3.1.3	L^3	m^3
V_T	Volume of tumor	Eq. 5.5	L^3	m^3
$V^{(e)}$	Volume of finite element e	Eq. 5.4	L^3	m^3
w_b	Mass flow rate of blood per unit volume of tissue	Eq. 2.2	M/t-L^3	kg/s-m^3
$w_b c_{b\ cat}$	Tissue perfusion in catheter model	Sec. 3.2.3	E/t-L^3-T	J/s-m^3-C
$w_b c_{b\ s}$	Tissue perfusion in thermoseed model	Sec. 3.2.3	E/t-L^3-T	J/s-m^3-C
w_i	Linear interpolating function	Sec. 2.2	–	–
$\mathbf{w}$	Column vector of linear interpolating functions	Eq. A.6	–	–
$\mathbf{w}_x$	Column vector of the x derivative of the linear interpolating functions	Eq. A.6	1/L	1/m
$\mathbf{w}_y$	Column vector of the y derivative of the linear interpolating functions	Eq. A.6	1/L	1/m
$\mathbf{w}^T$	Row vector of linear interpolating functions	Eq. A.6	–	–
$\mathbf{w}_x^T$	Row vector of the x derivative of the	Eq. A.6	1/L	1/m

	linear interpolating functions			
$\mathbf{w}_y^T$	Row vector of the y derivative of the linear interpolating functions	Eq. A.6	1/L	1/m
x	Denotes x-direction in rectangular coordinate system	Eq. 2.1	L	m
x_i, x_j, x_k	Denotes x-coordinate of nodes i , j and k of finite element e	Fig. 5.4	L	m
x^*	Denotes nondimensional x-direction in rectangular coordinate system	Eq. 4.6a	–	–
x	Induction number ($= a\sqrt{\omega\sigma\mu}$)	Eq. 4.2	–	–
y	Denotes y-direction in rectangular coordinate system	Eq. 2.1	L	m
y_i, y_j, y_k	Denotes y-coordinate of nodes i , j and k of finite element e	Fig. 5.4	L	m
y_1, y_2, y_3	Denotes linear equation fits to nodes i, j and k of finite element e in Fig. 5.4	Eq. 5.14	L	m
y^*	Denotes nondimensional y-direction in rectangular coordinate system	Eq. 4.6b	–	–
z	Denotes z-direction in rectangular coordinate system	Eq. 2.1	L	m

Greek Symbol	Definition	Location	Dimension	SI Units
γ	Scalar weighting factor	Eq. 5.6 (Sec. 5.2.3.1.2)	–	–
δ_i, δ_j, δ_k	Linear interpolating functions	Eq. A.34	–	–
ΔL_{N_2}	Length of normal tissue below $T_{min,\ thera.}$	Fig. 5.3d	–	–
ΔL_{T_2}	Length of tumor below $T_{min,\ thera.}$	Fig. 5.3b	–	–
η_1, η_2	Fraction of tumor tissue killed in tissue model 1 and 2	Sec. 5.3.2.1.1	–	–
θ	Temperature difference	Eq. 3.2	T	C
θ	Denotes angular distance	Sec. 3.2	–	–
μ	Magnetic permeability of thermoseed	Eq. 4.1	$t^4/M\text{-}L^3$	tesla-m/A
μ_o	Magnetic permeability of free space	Eq. 4.1	$t^4/M\text{-}L^3$	tesla-m/A
$\widehat{\mu}$	Average magnetic permeability of thermoseed	Eq. 4.3	$t^4/M\text{-}L^3$	tesla-m/A
ξ_i, ξ_j, ξ_k	Linear interpolating functions	Eq. 5.10	–	–
Φ	Objective function	Eq. 1.1	–	–
π	Constant [= 4 $\tan^{-1}$ (1)]	Eq. 4.2	–	–
ρ_b	Density of blood	Eq. 2.1	M/L^3	kg/m^3
ρ_t	Density of tissue	Eq. 2.1	M/L^3	kg/m^3
σ	Electrical conductivity of thermoseed	Eq. 4.2	$M\text{-}L/t^3$	1/Ω-m
$\Psi_{Tis.\ Type}$	Fraction of tissue killed in volume V_T (*Tis. Type* = normal or tumor tissue)	Eq. 5.5	–	–
Ψ_N	Fraction of normal tissue killed, non-dimensionalized to volume V_T	Eq. 5.6	–	–
Ψ_T	Fraction of tumor killed in volume V_T	Eq. 5.6	–	–
Ψ_{T_1}	Fraction of death in tumor model 1	Sec. 5.2.3.1.1	–	–
Ψ_{T_2}	Fraction of death in tumor model 2	Sec. 5.2.3.1.1	–	–
ω	Angular velocity (=$2\pi f$)	Eq. 4.2	1/t	1/s

Numerical Operator	Definition	Location	Dimension	SI Units
d	Ordinary derivative operator	Eq. 3.1	–	–
∂	Partial derivative operator	Eq. 2.1	–	–
Σ	Summation sign	Eq. 5.5	–	–
$\int$	Boundary integral	Eq. A.4	–	–
$\iint$	Area integral	Eq. 2.3	–	–

Chapter 1

Introduction

This introductory chapter consists of several sections. A brief discussion of cancer and the four main types of cancer are discussed in Sec. 1.1. The several methods available today for treating cancer are reviewed in Sec. 1.2. The method of treating cancer known as hyperthermia, its use alone in treating tumors and in combination with radiation is presented in Sec. 1.3. The many techniques available for delivering hyperthermia treatments are discussed in Sec. 1.4. Hyperthermia delivered with interstitial ferromagnetic thermoseeds is discussed in Sec. 1.5. A review of theoretical studies that sought to optimize hyperthermia treatments is discussed in Sec. 1.6. The objective and significance of this study are presented in Sec. 1.7.

1.1 What is Cancer?

Cancer is an abnormal growth of tissue. There are four main types of cancer: (1) carcinomas, (2) sarcomas, (3) lymphomas and (4) leukemias. Carcinomas are malignant tissues that develop in the body's lining including the skin, the inside and outside of the body's organs, the glands, the lungs, and the digestive tract. Approximately 88 out of 100 human cancers are carcinomas. Sarcomas develop in the muscles, bones, fat and connective tissues of the body. About two cancers in 100 are sarcomas. A third type of cancer affects cells of the lymphatic system and is called lymphoma. Lymph is the clear

body fluid that carries disease-fighting white blood cells which flows through the body in tubes and collects in tiny pockets. Cancerous cells can travel throughout the lymph system, spreading from the origin of the tumor and metastasizing to other locations in the body. About five or six cancers in 100 are lymphomas. Leukemia is a fourth type of cancer and most often strikes children. Leukemia is cancer of the bone marrow which is a sponge-like, red tissue where the body creates red blood cells. Three or four cancers in a hundred are leukemias.

1.2 Methods of Cancer Treatment

Cancer is treated by one or a combination of several modalities or methods. These methods include surgical removal, chemotherapy, radiation, immunotherapy, hyperthermia, and most recently, gene therapy. Clinical treatment of cancer is directed by medically-trained physicians called oncologists. Surgical oncologists remove tumor masses from their patients. Medical oncologists administer chemotherapeutic and immunotherapeutic drugs. Radiation oncologists determine the type and quantity of radiation to deliver to tumors. The types of radiation include photons, electrons and neutrons. Radiation can be delivered to tumors with external beams from a linear accelerator. Another form of radiation therapy is brachytherapy where radiation emanates from implants that are placed surgically within interstitial and intercavitary catheters. Hyperthermia is the heating of tissue temperature above normal body temperature and may be used as an adjunct to radiation therapy and chemotherapy.

1.3 What is Hyperthermia?

Hyperthermia is generally understood today as a form of cancer therapy in which tissue is heated into a therapeutic temperature range to either directly kill tumor cells

and/or sensitize cancerous tissues to other forms of therapy. Hyperthermia is the antithesis of the more generally known form of 'thermia', hypothermia, which is the lowering of body temperature below normal body temperature.

1.3.1 Mechanisms of Cell Lethality

The mechanisms by which heat kills cells are far from understood. It is possible that various mechanisms and targets are involved (Hall, 1988). The targets include:

Plasma Membrane: The membrane consists of a phospholipid bilayer. The viscosity of the membrane varies with temperature. Agents can increase the fluidity of the plasma membrane and can increase the damage caused by a heat treatment. It is possible that damage to the plasma membrane may be a principle cause of cell death.

Proteins: The amount of energy required to kill cells by heat is nearly equal with that needed to damage proteins and inhibit protein synthesis. There is evidence that cells in the G-1[1] phase of the cell cycle die from membrane damage before reaching the next mitosis.

DNA: Abnormalities in chromosomes are produced at 45 C.

Hyperthermia has a direct cytotoxic effect. Heat can control experimental tumors without causing much damage to surrounding normal tissues (Crile 1963, Dickson *et al.* 1977; Marmor *et al.* 1979; Marmor *et al.* 1977; Overgaard 1978; Overgaard and Overgaard 1972; Overgaard and Suit 1979; Suit 1977). The cytotoxicity is enhanced by

---

[1]In tissue culture studies, the cyclic changes of the cell growth cycle are divided into specific periods or phases: the DNA synthesis or S phase; the G-2 phase or gap; the M or mitotic phase; and the G-1 phase.

increased cellular acidity, chronic hypoxia (low O_2) and insufficient nutrition (Dewey *et al.* 1977b; Freeman *et al.* 1977; Gerweck *et al.* 1979; Hahn 1974; Hill and Denekamp 1978; Overgaard 1978; Overgaard 1977; Overgaard 1976; Overgaard and Nielsen 1980; Suit Gerweck 1979). Furthermore, hyperthermia can alter tumor metabolism into a more anaerobic state by damaging the local vasculature and therefore reducing the blood flow in heated tumors (Cavaliere *et al.* 1967; Overgaard 1977; Song 1978; Storm *et al.* 1979).

1.3.2 Hyperthermia Alone

It is generally agreed that local hyperthermia by itself has a limited role in cancer therapy. The data to support this conclusion has been summarized by Overgaard (1982). The complete response rate (or elimination of the tumor) to heat alone does not exceed about 10% (Overgaard 1982).

1.3.3 Hyperthermia and Radiation

The interaction between hyperthermia and radiation *in vivo* (in living tissue) is complex. The ability to increase the effect of ionizing radiation is caused by both an increased direct radiosensitivity and a reduced ability to repair radiation damage (Ben-Hur *et al.* 1978; Bronk 1976; Dewey *et al.* 1980; Dewey *et al.* 1977a; Gerweck *et al.* 1975; Westra and Dewey 1971).

The use of hyperthermia combined with radiation in the treatment of local tumors offers significant advantages. Evidence from clinical trials indicates that the addition of heat may significantly enhance tumor destruction compared with radiation alone (Overgaard 1982). Several studies have shown that the frequency of complete response is usually doubled by the addition of heat compared with radiation alone (Overgaard 1982). Success has been reported in the treatment of superficial malignant tumors with

heat in combination with radiation (Emami *et al.* 1987; Perez and Emami, 1989). However, experience with hyperthermia in deep-seated tumors is still limited (Petrovich *et al.* 1989) and has shown no dramatic therapeutic advantage (Emami *et al.* 1991).

1.4 Hyperthermia Treatment Methods

Hyperthermia treatments can be given with any one of several methods. The location and size of the tumor often determine which method will provide the best treatment. Systemic cancers, especially tumors that have metastasized to multiple sites within the body, are generally treated with whole-body techniques. Tumors which are located predominantly in one site are treated with either non-invasive (externally applied) or invasive (interstitial) hyperthermia methods.

1.4.1 Whole-body Hyperthermia

Many whole-body hyperthermia methods have been used to increase core temperature. One of the oldest methods to increase core temperature is inducing fever by administration of bacteria or bacterial toxins which resets the patient's thermostat to a higher set-point (Coley 1893; Nauts 1982). Other methods can be divided into two forms – invasive and non-invasive. Applying energy to the body surface is characteristic of non-invasive techniques which include hot air (Pettigrew *et al.* 1974); hot water (Barlogie *et al.* 1979), either in direct contact with the skin or within bags, mattresses or suits; infrared electromagnetic radiation (Robins *et al.* 1985); or a combination of these methods. Invasive techniques include peritoneal irrigation with heated fluids (Priesching 1976) and extracorporeal circulation (Parks *et al.* 1979).

One advantage of whole-body hyperthermia is that a homogeneous temperature distribution can be reached throughout a deep-seated tumor. Disadvantages of whole-

body hyperthermia are that the tumor cannot be heated preferentially and that the maximum temperature tolerated is between 41.8 and 42 C (Pettigrew *et al.* 1974). Nonetheless, it has been shown that cells of certain tumors can be killed with temperatures between 41.8 and 42 C.

1.4.2 Non-invasive Hyperthermia

Electromagnetic and ultrasound heating are non-invasive hyperthermia methods which have been administered to superficial and deep-seated tumors. Clinical work in the mid 1970s using electromagnetic and ultrasound applicators was limited initially to the treatment of small (< 30-40 mm diameter) tumors (Kapp and Meyer 1990). Deep-seated tumors have been treated with radiofrequency capacitive methods (Song *et al.* 1986), radiofrequency inductive methods (Storm *et al.* 1985), external radiating electromagnetic methods (Turner 1984; Gibbs 1984; Oleson *et al.* 1986; Samulski *et al.* 1987; Kapp *et al.* 1988), and ultrasound methods (Hahn *et al.* 1981; Fessenden *et al.* 1985; Fessenden *et al.* 1984; Lele 1983; Swindell *et al.* 1982; Hynynen *et al.* 1987; Shimm *et al.* 1988).

1.4.3 Interstitial Hyperthermia

Interstitial hyperthermia can be produced with inductively heated ferromagnetic thermoseeds (Atkinson *et al.* 1984; Brezovich and Atkinson 1984; Kobayashi *et al.* 1986; Stauffer *et al.* 1984a), localized current field heating between pairs of temporarily implanted metallic electrodes (Astrahan and Normal 1982; Emami *et al.* 1987; Stauffer 1984; Strohbehn 1983; Vora *et al.* 1982; Zhu and Gandhi 1988), temporarily implanted microwave antennas (Coughlin *et al.* 1985; Emami *et al.* 1987; Salcman and Samaras 1983; Satoh and Stauffer 1988; Strohbehn *et al.* 1979), resistively heated wires, hot water

perfusion (Brezovich *et al.* 1989; Hand *et al.* 1991), or laser irradiation via fiber-optics (Daikuzono *et al.* 1987).

1.5 Interstitial Ferromagnetic Hyperthermia

Hyperthermia delivered with inductively heated ferromagnetic thermoseeds is a promising modality for heating deep-seated tumors (Brezovich and Meredith 1989). Thermoseeds are implanted surgically into a tumor volume and heated inductively by electromagnetic waves created by a concentric coil placed around the patient (Fig. 1.1). With this method, thermoseeds heat tissue locally via thermal conduction. Constant

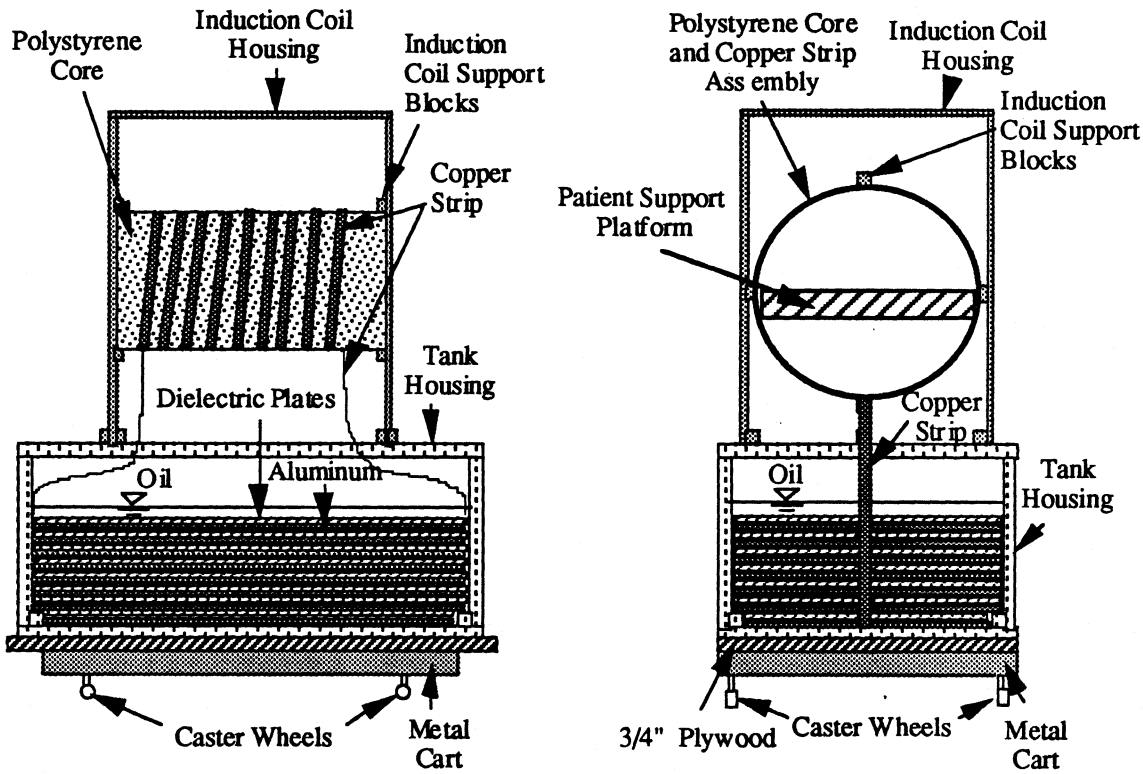

Figure 1.1 Electromagnetic coil used to inductively heat ferromagnetic thermoseeds. (Coil design was developed by collaborators at the University of Alabama-Birmingham.)

power and/or self-regulating thermoseeds have been investigated in both theoretical (Atkinson *et al.* 1984; Brezovich and Atkinson 1984; Chin and Stauffer 1991; Matloubieh *et al.* 1984; Mechling and Strohbehn 1986; Stauffer *et al.* 1984b; Vanderby *et al.* 1988; Tompkins *et al.* 1992b) and animal studies (Brezovich *et al.* 1990; Lilly *et al.* 1985; Partington *et al.* 1989; Tompkins *et al.* 1992a). Self-regulating thermoseeds have been shown to produce better tumor temperature distributions than constant-power seeds (Brezovich and Atkinson 1984; Matloubieh *et al.* 1984).

The ability of these thermoseeds to self-regulate is a consequence of their magnetic properties. Above a critical temperature known as the Curie point, thermoseeds lose their ability to absorb power. Self-regulating thermoseeds are composed of Ni-Cu (Brezovich and Atkinson 1984), Ni-Si (Chen *et al.* 1988; Oleson and Cetas 1982), Ni-Pd (Kobayashi *et al.* 1986) and other alloys (Burton *et al.* 1971; Moidel *et al.* 1976) and have well described Curie points. The Curie point can be made different for each thermoseed by altering the mass fraction of the diluent (*e.g.*, Cu, Si or Pd) in the thermoseed.

An advantage of self-regulating thermoseeds is their ability to absorb power so that the temperature along the length of the thermoseed is generally maintained within a few degrees of its operating temperature[2]. This method of regulation is advantageous since it is based upon an intrinsic material property of the implants. A potential disadvantage of ferromagnetic hyperthermia is that it is difficult to alter the temperature of individual thermoseeds during a hyperthermia treatment since there is no physical contact with thermoseeds. Thus there is a need to perform computerized pretreatment planning, similar to that used in radiotherapy, to predict temperature distributions *a priori*.

---

[2]The operating temperature of a thermoseed is defined as the temperature where 10 W of energy is absorbed per meter of length. The Curie point of a thermoseed is generally between 2.5 and 5 C higher than the operating temperature. The operating temperature, rather than the Curie point, is used throughout this study because thermoseed temperatures achieved and maintained during a hyperthermia treatment are closer to the operating temperature than the Curie point.

1.6 Optimization Studies

The following studies have been performed to determine optimum values of treatment variables in the delivery of hyperthermia: (1) A set of simulation input variables was determined to optimize a heat treatment for multiple electromagnetic applicators (De Wagter 1986); (2) A numerical method was developed to determine power deposition patterns for localized hyperthermia (Ocheltree and Frizzell 1988); (3) An optimization routine was used in a two-dimensional theoretical investigation to select the amplitudes and phases of a non-invasive microwave hyperthermia system for deep-seated tumors (Strohbehn *et al.* 1989); (4) Optimum amplitudes and phases were selected for 915 MHz peripheral sources to focus energy so that power outside a focal region was kept below a threshold (Arcangeli *et al.* 1984); (5) Yuan *et al.* (1990) optimized amplitudes and phases by comparing the theoretically computed results of eight concentric, fixed microwave apertures and a 4-applicator phased-array with movable apertures; (6) A theoretical study found that optimum power absorption per unit volume of cylindrical Ni-Si ferromagnetic thermoseed occurred when the applied magnetic field was axially parallel to the long-axis of the thermoseed and when the induction number was between 2 and 3 (Haider *et al.* 1991); (7) An *in vivo* study investigated the effect of thermoseed orientation within an electromagnetic coil, interseed spacing, generator power level and the presence of interstitial catheter sleeves on temperature distributions achieved with interstitial ferromagnetic hyperthermia (Tompkins *et al.* 1992a).

1.6.1 Temperature Based Objective Functions

An objective function is a mathematical equation. The maximum (or conversely, the minimum) of an objective function is expected to yield a set of conditions that will maximize (or minimize) a particular treatment goal. A systematic study of seven objective

functions was conducted to determine an optimal set of scanning parameters of an ultrasound hyperthermia system (Win-Li 1990). The objective functions were based on either ideal temperature distributions in tumor tissue, normal tissue, the boundary of normal and tumor tissues, or a combination of these. Criteria that were used to determine the suitability of a temperature distribution included: (1) all tumor tissue ≥ 43 C; (2) maximum tumor temperature ≤ 47 C; (3) tumor-normal tissue boundary = 43 C; (4) small volume of normal tissue ≥ 40 C; (5) maximum temperature of normal tissue ≤ 43 C; (6) presence of a unique minimum of the objective function; (7) sensitivity of the optimal scanning parameters to a weighting factor; (8) sensitivity of objective function values to variations in the scanning parameters at the minimum point; and (9) sensitivity of optimal scanning parameters to blood flow in tumor and normal tissue. For example, one of the seven objective functions proposed to obtain a uniform temperature of 45 C within the tumor model and a uniform temperature of 37 C within the normal tissue model. The temperature distribution was determined with a finite difference method, and the objective function is given by

$$\Phi = \frac{\sum (T_n - T_{n,\,set})^2}{N_n} + q\,\frac{\sum (T_t - T_{t,\,set})^2}{N_t} \tag{1.1}$$

In Eq. 1.1, N_n is the total number of finite difference nodes within the simulated normal tissue; N_t is the total number of finite difference nodes within the simulated tumor; T_n is the temperature of normal tissue at finite difference node n; T_t is the temperature of tumor tissue at finite difference node t; $T_{n,\,set}$ is a set temperature for normal tissue; $T_{t,\,set}$ is a set temperature for tumor tissue; and q is a scalar weighting factor.

Results from the study (Win-Li 1990) revealed that all objective functions had numerous local minima and therefore criteria 6 (above) could not be used to choose the *best* objective function. Three of the seven objective functions had a large range of suitable weighting factors which met all nine criteria above. Thus it was concluded that these three objective functions were satisfactory and the other four were less desirable. In words, these three objective functions are:

Objective Function 1: Maximize the ratio of the minimum temperature elevation within the tumor to the maximum temperature elevation within the normal tissue and require a uniform temperature on the tumor boundary of 43 C;

Objective Function 2: Require the minimum temperature within the tumor volume to be higher than 43 C, a uniform temperature on the boundary of the tumor and normal tissues at 43 C and a maximum temperature within the normal tissue lower 40 C;

Objective Function 3: Require a uniform temperature of 45 C within the tumor, a uniform temperature on the boundary of the tumor and normal tissues at 43 C, and a maximum temperature within the normal tissue lower than 40 C.

1.7 Objective and Significance

At the University of Wisconsin-Madison, several patients have been treated with a combination of interstitial brachytherapy and ferromagnetic hyperthermia. The hyperthermia treatment usually precedes (and occasionally follows) the brachytherapy treatment. Ferromagnetic thermoseeds are inserted within catheters whose locations have

been predetermined by brachytherapy treatment planning. In general, therefore, the challenge with ferromagnetic hyperthermia is to determine a combination of treatment variables, such as the interseed spacing and operating temperatures of thermoseeds, that will achieve the *best* temperature distribution in the tumor.

The major purposes of this study are to: (1) develop software to predict two-dimensional temperature distributions in tissue, (2) develop a heat transfer model which will simulate the thermal behavior of ferromagnetic thermoseeds and catheters, and (3) develop a physiologically-based objective function to determine optimum seed spacing and thermoseed operating temperatures used in ferromagnetic hyperthermia, (4) utilize temperature-dependent blood flow models in simulations, and (5) use a patient-specific tissue model in simulations. Unique to this study are items (3) and (4). Computerized pretreatment planning of interstitial ferromagnetic hyperthermia should be possible by accomplishing these tasks.

This study is described within Chapters 2 through 8. Chapter 2 discusses the bioheat transfer equation and the modification of a software program to solve the bioheat equation. Heat transfer models of self-regulating ferromagnetic thermoseeds and catheters are developed in Chapter 3. The implementation of realistic temperature-dependent power absorption of self-regulating thermoseeds in the finite element heat transfer model is discussed in Chapter 4. The formulation of an objective function to determine optimum values of hyperthermia treatment variables is presented in Chapter 5. The performance of the objective function to determine optimum thermoseed spacings and operating temperatures of thermoseeds is presented in Chapter 6. Simulations in Chapter 6 are preformed with a square array of thermoseeds which has been placed in a square tissue model with homogeneous and nonhomogeneous, temperature-independent blood flow rates. In Chapter 7, the objective function is used to determine optimum operating

temperatures of thermoseeds in the tissue model of a human patient. The effect of temperature-independent and temperature-dependent blood flow rates on optimum thermoseed temperatures is evaluated. Conclusions of the pretreatment planning model and recommendations for further research are discussed in Chapter 8.

Chapter 2

Tissue Temperature Prediction Using Bioheat Transfer Equation

Chapter 2 discusses the bioheat transfer equation and its finite element formulation (Secs. 2.1 and 2.2). An existing computer program was modified to solve the bioheat transfer equation. The capabilities of the computer software program are presented in Sec. 2.3. Some concluding remarks are made in Sec. 2.4.

2.1 Bioheat Transfer Equation

The partial differential equation used for predicting tissue temperatures in all hyperthermia models to date is based on the bioheat transfer equation by Pennes (1948)

$$\frac{\partial}{\partial x}(k_t \frac{\partial T}{\partial x}) + \frac{\partial}{\partial y}(k_t \frac{\partial T}{\partial y}) + \frac{\partial}{\partial z}(k_t \frac{\partial T}{\partial z}) + g_m''' + g_a'''$$

$$- \rho_t \rho_b c_b m (T - T_b) = \rho_t c_t \frac{\partial T}{\partial t} \qquad (2.1)$$

In Eq. 2.1, k_t is the thermal conductivity of tissue [W/m-C]; ρ_t is the density of tissue [kg/m^3]; ρ_b is the density of blood [kg/m^3]; c_t is the specific heat of tissue [J/kg-C]; c_b is the specific heat of blood [J/kg-C]; m is the volumetric flow rate of blood per unit mass of tissue [m^3/s-kg]; g_m''' is the energy dissipation rate per unit volume due to metabolic

processes [W/m^3]; g_a''' is the energy absorption rate per unit volume of tissue from an applied energy field [W/m^3]; T is tissue temperature [C]; T_b is the blood temperature [C]; t is time [s]; and x, y and z are the orthonormal directions [m] in a rectangular coordinate system.

Some assumptions can be made to simplify Eq. 2.1. One assumption is that tissue absorbs a negligible amount of energy at the electromagnetic field frequencies (~95 kHz) used in ferromagnetic hyperthermia. Therefore, $g_a''' \sim 0$. Another assumption is that the rate of energy dissipated in tissue due to metabolic processes g_m''' can be small relative to the energy applied to the tissue by a hyperthermia system (Jain 1983). Therefore, $g_m''' \sim 0$. In addition to these assumptions, the transient time during the hyperthermia treatment is often small relative to the steady-state time (Partington *et al.* 1989; Tompkins *et al.* 1992a). Hence steady-state solutions to Eq. 2.1 are usually sought.

Setting the mass flow rate of blood per unit volume of tissue w_b [kg/s-m^3] equal to $\rho_t \rho_b m$, the two-dimensional, steady-state form of Eq. 2.1 becomes

$$\frac{\partial}{\partial x}\left(k_t \frac{\partial T}{\partial x}\right) + \frac{\partial}{\partial y}\left(k_t \frac{\partial T}{\partial y}\right) - w_b c_b (T - T_b) = 0 \qquad (2.2)$$

Equation 2.2 is only an approximation. The major assumption with the use of Eq. 2.2 is that heat transfer occurs between tissue and blood in the capillary bed, which is made of many small, 6μ-diameter (Ganong 1967) blood vessels. The blood vessels in the capillary bed are assumed to be nondirectional. The number density of arterioles (30 μ-diameter), capillaries, and venules (20 μ-diameter) are sufficiently large and the blood flow sufficiently low that the temperature of tissue and the blood at the ends of the capillaries are assumed equal. Thus blood enters the local tissue volume at the arterial

temperature and leaves this volume at the local tissue temperature. Pennes (1948) modeled the net energy transfer between tissue and blood as a linear heat sink as defined by the third term on the left-hand side of Eq. 2.2.

There are other limitations to Eq. 2.2. The equation neglects the heat transfer related to the mass transfer of blood and the cooling of individual large vessels. Equation 2.2 also neglects the energy transfer between tissue and the venous system by assuming an infinite thermal equilibration length for all venous vessels. In reality, heat transfer is not limited to energy transfer between tissue and capillaries but occurs also in arteries and veins (Chen and Holmes 1980; Mitchell *et al.* 1970; Perl 1965; Wissler 1963). Countercurrent heat transport between adjacent vessels has also been shown to be significant (Weinbaum and Jiji 1985; Johnsen 1989; Mitchell *et al.* 1970). Nonetheless, temperature distributions as predicted by Eq. 2.2 have been shown to be useful and accurate (Matloubieh *et al.* 1984). Additional details on the formulation and limitations of the bioheat transfer equation can be found elsewhere (Bowman *et al.* 1975; Roemer 1988).

Other bioheat transfer equations have been developed which model the vascular architecture of the body more directly than the Pennes equation (Chen and Holmes 1980; Lagendijk 1982; Weinbaum *et al.* 1984; Weinbaum and Jiji 1985). These equations are generally more complex than the Pennes equation. For example, the bioheat transfer equation of Weinbaum *et al.* (1984) has tensor thermal conductivity terms to model heat transfer in tissue where the blood flow has a strong directional dependence. Equations of these type often require vast details of the vascularity in the tissue. Since anatomical details of this complexity are limited, heat transfer modelers have not, to date, used these other bioheat transfer equations to predict temperatures for hyperthermia pretreatment planning.

Material and thermal properties of tissue and blood are generally independent of temperature and considered uniform throughout each tissue type. Blood flow rates, however, can depend on temperature. Experiments with muscle and skin tissues of mice have revealed large increases in blood flow rates with increasing temperature (Song *et al.* 1984). Simulations in the present study will be performed for several constant blood flow rates ranging from $m = 0$ to 1 l/min-kg (see Chapters 3 through 7). In addition, the effect of temperature-dependent blood flow rates on temperature distributions will be studied in Chapter 7.

2.2 Finite Element Formulation of Bioheat Transfer Equation

Equation 2.2 has exact analytical solutions when applied to a square domain with various boundary conditions (Carslaw and Jaeger 1959). Solving the bioheat transfer equation for realistic tissue models, however, requires a numerical solution since the anatomical structure of tissues is complex. Tumors and surrounding normal tissues are often made up of several different tissue types, each with their own thermal properties and blood flow rates. It is therefore not practical to obtain an analytical solution of the bioheat transfer equation for realistic tissue models. Thus the finite element numerical method was used to solve Eq. 2.2. The following is a brief overview of the Galerkin approach of the finite element method (Myers 1989).

After rearranging terms, Eq 2.2 can be multiplied by a weighting function f(x,y) and then integrated over the tissue area to give

$$\iint_{Tissue} f(x,y) \left\{ \rho_t c_t \frac{\partial T}{\partial t} + \left[\frac{\partial}{\partial x} \left(-k_t \frac{\partial T}{\partial x}\right) + \frac{\partial}{\partial y} \left(-k_t \frac{\partial T}{\partial y}\right) \right] + w_b c_b (T - T_b) \right\} dx\, dy = 0 \qquad (2.3)$$

It is assumed that the temperature distribution within the tissue can be approximated by N terms

$$T\ (x,y,t) = w_1(x,y)\ T_1(t) + w_2(x,y)\ T_2(t) + \cdots + w_i\ (x,y)\ T_i(t) + \cdots + w_N\ (x,y)\ T_N(t)$$

where $w_i\ (x,y)$ are linear interpolating functions and $T_i(t)$ are temperatures at specific points within the tissue region. A set of N differential equations can be obtained by using N independent functions $f_1\ (x,y), \ldots, f_i\ (x,y), \ldots, f_N\ (x,y)$. The Galerkin technique requires that each $f_i\ (x,y) = w_i\ (x,y)$. After performing several integrations, utilizing matrix techniques and algebra (see Appendix A), Eq. 2.3 can be cast into a system of N ordinary differential equations. In matrix notation, these equations are

$$\mathbf{C}\dot{\mathbf{T}} + (\mathbf{K} + \mathbf{B})\mathbf{T} = \mathbf{b} + \mathbf{q_o} \tag{2.4}$$

In Eq. 2.4, **C** [J/m-C], **K** [W/m-C] and **B** [W/m-C] are the capacitance, conduction and perfusion matrices, respectively; **T** [C] is the temperature vector; $\dot{\mathbf{T}}$ [C/s] is the vector containing the time rate of change of **T**; **b** [W/m] is the perfusion vector; and $\mathbf{q_o}$ [W/m] is the vector containing the energy inflows at the boundaries of the tissue model. Notation for the **C** and **K** matrices and the **T**, $\dot{\mathbf{T}}$ and $\mathbf{q_o}$ vectors were defined previously by Myers (1987).

2.3 Numerical Solution Software

The finite element heat transfer computer program called FEHT (pronounced 'feet') that was developed previously to solve heat conduction problems (Klein *et al.* 1988) was modified to solve Eq. 2.4. The modification required the inclusion of the

perfusion matrix **B** and perfusion vector **b** into the equation solving routine FEM2D (Myers 1987) of FEHT.

The modification of FEHT to solve bioheat problems is illustrated by the 'Bio-Heat Transfer' menu item in the 'Subject' menu of FEHT (Fig. 2.1). By simply selecting the 'Bio-Heat Transfer' menu item, the user is capable of solving Eq. 2.1 numerically with the finite element method. The blood temperature T_b (see Eq. 2.1) can be specified by selecting the 'Blood Temperature' menu item located at the bottom of the 'Setup' menu in FEHT (Fig. 2.2). The modifications to FEHT shown in Figs. 2.1 and 2.2 were made by Klein (1989).

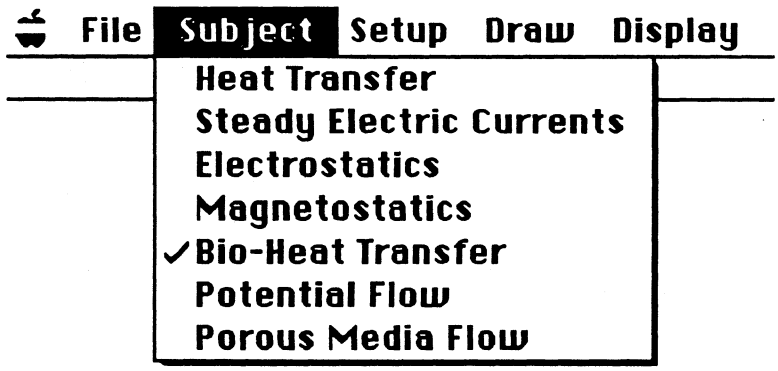

Figure 2.1 A screen display of the 'Subject' menu in FEHT depicting the selection of the 'Bioheat Transfer' menu item. By selecting the 'Bio-Heat Transfer' menu item, the user can solve problems which are described mathematically by Eq. 2.1. The 'Bio-Heat Transfer' menu item was created by Klein (1989).

FEHT can predict either steady-state or transient temperature distributions (Klein *et al.* 1988). Steady-state temperatures are determined by solving a set of algebraic equations (Appendix A). Transient temperature distributions are obtained by solving Eq. 2.4 with either the Crank-Nicolson or the Euler method (Appendix A). FEHT has been

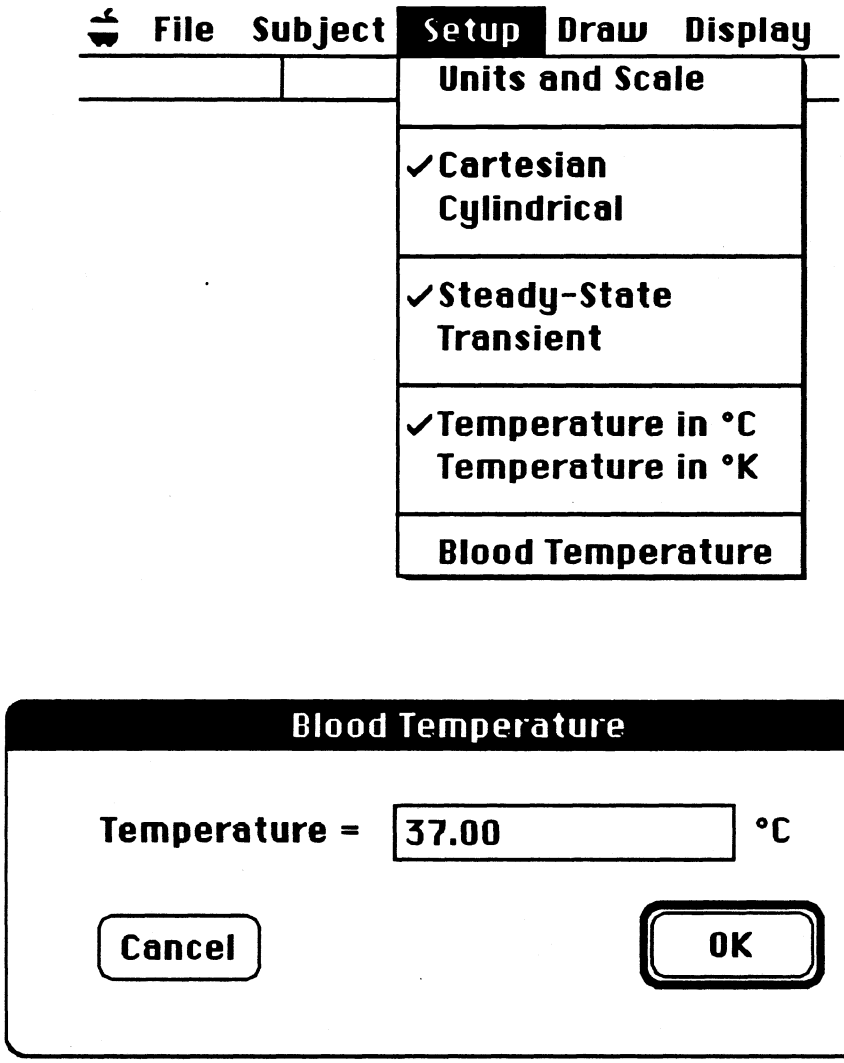

Figure 2.2 A screen display of the 'Setup' menu in FEHT displaying the 'Blood Temperature' menu item. By selecting the 'Blood Temperature' menu item, the user can set the blood temperature T_b in Eq. 2.1. The 'Blood Temperature' menu item and dialog box were created by Klein (1989).

designed for use on Macintosh computers. FEHT will allow either constant, spatially-dependent, temperature-dependent or time-dependent properties (Klein *et al.* 1988). The accuracy of the temperature distribution computed by FEHT was evaluated for a simple tissue model (Appendix B).

FEHT contains its own preprocessor to define tissue regions (Klein *et al.* 1988). Contours of tissue regions can be 'pasted' into FEHT via the Macintosh clipboard feature. Using pull-down menus and internal algorithms, arbitrarily-shaped tissue regions can be outlined. The simulated tissue regions are then discretized into several triangular-shaped areas called *finite elements*. The vertices of the triangular-shaped elements are called *nodes*, and the lines connecting the nodes are called *element lines*. Finite element nodes

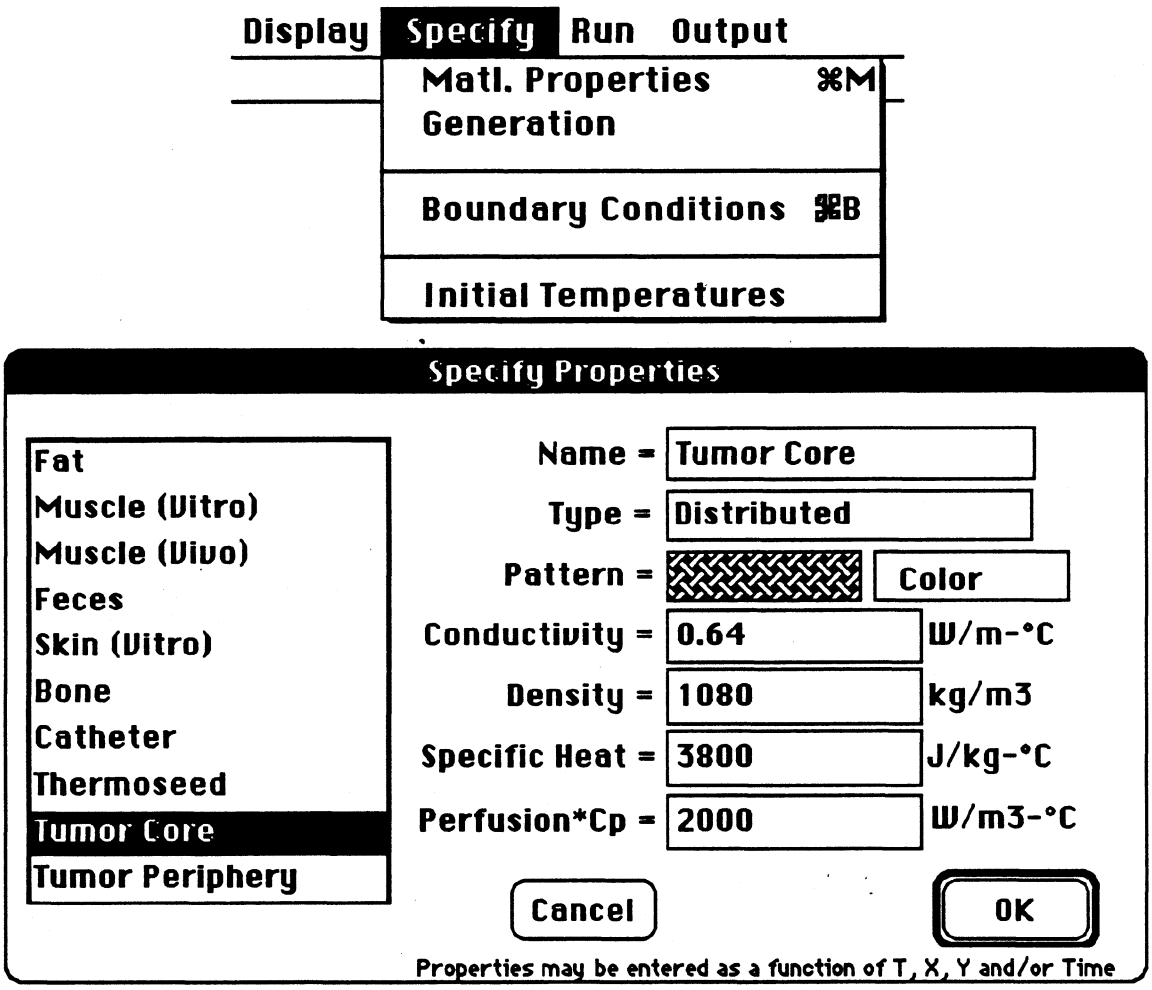

Figure 2.3 A screen display of the 'Specify' menu in FEHT showing the 'Matl. Properties' menu item. By selecting the 'Matl. Properties' menu item, the user can specify tissue properties including thermal conductivity k_t, density ρ_t, specific heat c_t, and tissue perfusion $w_b c_b$. Properties can be entered as a function of x, y, temperature T and/or time t. The addition of the 'Perfusion*Cp =' feature to the 'Specify Properties' dialog box was performed by Klein (1989).

and lines are created by FEHT with simple, computer-based 'mouse' operations. An automatic finite element mesh reduction capability is provided (Klein *et al.* 1988).

Material, thermal and blood flow properties of each tissue are specified by 'mouse' operations and keyboard entries (Fig. 2.3). The numerical expressions for spatially-dependent, temperature-dependent or time-dependent blood flow rates can be entered with keyboard entries (Klein 1989). Boundary conditions including constant temperature, specified heat-flux and convective boundaries can be specified easily with FEHT. A check to ensure the completeness of the finite element mesh can be made with a pull-down menu. These and several other capabilities including a text editor are discussed in the FEHT reference manual (Klein *et al.* 1988).

FEHT has several post-processing features (Klein *et al.* 1988). Temperatures predicted by FEHT can be viewed at nodal locations or as contours of iso-lines or multi-colored shaded bands. Heat flows across element lines and nodal energy balances can also be displayed. Solutions to transient problems can be viewed such as the temperature or energy flow versus time. Lastly, FEHT produces a report which includes all input data and output data such as the predicted temperatures and energy balances of all nodes (Klein *et al.* 1988).

2.4 Concluding Remarks

The bioheat transfer equation (Pennes 1948) is used in this study to predict temperature distributions in tissue. The assumptions and limitations of the bioheat transfer equation by Pennes were discussed. The Pennes bioheat equation has been shown to adequately predict temperature distributions in tissue models simulating hyperthermia treatments (Matloubieh *et al.* 1984). In addition, other proposed bioheat transfer equations were discussed. These other bioheat transfer equations, such as the

Weinbaum and Jiji (1984) bioheat equation, generally require details of vascular anatomy that are not yet tractable for routine use in thermal modeling of tissue systems. Thus the bioheat equation of Pennes was used in this study.

The finite element method was used to transform the bioheat equation into a system of equations which can be solved with a computer. The existing computer program FEHT was modified by Klein (1989) to solve the bioheat equation. The capabilities of the FEHT program were discussed.

Chapter 3

Ferromagnetic Thermoseed and Catheter Models

Thermal models of ferromagnetic thermoseeds have been developed previously. An analytical model simulating thermoseeds as point sources of heat was developed (Atkinson *et al.* 1984; Brezovich and Atkinson 1984). The studies of Atkinson *et al.* (1984) and Brezovich and Atkinson (1984) revealed that the temperature uniformity in tumors heated by self-regulating thermoseeds was better than that in tumors with constant power implants. The difference in temperature uniformity became obvious in tumor models with very large or very small rates of blood flow and in tumors heated with irregular implant spacings. By modeling thermoseeds as point sources, Brezovich and Atkinson (1984) neglected the finite size of the thermoseeds and catheters where no tissue perfusion is present. In another finite difference model, parametric studies were performed to study the effect of blood flow on temperature distributions (Vanderby *et al.* 1988).

A finite difference model was developed by Matloubieh *et al.* (1984) and subsequently used by others (Chen 1989; Chen *et al.* 1991; Haider *et al.* 1991). An empirical power absorption formula developed by Haider *et al.* (1991) for thermally self-regulating Ni-Si ferromagnetic thermoseeds was used to compare two- and three-dimensional simulations for ferromagnetic implant hyperthermia (Chen *et al.* 1991). The results show that two-dimensional simulations can significantly over estimate

temperatures. However, Chen *et al.* (1991) also concluded that for ferromagnetic seeds longer than 30 mm, two-dimensional calculations will yield reasonable estimates for the central cross-sections.

The finite element method has been used to compute temperature distributions resulting from an implant array of thermoseeds and were compared with the heating patterns of interstitial microwave antennas and radiofrequency electrode needles (Mechling *et al.* 1986). In a parametric study, Mechling *et al.* (1986) showed that microwave antennas adequately heated a larger number of simulated tissues to therapeutic temperatures than either ferromagnetic thermoseeds or radiofrequency electrode needles.

The finite element method was also used to compare two- and three-dimensional thermal models of thermoseeds and determine the appropriate use and limitations of the two-dimensional model (Chin and Stauffer 1991). Chin and Stauffer (1991) showed that the two-dimensional thermal model, which assumes infinite extent of the ferromagnetic seed(s), is applicable for calculating temperature distributions in any plane perpendicular to the axes of the thermoseed(s) up to 10 mm from the ends of the seed(s).

An analytical thermal model of a single thermoseed implanted in tissue is developed in this chapter (Sec. 3.1). Numerical thermal models of thermoseeds (and catheters) including a point-source and two finite-sized thermal models are developed in Sec. 3.2. Temperature distributions from the analytical model are compared with the finite-sized numerical thermal models (Sec. 3.3). A method for placing finite-sized models of thermoseeds and catheters in finite element meshes created by FEHT is presented in Sec. 3.4. Concluding remarks are discussed in Sec. 3.5.

3.1 Analytical Thermal Model

An energy balance was performed on a small circumferential element of tissue to determine the analytical steady-state temperature distribution $T(r)$ in the tissue model shown in Fig. 3.1. The tissue model in Fig. 3.1 is the radial cross-section of a cylindrically-shaped tissue system in which the long axis of a thermoseed was placed along the centerline of the tissue.

The following assumptions were made in the development of the analytical thermal model: i) the ferromagnetic thermoseed is assumed infinite in length and the cross-section in Fig. 3.1 is at the central plane, therefore, thermal conduction was in the radial direction only (Chen *et al.* 1991, Chin and Stauffer 1991); ii) energy entered and left the system via blood flow; iii) the thermal conductivity k_t of the tissue was that of resting muscle tissue (k_t = 0.64 W/m-C) and was constant and uniform throughout the simulated tissue; iv) the specific heat c_b of blood (c_b = 3900 J/kg-C) was also constant and uniform; v) the tissue absorbed a negligible amount of energy at the electromagnetic field frequencies (~ 95 kHz) used in ferromagnetic hyperthermia; vi) the rate of energy dissipation by metabolic processes within the tissue was negligible (Jain 1983); vii) the blood temperature was constant and equal to the body core temperature of 37 C; viii) the thermal contact resistance at the interface of the thermoseed and tissue was negligible.

With the assumptions discussed above, an energy balance on the circumferential element of tissue yields

$$\frac{d}{dr}\left(r\,\frac{dT}{dr}\right) - n^2 r\,(T - T_b) = 0 \tag{3.1}$$

In Eq. 3.1, r is the radial length [m] and n is a parameter equal to $= \sqrt{w_b c_b / k_t}$ [m^{-1}]. Substituting $\theta(r) = T(r) - T_b$, Eq. 3.1 becomes

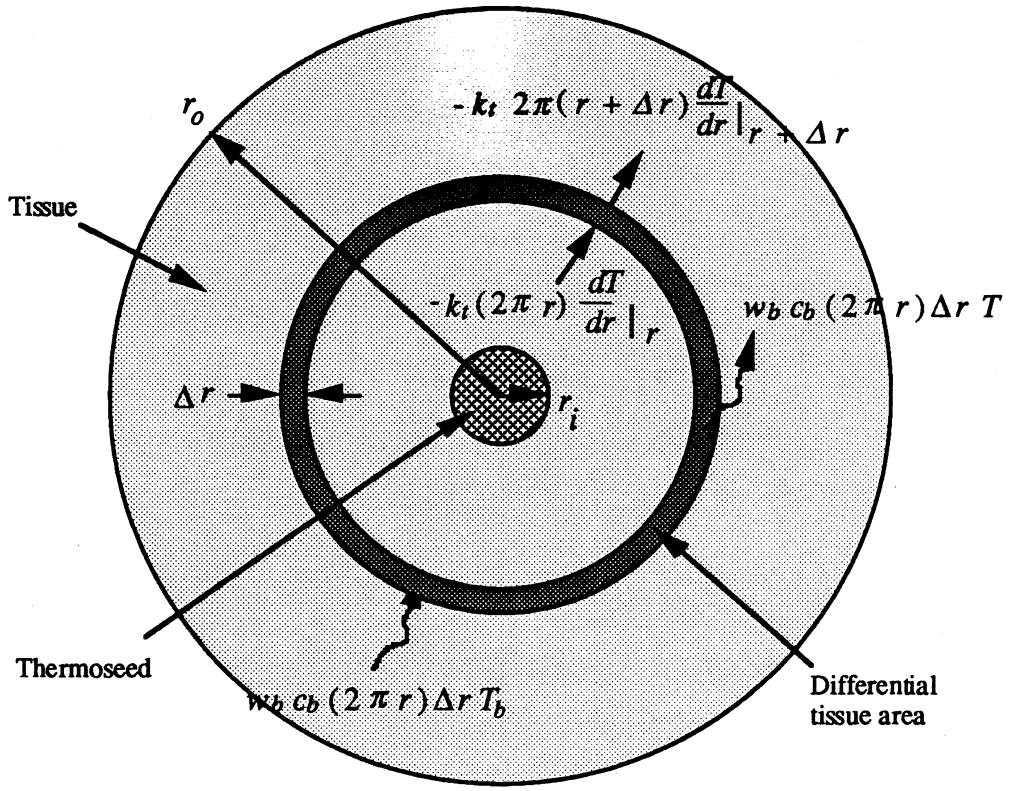

Figure 3.1 Radial cross-section of a thermoseed (cross-hatched-shaded circle) implanted at the center of a cylindrical tissue model (light-shaded region). Conductive and convective-like energy inflows and outflows into the differential tissue area (dark-shaded region) are shown.

$$\frac{d}{dr}\left(r\frac{d\theta}{dr}\right) - n^2 r\,\theta(r) = 0 \tag{3.2}$$

Since thermoseeds are heated inductively by eddy currents (Sec. 4.1.1), a heat flux q'' [W/m^2] is produced at the inner radius r_i of the tissue model. The outer radius r_o of the tissue model was assumed to have a temperature equal to body core temperature (= T_b). Thus the boundary conditions for Eq. 3.2 are given by

$$r = r_i: \quad q'' = \frac{P'i}{A_s} = -k_t \frac{d\theta}{dr}\Big|_{r=r_i} \tag{3.3a}$$

$$r = r_o: \quad \theta = 0 \tag{3.3b}$$

In Eq. 3.3a, P' [W/m] is the energy absorption rate per unit length of a thermoseed which is parallel to an electromagnetic field (Sec. 4.1.1), i is a unit length multiplier, and A_s [m^2] is the cross-sectional area of the thermoseed. The solution to Eq. 3.2 for the temperature distribution in the tissue as a function of radial distance was found to be

$$\theta(r) = \frac{P' r_i}{2 A_s n k_t} \frac{\left[I_0(nr_o) K_0(nr) - K_0(nr_o) I_0(nr)\right]}{\left[I_1(nr_i) K_0(nr_o) + I_0(nr_o) K_1(nr_i)\right]} \tag{3.4}$$

In Eq. 3.4, I_0 and K_0 are modified Bessel functions of the first and second kind of order 0, respectively, and I_1 and K_1 are modified Bessel functions of the first and second kind of order 1, respectively (Abramowitz and Stegun 1964).

3.2 Numerical Thermal Model

The development of a numerical thermal model for a ferromagnetic thermoseed begins with a discussion of the appropriate form of the energy equation (Sec. 3.2.1). A point-source thermal model of a thermoseed is discussed in Sec. 3.2.2 and the finite-sized thermal model is developed in Sec. 3.2.3.

3.2.1 Energy Equation

All of the assumptions discussed in Sec. 3.1 are valid in the development of the numerical thermal model of a thermoseed. The heat conduction in the simulated tissue in Fig. 3.1 is assumed to be one-dimensional, and the solution for the temperature distribution using the numerical method is sought for heat conduction in only the radial

direction. Because FEHT determines temperature distributions in two dimensions, Eq. 2.2 is the energy equation which will be solved with the finite element method.

3.2.2 Point-source Thermal Model

The finite element mesh of a symmetrical portion of the circular tissue model shown in Fig. 3.1 was created with FEHT and displayed in Fig. 3.2. Five finite element meshes

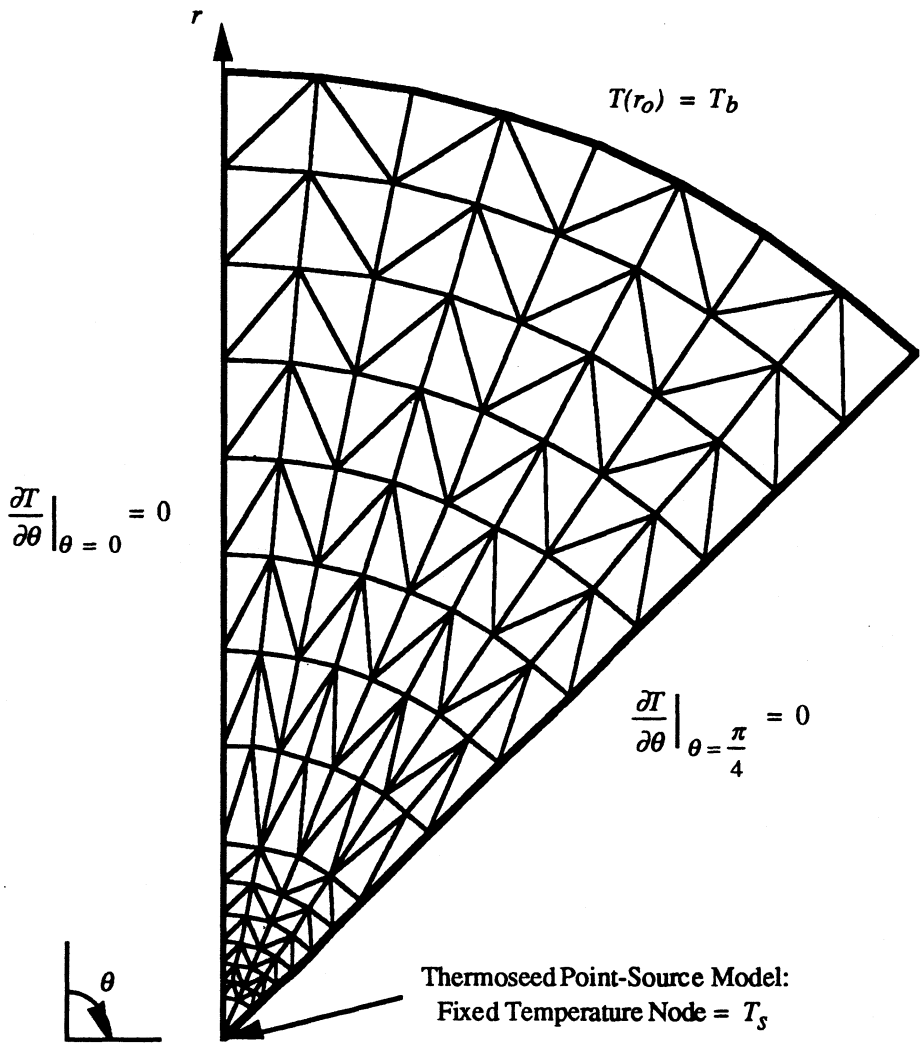

Figure 3.2 The finite element mesh of a symmetrical portion of the thermoseed and tissue shown in Fig. 3.1. The thermoseed is modeled as a node of fixed temperature T_s. The two radial edges at $\theta = 0$ and $\theta = \pi/4$ are adiabatic boundaries since they are lines of symmetry. The outer edge at $r = r_o$ is fixed at the body core temperature T_b.

were created consisting of 172, 176, 180, 184 and 736 elements. The meshes with 176, 180 and 184 elements were created by increasing the number of finite elements near the thermoseed of the mesh with 172 elements. The finite element mesh of 736 elements was created by reducing uniformly the mesh of 184 elements. (Thus there were four finite elements in the mesh with 736 finite elements for every element in the mesh with 184 elements.) The lower corner of each mesh is enlarged to show details of the finite element mesh near the point source (Fig's. 3.3a through 3.3e). In each mesh in Fig. 3.3, the finite element node in the lower left-hand corner was used to simulate a ferromagnetic thermoseed as point source of heat.

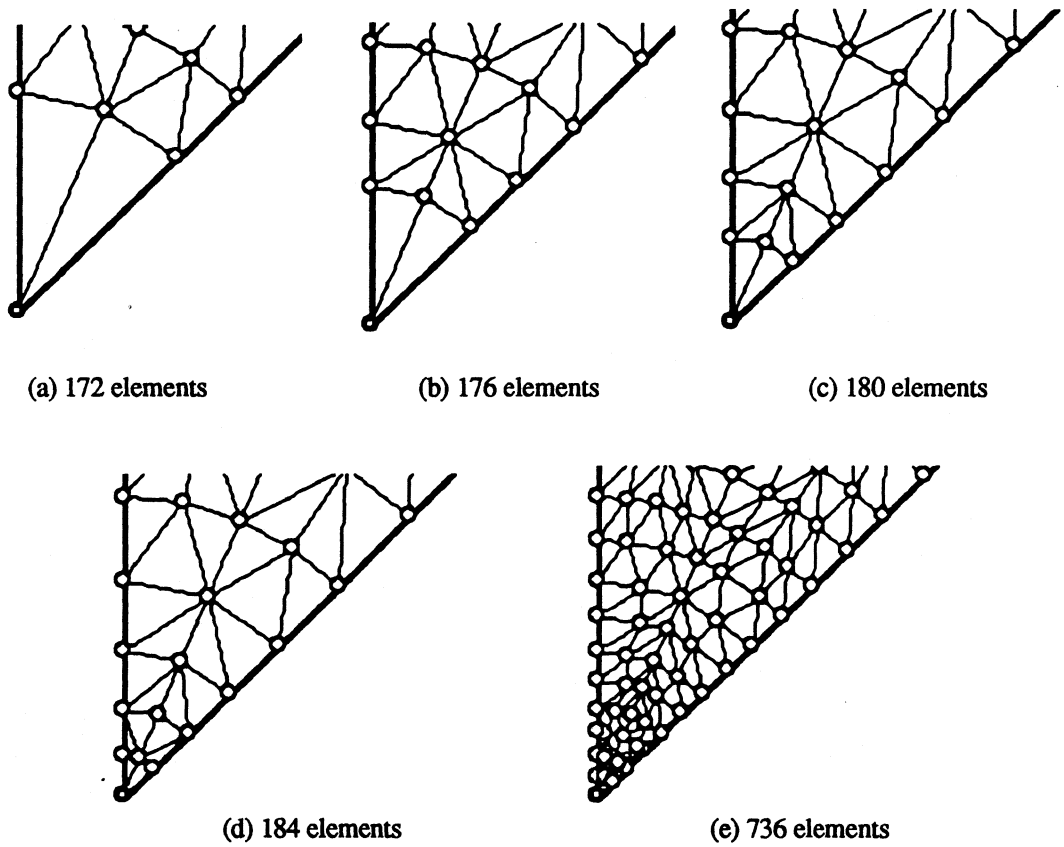

(a) 172 elements (b) 176 elements (c) 180 elements

(d) 184 elements (e) 736 elements

Figure 3.3 Enlarged lower corner of the finite element mesh shown in Fig. 3.2. Meshes contained either (a) 172 elements, (b) 176 elements, (c) 180 elements, (d) 184 elements or (e) 736 elements. Circles designate finite element node locations.

The power per unit length P' leaving the thermoseed point-source model was computed by performing an energy balance on a differentially-sized area around the simulated-thermoseed node (Sec. A.2.4 in Appendix A). The differentially-sized area is the summation of 1/3 of the area of each finite element surrounding the simulated-thermoseed node. The energy balance was computed with FEHT and equaled the power P' that would leave the thermoseed point-source model.

Simulations were performed to study the influence of element discretization and blood flow rate on the power P' leaving a thermoseed. Simulations were performed with blood flow m of 0.01, 0.1 and 1 l/min-kg[3]. The thermoseed was modeled as a node with a fixed temperature T_s = 60 C (Fig. 3.2). The two radial edges of the tissue model are specified adiabatic boundaries (lines of symmetry). The outer edge of the tissue at $r = r_o$ was at body core temperature of T_b = 37 C (Fig. 3.2).

Results of the simulations are shown in Table 3.1 and Fig. 3.4. In Fig. 3.4, the power per unit length P' leaving the simulated-thermoseed point-source model is shown versus the normalized nodal area. For the five finite element meshes, the nodal area around the point source was normalized to the largest nodal area, that of the mesh with 172 elements (as labelled with vertical arrows in Fig. 3.4). The power P' leaving the thermoseed-node decreased with decreasing nodal area. As shown by the three curves in Fig. 3.4, P' approaches zero as the nodal area approaches zero. In the limit, therefore, the temperature gradient at the *surface* of the thermoseed would be infinite.

In conclusion, the zero-area, point-source thermoseed model is an invalid model to simulate the thermal behavior of a thermoseed. Other studies are consistent with the re-

---

[3]Often blood flow rates are given in units of ml/min-(100 g of tissue). However, the units of ml, min and g are all non SI. To be in more agreement with SI standards, blood flow rates in the present study will have units of l/min-kg. To convert from ml/min-(100 g of tissue) to l/min-kg, simply divide by 100.

Table 3.1 Power P' of the Point-Source Numerical Thermoseed Model

Number of Finite Elements	Energy Balance Area (m^2)	Blood Flow Rate, m (l/min-kg)	Nodal Energy Balance, P' (W/m)
172	2.25e-6	0.01	2.90
"	"	0.1	4.10
"	"	1	7.37
176	1.05e-6	0.01	2.65
"	"	0.1	3.61
"	"	1	5.81
180	3.76e-7	0.01	2.38
"	"	0.1	3.11
"	"	1	4.56
184	7.91e-8	0.01	2.03
"	"	0.1	2.60
"	"	1	3.50
736	1.98e-8	0.01	1.83
"	"	0.1	2.24
"	"	1	2.87

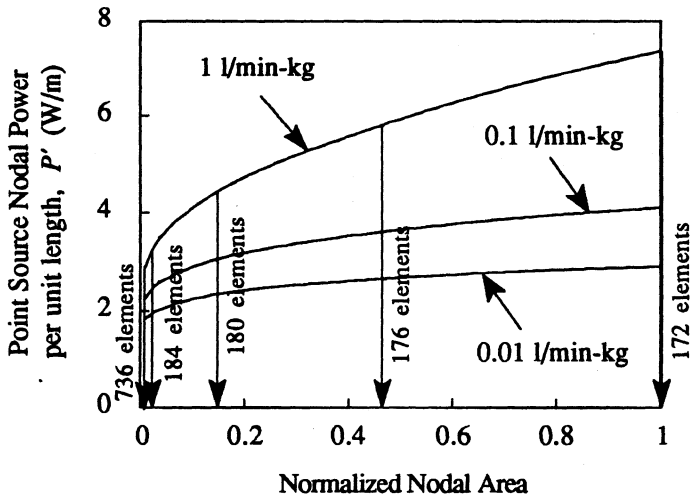

Figure 3.4 Power per unit length P' leaving the point-source numerical thermoseed model versus the normalized nodal area. Simulations were performed with blood flow in tissue m = 0.01, 0.1 and 1 l/min-kg and with finite element meshes consisting of 172, 176, 180, 184 and 736 elements.

sults obtained with the thermoseed point-source model. Chen (1989) and Haider *et al.* (1991) have shown that modeling thermoseeds as line sources in three dimensions can not accurately represent the physical behavior of thermoseeds.

3.2.3 Finite-Sized Thermal Model

Although thermoseeds are circular in radial cross-section, the finite element method uses linear elements. Thus the finite-sized numerical thermal models of the circular thermoseed were approximated by straight-line segments. A regular hexagon and a dodecagon (12-sided polygon) were studied as models for thermoseeds (Fig. 3.5). The cross-sectional areas of the hexagonal $A_{s,\ reg.\ hexagon}$ and dodecagonal $A_{s,\ dodecagon}$ thermoseed models were equal to the cross-sectional area A_s of a thermoseed.

The thermoseed was modeled as a thermally-lumped material because of its high thermal conductivity ($k_s \sim 25$ W/m-C) and its small thickness ($2a = 0.9$ mm diameter). Thus the thermal conductivity of the thermoseed is assumed to be infinite since this model assumes there is a negligible temperature gradient within the thermoseed[4]. The

---

[4]The temperature profile $T(r)$ within a thermoseed with energy generation $g_s''' = 1.5e7$ W/m^3, a thermal conductivity $k_s = 25$ W/m-C (55% Cu and 45% Ni, Incropera and Dewitt 1985), no blood flow, a seed radius $a = 0.45$ mm and a seed surface temperature $T_s = 48$ C can be determined with the following equation

$$T(r) = \frac{g_s''' a^2}{4 k_s} [1 - (r/a)^2] + T_s$$

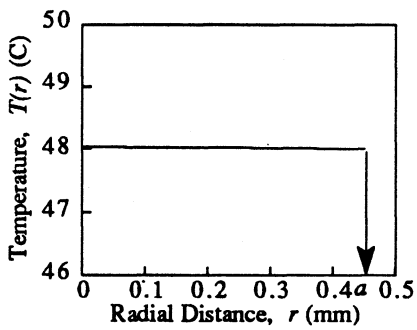

Notice the flat temperature profile within the thermoseed. Therefore the assumption of a negligible temperature gradient within the thermoseed is justified.

thermoseed was modeled with zero blood flow ($w_b c_{b\,s} = 0$). The thermoseed was also modeled with an energy absorption rate per unit volume g_s''' which was numerically equal to the energy absorption rate per unit length P' divided by the cross-sectional area of a thermoseed A_s. The catheter[5] was modeled as a region of distributed temperature with a thermal conductivity k_{cat} = 0.34 W/m-C (Clay-Adams Co., 1991) and with zero blood flow ($w_b c_{b\,cat} = 0$). The area of the catheter model was equal to the area of an actual catheter with a wall thickness t_{cat} 0.35 mm. It is assumed that the thermoseed and catheter are in perfect contact, and therefore, there is no temperature drop across the interface of the catheter and thermoseed models.

The transfer of energy from the thermoseed to the surrounding tissue (or catheter, if present) was modeled with a convection boundary coefficient h_{ij}. The product $h_{ij}A_{ij}$ represents the thermal conductance between thermoseed i and finite element node j of the thermoseed, where A_{ij} is the boundary-segment area of node j (Fig. 3.5). A simulation study was performed to determine an adequate numerical value for h_{ij} such that the thermal resistance ($1/h_{ij}A_{ij}$) between the thermoseed and tissue (or catheter) is negligible. (Using extremely large values of h_{ij} results in numerical problems for FEHT.[6]) Simulations were performed with a finite element mesh created for a symmetrical portion of the tissue model in Fig. 3.1 (Fig. 3.6). An enlargement of the dodecagonal thermoseed model and surrounding finite elements in the tissue model are shown in Fig. 3.7. In the simulations, the energy absorption rate per unit volume of thermoseed g_s''' (= $P'/A_{s,\,dodecagon}$) was 2.02e7 W/m^3. The FEHT program was used with values of h_{ij} between 1e2 and 1e6. Temperatures $T_{s,\,surface\,j}$ at five finite element nodes (j = 1, 2, ...,

---

[5]The catheter is a small-diameter polyetheylene tube that is placed in the body and is used as a sleeve for thermoseeds.

[6]Simulations in this study used versions of FEHT less than Ver. 6.2. However, since double-precision is used in all calculations with Ver. 6.2 or greater, the numerical instability problem with h_{ij} can most likely be avoided.

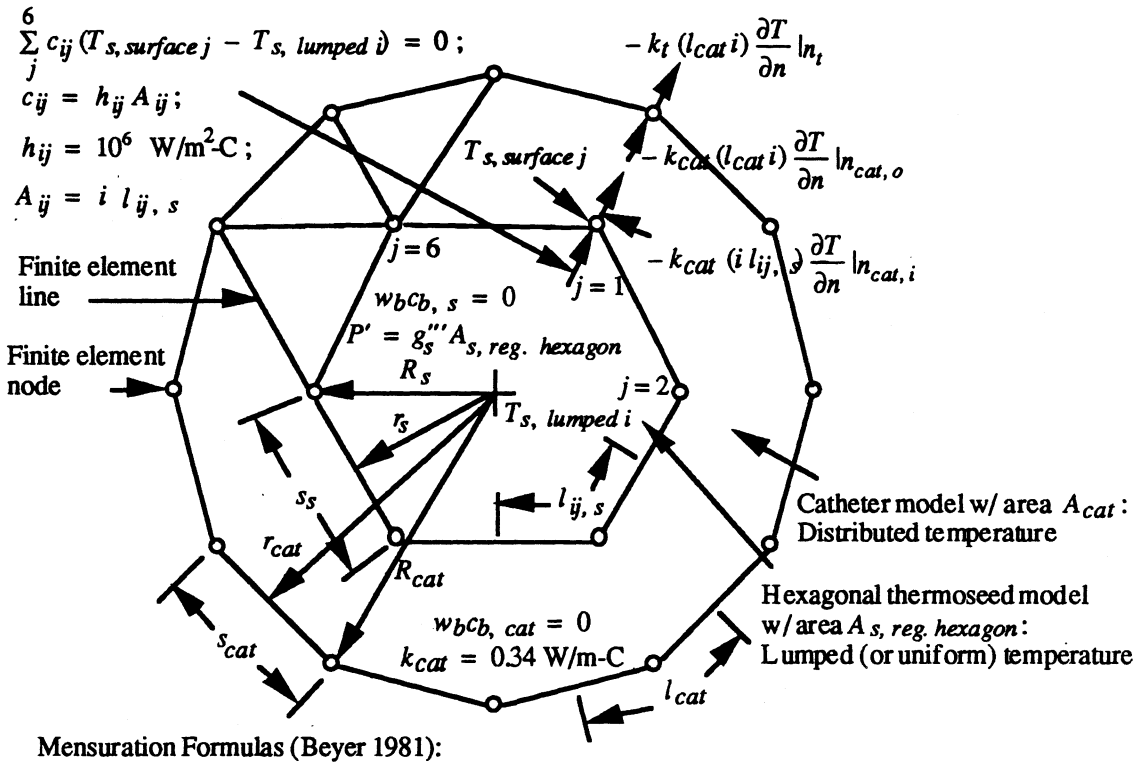

Mensuration Formulas (Beyer 1981):

Hexagonal Thermoseed Model:

n_s = number of sides = 6

r_s = Radius of inscribed circle = $\frac{s_s \cot(180/n_s)}{2}$

R_s = radius of circumscribed circle = $\frac{s_s \csc(180/n_s)}{2}$

$A_{s,\,reg.\,hexagon} = \frac{n_s s_s^2 \cot(180/n_s)}{4} = A_{s,\,circle} = \pi a^2$

Catheter Model:

n_{cat} = number of sides = 12

r_{cat} = Radius of inscribed circle = $\frac{s_{cat} \cot(180/n_{cat})}{2}$

R_{cat} = radius of circumscribed circle = $\frac{s_{cat} \csc(180/n_{cat})}{2}$

$A_{cat} = \frac{n_{cat} s_{cat}^2 \cot(180/n_{cat})}{4} = \pi(t_{cat}^2 + 2\, a\, t_{cat}) =$

$(A_{s,\,circle} + A_{cat,\,circular}) - A_{s,\,circle}$

Figure 3.5a Finite-element thermoseed and catheter models: (a) regular hexagon thermoseed model and (b) dodecagonal thermoseed model. Mensuration formulas are used to determine several dimensions in the models. A unit length multiplier i is shown in several locations. Four thermal boundary conditions are shown.

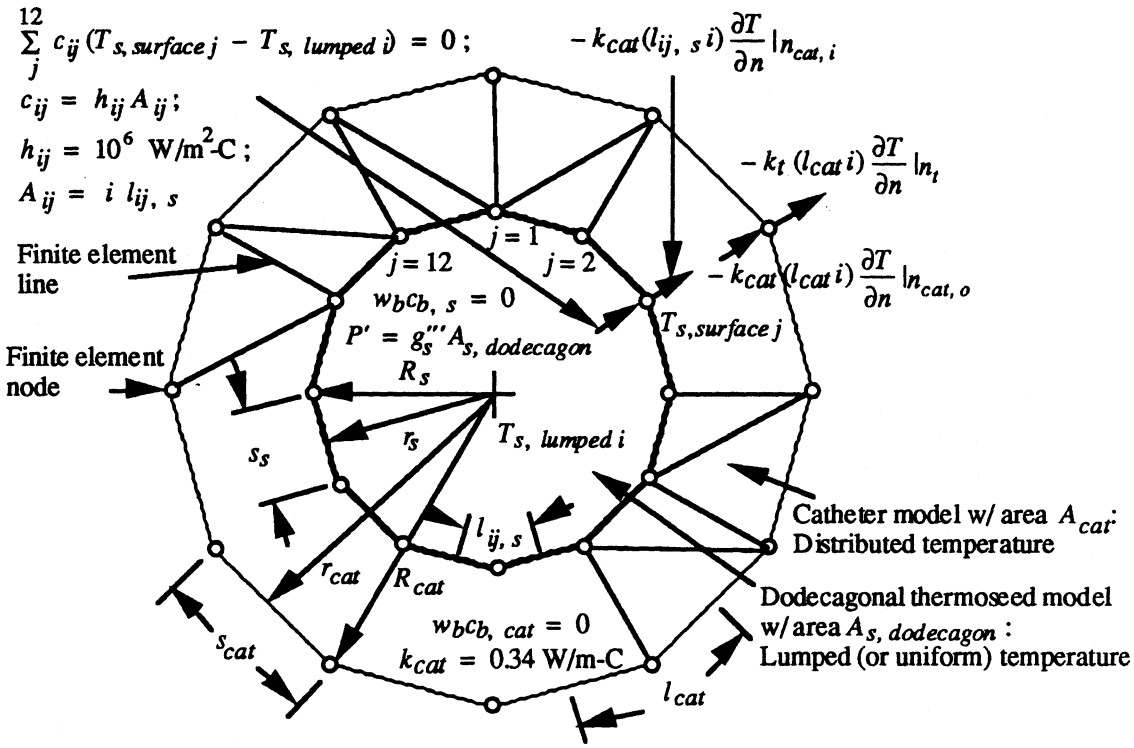

Mensuration Formulas (Beyer 1981):

Dodecagonal Thermoseed Model:

n_s = number of sides = 12

r_s = Radius of inscribed circle = $\frac{s_s \cot(180/n_s)}{2}$

R_s = radius of circumscribed circle = $\frac{s_s \csc(180/n_s)}{2}$

$A_{s,\,dodecagon} = \frac{n_s s_s^2 \cot(180/n_s)}{4} = A_{s,\,circle} = \pi a^2$

Catheter Model:

See Fig. 3.5a.

Figure 3.5b Finite-element thermoseed and catheter models: (a) regular hexagon thermoseed model and (b) dodecagonal thermoseed model. Mensuration formulas are used to determine several dimensions in the models. A unit length multiplier i is shown in several locations. Four thermal boundary conditions are shown.

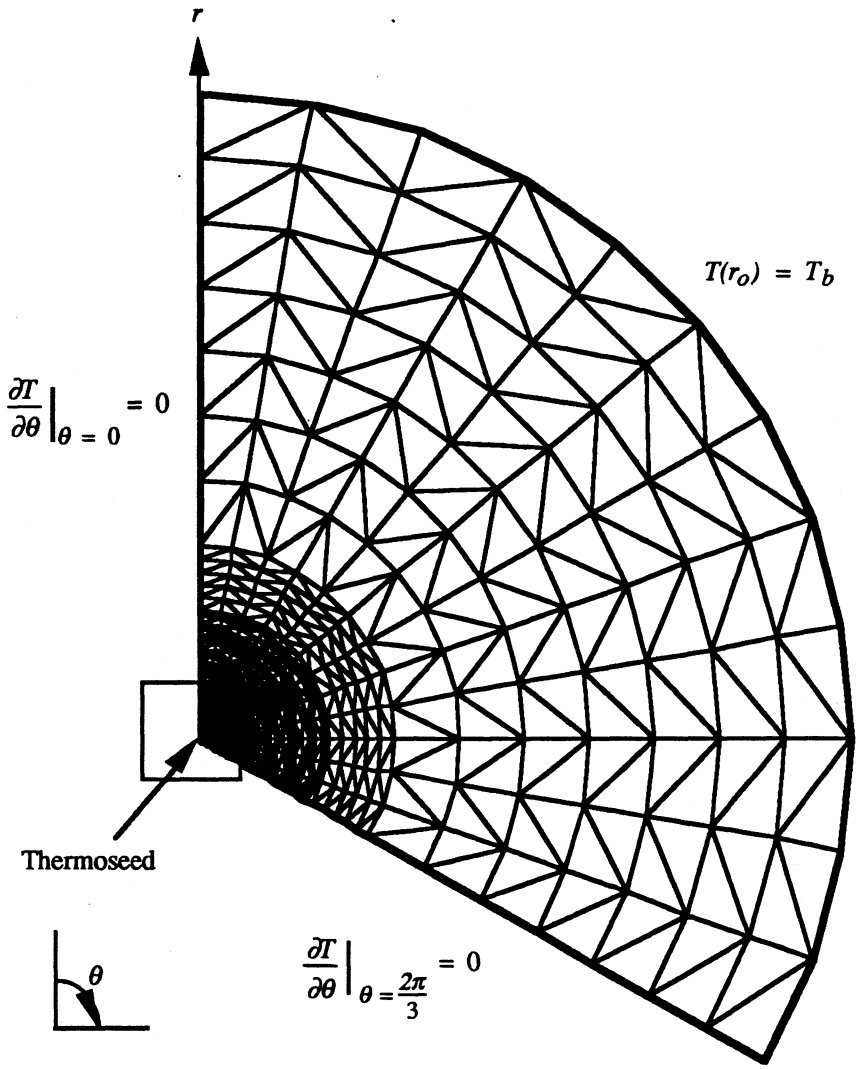

Figure 3.6 The finite element mesh of symmetrical portion of the thermoseed and tissue in Fig. 3.1. The two radial edges at $\theta = 0$ and $\theta = 2\pi/3$ are adiabatic boundaries since they are lines of symmetry. The outer edge at $r = r_o$ is fixed at the body core temperature T_b. The region enclosed by the square is enlarged and illustrated in Fig. 3.7. The dark-colored region near the thermoseed is the result of a finely graded mesh.

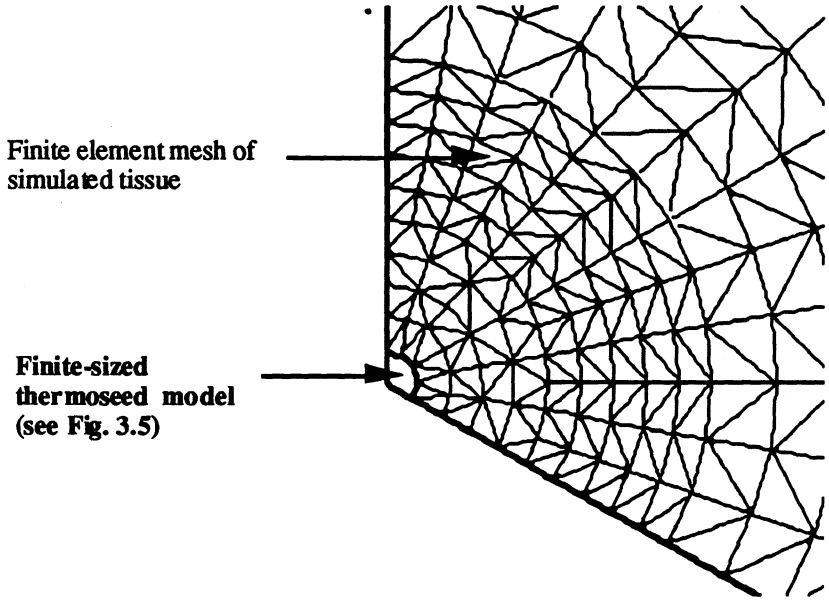

Figure 3.7 Enlargement of area enclosed by the square in Fig. 3.6. The outer edge of the (dodecagonal) thermoseed model has four line segments. There is no catheter in this model.

Table 3.2 Thermal Conductance Study of Finite-Sized Thermoseed Model

Convection Coefficient, h_{ij} (W/m^2-C)	Nodal Thermoseed Surface Temperatures, $T_{s,\ surface\ j}$ (C)					Lumped Thermoseed Temperature, $T_{s,lumped}$ (C)
	$j = 1$	$j = 2$	$j = 3$	$j = 4$	$j = 5$	
1e2	49.5	49.4	49.4	49.5	49.4	95.6
1e3	49.5	49.4	49.4	49.5	49.4	54.0
1e4	49.5	49.4	49.4	49.5	49.4	49.9
1e5	49.4	49.4	49.4	49.4	49.4	49.5
1e6	49.4	49.4	49.4	49.4	49.4	49.4

5 in Fig. 3.5b) on the surface of the thermoseed and the lumped temperature $T_{s,\ lumped}$ of the thermoseed are shown in Table 3.2. A convection boundary coefficient of 1e6 was an adequate value for h_{ij}, since the surface temperatures $T_{s,\ surface\ j}$ of the thermoseed were within 0.05 C of the lumped temperature $T_{s,\ lumped}$ of the thermoseed.

3.3 Thermoseed Model Validation: Numerical vs. Analytical Solutions

Temperature distributions were computed with FEHT using the hexagonal and dodecagonal thermoseed models and the finite element mesh in Fig. 3.6. The numerically-determined temperature distributions were compared to the analytical solution

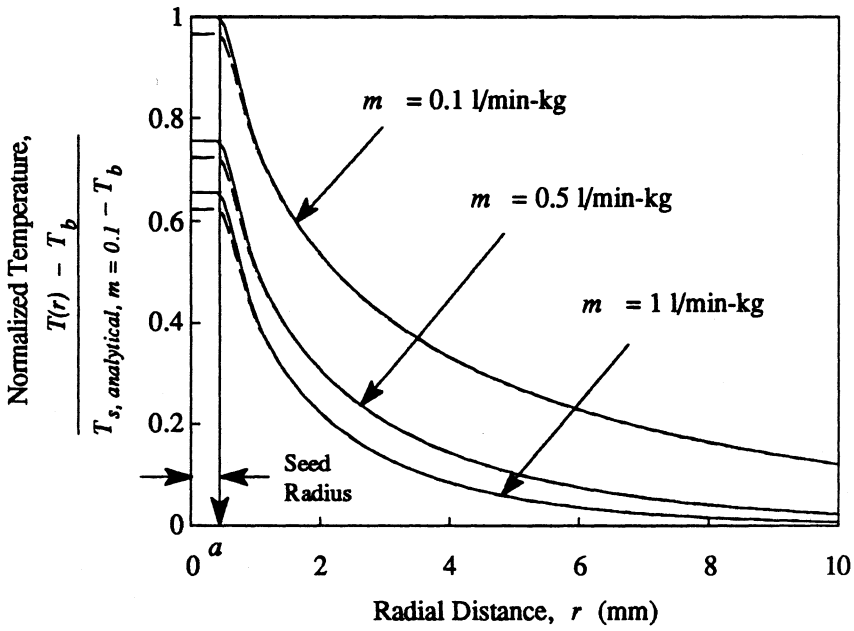

Figure 3.8 Normalized temperatures as a function of radial distance r for blood flows m = 0.1, 0.5 and 1 l/min-kg. Solutions were obtained with the analytical thermoseed model (solid lines) and the numerical hexagonal (short dashed lines) and dodecagonal thermoseed (long dashed lines) models. The power absorption per unit length P' of thermoseed used in these calculations was 17.17 W/m which gave a normalized thermoseed temperature of 1 for the analytical model with a blood flow m = 0.1 l/min-kg.

(Eq. 3.4) for blood flow rates of m = 0.1, 0.5 and 1 l/min-kg (Fig. 3.8). In Fig. 3.8, the temperature distributions were normalized by subtracting the numerical and analytical solutions $T(r)$ from T_b and then dividing by the temperature elevation above body core temperature (= $T_{s,\,analytical,\,m\,=\,0.1} - T_b$). Thermoseed temperatures T_s ($r = a$) computed by FEHT were approximately 0.5 C lower than the analytical solution for all three blood

flow rates (m = 0.1, 0.5 and 1 l/min-kg). Thermoseed temperatures of the numerical models were lower than that of the analytical model because of the geometric approximation of a circle by a regular hexagon and a dodecagon. Nonetheless, the temperature distributions in the tissue computed by FEHT for both numerical thermoseed models agree well with the analytical solutions (Fig. 3.8).

3.4 Placement of Thermoseed Model using FEHT

The creation of finite element thermoseed and catheter models using the 'Outline' and 'Element Line' features within FEHT typically requires about 10 to 15 min[7] per thermoseed. Often ferromagnetic hyperthermia patients will be implanted with 8 to 16 catheters, each containing one or several thermoseeds. Thus finite element modelers can expect to spend approximately 1.5 to 3 hours creating thermoseed and catheter models with the 'Outline' and 'Element Line' features in FEHT.

Fortunately, an algorithm for placing models of thermoseeds within a finite element mesh was developed by Klein (1989) and incorporated into the FEHT program. Only two steps are required to 'place' a thermoseed model within the finite element mesh. First, the 'Add Seed' menu item from the 'Draw' menu in FEHT is selected (Fig. 3.9). By selecting the 'Add Seed' menu item, the Macintosh mouse arrow changes into a cross-hair. By moving the mouse, the cross-hair can be positioned over the center of the desired location of a thermoseed. Then, by pressing the mouse button, the dodecagonal thermoseed model, surrounded by the catheter model consisting of 24 finite elements (Fig. 3.5) and another 44 finite elements in the tissue are placed with the mesh. An

---

[7]Most of the time is spent painstakingly positioning the cross-hair exactly in the correct position for each finite element node so that the area of the thermoseed model $A_{s,\ dodecagonal}$ and the catheter model A_{cat} are equal to the area of real thermoseeds and catheters. This process often involves several (frustrating!) attempts until the areas are equal.

example of the 'before' and 'after' images of placing the thermoseed model with the finite element mesh is illustrated in Fig. 3.10. With the aid of the 'Add Seed' algorithm, models of 8 to 16 thermoseeds and catheters can be created within about three to five minutes.

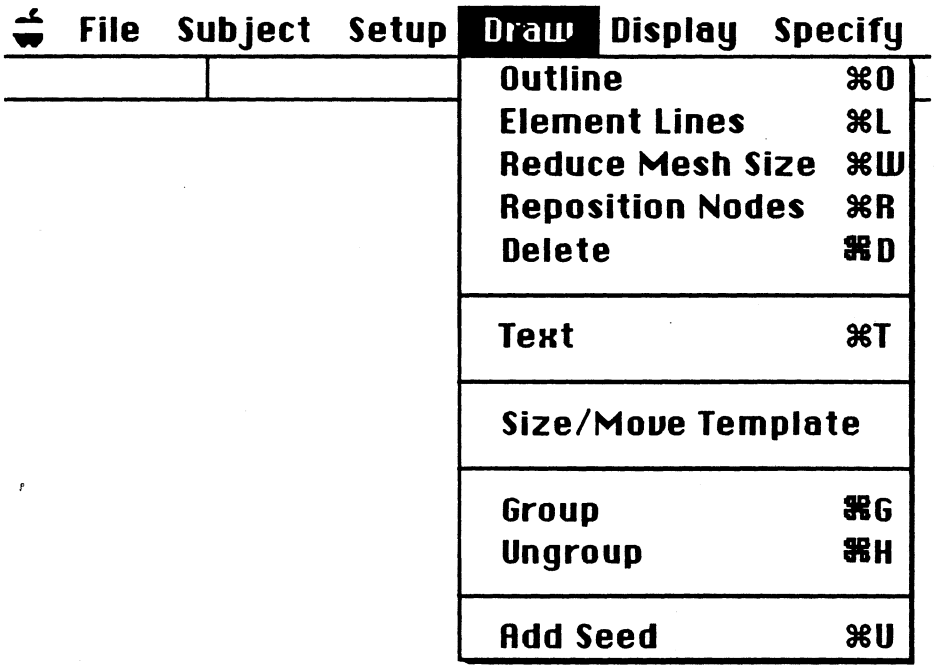

Figure 3.9 Display of the 'Add Seed' menu item in the 'Draw' menu of FEHT. The 'Add Seed' menu item was created by Klein (1989).

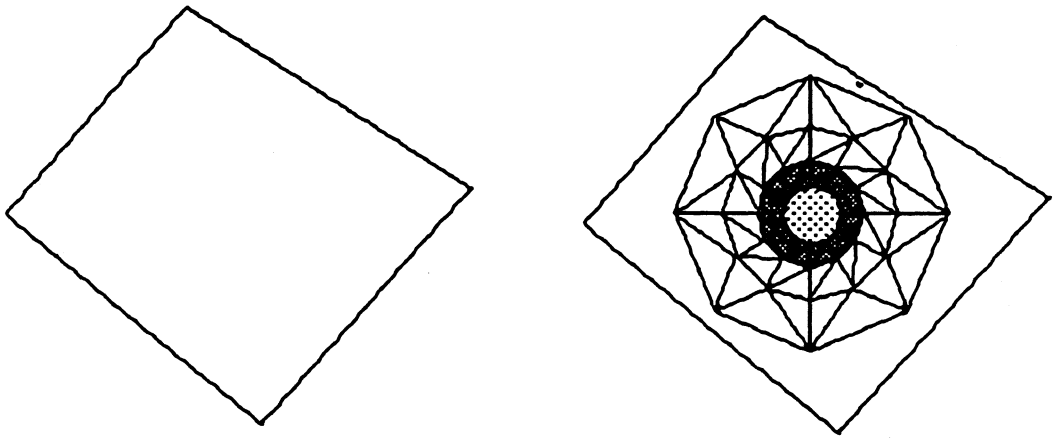

(a) Tumor region before 'Add Seed' (b) Tumor region after 'Add Seed'

Figure 3.10 The finite element representation of the (a) 'before' and (b) 'after' images upon utilizing the 'Add Seed' algorithm within FEHT. The 'after' image shows the dodecagonal thermoseed model (light-shaded region), the catheter model (dark-shaded region) and 44 finite elements in the tumor model.

Some recommendations are in order regarding the use of the 'Add Seed' thermoseed placement algorithm:

1. It is recommended that the zoom (or magnification) feature in FEHT be used prior to placement of the thermoseed. Since thermoseeds have a small radius ($r_s = a =$ 0.45 mm) compared to the dimensions of the tissue(s), (fully) magnifying the tissue region where a thermoseed model is to be placed will reduce the possibility of having finite element nodes placed on top of one another when the "Add Seed' algorithm is performed.

2. The time and effort required to create thermoseed models with the 'Add Seed' algorithm is a small fraction of the total time needed to create the entire finite element mesh. Thus it is recommended that the placement of the thermoseed models be left as one of the last tasks before completing the entire finite element mesh. Having a *saved* version of the nearly completed mesh prior to placement of thermoseed models will allow the user to study different thermoseed locations without having to create entirely new finite element meshes.

3. The 'Add Seed' algorithm places 44 finite elements within several millimeters from the outer edge of the catheter model (Fig. 3.10b). Therefore leave an adequate amount of space in the finite element mesh to avoid overlapping of existing and newly-placed finite elements.

3.5 Conclusion

Analytical and numerical thermal models of ferromagnetic thermoseeds were developed in this chapter. Results from the point-source numerical thermoseed model showed that the thermoseed power P' goes to zero as the nodal area around the seed, over which the energy balance is performed, approached zero. In this case, the temperature gradient at the *surface* of the thermoseed would be infinite. Thus the point-source model is an invalid model. The finite-sized thermoseed models in radial cross-section consisted of regular hexagons and dodecagons (12-sided polygons). Figure 3.8 shows that temperature distributions produced by the hexagonal and dodecagonal thermoseed models are very similar. The dodecagonal thermoseed model is the preferred model because its shape more closely resembles the shape of a thermoseed in radial cross-section. An algorithm was incorporated into FEHT to place dodecagonal thermoseed and catheter models within finite element meshes.

The thermoseed models in this chapter were developed with a symmetrical tissue model in which the temperature distribution was assumed to be one-dimensional. The hexagonal and dodecagonal thermoseed models are, however, general in their design. Thus the numerical thermoseed models can be used in two-dimensional simulations (see Chapters 6 and 7).

Chapter 4

Power-versus-Temperature Dependence of Ferromagnetic Thermoseed

In this chapter, the computational modeling of self-regulating thermoseeds as finite-sized, thermal sources of constant temperature is compared with modeling thermoseeds as thermal sources whose power absorption is dependent on temperature. The theoretical power-versus-temperature dependence of thermoseeds for use in dimensional and nondimensional tissue models is discussed in Sec. 4.1. Simulations are performed with dimensional and nondimensional tissue models. Descriptions of the tissue models are presented in Sec. 4.2. The effects of interseed spacing with uniform and nonuniform, constant blood flow models and the presence of catheter models on thermoseed and tissue temperatures are discussed in Sec. 4.3. The effect of varying the value of a nondimensional variable on thermoseed temperature in the nondimensional tissue model is presented in Sec. 4.4. Concluding remarks are made in Sec. 4.5.

4.1 Theoretical Power-Temperature Dependence of Thermoseeds

The temperature dependence of thermoseeds is developed in Sec. 4.1.1 for use in simulations of dimensional tissue models. Later the power-versus-temperature dependence is nondimensionalized for use in simulations of nondimensional tissue models (Sec. 4.1.2).

4.1.1 Power-Temperature Dependence for Use in Dimensional Tissue Models

Thermoseeds are inductively heated when placed in an electromagnetic field. Energy from an externally applied electromagnetic field produces eddy currents within a thermoseed. Lattice vibrations caused by the eddy currents result in heat dissipation and subsequent warming of the thermoseed. The rate of heat flow from a thermoseed can be determined from physical properties of the alloy. If the relationship between the magnetization M [tesla] and the applied magnetic field strength H [A/m] is linear, the permeability μ [tesla-m/A] of the ferromagnetic material

$$\mu = \frac{M}{H} + \mu_o \tag{4.1}$$

will be constant where μ_o is the permeability of free space. When the M-H relation is assumed linear, the heating power per unit length P' of a (infinitely) long cylindrical thermoseed in the presence of an electromagnetic field applied parallel to the cylinder axis is given by (Davies and Simpson 1979)

$$P' = \frac{\pi H^2}{\sigma} \frac{ber(x)\, ber'(x) + bei(x)\, bei'(x)}{ber^2(x) + bei^2(x)} \tag{4.2}$$

In Eq. 4.2, x is the induction number and equal to $a\sqrt{\omega \sigma \mu}$ and is dimensionless; σ is the electrical conductivity of the thermoseed [1/Ω-m]; a is the thermoseed radius [m]; ω is equal to $2\pi f$ [1/sec]; f is the frequency of the magnetic field [Hz]; *ber* and *bei* are Kelvin functions (Abramowitz and Stegun 1964); and *ber'* and *bei'* are first derivatives of Kelvin functions (Abramowitz and Stegun 1964). The electrical conductivity σ and the

permeability of the ferromagnetic material μ are the only parameters in Eq. 4.2 which can depend on temperature over the range of temperatures encountered during a hyperthermia treatment. In the present analysis the electrical conductivity is assumed constant.

By examination of hysteresis curves, Brezovich and Atkinson (1984) showed that the *M-H* relation of thermoseeds was nearly linear only at temperatures close to the maximum temperature of the thermoseed or the Curie point. The *M-H* relation was, however, highly nonlinear at lower temperatures. Since a general theory does not exist to account for this nonlinear behavior, Brezovich and Atkinson (1984) defined an *average* permeability,

$$\hat{\mu} = \frac{M(H_o)}{H_o} + \mu_o \tag{4.3}$$

In Eq. 4.3, H_o is the amplitude of the magnetic field and $M(H_o)$ is the magnetization at that field intensity. Brezovich and Atkinson (1984) concluded that, since the *average* permeability ($\hat{\mu}$) given by Eq. 4.3 is constant and that the linear theory only slightly underestimates the heating power, Eq. 4.3 can be used to evaluate Eq. 4.2 for any desired thermoseed temperature. Brezovich and Atkinson (1984) showed that the error introduced by this simplification decreased and became negligible as the Curie point is reached.

The magnetization as a function of temperature for thermoseeds with an operating temperature of 48.1 C was measured by Brezovich and Atkinson (1984) and is reproduced in Fig. 4.1. The heating power versus temperature of the 48.1 C-type thermoseed (Fig. 4.2) was computed with Eq. 4.2 using the magnetization data of the 48.1 C-type thermoseed in Fig. 4.1. In the calculation of the absorbed power (Eq. 4.2),

σ = 2.57e6 $(\Omega\text{-m})^{-1}$, H_o = 3.98e3 A/m, μ_o = 10e7 tesla-m/A, f = 90 kHz and a = 0.45 mm.

Since the operating temperature of Ni-Cu thermoseeds can be made different by altering the mass fraction of Cu, the power-versus-temperature dependence of thermoseeds with higher operating temperatures of 54.1 and 60.1 C were also computed

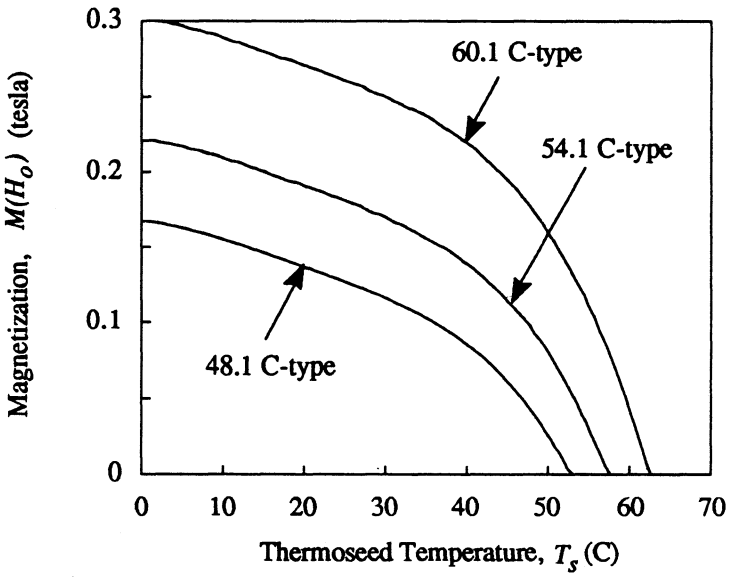

Figure 4.1 Magnetization $M(H_o)$ of Ni-Cu self-regulating thermoseeds as a function of temperature T_s. The curve for the 48.1 C-type thermoseed is reproduced from data by Brezovich and Atkinson (1984). The magnetizations of the 54.1 C- and 60.1 C-type thermoseeds were assumed to be larger than the magnetization of 48.1 C-type thermoseeds by a constant 0.054 and 0.134 tesla, respectively, over the temperature range shown.

with Eq. 4.2 (Fig. 4.2). Since published empirical data on the magnetization versus temperature of 54.1 C- and 60.1 C-type Ni-Cu thermoseeds are unavailable, the magnetization of 54.1 C- and 60.1 C-type thermoseeds was assumed to be larger than the magnetization of 48.1 C-type thermoseeds by a constant 0.054 and 0.134 tesla,

respectively, over the temperature range shown in Fig. 4.1. With the constants 0.054 and 0.134 tesla, the energy absorption rate per unit length P' (Eq. 4.2) was 10 W/m and the operating temperature of the thermoseeds was 54.1 and 60.1 C, respectively. In effect, the assumed magnetization-versus-temperature data of 54.1 C- and 60.1 C-type thermoseeds shifted the power-versus-temperature curve of the 48.1 C-type thermoseed to the right (Fig. 4.2). The shift of the power-versus-temperature curve for 54.1 C- and 60.1 C-type thermoseeds is expected, since, for the same absorbed power, thermoseeds with higher operating temperatures should achieve higher temperatures.

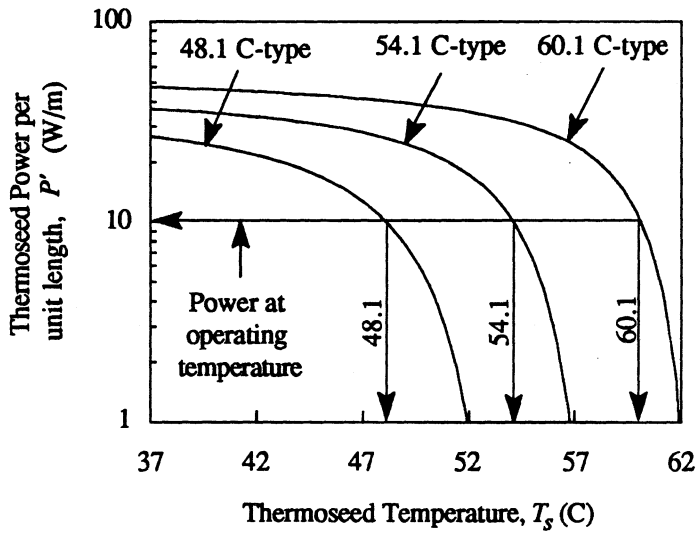

Figure 4.2 Power per meter length P' absorbed by a self-regulating thermoseed as a function of temperature T_s. The curves for thermoseeds with operating temperatures of 48.1, 54.1 and 60.1 C were generated using Eq. 4.2. A horizontal reference line at 10 W/m was used to determine the operating temperatures. The Cuire points for 48.1 C-, 54.1 C- and 60.1 C-type Ni-Cu thermoseeds are approximately 53, 57.6 and 62.6 C.

4.1.1.1 Newton-Raphson Iteration Technique

An s-dimensional Newton-Raphson technique (Shoup 1979), where s is the number of thermoseeds, was implemented into the finite element model to iteratively determine the temperature of each thermoseed for the power supplied. It was therefore necessary to

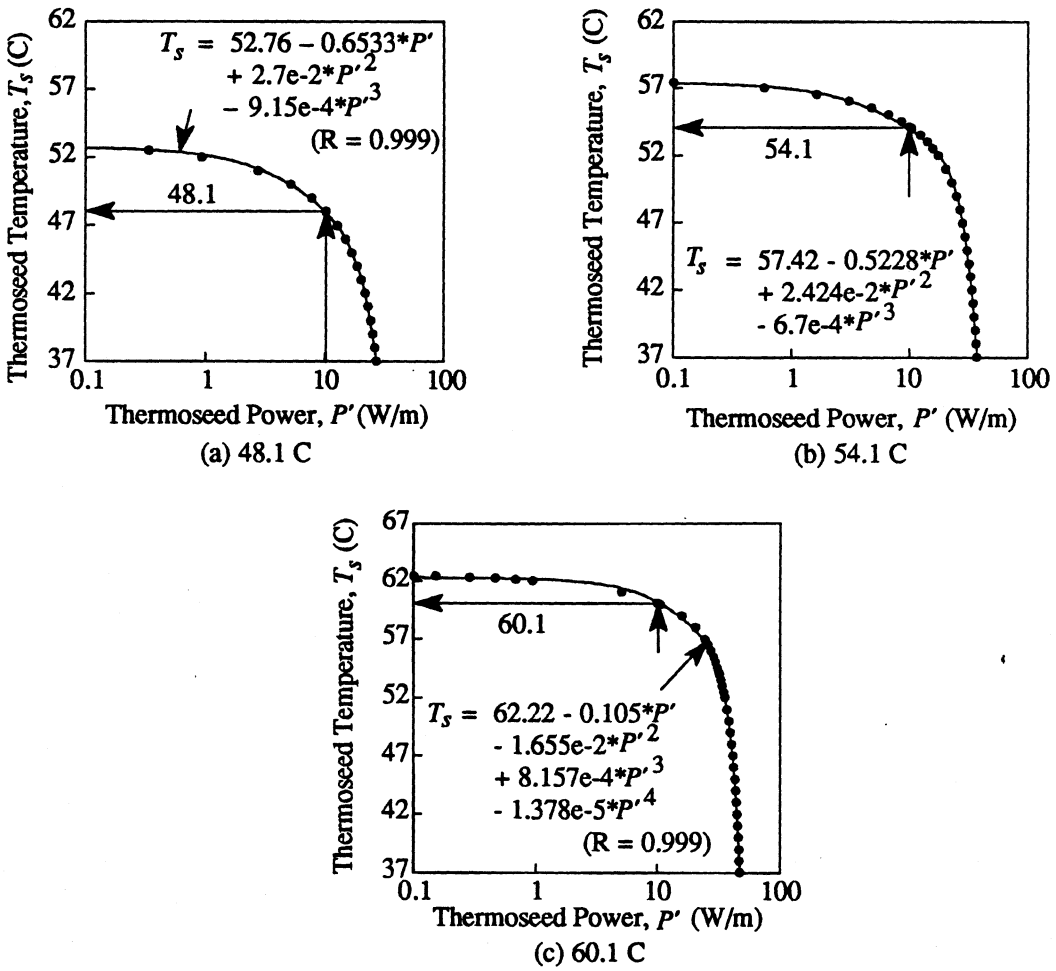

Figure 4.3 Thermoseed temperature T_s versus power per unit length P' for thermoseeds with operating temperatures of (a) 48.1 C, (b) 54.1 C and (c) 60.1 C. This figure is a cross-plot of the data in Fig. 4.3. The circles are data points from Fig. 4.2 and the solid lines are approximations of that data. The Curie temperature for thermoseeds with operating temperatures of 48.1, 54.1 and 60.1 C are approximately 53, 57.6 and 62.6 C.

have the thermoseed temperature as a function of its power. A cross-plot of the data shown in Fig. 4.2 is displayed in Fig. 4.3. Since there is no convenient theoretical relationship for thermoseed temperature as a function of its power, the data in Fig. 4.3 were approximated with polynomials. Each approximation in Fig. 4.3 is unique to the particular operating temperature of the thermoseed.

In the iteration scheme, the heating power was initialized at $P'_{s,j}$ (thermoseed s and iteration j) and then the finite element method was used to compute the temperature of each thermoseed $T_{s,j\,FEHT}$ and the temperature distribution throughout the remaining simulated tissue region. The temperature $T_{s,j\,Curve}$ that each thermoseed would actually produce at the power $P'_{s,j}$ was determined using the temperature-versus-power relationship of the thermoseed (Fig. 4.3). If the temperature $T_{s,j\,FEHT}$ was different than $T_{s,j\,Curve}$, then the Newton-Raphson method was used to determine the next value of $P'_{s,j}$. This procedure was repeated until $T_{s,j\,FEHT}$ and $T_{s,j\,Curve}$ converged. The convergence criterion was $|T_{s,j\,FEHT} - T_{s,j\,Curve}| < \text{Tol}$. A tolerance of Tol = 5e-3 was found to be adequate for convergence of the iteration scheme (Sec. 4.3.2.1).

4.1.2 Power-Temperature Dependence for Use in Nondimensional Tissue Models

Later in this chapter the thermoseed power P' and thermoseed temperature T_s will be nondimensionalized for studies of a nondimensional tissue model (Sec. 4.2.2). The nondimensional thermoseed power will be designated as P^* and the nondimensional thermoseed temperature as T_s^*.

In order to compare the results from simulations with 48.1 C- and/or 54.1 C-type thermoseeds with the results from simulations with 60.1 C-type thermoseeds, P^* for

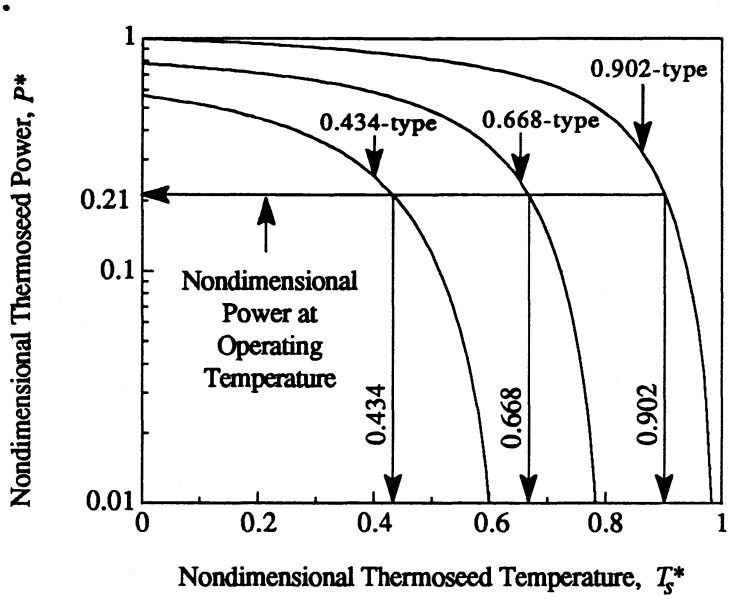

Figure 4.4 Nondimensional power P^* of self-regulating thermoseeds as a function of nondimensional temperature T_s^*. The nondimensional power P^* and temperature T_s^* are discussed in detail in Sec. 4.2.2. The nondimensional power at the operating temperature was 0.21 (= $10/P'_{max}$).

48.1 C- and 54.1 C-type thermoseeds is determined by dividing P' by P'_{max} of the 60.1 C-type seeds. P'_{max} for 60.1 C-type thermoseeds at 37 C is 47.36 W/m (Fig. 4.2). A plot of P^* versus T_s^* for 48.1 C-, 54.1 C- and 60.1 C-type seeds is shown in Fig. 4.4. Again, since it is necessary to have T_s^* as a function of P^* for use in the iteration scheme described in Sec. 4.1.1, a cross-plot of the data in Fig. 4.4 is shown in Fig. 4.5. The data in Fig. 4.5 were approximated with polynomials.

4.1.2.1 Newton-Raphson Iteration Technique

The s-dimensional Newton-Raphson technique described earlier (Sec. 4.1.1.1) was implemented into the finite element model to determine the nondimensional thermoseed temperature for the power supplied. The nondimensional temperature

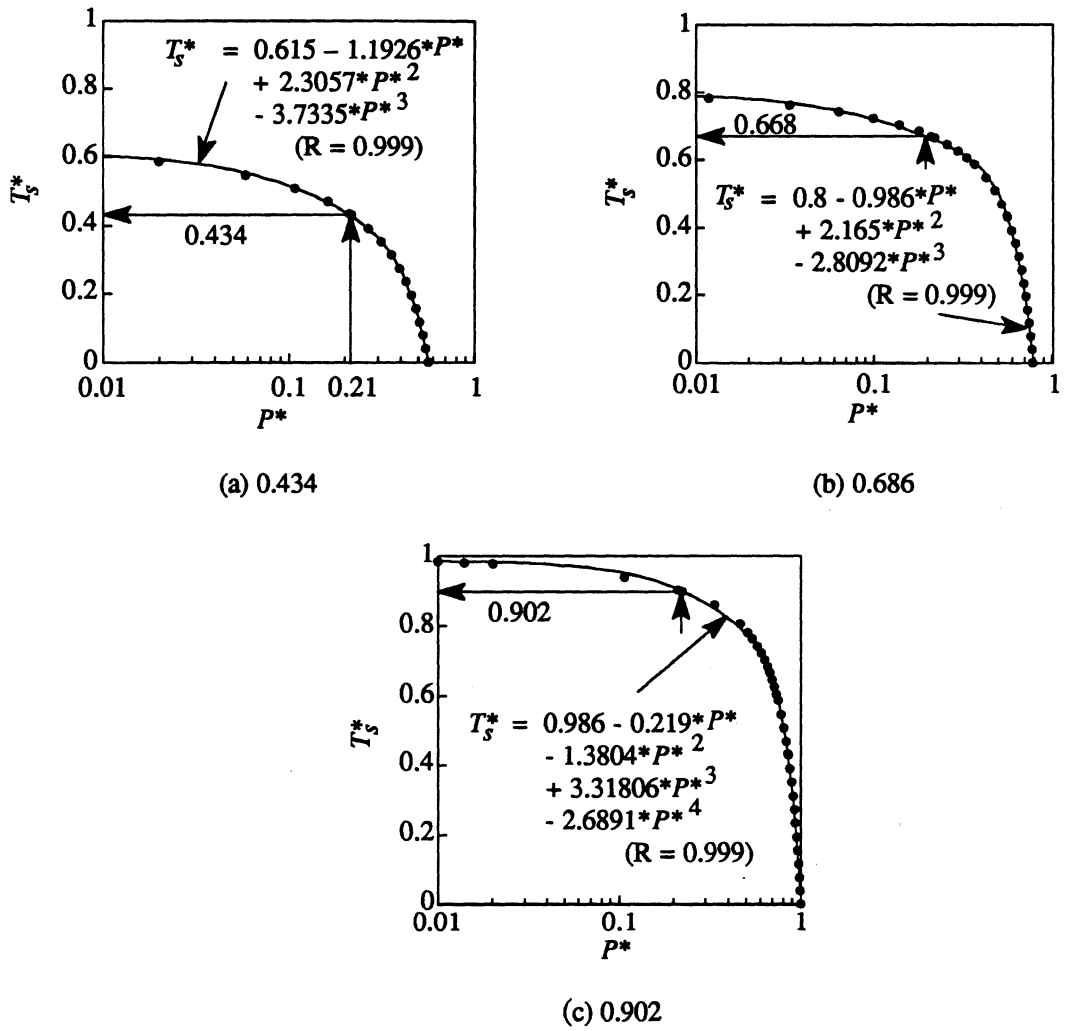

Figure 4.5 Nondimensional thermoseed temperature T_s^* versus nondimensional thermoseed power P^* for thermoseeds with nondimensional operating temperatures of (a) 0.434, (b) 0.686 and (c) 0.902. This figure is a cross-plot of the data in Fig. 4.5. The circles are data points from Fig. 4.5 and the solid lines are approximations of that data.

$T^*_{s,j\ Curve}$ that each thermoseed would actually produce at the power $P^*_{s,j}$ was determined using the temperature-versus-power relationship of the thermoseed (Fig. 4.5). If the temperature $T^*_{s,j\ FEHT}$ was different than $T^*_{s,j\ Curve}$, then the Newton-Raphson method was used to determine the next value of $P^*_{s,j}$. This procedure was repeated until thermoseed temperatures $T^*_{s,j\ FEHT}$ and $T^*_{s,j\ Curve}$ converged. The convergence criterion

was $|T^*_{s,j\,FEHT} - T^*_{s,j\,Curve}| <$ Tol. A tolerance of Tol = 5e-3 was found to be adequate for convergence of the iteration scheme (Sec. 4.3.2.1).

4.2 Description of Tissue Models

Simulations are performed in a tissue model with known dimensions. Several thermoseed spacings are studied in the dimensional tissue model. The description of the dimensional tissue model and the equation used to predict temperatures are given in Sec. 4.2.1. The dimensional tissue model and equations are nondimensionalized in Sec. 4.2.2. The solution to the nondimensional equation provides an opportunity to understand the influence of changes in one nondimensional variable on thermoseed temperature rather than changes in several independent variables.

In simulations with the dimensional and nondimensional tissue models, the numerical dodecagonal thermoseed model (Sec. 3.2.3) and the Newton-Raphson technique (Secs. 4.1.1.1 and 4.1.2.1) were used to determine thermoseed temperatures.

4.2.1 Dimensional Tissue Model with Heat Transfer in Two-Dimensions

Simulations were performed with a two-dimensional model of a square tissue model[8]. The tissue model consisted of a square tumor with an arbitrarily chosen length of 47 mm (= $2L_T$) (Fig. 4.6). The simulated tumor was implanted with a square 4x4 array of thermoseeds. The length of the tumor was chosen so that thermoseed spacings l up to 15 mm in the 4x4 array could be investigated. Since the blood flow in the tumor

[8]The two-dimensional model is assumed to be a cross-section near the central plane of the three-dimensional tissue system and the thermoseeds are 65 mm long. Thus this tissue model satisfies constraints of two-dimensional models reported previously (Chen *et al.* 1991, Chin and Stauffer 1991).

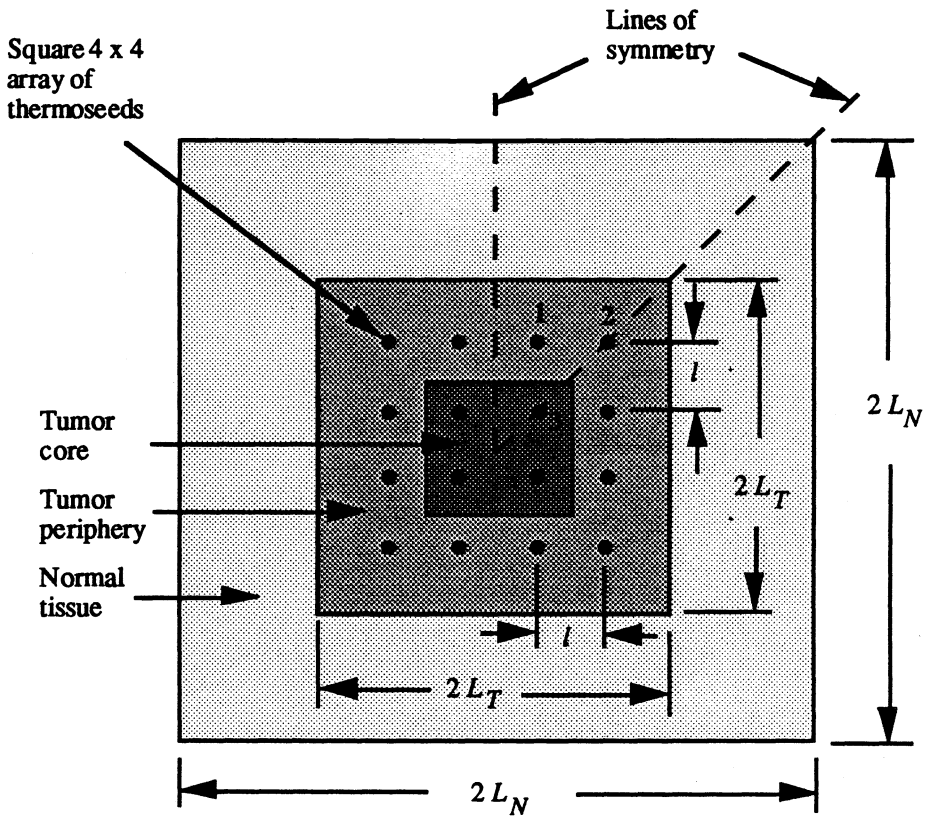

Figure 4.6 Two-dimensional cross-section of tissue model. The darkest shaded region is the simulated tumor core, the medium-shaded region is the tumor periphery with a length of $2L_T$ and the lightly shaded region is the simulated normal tissue with a length of $2L_N$. Thermoseed locations are represented by black circles within the tumor and are separated by a distance l. Thermoseeds 1, 2 and 3 are numbered for reference.

periphery can be quite different than that in the tumor core[9], the tumor model was divided into a square inner core with a length of 24 mm surrounded by an outer periphery. The tumor core was centered squarely within the tumor model. The normal tissue had an arbitrarily chosen length of 180 mm (= $2L_N$). A length of 180 mm for the normal tissue

[9]Earlier studies and clinical experience have shown that often, the inner core of the tumor is a tough, fibrous tissue and may have a blood flow that differs vastly from the outer periphery of the tumor. Thus the tumor was modeled as two distinct regions consisting of an inner core and an outer periphery.

was adequate to ensure that there is no boundary effect due to a temperature gradient at the outer edge of the normal tissue.

Using geometrical symmetry conditions, only 1/8 of the tissue model in Fig. 4.6 needed to be discretized into a mesh of finite elements (Fig. 4.7). By utilizing these symmetry conditions, the number of thermoseeds in the problem was reduced from 16 to 3. Finely-graded meshes were used near thermoseeds where large temperature gradients

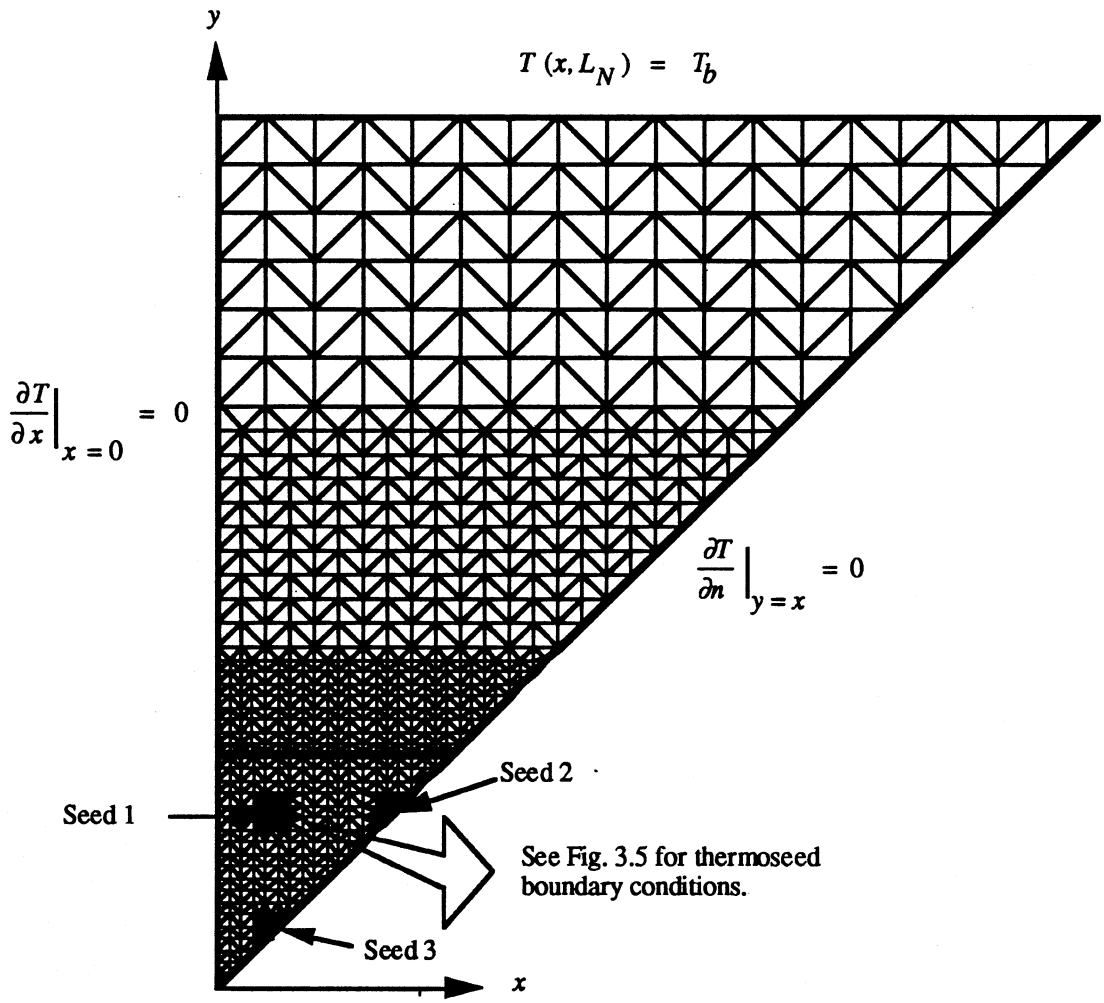

Figure 4.7 Finite element mesh of normal and tumor tissue model with adiabatic boundaries ($x = 0$ and $y = x$) and a constant-temperature boundary ($y = L_N$). Blackened areas around the thermoseeds are the result of a finely graded mesh. Thermoseeds are numbered for reference.

can occur. Simulations were performed with thermoseeds centered squarely within the tumor. The operating temperature of each thermoseed in the array is shown in Table 4.1. Thermoseed models were spaced uniformly in the x and y directions by a distance l between 9 and 15 mm. Thus there was 1 mm between the outer edge of the thermoseed array and the boundary between the tumor and normal tissues at the maximum thermoseed spacing of l = 15 mm.

Table 4.1 Operating Temperature of Thermoseeds in Simulations

Thermoseed Array Number	Operating Temperature (Fig. 4.2 and 4.3) Thermoseed Number (see Figs. 4.6 and 4.7)		
	1	2	3
1	48.1	48.1	48.1
2	54.1	54.1	54.1
3	60.1	60.1	60.1

The temperature distribution in the simulated tissue (Fig. 4.7) is determined by solving Eq. 2.2 with constant thermal conductivity k_t. Equation 2.2 with constant k_t is given by

$$k_t\left[\frac{\partial^2 T}{\partial x^2} + \frac{\partial^2 T}{\partial y^2}\right] - w_b c_b (T - T_b) = 0 \tag{4.4}$$

Equation 4.4 is solved with boundary conditions on the perimeter of the simulated tissue. The adiabatic boundary conditions due to the symmetry of the problem are

$$\frac{\partial T}{\partial x}\Big|_{x=0} = 0 \tag{4.5a}$$

$$\frac{\partial T}{\partial n}\Big|_{y=x} = 0 \tag{4.5b}$$

The constant temperature boundary condition is given by

$$T(x, L_N) = T_b \tag{4.5c}$$

As discussed in Sec. 3.2.3, there is a heat flow q' [W/m] condition at the edge of the simulated thermoseed that is given by

$$q' = P' = g_s''' A_s \tag{4.5d}$$

Additional assumptions about the geometry and blood flow in the tissue model include a boundary between tumor and normal tissue that is explicitly known. Thus all thermoseeds were implanted in the tumor. The outer edge of normal tissue was at body core temperature T_b. Tissue perfusion $w_b c_b$ in the tumor and normal tissues was independent of temperature. Blood flow rates in tumor tissue are typically lower than in normal tissues (Song *et al.* 1984). Simulations were therefore performed with blood flow rates of 0.1, 0.25, 0.5 and 1 l/min-kg in normal tissue and 0.1, 0.25 and 0.75 l/min-kg in the tumor.

In clinical practice, thermoseeds are placed percutaneously into catheters that have been inserted surgically into tissue to deliver brachytherapy treatments. To study the necessity of modeling catheters, simulations were performed with an array of thermoseeds, each within 0.35 mm-thick polyethylene tubing. (The complete description of the catheter model can be found in Sec. 3.2.3). The thermoseed spacing l in these simulations was 10 mm.

4.2.1.1 Discretization Study

As with any numerical technique, the accuracy of the predicted temperature distribution depends on an adequate choice of the finite element mesh. Therefore mesh sizes with 730, 1530 and 2769 finite elements were used in simulations. The meshes with 1530 and 2769 finite elements were created by reducing quasi-uniformly the mesh with 730 elements. The finite element reduction was concentrated near the thermoseed, in the tumor and in the normal tissue near the boundary of the tumor and normal tissues. Uniform blood flow rates of m = 0, 0.25, 0.5 and 1 l/min-kg in the tumor and normal tissue were studied in the simulations.

The effect of reducing the finite element mesh size on thermoseed temperatures is shown in Table 4.2. Thermoseed temperatures were weakly dependent on mesh size at blood flow rates of 0 and 0.25 l/min-kg. Thermoseed temperatures were, however, slightly more dependent on mesh size with blood flow rates of 0.5 and 1 l/min-kg. In summary, the mesh with 1530 finite elements had sufficient discretization and was used to predict temperature distributions in the simulations.

Table 4.2 Finite Element Mesh Study
(4x4 array of bare 54.1 C-type thermoseeds with spacing l = 12 mm)

Uniform Blood Flow, m (l/min-kg)	Number of Finite Elements	Thermoseed Temperature, T_s (C) (See Fig. 4.6)			% Tumor > 42 C	% Normal Tissue>42 C
		Seed 1	Seed 2	Seed 3		
0	730	56.06	55.49	56.71	100	34.9
0	1530	56.06	55.51	56.70	100	34.8
0	2769	56.05	55.52	56.68	100	34.8
0.25	730	51.65	51.41	51.94	75	0
0.25	1530	51.65	51.41	51.94	75.3	0
0.25	2769	51.65	51.41	51.94	75	0
0.5	730	50.37	50.16	50.52	16.4	0
0.5	1530	50.43	50.31	50.58	16	0
0.5	2769	50.53	50.41	50.68	15.5	0
1	730	49.18	49.04	49.22	7.3	0
1	1530	49.27	49.23	49.32	6.8	0
1	2769	49.39	49.36	49.44	6.8	0

4.2.2 Nondimensional Tissue Model

The tissue model and equations described in Sec. 4.2.1 can be nondimensionalized. The rectangular coordinate directions x and y can be nondimensionalized by defining x^* and y^* and are given by

$$x^* \equiv \frac{x}{l} \tag{4.6a}$$

$$y^* \equiv \frac{y}{l} \tag{4.6b}$$

The distance l between the thermoseeds was chosen as an appropriate length scale since l is a variable of considerable interest in thermoseed implant arrays. Temperatures can be normalized by defining T^* which is given by

$$T^* \equiv \frac{T - T_b}{T_{s,\,c.p.} - T_b} \tag{4.7}$$

Since the temperatures in the tissue model will never be lower than T_b and never higher than the Cuire point $T_{s,\,c.p.}$ (Sec. 1.5) of the hottest thermoseed, T^* will be between 0 and 1.

Substituting Eqs. 4.6 and 4.7 into Eq. 4.4 and dividing Eq. 4.4 by k_t gives

$$\frac{\partial^2 T^*}{\partial x^{*2}} + \frac{\partial^2 T^*}{\partial y^{*2}} - Bi_I\, T^* = 0 \tag{4.8}$$

The dimensionless parameter Bi_I appearing in Eq. 4.8 is termed the *Implant-Biot number* and is given by

$$Bi_I \equiv \frac{w_b c_b l^2}{k_t} = \frac{\frac{l}{k_t}}{\frac{1}{w_b c_b l}} = \frac{R_{conduction}}{R_{blood\ flow}} \tag{4.9}$$

The Implant-Biot number is the ratio of the resistance to heat flow via thermal conduction to the resistance of heat flow via blood flow. According to Eq. 4.9 and illustrated in Fig. 4.8, the Implant-Biot number provides a measure of the temperature drop between two thermoseeds. For small Implant-Biot numbers ($Bi_I << 1$), the temperature drop between thermoseeds is negligible as the resistance to heat flow via blood flow is large. For large Implant-Biot numbers ($Bi_I >> 1$), the temperature decrease between thermoseeds is large as the resistance to heat flow via blood flow is small.

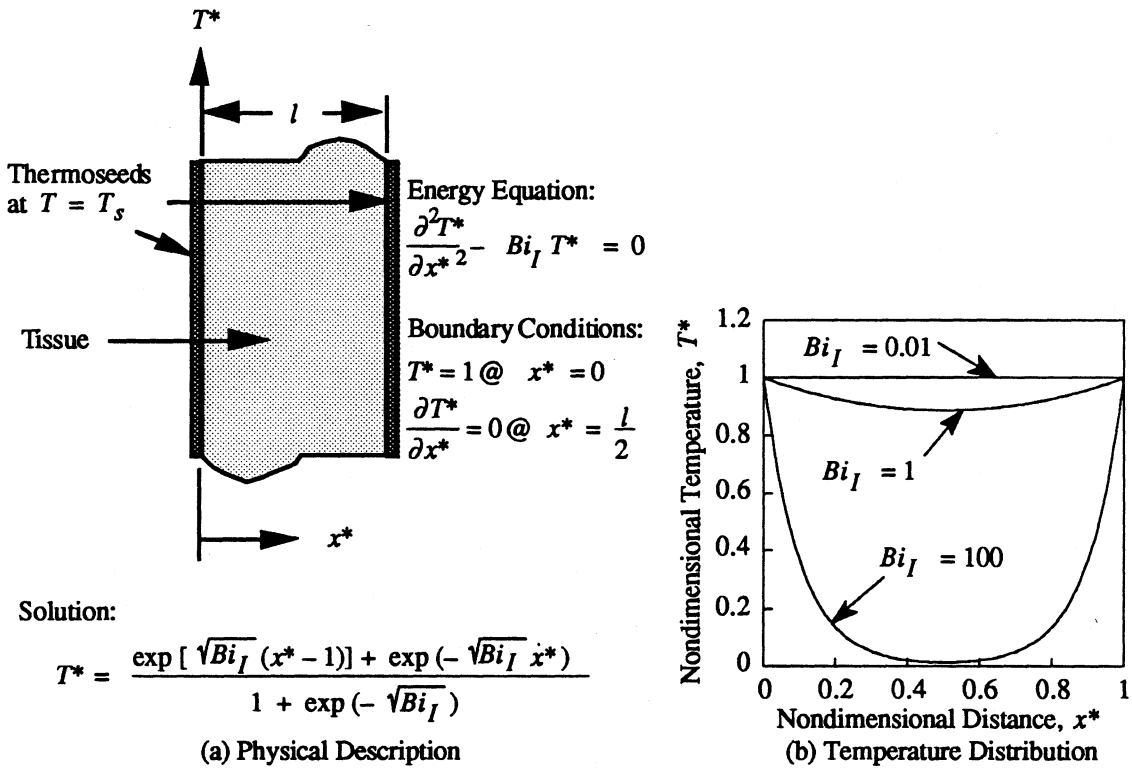

Figure 4.8 Effect of Implant-Biot number on steady-state temperature distribution between between two thermoseeds. A physical description of the problem set-up and the solution to the energy equation is shown in part (a) while the nondimensional temperature distribution for $Bi_I = 0.01$, 1, and 100 is shown in part (b).

The Implant-Biot number is similar to the classical *Biot number, Bi,* which plays a fundamental role in conduction heat transfer problems that involve surface convection effects. The Biot number is given by

$$Bi \equiv \frac{hL}{k} = \frac{\frac{L}{k}}{\frac{1}{h}} = \frac{R_{conduction}}{R_{convection}} \tag{4.10}$$

and is the ratio of the resistance of heat flow via thermal conduction to the resistance of heat flow via convection.

The boundary conditions of the dimensional tissue model (Fig. 4.7) given by Eq. 4.5 must be nondimensionalized. The nondimensional boundary conditions can be shown to be

$$\frac{\partial T^*}{\partial x^*}\Big|_{x^*=0} = 0 \tag{4.11a}$$

$$\frac{\partial T^*}{\partial n^*}\Big|_{y^*=x^*} = 0 \tag{4.11b}$$

$$T^*(x^*l, \frac{L_N}{l}) = 0 \tag{4.11c}$$

The heat flow condition at the edge of the thermoseed (Eq. 4.5d) is nondimensionalized by defining P^* which is given as

$$P^* \equiv \frac{q'}{P'_{max}} = \frac{P'}{P'_{max}} = \frac{g'''_s A_s}{P'_{max}} \tag{4.11d}$$

In Eq. 4.11d, P'_{max} is the maximum power output of a thermoseed at T_b. The equivalent finite element mesh of Fig. 4.7 with nondimensional length and boundary conditions is shown in Fig. 4.9.

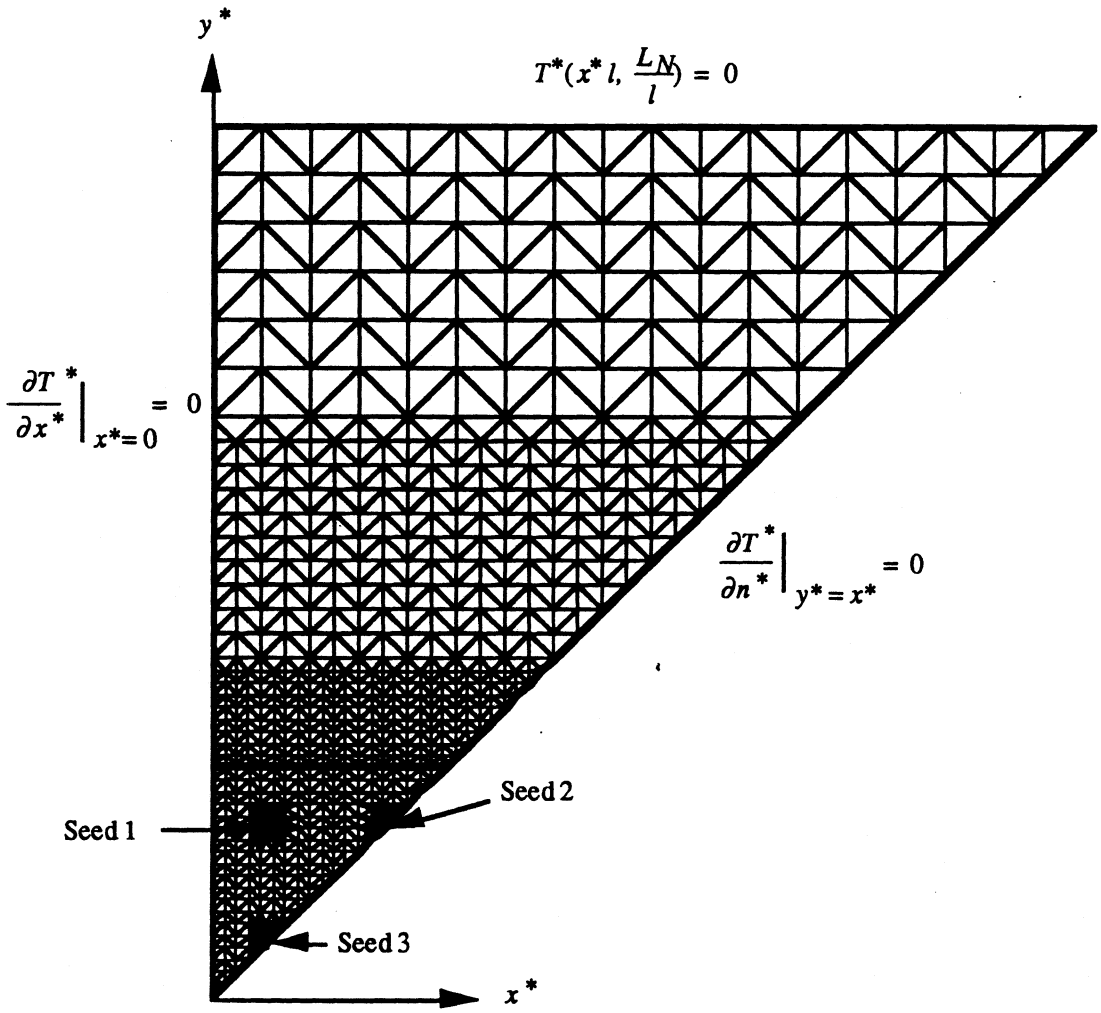

Figure 4.9 Finite element mesh of nondimensionalized normal and tumor tissue model with adiabatic boundaries ($x^* = 0$ and $y^* = x^*$) and a constant temperature boundary ($y^* = L_N/l$). Dark-colored areas around the thermoseeds are the result of a fine mesh. Thermoseeds are numbered for reference.

Simulations were performed for Implant-Biot numbers Bi_l between 0 and about 15,000. In the simulations, tissue thermal conductivity k_t was set to 1 W/m-C and thermoseed spacing l was set to 10 mm. Thus Implant-Biot numbers Bi_l were increased by increasing tissue perfusion $w_b c_b$ from 0 to 1.5e8 uniformly in the tumor and normal tissue. The Newton-Raphson technique was used to determine the nondimensional thermoseed temperature T^* as a function of absorbed power P^* (Sec. 4.1.2.1). The mesh with 1530 finite elements had sufficient discretization and was used to predict temperature distributions in the simulations (Sec. 4.2.1.1).

4.3 Thermoseed and Tissue Temperatures in Dimensional Tissue Models

Thermoseed temperatures were determined in tissue models where the heat transfer was assumed to be one-dimensional (Sec. 4.3.1) and two-dimensional (Sec. 4.3.2). The effect of the thermoseed temperatures on tissue temperatures is discussed (Sec. 4.3.2.3.3). The influence of catheter models on thermoseed and tissue temperatures is presented in Sec. 4.3.3.

4.3.1 Tissue Model with One-Dimensional Heat Transfer

The power-versus-temperature relationship of thermoseeds was used to determine the temperature of a single thermoseed implanted at the center of a circular tissue model (Fig. 3.1). The analytically-derived expression for the temperature distribution (Eq. 3.4) in the circular tissue model and the temperature versus absorbed power of thermoseeds with operating temperature of 48.1, 54.1 and 60.1 C (see polynomials in Fig. 4.3) were solved simultaneously to determine thermoseed temperatures. The solutions to the system of equations were obtained with Engineering Equation Solver (EES) (Klein and Alvarado,

1989). Thermoseed temperatures were obtained with Eq. 3.4 by setting $r = r_i$, $r_o \sim \infty$, k_t = 0.64 W/m-C, a = 0.45 mm and T_b = 37 C.

Thermoseed temperatures were determined for tissue perfusion rates $w_b c_b$ between 1 and 10^5 W/m^3-C (Fig. 4.10) which corresponds to blood flow rates m between 1.34e-5 and 1.34 l/min-kg assuming ρ_t = 1080 kg/m^3 and ρ_b = 1060 kg/m^3. At a tissue perfusion rate of $w_b c_b$ = 0 W/m^3-C, the thermoseed temperature equals the Curie point ($T_{c.p.}$) of the thermoseed. The tissue perfusion rate near $w_b c_b = 10^{12}$ W/m^3-C was the upper limiting value for $w_b c_b$, because at this perfusion rate, the thermoseed temperature was equal to the blood temperature T_b.

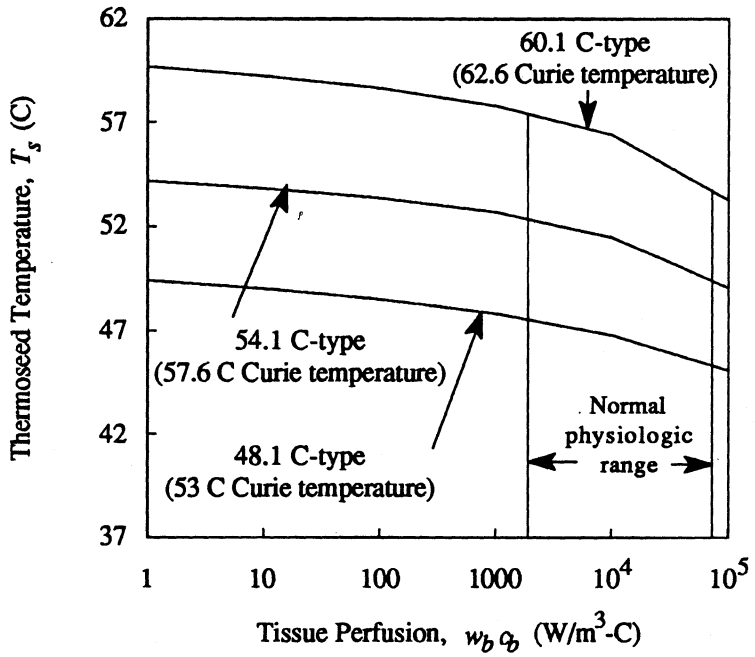

Figure 4.10 Thermoseed temperature T_s versus tissue perfusion $w_b c_b$ for a thermoseed with operating temperatures of 48.1, 54.1 and 60.1 C. The curves were obtained by solving Eq. 3.4 and the thermoseed temperature-power relationship (T_s versus P' in Fig. 4.3) simultaneously. The simulations were performed on the tissue model in Fig. 3.1 where $r_o \sim \infty$, $r = r_i$, k_t = 0.64 W/m-C, a = 0.45 mm and T_b = 37 C. Tissue perfusion in the normal physiologic range is between 2000 and 75,000 W/m^3-C, which corresponds to blood flows m between 0.027 and 1 l/min-kg.

For a single thermoseed placed at the center of the circular tissue model, the temperature of 48.1 C-type thermoseeds drops 26.9% between tissue perfusion rates of 1 and 10^5 W/m^3-C. Similarly, the temperature of 54.1 C- and 60.1 C-type thermoseeds drops about 25% between tissue perfusion rates of 1 and 10^5 W/m^3-C. Thus it is probable that estimates of thermoseed temperature will be more accurate than assuming a constant temperature model, if the power-temperature relationships of thermoseeds are used to determine thermoseed temperature.

4.3.2 Tissue Model with Two-Dimensional Heat Transfer

The convergence of the Newton-Raphson scheme is discussed in Sec. 4.3.2.1 and the effect of interseed spacing on thermoseed temperatures with uniform blood flow models is presented in Sec. 4.3.2.2.

4.3.2.1 Convergence Criteria

Simulations were performed to determine the sensitivity of the tolerance (Tol) value in the Newton-Raphson scheme discussed in Sec. 4.1.1.1. The simulations were conducted with an array of bare, 60.1 C-type thermoseeds with interseed spacing l = 10 mm in the compartmentalized blood flow model ($m_{t,\ core}$ = 0.1 l/min-kg $m_{t,\ periphery}$ = 0.75 l/min-kg and m_n = 0.5 l/min-kg). The results of these simulations are shown in Table 4.3. A satisfactory tolerance for convergence of the Newton-Raphson scheme was Tol = 5e-3. With a Tol = 5e-3, the difference in thermoseed temperatures $|T_{s,j\ FEHT} - T_{s,j\ Curve}|$ was less than 0.01 C.

The time required to determine thermoseed temperatures was reduced *significantly* by replacing the Newton-Raphson method with the variable-property routine in FEHT (Klein *et al.* 1988). By using the temperature-dependent generation ($g_s''' = P'/A_s$) rou-

Table 4.3 Convergence of the Newton-Raphson iteration scheme.
(Calculations were performed on a Macintosh IIci.)

Tolerance (Tol)	No. of Iterations	Calculation Time (min)	Thermoseed Temperatures, Ts (C)					
			Seed 1		Seed 2		Seed 3	
			FEHT	Curve*	FEHT	Curve*	FEHT	Curve*
5e-1	4	25	55.59	55.52	54.78	54.6	58.37	58.39
5e-2	5	28	55.59	55.58	54.76	54.75	58.37	58.38
5e-3	6	35	55.59	55.59	54.76	54.76	58.38	58.38

*See Fig. 4.3c.

tine in FEHT for each of the three thermoseeds in Fig. 4.7, only nine minutes were needed for convergence of the variable-property iteration scheme. Thus a reduction in the computation time by about a factor of 4 was achieved. Nine iterations of the variable-property routine were required and seed temperatures were identical to those in Table 4.3.

4.3.2.2 Effect of Interseed Spacing with Uniform Blood Flow Models

Temperatures predicted by FEHT for a uniformly spaced, 4x4 array of ferromagnetic thermoseeds with operating temperatures of 48.1, 54.1 and 60.1 C are plotted in Fig. 4.11 as a function of thermoseed spacing in the absence of blood flow. These simulations were performed to determine thermoseed temperatures in a purely conductive medium. Temperatures of 48.1 C-type thermoseeds were from 2.6 C (seed 2, l = 15 mm) to 4 C (seed 3, l = 9 mm) higher than the operating temperature and from 1.4 C (seed 3, l = 9 mm) to 2.8 C (seed 2, l = 15 mm) below the 53 C Curie temperature. Temperatures of 54.1 C-type thermoseeds were from 1.2 C (seed 2, l = 15 mm) to 2.7 C (seed 3, l = 9 mm) higher than the operating temperature. Temperatures of 60.1 C-type thermoseeds were from 0.16 C (seed 2, l = 15 mm) to 1.8 C (seed 3, l = 9 mm) higher than the operating temperature.

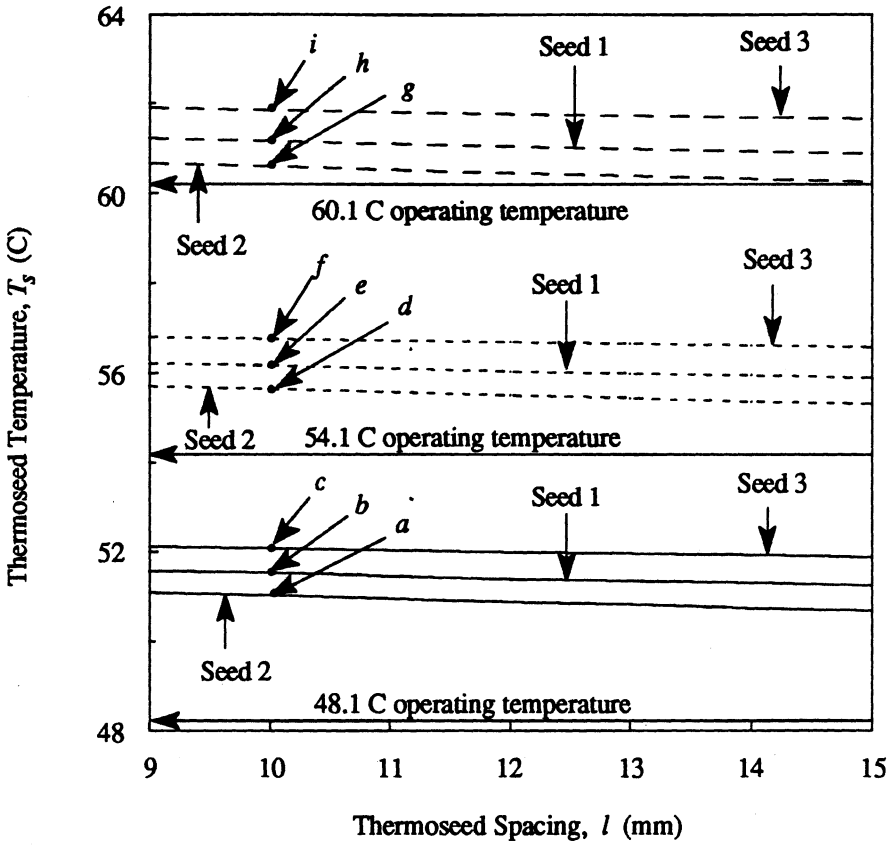

Figure 4.11 Effect of interseed spacing l on thermoseed temperatures T_s for a square, 4x4 array of thermoseeds with operating temperatures of 48.1 C (solid lines), 54.1 C (short dashed lines) and 60.1 C (long dashed lines). The simulations were performed with a tissue model in the absence of blood flow. For locations of seeds 1, 2 and 3 refer to Fig. 4.7.

Temperatures of all three types of thermoseeds were weakly dependent on interseed spacing, decreasing no more than 0.4 C (seed 2) between l = 9 and 15 mm. Thermoseed 3 is closest to the center of the thermoseed array (Fig. 4.7) and achieved the highest temperatures resulting in the least power absorption, while thermoseed 2 is furthest and thus at the lowest temperature and had the highest power absorption. This prediction was consistent for interseed spacings between l = 9 and 15 mm.

Thermoseed temperatures are plotted in Fig. 4.12 for all three types of thermoseeds in tissue with a uniform blood flow rate of m = 0.25 l/min-kg. Temperatures of 48.1 C-type thermoseeds ranged from 0.3 C (seed 3, l = 9 mm) to 1.6 C (seed 2, l = 15 mm) below the operating temperature. Temperatures of 54.1 C-type thermoseeds varied from 1.4 C (seed 3, l = 9 mm) to 3 C (seed 2, l = 15 mm) below the operating temperature while temperatures of 60.1 C-type thermoseeds ranged from 2.3 C (seed 3, l = 9 mm) to 4.2 C (seed 2, l = 15 mm) below the operating temperature. With a 10 mm spacing between 48.1 C-type thermoseeds, a uniform blood flow rate of m = 0.25 l/min-kg lowered the temperature of thermoseeds 1, 2 and 3 by 4.3, 4.1 and 4.6 C, respectively, below the temperature of thermoseeds in a purely conductive medium (compare temperatures at points *a*, *b* and *c* in Figs. 4.11 and 4.12). For similar blood flow rates, the temperatures of 54.1 C-type thermoseeds 1, 2 and 3 decreased by 4.2, 4.0 and 4.4 C, respectively (compare temperatures at points *d*, *e* and *f* in Figs. 4.11 and 4.12). Likewise, temperatures of 60.1 C-type thermoseeds 1, 2 and 3 decreased by 4.3, 4.1 and 4.5 C, respectively (compare temperatures at points *g*, *h* and *i* in Figs. 4.11 and 4.12) As with thermoseeds in a purely conductive medium, the temperature of thermoseed 2 in tissue with a blood flow rate of 0.25 l/min-kg was lower than the temperature of thermoseeds 1 and 3 which were closer to the center of the thermoseed array.

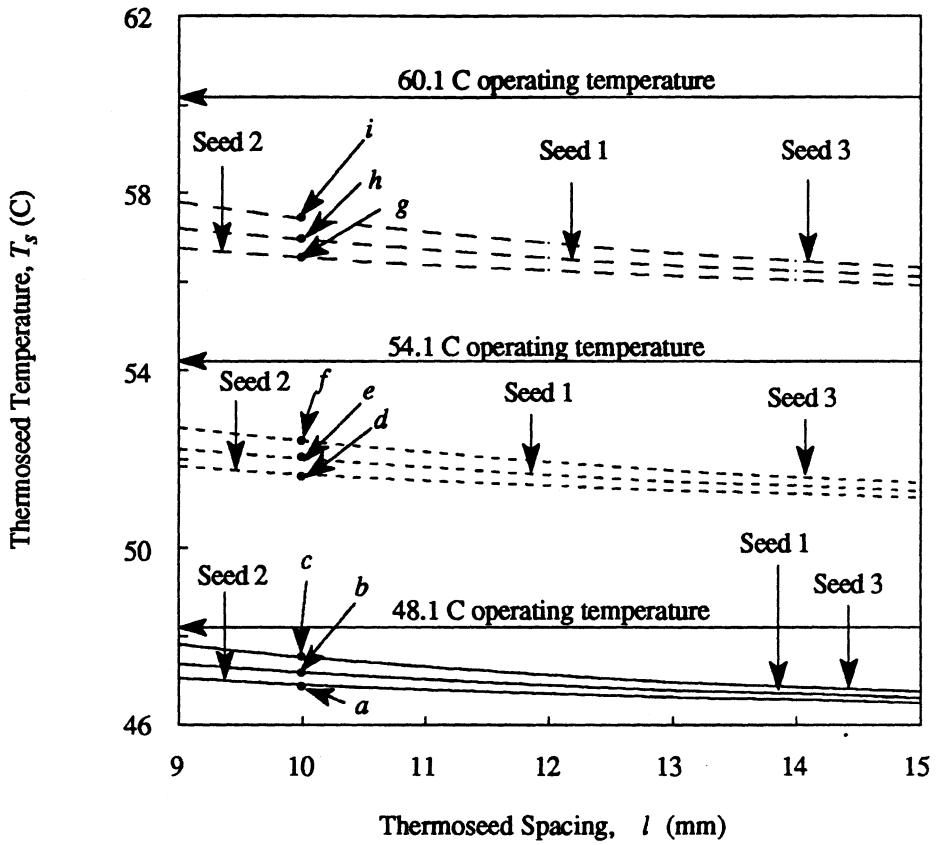

Figure 4.12 Effect of interseed spacing on thermoseed temperatures with a uniform blood flow model (m = 0.25 l/min-kg) and a square, 4x4 array of thermoseeds with operating temperatures of 48.1 C (solid lines), 54.1 C (short dashed lines) and 60.1 C (long dashed lines). For locations of seeds 1, 2 and 3 refer to Fig. 4.7.

4.3.2.3 Effect of Interseed Spacing with a Nonuniform Blood Flow Model

The differences between thermoseed temperature and the operating temperatures of 48.1, 54.1 and 60.1 C were largest for thermoseed 2 than for thermoseeds 1 and 3 (recall Figs. 4.11 and 4.12). Thus the discussion in Secs. 4.3.2.3.1 and 4.3.2.3.2 will be limited to thermoseed 2.

4.3.2.3.1 Uniformly-varying Blood Flow in Normal Tissue

The effect of blood flow in normal tissue on the temperature of thermoseed 2 is shown in Fig. 4.13 for all three types of thermoseed arrays. There was a 0.3 C temperature drop in thermoseed 2 as normal tissue blood flow increased by an order-of-magnitude in simulations with all three types of arrays, l = 10 mm spacing and with tumor blood flow of m_t = 0.1 l/min-kg. The temperature of thermoseed 2 dropped by 1.4, 1.8 and 2.1 C in simulations with arrays of 48.1 C-, 54.1 C- and 60.1 C-type thermoseeds,

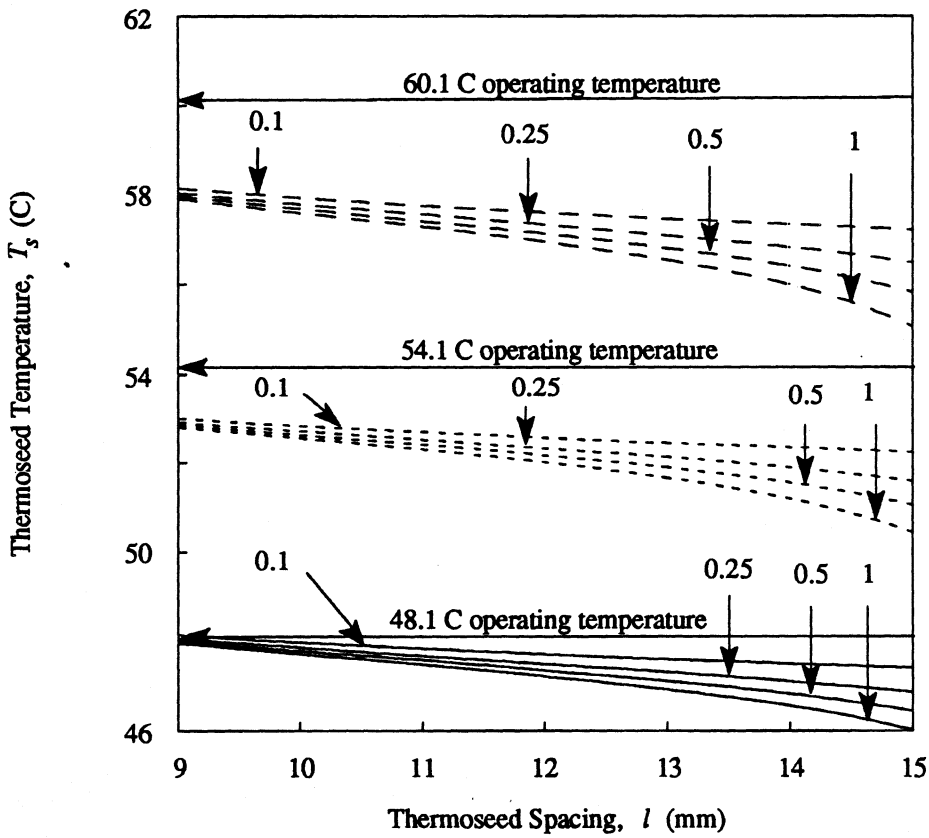

Figure 4.13 Effect of blood flow in normal tissue on the temperature of thermoseed 2 (Fig. 4.7) in a 4x4 array of thermoseeds with operating temperatures of 48.1 C (solid lines), 54.1 C (short dashed lines) and 60.1 C (long dashed lines). The simulations were performed with tumor blood flow of m_t = 0.1 l/min-kg and normal tissue blood flow m_n [l/min-kg] as labelled in the figure.

respectively, with an interseed spacing of l = 15 mm. The larger decreases in the temperature of thermoseed 2 with wider interseed spacing versus narrow interseed spacing is due to the closer proximity of thermoseed 2 to the boundary of the tumor and normal tissue.

4.3.2.3.2 Uniformly-varying Blood Flow in Tumor

The effect of tumor blood flow on the temperature of thermoseed 2 is shown in Fig. 4.14 for all three types of arrays with a blood flow in normal tissue of m_n = 0.25

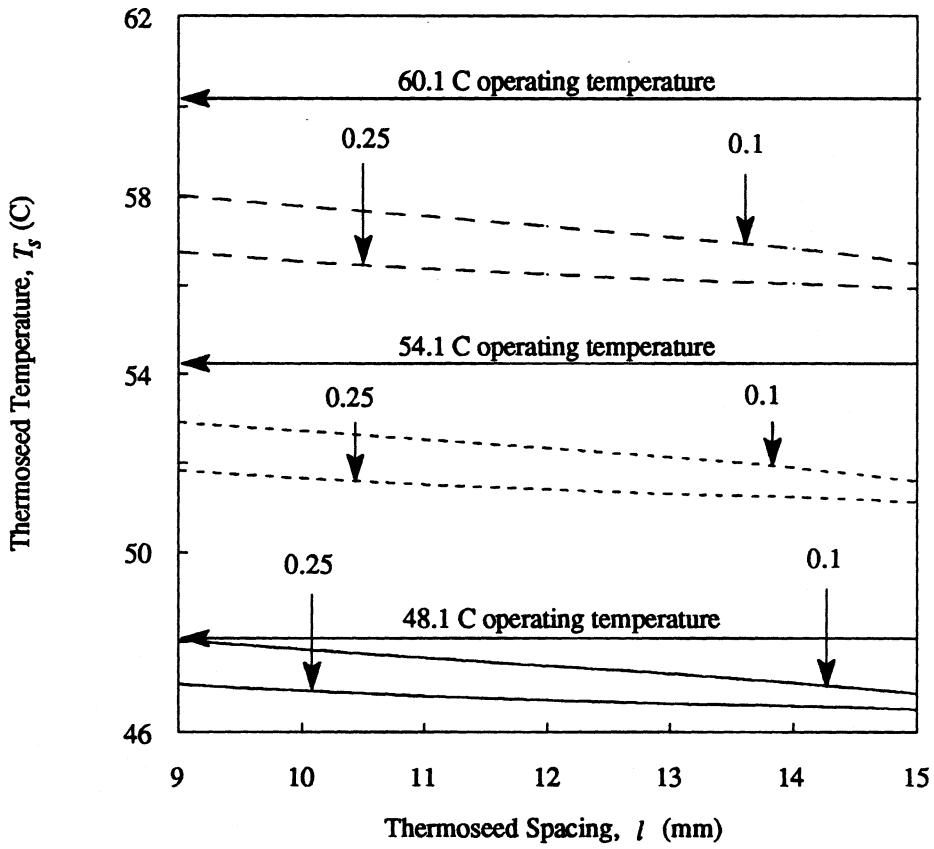

Figure 4.14 Effect of tumor blood flow on the temperature of thermoseed 2 (Fig. 4.7) in a 4x4 array of thermoseeds with operating temperatures of 48.1 C (solid lines), 54.1 C (short dashed lines) and 60.1 C (long dashed lines). The simulations were performed with blood flow in normal tissue of m_n = 0.25 l/min-kg and tumor blood flow m_t [l/min-kg] as labelled in the figure.

l/min-kg. In simulations with all types of arrays and with seed spacing of 10 mm, the temperatures of thermoseed 2 in tumor blood flow of m_t = 0.25 l/min-kg was approximately 1 C lower than the temperatures predicted with a tumor blood flow of m_t = 0.1 l/min-kg. The temperature of seed 2, over the same decrease in tumor blood flow from m_t = 0.25 to 0.1 l/min-kg, decreased by about 0.4 C with a seed spacing of l = 15 mm.

4.3.2.3.3 Effect of Compartmentalized Tumor Blood Flow Model

Thermoseed temperatures are plotted in Fig. 4.15 for all three types of thermoseed

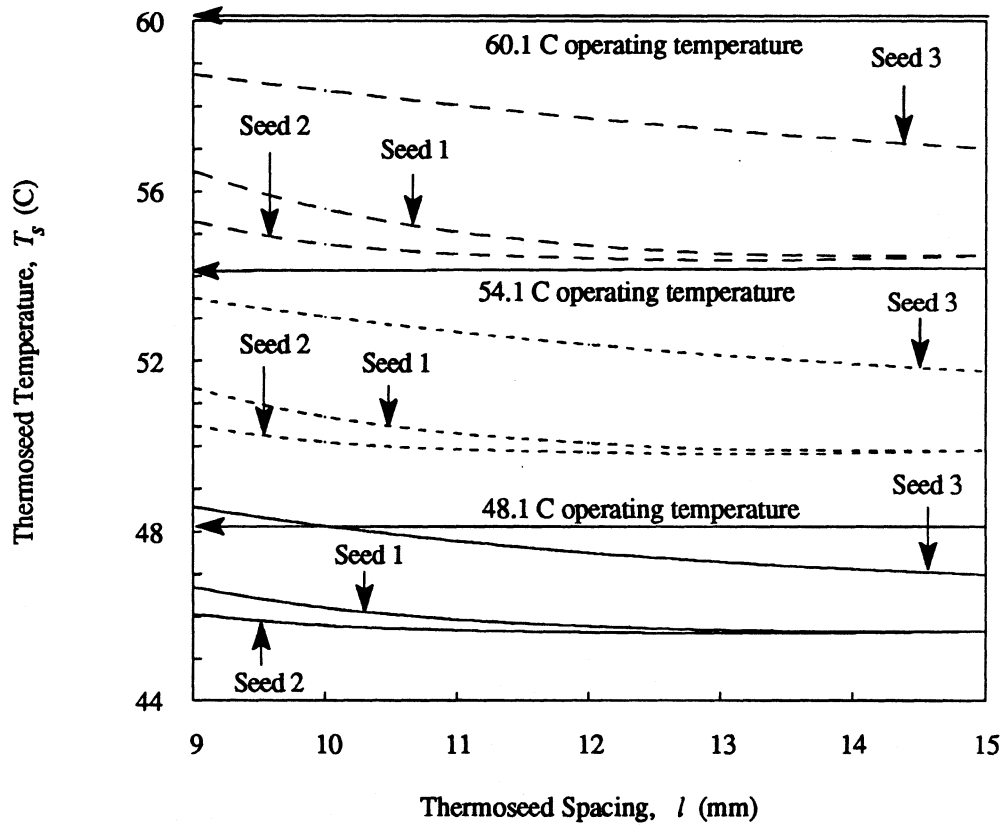

Figure 4.15 Effect of interseed spacing on thermoseed temperatures with the two-compartment tumor blood flow model ($m_{t,\ core}$ = 0.1 l/min-kg, $m_{t,\ periphery}$ = 0.75 l/min-kg, m_n = 0.5 l/min-kg) and a square, 4x4 array of thermoseeds with operating temperatures of 48.1 C (solid lines), 54.1 C (short dashed lines) and 60.1 C (long dashed lines). For locations of seeds 1, 2 and 3 refer to Fig. 4.7.

arrays (Table 4.1) in simulations with blood flow in the tumor core of $m_{t,\,core}$ = 0.1 l/min-kg, tumor periphery of $m_{t,\,periphery}$ = 0.75 l/min-kg, and normal tissue of m_n = 0.5 l/min-kg. Temperatures of all three thermoseeds dropped with increasing spacing due to the decreased heating effect that thermoseeds have on each other with wider spacings. Temperatures of thermoseeds 1 and 2 dropped between one and two degrees over seed spacings between 9 and 13 mm, while the temperature of thermoseed 3 continued to decrease beyond l = 13 mm.

So far discussion in Sec. 4.3 has been limited to the influence of blood flow on thermoseed temperatures. The influence on tissue temperatures is, however, the primary concern. In other words, what effect does using thermoseed temperatures determined with the power-versus-temperature relationship compared with the constant-temperature thermoseed modeling assumption have on tissue temperatures? Fractions of tumor greater than 43 C were determined with three types of simulations (Fig. 4.16). In the first type of simulation, thermoseed temperatures were determined with the power-versus-temperature relationship (Fig. 4.2). In the second type, the operating temperatures of the thermoseeds were used as constant-temperature modeling assumptions. Similarly, the third type of simulation used Curie temperatures as constant-temperature, modeling assumptions. Fractions of tumor greater than 43 C in simulations with an array 48.1 C-type were between 16 and 45% lower over all thermoseed spacings when the power-versus-temperature relationship was used to determine thermoseed temperature than when the operating temperature was used as the constant-temperature modeling assumption (Fig. 4.16a). Similarly, tumor fractions greater than 43 C in simulations with 54.1 C- and 60.1 C-type thermoseeds, were between 10 and 50% and between 8 and 40 % lower, respectively, over all l's when the power-versus-temperature relationship was used to determine thermoseed temperature than when the operating temperature was used (Figs.

4.16b and 4.16c). Isotherms from a simulation with an array of 60.1 C-type thermoseeds separated by 12 mm also reveal that smaller fractions of tumor are above 43 C (Fig. 4.17). The results from these simulations show that using the Cuire and operating

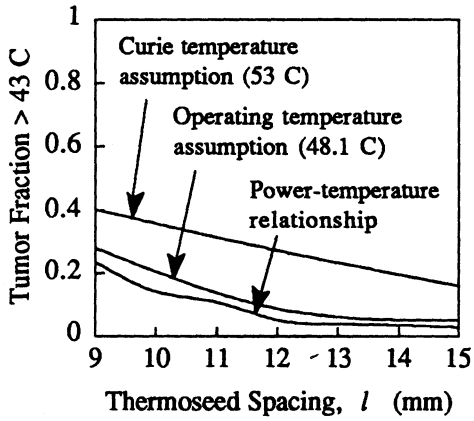

(a) 48.1 C-type

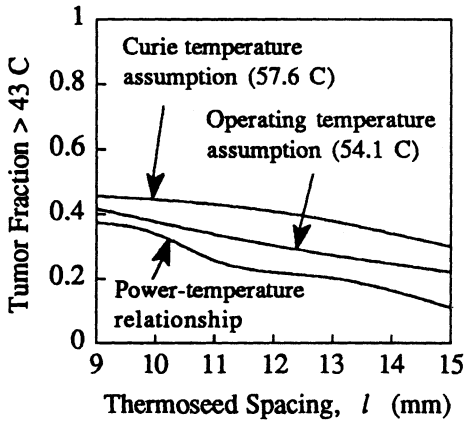

(b) 54.1 C-type

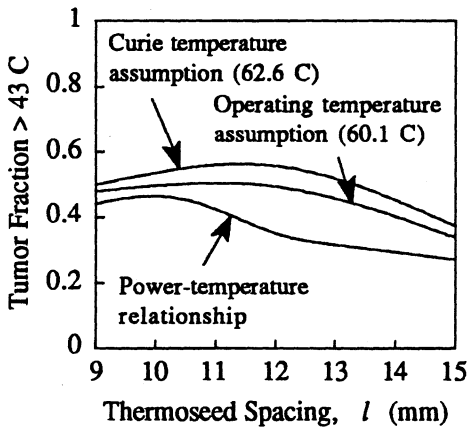

(c) 60.1 C-type

Figure 4.16 Fraction of tumor above 43 C versus thermoseed spacing from simulations with arrays of (a) 48.1 C-, (b) 54.1 C- and (c) 60.1 C-type thermoseeds. Simulations were performed where thermoseed temperatures were determined using the power-versus-temperature relationship and using the operating and Curie temperatures as constant-temperature modeling assumptions of thermoseeds. Simulations were performed with the two-compartment tumor blood flow model ($m_{t,\ core}$ = 0.1 l/min-kg, $m_{t,\ periphery}$ = 0.75 l/min-kg, m_n = 0.5 l/min-kg).

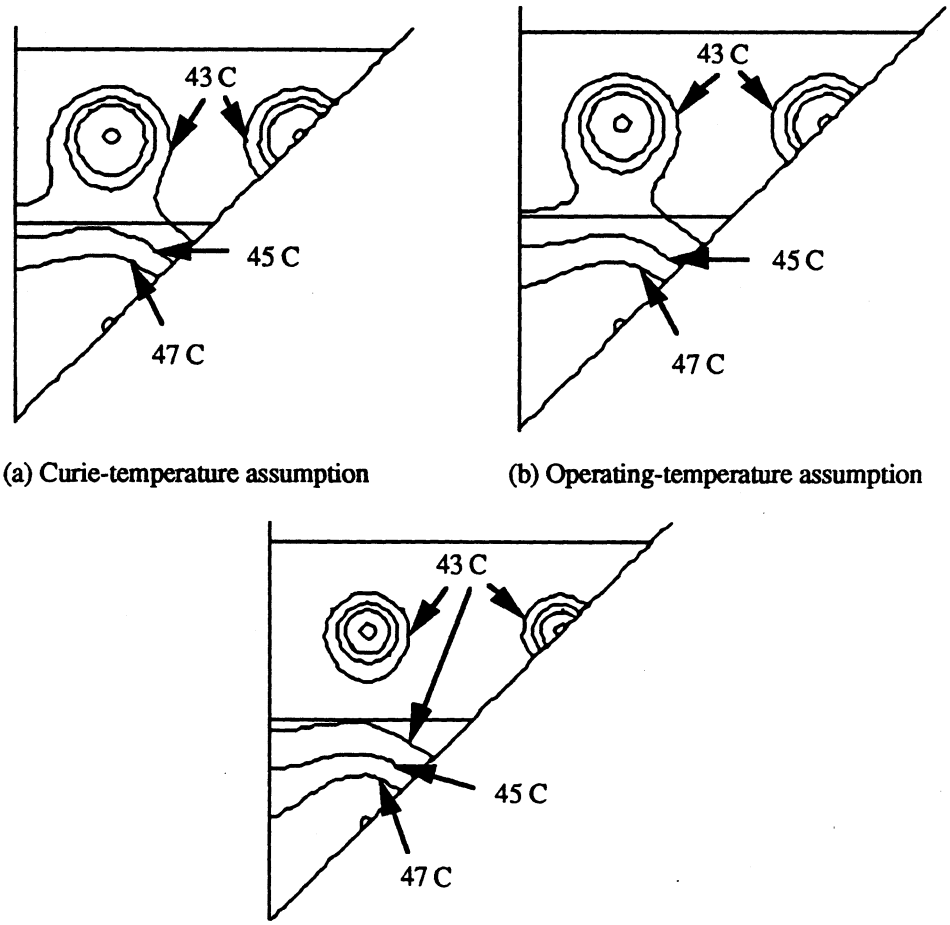

(a) Curie-temperature assumption

(b) Operating-temperature assumption

(c) Power-temperature relationship

Figure 4.17 The 43, 45 and 47 C isotherms from simulations with an array of 60.1 C-type thermoseeds and seed spacing l = 12 mm. Blood flow was $m_{t,\ core}$ = 0.1 l/min-kg, $m_{t,periphery}$ = 0.75 l/min-kg and m_n = 0.5 l/min-kg. Thermoseed temperatures were (a) equal to the Curie temperature of 62.6 C, (b) equal to the operating temperature of 60.1 C, and (c) determined with the power-versus-temperature relationship (Fig. 4.2).

temperatures as constant-temperature modeling assumptions significantly over-estimates the fraction of tumor greater than 43 C versus that when the power-temperature relationship is used.

4.3.3 Effect of Catheter Model

The temperatures of thermoseed 2 versus normal tissue blood flow in simulations with tumor blood flow rates of m_t = 0.1 and 0.25 l/min-kg in a configuration of *bare* 48.1 C-type thermoseeds are compared with those in which thermoseed *and* catheter models (Sec. 3.2.3) were used (Fig. 4.18). Interseed spacing in these simulations was l = 10 mm. The temperature of thermoseed 2 in simulations with m_t = 0.1 l/min-kg and with thermoseeds placed inside catheters was 0.4 C higher than in simulations with bare thermoseeds. The 0.4 C increase in the temperature of thermoseed 2 was uniform over normal tissue blood flow rates between m_n = 0.1 and 1 l/min-kg (solid lines in Fig. 4.18). Similarly, the temperature of thermoseed 2 in simulations with tumor blood flow

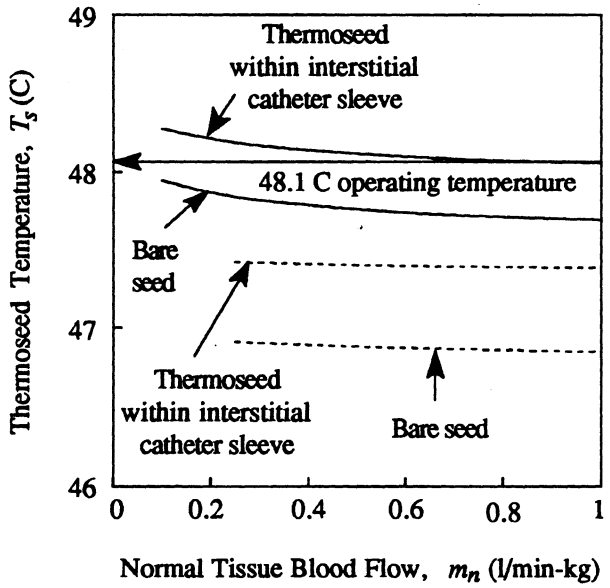

Figure 4.18 Effect of catheter on temperature of thermoseed 2 (Fig. 4.7) as a function of normal tissue blood flow m_n for tumor blood flows of m_t = 0.1 l/min-kg (solid lines) and 0.25 l/min-kg (dashed lines). Simulations were performed with 48.1 C-type thermoseeds with an interseed spacing of l = 10 mm. Catheter wall thickness was 0.35 mm.

of m_t = 0.25 l/min-kg was 0.5 C higher in simulations with thermoseeds inside catheters versus simulations with bare thermoseeds. The 0.5 C increase was uniform over normal tissue blood flow rates between m_n = 0.25 and 1 l/min-kg (see dashed curves in Fig. 4.18).

Simulations were performed with all three types of thermoseed arrays in which thermoseeds *and* catheter sleeves were modeled. The simulations were performed with a spacing of l = 10 mm and with several blood flow models. The drop in temperature from the inner wall to the outer wall of the catheter for all thermoseeds are shown in Table 4.4. Temperatures through the catheter wall surrounding 48.1 C-type thermoseeds decreased by 1.7 to 3.4 C over all blood flow models studied (Table 4.4a). The temperature drops are larger with higher temperature thermoseeds. Temperatures through the catheter wall surrounding 54.1 C-type thermoseeds decreased by 2.3 to 5.0 C (Table 4.4b), while temperatures through catheter walls surrounding 60.1 C-type thermoseeds dropped by 3.2 to 6.8 C (Table 4.4c). The temperature drop through the catheter wall was due to the thickness and thermal conductivity of the catheter and absence of blood flow. Because of the temperature drop through the catheters, the fraction of tumor greater than 42 C for all three types of thermoseed arrays in simulations with thermoseed and catheter models were between 1 and 45.3% lower over all blood flow models studied than in simulations with bare thermoseeds (Table 4.5). In summary, because of the modest to dramatic temperature drops through catheter walls and the smaller fractions of tumor above 42 C for thermoseeds within catheter models versus bare thermoseeds, more realistic temperature distributions will be obtained if catheter models are included in computer simulations.

Table 4.4 Average Temperature Drop Through Catheter Wall
Simulations were performed with arrays of thermoseeds spaced l = 10 mm apart.

a. 48.1 C-type thermoseeds

Blood flow (l/min-kg)		Temperature Drop Through Catheter Wall (C)		
Tumor, m_t	Normal, m_n	Catheter 1	Catheter 2	Catheter 3
0.1	0.1	2.1	2.3	1.8
0.1	0.25	2.1	2.3	1.7
0.1	0.5	2.1	2.3	1.8
0.1	1	2.1	2.3	1.8
0.25	0.25	2.8	2.9	2.5
0.25	0.5	2.8	2.9	2.5
0.25	1	2.7	2.9	2.5
0.1 (c); 0.75 (p)	0.5	3.2	3.4	2.3

b. 54.1 C-type thermoseeds

Blood flow (l/min-kg)		Temperature Drop Through Catheter Wall (C)		
Tumor, m_t	Normal, m_n	Catheter 1	Catheter 2	Catheter 3
0.1	0.1	2.9	3.4	2.3
0.1	0.25	3.1	3.5	2.5
0.1	0.5	3.1	3.5	2.6
0.1	1	3.2	3.5	2.5
0.25	0.25	4.1	4.2	3.8
0.25	0.5	4.0	4.3	3.7
0.25	1	4.0	4.2	3.7
0.1 (c); 0.75 (p)	0.5	4.8	5.0	3.2

c. 60.1 C-type thermoseeds

Blood flow (l/min-kg)		Temperature Drop Through Catheter Wall (C)		
Tumor, m_t	Normal, m_n	Catheter 1	Catheter 2	Catheter 3
0.1	0.1	4.0	4.4	3.2
0.1	0.25	4.0	4.6	3.2
0.1	0.5	4.1	4.7	3.3
0.1	1	4.1	4.8	3.3
0.25	0.25	5.4	5.7	5.0
0.25	0.5	5.4	5.7	5.0
0.25	1	5.5	5.8	5.0
0.1 (c); 0.75 (p)	0.5	6.5	6.8	4.3

Table 4.5 Fraction of Tumor Above 42 C
Simulations were performed with arrays of thermoseeds spaced l = 10 mm apart.

a. 48.1 C-type thermoseeds

Blood flow (l/min-kg)		Fraction of Tumor > 42 C		
Tumor, m_t	Normal, m_n	w/o Catheter	w/ Catheter	Difference (%)
0.1	0.1	0.68	0.64	5.8
0.1	0.25	0.64	0.60	5.6
0.1	0.5	0.62	0.59	5.5
0.1	1	0.60	0.57	5.5
0.25	0.25	0.35	0.19	44.6
0.25	0.5	0.34	0.19	44.9
0.25	1	0.33	0.18	45.3
0.1 (c); 0.75 (p)	0.5	0.24	0.18	24.6

b. 54.1 C-type thermoseeds

Blood flow (l/min-kg)		Fraction of Tumor > 42 C		
Tumor, m_t	Normal, m_n	w/o Catheter	w/ Catheter	Difference (%)
0.1	0.1	0.88	0.83	5.1
0.1	0.25	0.80	0.76	5.4
0.1	0.5	0.76	0.73	4.3
0.1	1	0.73	0.70	4.6
0.25	0.25	0.62	0.58	6.5
0.25	0.5	0.61	0.58	4.9
0.25	1	0.61	0.57	6.6
0.1 (c); 0.75 (p)	0.5	0.41	0.37	9.8

c. 60.1 C-type thermoseeds

Blood flow (l/min-kg)		Fraction of Tumor > 42 C		
Tumor, m_t	Normal, m_n	w/o Catheter	w/ Catheter	Difference (%)
0.1	0.1	0.96	0.95	1.0
0.1	0.25	0.92	0.89	3.3
0.1	0.5	0.87	0.84	3.4
0.1	1	0.82	0.80	2.4
0.25	0.25	0.73	0.69	5.5
0.25	0.5	0.71	0.68	4.2
0.25	1	0.70	0.67	4.3
0.1 (c); 0.75 (p)	0.5	0.53	0.49	7.5

4.4 Thermoseed Temperature in Nondimensional Tissue Model

The nondimensional temperature T^* of thermoseeds 1, 2 and 3 as a function of the Implant-Biot number Bi_I are illustrated in Fig. 4.19. The maximum nondimensional thermoseed temperatures are near the Curie temperature of each thermoseed and occurred with a $Bi_I \sim 0$. The minimum thermoseed temperature T_s^* was ~ 0 (*i.e.*, $T_s \sim T_b$) and occurred with a Bi_I of approximately 15,000. As in the results from the dimensional tissue model (Sec. 4.3.2), nondimensional thermoseed temperatures are lower for thermoseeds further from the center of the thermoseed array.

The decrease in the temperature of thermoseeds 1, 2 and 3 for Implant-Biot numbers Bi_I between 0 and 7 are in Table 4.6. The change in Bi_I from 0 to 7 corresponds to a change in blood flow from m = 0 to 1 l/min-kg for k_t = 1 W/m-C and l = 10 mm. The temperature of thermoseeds with higher operating temperatures decreased more than that with lower operating temperature thermoseeds.

The Implant-Biot number is proportional to tissue perfusion $w_b c_b$, to the square of thermoseed spacing l and inversely proportional to tissue thermal conductivity k_t (recall Eq. 4.9). Thus thermoseed temperature will decrease with increasing thermoseed separation, increasing blood flow and decreasing tissue thermal conductivity. Since Bi_I is proportional to the square of thermoseed spacing, changes in thermoseed spacing will have a larger influence on thermoseed temperature than the for the same change in blood flow rate. The effects of increasing blood flow, thermoseed spacing and the operating temperature by a factor of 1.54[10] are in Table 4.7. Increasing tissue perfusion from 2009 to 3094 W/m^3-C decreased thermoseed temperatures by approximately 0.6 to 0.9 C for all

[10]A factor of 1.54 was used since the nondimensional operating temperature of the 0.668-type thermoseed is 1.54 times greater than the 0.434-type seed.

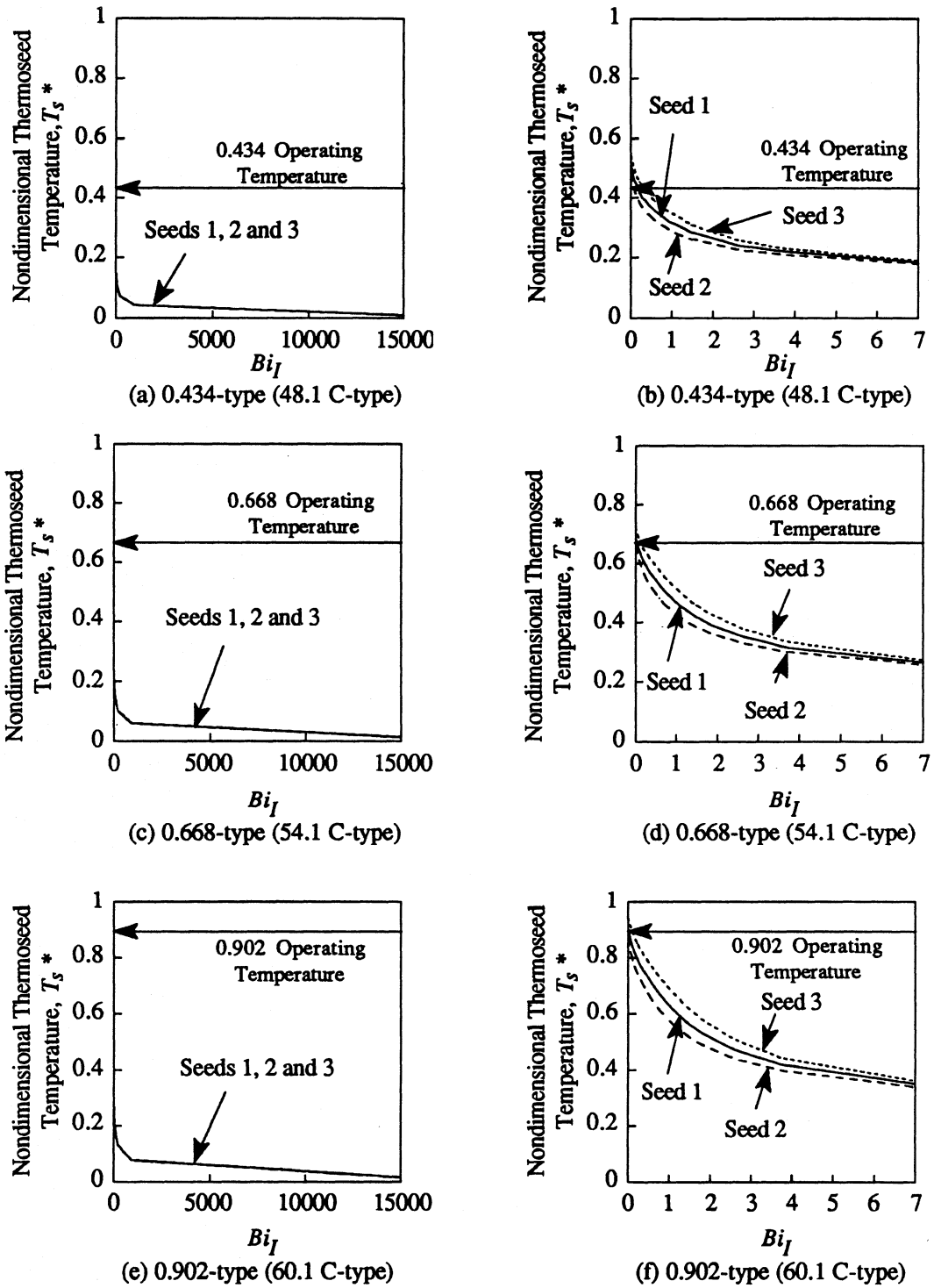

Figure 4.19 Nondimensional thermoseed temperature T_s* as a function of Implant-Biot number Bi_I for thermoseeds 1, 2 and 3. Simulations were performed with arrays of (a and b) 0.434-, (c and d) 0.668- and (e and f) 0.902-type thermoseeds. For seed location refer to Fig. 4.9.

Table 4.6 Nondimensional Temperature Drop of Thermoseeds for Implant-Biot numbers Bi_I between 0 and 7

Thermoseed Type in Array	Nondimensional Thermoseed Temperature Drop		
	Seed 1*	Seed 2*	Seed 3*
0.434	0.33	0.31	0.36
0.668	0.43	0.41	0.46
0.902	0.56	0.53	0.59

*See Fig. 4.9 for seed location.

three thermoseed types. Increasing thermoseed spacing from 10 to 15.4 mm decreased thermoseed temperatures by 1.3 to 2 C. Thus thermoseed temperatures were reduced by about twice the amount for increasing thermoseed spacing versus the same increase in tissue perfusion. An increase in the operating temperature of thermoseeds from 0.434 to 0.668, increased the temperature of thermoseeds 1, 2 and 3 by 4.8, 4.6 and 4.9 C, respectively, at a seed spacing of l = 10 mm and perfusion of $w_b c_b$ = 2009 W/m^3-C.

Table 4.7 Effect of Spacing, Tissue Perfusion, and Thermoseed Operating Temperature on Thermoseed Temperature
(Thermoseed temperatures T_s (C) are shown in parentheses.)

Thermoseed Spacing, l (mm) =	10	10	15.4
Perfusion, $w_b c_b$ (W/m^3-C) =	2009	3094	2009
Thermoseed	Implant-Biot No., Bi_I		
Array Type	0.2	0.31	0.48
0.434-type (48.1 C-type)			
Seed 1:	0.422 (47.8)	0.397 (47.2)	0.370 (46.5)
Seed 2:	0.389 (47.0)	0.365 (46.3)	0.339 (45.7)
Seed 3:	0.459 (48.8)	0.434 (48.1)	0.406 (47.4)
0.668-type (54.1 C-type)			
Seed 1:	0.609 (52.6)	0.583 (51.9)	0.549 (51.1)
Seed 2:	0.570 (51.6)	0.540 (50.8)	0.504 (49.9)
Seed 3:	0.651 (53.7)	0.628 (53.1)	0.597 (52.3)
0.902-type (60.1 C-type)			
Seed 1:	0.808 (57.7)	0.775 (56.8)	0.734 (55.8)
Seed 2:	0.759 (56.4)	0.723 (55.5)	0.678 (54.4)
Seed 3:	0.861 (59.0)	0.830 (58.2)	0.793 (57.3)

4.5 Conclusion

Figure 4.16 illustrates that fractions of tumor greater than 43 C are smaller in simulations when thermoseed temperatures depend on power versus models which assume a constant thermoseed temperature such as the Curie or operating temperature. Fractions of tumor greater than 43 C are between 8 and 40% lower when thermoseed temperatures depend on power versus models which assume a constant temperature equal to the operating temperature. Fractions of tumor greater than 43 C are even larger than those achieved with the constant operating-temperature assumption if the Curie temperature is used as the assumed constant temperature.

It has been stated that little change in thermoseed temperature occurs for variations in tissue cooling rates within an array of thermoseeds (Stauffer 1990). Results from the simulations in this chapter should help to quantify the conclusion made by Stauffer (1990). In all simulations, the temperature of thermoseeds furthest from the center of the thermoseed array absorbed more power and were at lower temperatures than thermoseeds located closer to the center of the array. In simulations with all three types of arrays and where the seed spacing was 10 mm and the tumor blood flow was 0.1 l/min-kg, the temperature of thermoseeds located furthest from the center of the array dropped by 0.3 C as normal tissue blood flow increased by an order-of-magnitude from 0.1 to 1 l/min-kg (Fig. 4.13). The temperature of these thermoseeds dropped by 1.4, 1.8 and 2.1 C in simulations with arrays of 48.1 C-, 54.1 C- and 60.1 C-type thermoseeds, respectively, with an interseed spacing of 15 mm. In simulations with all three types of arrays and with seed spacing of 10 mm, the temperature of the furthest thermoseed in a tumor with blood flow of 0.25 l/min-kg was approximately 1 C lower than the temperature predicted with a tumor blood flow of 0.1 l/min-kg. The temperature of the furthest thermoseed,

over the same decrease in tumor blood flow from 0.25 to 0.1 l/min-kg, decreased by about 0.4 C with a seed spacing of 15 mm.

In a theoretical study with constant temperature thermoseeds the periphery of tissue outside the thermoseed array did not heat as well as tissue between thermoseeds (Mechling and Strohbehn 1986). The study by Mechling and Strohbehn (1986) suggests that the periphery of a thermoseed array may be a likely site for placing thermoseeds with higher operating temperatures. Stauffer (1990) has made a similar suggestion. Results from the present study, where the power-versus-temperature dependence of thermoseeds was used in modeling thermoseeds, revealed that thermoseeds furthest from the center of the thermoseed array were cooler than thermoseeds closer to the center of the array (Fig's. 4.11 and 4.12). The lower temperature thermoseeds near the periphery of the tumor supports the conclusion that the tumor periphery is a likely site for thermoseeds with higher temperatures.

It has been shown that catheters can affect temperature fields in the tissue and, therefore, should be considered explicitly in simulations (Haider *et al.* 1991). The temperature of 48.1 C-type thermoseeds were approximately 0.5 C higher in simulations with thermoseeds inside catheter models versus simulations with bare thermoseeds (Fig. 4.18). Thus the modeling of catheters around thermoseeds was shown to decrease the absorbed power of thermoseeds and increase their temperature versus modeling thermoseeds without catheters. Seed temperatures were higher for thermoseeds within catheters than bare thermoseeds because the cooling effect of blood flow was absent at the surface of thermoseeds inside catheter sleeves. The drops in temperature through the catheter walls were significant. The temperatures at the outer surface of catheters were between 1.7 and 6.8 C below the temperatures at the inner surface over a wide range of blood flow models and thermoseed types (Table 4.4). Because of the temperature drop

through the catheters, the fraction of tumor greater than 42 C in simulations using thermoseed and catheter models were between 1 and 45.3% lower over all blood flow models and thermoseed array types studied than in simulations with bare thermoseeds. In summary, because of the modest to dramatic temperature drops through catheter walls and the smaller fractions of tumor above 42 C in simulations with thermoseed and catheter models versus *bare* thermoseed models (*i.e.*, without catheter models), more realistic temperature distributions will be obtained if catheter models are included in computer simulations.

It was shown with simulations that increasing thermoseed spacing caused twice the drop in thermoseed temperature than for the same increase in tissue perfusion (Sec. 4.4). In conclusion, when considering ferromagnetic hyperthermia variables that affect treatment planning such as blood flow, thermoseed spacing and thermoseed operating (or Curie) temperatures, changes in thermoseed spacing have a greater effect on thermoseed temperature than for the same *relative* change in tissue perfusion. It was also shown that thermoseeds with higher Curie points of the same *relative* increase in operating temperature can more than off-set the drop in thermoseed temperature resulting from increased seed spacing or higher blood flow rates.

Chapter 5

Physiologically-Based Objective Function

The objective function is a mathematical formulation of hyperthermia treatment goals. This chapter discusses the physiological basis that was used to formulate the objective function (Sec. 5.1). The formulation of the objective function is presented in Sec. 5.2. In Sec. 5.3, numerically computed objective functions are compared to analytically computed values for simple tissue geometries. Some concluding remarks are made in Sec. 5.4.

5.1 Hyperthermia Treatment Goals

There are at least two concerns with transferring laboratory-generated biological hyperthermia data to the clinic. This first concern is, how well do cell-survival data from laboratory experiments with assays of neoplasms predict the survival of human tumors? The answer to this question is the subject of much research. Clearly all the physiological conditions of a human neoplasm including the aerobic state, pH level, and nutrient supply cannot be simulated identically in the laboratory. The physiological conditions can differ from tumor to tumor and from location to location within the same neoplasm. The conditions also vary temporally (with time).

The second concern is, which temperature descriptor within the tumor determines the survival of the tumor? This broad concern of dose is more acute for hyperthermia

than for radiation, since temperature distributions are inhomogeneous for hyperthermia and suffer from temporal variations due to changes in blood flow rates. Tumor cure might be expected to correlate best with minimum temperatures within the target volume, since clonogens surviving in any region of lower temperature may be a site for regrowth of the tumor. Research has shown that a hyperthermia treatment is successful if the steady-state temperatures throughout the tumor are at or above a minimum temperature (Dewhirst *et al.* 1984, Van Der Zee *et al.* 1986). Other research has suggested that stronger predictors of histopathological outcome are T_{90} and T_{50} temperature descriptors (Leopold *et al.* 1992). The T_{90} and T_{50} are the temperatures at which 90% and 50%, respectively, of all measured temperatures are at or above.

The energy required for inactivation (or death) of mammalian cells in culture supports the theory that maintaining tumor temperatures above a minimum is the preferred treatment goal. A plot of the reciprocal of the slope in the exponential region of cell-survival curves versus the reciprocal of the absolute temperature (an Arrhenius plot) has shown that a significant change in slope occurs between 42 and 43 C (Dewey *et al.* 1977a). In other words, it is believed that the differences in inactivation energy above and below this temperature range may reflect different mechanisms of cell killing (Hall 1988).

In the hyperthermia clinic at the University of Wisconsin, treatments are given locally to tumors (usually 3 to 20 cm^3) with either an external microwave applicator or an array of ferromagnetic thermoseeds within interstitial catheter sleeves. When hyperthermia is delivered with the external microwave applicator, the treatment goal is to maintain the maximum measured tumor temperature at or near 43 C for 1 hour. In practice, however, the measured tumor temperatures that are achieved and maintained are influenced by the patient's tolerance of temperature. Sometimes maximum measured

tumor temperatures can be 1 or 2 C above or below 43 C. Tumor temperatures are measured within one or two catheters which are placed surgically into the tumor prior to the initial treatment. Tumor temperatures can be raised or lowered by adjusting applicator power, the position of the applicator and the amount of surface cooling provided by a water bolus. When hyperthermia is given with an array of ferromagnetic thermoseeds, the treatment goal is also to maintain the maximum measured tumor temperature close to 43 C for 1 hour.

5.2 Objective Function

The proposed objective function has a physiological basis which is based on cell-survival data. Discussion of the physiological basis and the cell-survival curves are presented in Secs. 5.2.1 and 5.2.2, respectively. The formulation of the objective function is presented in Sec. 5.2.3.

5.2.1 Physiological Basis

An objective function is a mathematical equation. In hyperthermia applications, objective functions are formulated so that when the objective function is maximized, a set of treatment variables is optimized. Within the limits of the model, the set of optimized treatment variables will deliver the *best* heat treatment. (Conversely, it is possible to formulate the objective function so that its minimum optimizes the treatment variables.) Objective functions that seek to optimize temperature distributions in tumor and normal tissues by selecting the *best* set of variables for delivering hyperthermia with ultrasound from a scanned focussed system have been mentioned (Sec. 1.6.1).

The proposed objective function utilizes cell-survival data where increased cell killing is achieved with temperatures above 42 to 43 C. It is known that heat kills cells in

culture in a predictable and repeatable manner (Dewey *et al.* 1977a). Moreover, higher temperatures kill more cells in culture than lower temperatures for the same heating period. If the goal of a hyperthermia treatment is to maximize tumor cell death and/or minimize normal cell destruction, use of cell-survival data may provide a basis for an alternative method to select the *best* set of treatment variables. An objective function with this physiological basis would utilize the effect of increased cell killing at temperatures above 42 to 43 C.

5.2.2 *In Vitro* Cell-Survival Curves

Survival curves are the basis of the objective function in this study. The following are the steps involved in performing a typical experiment to generate cell-survival curves. By using current techniques of tissue culture, samples from tumor or normal regenerative tissues are divided into small pieces and prepared as single-cell suspensions by the use of the enzyme trypsin, which dissolves adherent bonding on the outer cell membrane. Trypsin also causes the cells to coalesce and detach from the surface of the culture vessel. The number of cells per unit volume in a suspension is counted mechanically prior to the experiment. Then the cells are seeded into a dish. After the dish has been incubated for one to two weeks, each cell will divide many times and form a colony. Therefore, all cells comprising each colony are the offspring of a single ancestor. For a nominal 100 cells seeded into a dish, 50 to 90 colonies will form. Ideally, 100 colonies should form, but because of a suboptimal growth medium, errors and uncertainties in counting the cell suspension, and the trauma of trypsinization and handling, only a fraction of cells originally seeded form colonies (Hall 1988). The term *plating efficiency* (PE) gives the percentage of cells seeded that grow into colonies and

thus is a measure of the cells which did not reproduce. For example, in the case where there are 70 colonies counted, the plating efficiency would be 70%.

Cell survival of a heat treatment is determined by seeding a second dish with 100 cells, exposing it to a heat treatment at some temperature for a period time, and then incubating the dish for one to two weeks before the cells are fixed and stained. After this procedure, the following may be observed: (1) some of the seeded single cells are still single and have not divided; (2) some cells completed one or two divisions to form a tiny *abortive* colony; and (3) some cells have grown into large colonies that differ little from the unheated controls. The cells of (3) are said to have *survived.* If the plating efficiency was PE = 60%, only 60 cells would have grown into colonies if the dish had not been heated. If only 10 colonies were counted, then the fraction of cells surviving the heat treatment would be 0.167 (= 10/60). In general, the surviving fraction S is given by

$$S = \frac{\textit{Colonies counted}}{\textit{Cells seeded (PE/100)}} \tag{5.1}$$

Experiments like the one described above are repeated so that estimates of cell survival are obtained for a range of temperatures between 41 and 47 C and heating times from 30 minutes to several hours. The surviving fraction is plotted versus exposure to hyperthermia for several temperatures (Fig. 5.1).

5.2.3 Objective Function Formulation

The objective function is developed for use with dimensional tissue models in Sec. 5.2.3.1. There is a brief discussion in Sec. 5.2.3.2 on how the objective function might be used in simulations with nondimensional tissue models.

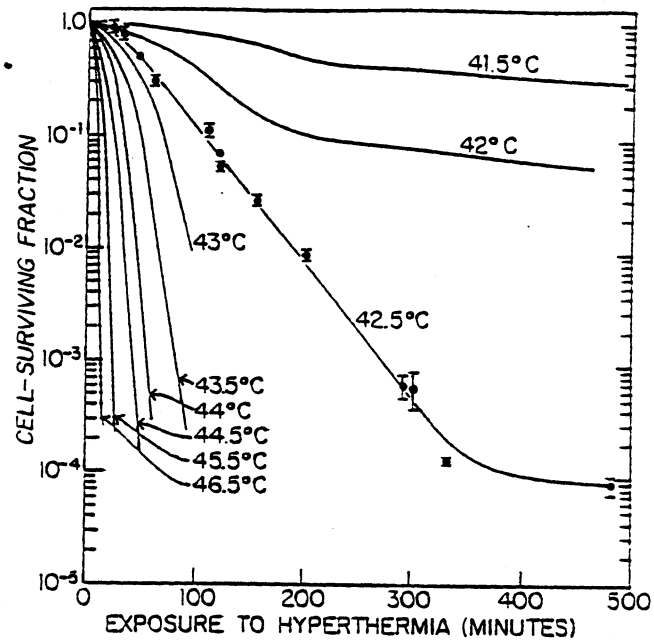

Figure 5.1 Survival curves for mammalian cells in culture (Chinese hamster CHO line). The surviving fraction S versus exposure time to hyperthermia is plotted for several temperatures. This figure is a reprint of data gathered by Dewey *et al.* (1977a).

5.2.3.1 Dimensional Tissue Models

The model for simulating cell survival is shown in Fig. 5.2. The model is not intended to represent cell survival of any particular established cell line, but rather cell survival in general. Nonetheless, the data in Fig. 5.1 is represented closely by the models in Fig. 5.2. It is possible to construct plots like the one shown in Fig. 5.2 from actual cell-survival data by a two-step process. First, an exposure time to hyperthermia is selected prior to treatment. The exposure time is typically 60 min. With the aid of a vertical line in Fig. 5.1 for a preselected exposure time, the surviving fraction of tissue can be determined at different temperatures. Then a plot is constructed of the surviving fraction versus temperature for the preselected exposure time.

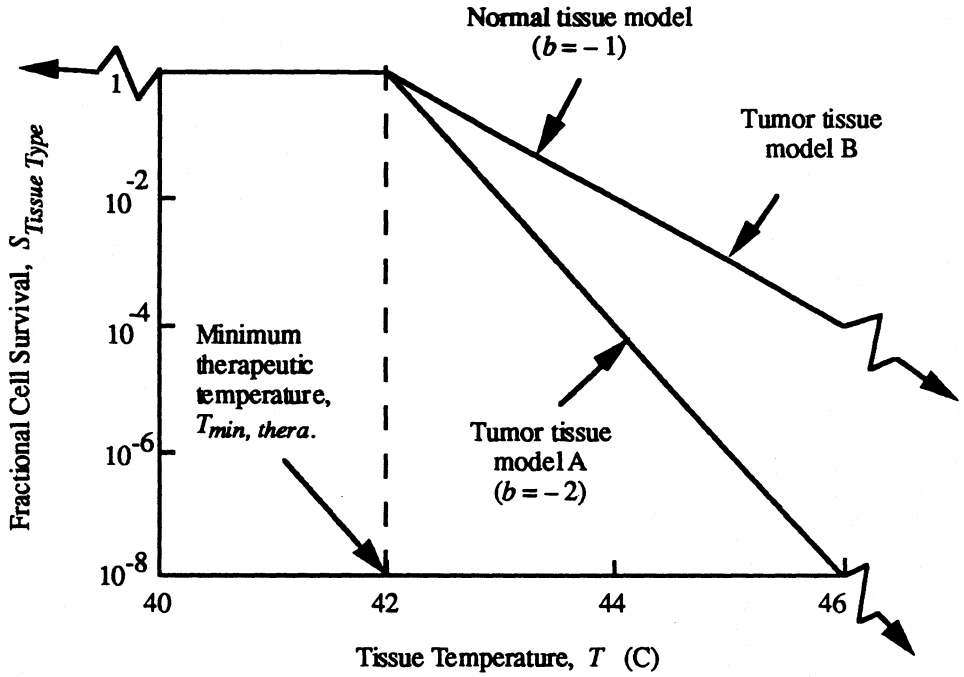

Figure 5.2 The models of the fractional cell survival S as a function of tissue temperature T for tumor and normal tissues. It is assumed that the hyperthermia treatment time for this data is 60 min. Two models (A and B) simulating the survival of tumor tissue are shown. $T_{min,\ thera.}$ is shown here to be 42 C. The coefficient b is the slope of the (logarithmic) cell-survival curves (Eq. 5.2).

It is assumed that tissue survival is solely a function of temperature for a preselected exposure time. Thus tissue survival is independent of the cell pH, available oxygen and nutrient levels, and cell cycle. A definition of cell survival relevant to hyperthermia was assumed. In other words, cells were assumed to suffer *reproductive death* when tissue temperature was above the minimum therapeutic temperature $T_{min,\ thera.}$. Therefore a particular fraction of cells were unable to divide and cause further regrowth at temperatures above $T_{min,\ thera.}$, while below $T_{min,\ thera.}$, it was assumed that no tissue was killed.

Although it is known that different cells have different sensitivities to heat, there is no *consistent* difference in the heat sensitivity between normal and malignant cells (Hall,

1988). One model for survival of tumor cells is, therefore, equal to the survival of normal cells (Fig. 5.2, tumor tissue model B). In spite of the fact that there is no *consistent* difference in the heat sensitivity between normal and malignant cells, Robins *et al.* (1983) have shown that AKR leukemia cells were more sensitive than normal cells to hyperthermia killing at 41.8 and 42.5 C. Thus the present study also investigates the effect of a difference in the sensitivity between normal and malignant cells to heat, with malignant cells being more sensitive (Fig. 5.2, tumor tissue model A).

The cell-survival data in Fig. 5.2 was approximated by logarithmic curves where the fraction of cells surviving a heat treatment $S_{Tissue\ Type}$ [dimensionless] was a function of tissue temperature T. The cell-survival data can be approximated by

$$S_{Tissue\ Type} = 1 \quad , \quad T \leq T_{min,\ thera.} \tag{5.2a}$$

$$S_{Tissue\ Type} = 10^{\,b\ (T\ -\ T_{min,\ thera.})} \quad , \quad T > T_{min,\ thera.} \tag{5.2b}$$

In Eq. 5.2, *Tissue Type* designates either tumor or normal tissue and b is the slope of the cell-survival curve. In simulations within this study, b has a value of -1 for normal tissues and a value of -1 or -2 for tumor tissues (Fig. 5.2). For other cell-survival models, though, b could have value other than -1 or -2.

Because of the spatial dependence of temperature in tissue, the *local* fraction of surviving cells $S_{Tissue\ Type}$ was integrated over the volume of tissue considered. The *volumetric*, fractional cell survival is designated $S_{V,\ Tissue\ Type}$ and is given by

$$S_{V,\ Tissue\ Type} = 1 \quad , \quad T \leq T_{min,\ thera.} \tag{5.3a}$$

$$S_{V,\,Tissue\ Type} = \frac{\int_V 10^{\,b\ (T - T_{min,\,thera.})}\ dV}{\int_V dV} \quad , \ T > T_{min,\,thera.} \qquad (5.3b)$$

Since the finite element method is used to determine the temperature distribution, Eq. 5.3 was computed using $S_{V,\,Tissue\ Type}$ in each finite element e. Therefore the volumetric fraction of cells surviving a heat treatment in finite element e, $S_{V(e),\,Tissue\ Type}$, was determined by integrating the surviving fraction with respect to the volume of the element $V^{(e)}$ [m^3] and then dividing by $V^{(e)}$. The expression for $S_{V(e),\,Tissue\ Type}$ is given by

$$S_{V^{(e)},\,Tissue\ Type} = 1 \quad , \ T^{(e)} \leq T_{min,\,thera.} \qquad (5.4a)$$

$$S_{V^{(e)},\,Tissue\ Type} = \frac{1}{V^{(e)}} \int_{V^{(e)}} 10^{\,b\ (T^{(e)} - T_{min,\,thera.})}\ dV \quad , \ T^{(e)} > T_{min,\,thera.} \qquad (5.4b)$$

In Eq. 5.4, $T^{(e)}$ is the temperature in finite element e.

The fraction of tissue killed during a single heat treatment is

$$\Psi_{Tissue\ Type} = \frac{\sum_{e=1}^{\substack{\text{Total Number of Finite Elements of } Tissue\ Type}} \left(1 - S_{V^{(e)},\,Tissue\ Type}\right) V^{(e)}}{V_T} \qquad (5.5)$$

In Eq. 5.5, V_T [m^3] is the volume of the tumor and $V^{(e)}$ is the volume of tissue above $T_{min,\,thera.}$. In words, the formulation of Eq. 5.5 is as follows. The surviving fraction of

tissue in finite element e was subtracted from one to give the fraction of tissue killed. Then the fraction of tissue killed in finite element e was weighted by $V^{(e)}$ and this product was summed for all finite elements of *Tissue Type*. The numerator was then divided by V_T to determine Ψ, the fraction of tissue killed in volume V_T.

By dividing by V_T in Eq. 5.5, comparisons of Ψ_T between tumors with different volumes can be made (see Sec. 5.2.3.1.1). In addition, Ψ_N is independent of the size and shape of normal tissue considered so long as the temperatures at the vertices of the finite elements in normal tissue at a sufficient distance from the heat sources are below $T_{min,\ thera.}$. In other words, $S_{V^{(e)},\ Normal}$ is equal to one for these finite elements and does not contribute to the summation in the numerator of Eq. 5.5. Since finite element modelers are free to select the location of the outer surface of normal tissue, subject only to known boundary conditions on the outer surface, the formulation of Ψ_N in Eq. 5.5 has the advantage of being independent of the size and shape of normal tissue.

The objective function consists of two terms and is given by

$$F = \gamma\ \Psi_T - (1-\gamma)\ \Psi_N \tag{5.6}$$

The first term on the right-hand side of the Eq. 5.6 is the fraction of tumor killed multiplied by a scalar weighting factor γ. The second term on the right-hand side of Eq. 5.6 is the fraction of normal tissue killed which is multiplied by $(1-\gamma)$. This second term is the penalty portion of the objective function. Since it is desired to maximize the fraction of tumor killed, there is a penalty for heating normal tissue above $T_{min,\ thera.}$[11]. Therefore the second term is subtracted from the first. Once a particular value for the

[11]Subjecting the tumor to very high temperatures will most likely kill all tumor cells but will also cause severe damage to surrounding normal tissues. Thus a penalty portion of the objective function is necessary.

weighting factor γ is selected, the mathematical goal is to maximize the objective function (Eq. 5.6) over a range of values of the hyperthermia treatment variables. The ferromagnetic hyperthermia treatment variables may include interseed spacing between thermoseeds and the operating temperatures of each thermoseed. The optimum hyperthermia treatment variables may also depend on the assumed models of the blood flow rate in tumor and normal tissues.

5.2.3.1.1 Fractional Cell Survival

By dividing by V_T in Eq. 5.5, Ψ_T can be used to compare the fraction of tissue killed in tumors with different volumes. As an example, consider two, one-dimensional tissue models. Tissue model 1 will have a tumor length of L_{T_1} and a normal tissue length of L_{N_1}. Similarly, tissue model 2 will have a tumor length of L_{T_2} $(> L_{T_1})$ and a normal tissue length of L_{N_2} $(< L_{N_1})$. Both tissue models will have a total length of L. It is assumed that there is no blood flow in these tissue models and the thermal conductivities of the tumor and normal tissues are k_T and k_N $(k_N > k_T)$. The maximum tumor temperature achieved in tissue models 1 and 2 are $T_{T_1, max}$ and $T_{T_2, max}$, respectively. Let η_1 and η_2 denote the fraction of tumor killed in tumors 1 and 2. Three separate cases will be considered:

Case 1 The temperature profiles for the two tissue models are shown in Figs. 5.3a and 5.3b. If $T_{T_1, max} = T_{T_2, max}$, then $\eta_1 > \eta_2$ since $L_{T_2} > L_{T_1}$. The fractions of tumor killed in L_{T_1} and L_{T_2} are

$$\Psi_{T_1} = \frac{\eta_1 L_{T_1}}{L_{T_1}} = \eta_1$$

$$\Psi_{T_2} = \frac{\eta_2 (L_{T_2} - \Delta L_{T_2})}{L_{T_2}} = \eta_2 \left(1 - \frac{\Delta L_{T_2}}{L_{T_2}}\right)$$

Since $\Psi_{T_1} > \Psi_{T_2}$, the temperature distribution in tumor 1 is more desirable.

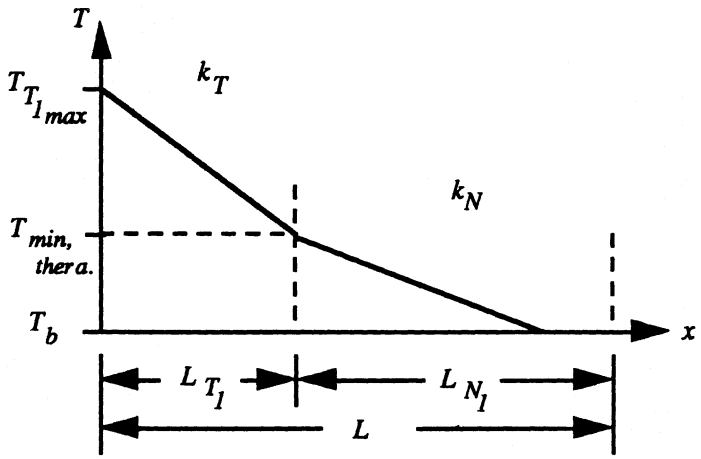

(a) Tissue Model 1

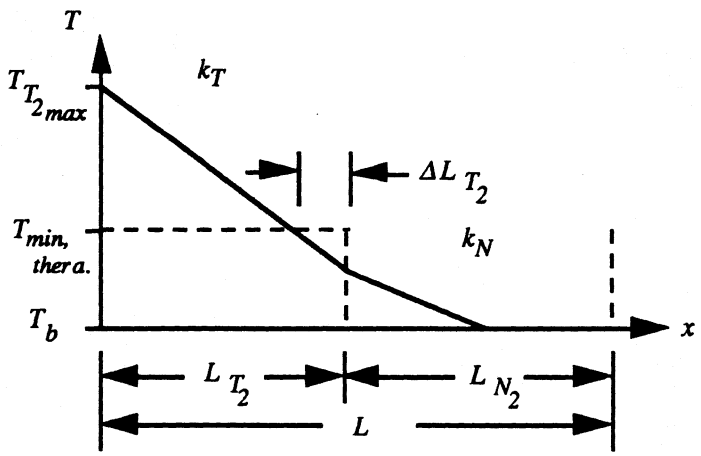

(b) Tissue Model 2

Figure 5.3a-b Temperature profiles in one-dimensional tissue models. Tumor lengths in tissue models 1 and 2 are L_{T1} and L_{T2} (> L_{T1}). The total length of both tissue models is L. There is no blood flow in these tissue models. In figures (a) and (b) $T_{T2,\,max} = T_{T1,\,max}$.

Case 2 The temperature profiles for the two tissue models are shown in Figs. 5.3a and 5.3c. If $T_{T_1,\,max} < T_{T_2,\,max}$ so that $T_{T_1}(x = L_{T_1}) = T_{T_2}(x = L_{T_2}) = T_{min,\,thera.}$ then $\eta_1 < \eta_2$. The fractions of tumor killed in L_{T_1} and L_{T_2} are

$$\psi_{T_1} = \frac{\eta_1 L_{T_1}}{L_{T_1}} = \eta_1$$

$$\psi_{T_2} = \frac{\eta_2 L_{T_2}}{L_{T_2}} = \eta_2$$

Since $\psi_{T_1} < \psi_{T_2}$, the temperature distribution in tumor 2 is more desirable.

Case 3 The temperature profiles for the two tissue models are shown in Figs. 5.3a and 5.3d. If $T_{T_1,\,max} < T_{T_2,\,max}$ so that $T_{T_1}(x = L_{T_1}) = T_{min,\,thera.} < T_{T_2}(x = L_{T_2})$ then $\eta_1 < \eta_2$. The fractions of tumor killed in L_{T_1} and L_{T_2} are

$$\psi_{T_1} = \frac{\eta_1 L_{T_1}}{L_{T_1}} = \eta_1$$

$$\psi_{T_2} = \frac{\eta_2 L_{T_2}}{L_{T_2}} = \eta_2$$

Since $\psi_{T_1} < \psi_{T_2}$, the temperature distribution in tumor 2 is more desirable. However, because a fraction of normal tissue is heated above $T_{min,\,thera.}$, the temperature distribution in the combined tumor *and* normal tissues of model 2 may be less desirable than the temperature distribution in tissue model 1.

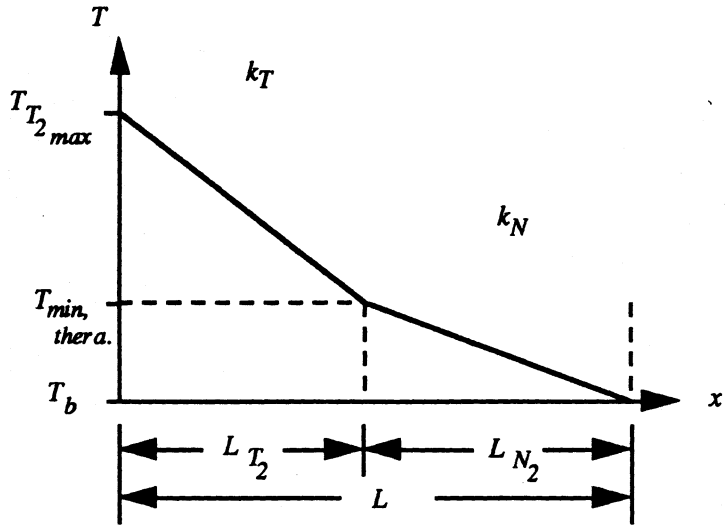

(c) Tissue Model 2

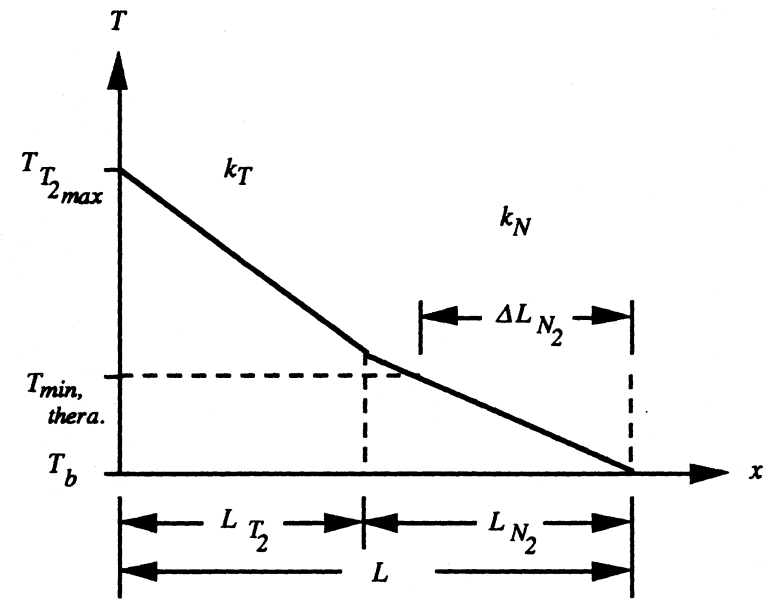

(d) Tissue Model 2

Figure 5.3c-d Temperature profiles in one-dimensional tissue models. Tumor length in tissue model is L_{T2} ($> L_{T1}$). The total length of the tissue model is L. There is no blood flow in these tissue models. In figures (a) and (c) $T_{T1,\,max} < T_{T2,\,max}$, and in figures (a) and (d) $T_{T1,\,max} < T_{T2,\,max}$.

5.2.3.1.2 Weighting Factor

The value of the weighting factor γ in Eq. 5.6 depends on treatment factors such as the therapeutic goal of the hyperthermia treatment and the thermal tolerance of normal tissues on the boundary of the tumor and normal tissues. The scalar weighting factor γ can have a value between 0 and 1. A guide for the selection of γ is shown in Table 5.1.

Table 5.1 Guide for Selecting γ

Hyperthermia Pretreatment Design Considerations	Weighting Factor, γ
Therapeutic Goal	
Minimize Normal Tissue Complications	0.2 – 0.5
Minimize Normal Tissue Complications & Maximize Tumor Death	0.6 – 0.8
Maximize Tumor Death	0.9 – 1
Thermal Tolerance of Normal Tissue near Tumor Periphery	
Low	0.2 – 0.4
High	0.9 – 1

The therapeutic goal of the heat treatment must be considered when selecting a value for γ. A treatment plan with $\gamma = 0$ would be impractical since this would minimize *completely* normal tissue complications and therefore not optimize the heating of the tumor. If the desired treatment goal is to minimize normal tissue complications, then γ should have a value between 0.2 and 0.5. If the treatment plan is designed to maximize tumor death but there is concern for normal tissue complications, then γ should have a value between 0.6 and 0.8. If the desired treatment goal is to maximize tumor death, then

γ should have a value between 0.9 and 1. Although a treatment plan with $\gamma = 1$ would maximize tumor death, normal tissues would not be spared and the treatment may cause significant normal tissue heating on the tumor boundary. Therefore, a treatment plan with $\gamma = 1$ should be used with caution.

Another consideration in the selection of γ is based on the thermal tolerance of normal tissues at the tumor periphery. If the thermal tolerance of normal tissues on the boundary of the tumor is low, then γ should have a value between 0.2 and 0.4. If normal tissue on the boundary *can* tolerate temperatures above $T_{min,\ thera.}$, then γ should have a value between 0.9 and 1. Normal tissues that have a low thermal tolerance generally have steep survival curves for temperatures 1 to 3 C above $T_{min,\ thera.}$. One tissue that is considered to have a high thermal tolerance to local heating is the sclera (Steeves *et al.* 1992).

In summary, choices of the weighting factor are somewhat arbitrary but the guidelines and reasonable estimates are provided in Table 5.1. Estimates of the values for the weighting factor are subject to further refinement via clinical observations and trials.

5.2.3.1.3 Upper & Lower Limit of Objective Function

The objective function F has an upper limit that approaches 1. If $\gamma = 1$, then the second term on the right-hand side in Eq. 5.6 vanishes and $F = \Psi_T$. The fraction of tumor killed Ψ_T will approach 1 as the survival of tumor tissue $S_{V(e),\ Tumor}$ (Eq. 5.5) approaches 0. However, $S_{V(e),\ Tumor}$ can never be identically equal to 0 since there will always be some (infinitesimal) fraction of tumor that survives (recall Fig. 5.2). In the limit, therefore, the objective function approaches 1.

The objective function has a negative lower limit that will approach the ratio of the volume of normal tissue V_N to the volume of tumor tissue V_T. When $\gamma = 0$, the first term

on the right-hand side of Eq. 5.6 vanishes and $F = -\Psi_N$. In Eq. 5.5, the fraction of normal tissue killed Ψ_N is equal to the ratio of the volume of normal tissue which is heated above $T_{min,\ thera.}$ to the volume of tumor V_T. If $S_{V(e),\ Normal}$ for all e in normal tissue approaches 0 and if $V_N = V_T$, then F approaches –1. If $V_N < V_T$ and $S_{V(e),\ Normal}$ is near 0 for all e, then F will be between 0 and –1. Otherwise, if $V_N > V_T$ and $S_{V(e),\ Normal}$ is near 0 for all e, F will be less than –1.

5.2.3.2 Nondimensional Tissue Models

The fraction of tissue surviving in finite element e, $S_{V(e),\ Tissue\ Type}$ (Eq. 5.4), the fraction of tissue killed in tumor or normal tissues $\Psi_{Tissue\ Type}$ (Eq. 5.5), and the objective function F (Eq. 5.6) can be determined for nondimensional tissue models. After determining T^* for the nondimensional tissue model, the tissue temperature T [C] can be determined with Eq. 4.7. Now Eqs. 5.4, 5.5 and 5.6 can be evaluated with the known values of T.

5.3 Numerically Computed Objective Function

The accuracy of the calculation of the objective function (Eq. 5.6) was studied by comparing analytical solutions (Sec. 5.3.1) to solutions obtained numerically with FEHT (Sec. 5.3.2).

5.3.1 Analytically Computed Objective Function

The tissue model considered in this analysis is 1/3 of a circular-shaped tissue region which has a thermoseed placed at the center (Fig. 3.6). Although the heat flow in the tissue model is assumed one-dimensional (Ch. 3), the following analysis will be performed in the x and y directions. (Unit depth in the z-direction is assumed.) Thus the

analysis will be developed for the cross-sectional area A of tissue not for the tissue volume V. The tissue model is composed of a circular-shaped, inner tumor with inner radius r_i and outer radius r_T surrounded by normal tissue with outer radius r_o. The inner radius of the tissue r_i is synonymous with the radius of the thermoseed r_s.

Recall that the analytically-determined, steady-state temperature distribution above T_b in the tissue model in Fig. 3.5 is denoted by θ (Eq. 3.4). Substituting Eq. 3.4 into Eq. 5.3b gives

$$S_{Tissue\ Type} = \frac{1}{A}\int_A 10^{b\ [(T_b+\theta)\ -\ T_{min,\ thera.}]}\, dA \tag{5.7}$$

A change in the variable of integration is possible by considering an elemental volume of tissue in Fig. 3.5. The limits of integration become

$$\int_A dA = \int_{r_i}^{r_o} \frac{2\pi r}{3}\, dr$$

With the change in the variable of integration, the integral in Eq. 5.7 becomes

$$S_{Tissue\ Type} = \frac{2\pi}{3A}\int_{r_k}^{r_l} 10^{b\ [(T_b+\theta)\ -\ T_{min,\ thera.}]}\ r\, dr$$

$$= \frac{2}{(r_l^2 - r_k^2)}\int_{r_k}^{r_l} 10^{b\ [(T_b+\theta)\ -\ T_{min,\ thera.}]}\ r\, dr \tag{5.8}$$

Evaluation of Eq. 5.8 for tumor and normal tissues and values of r_l and r_k are as follows. For the tumor, r_k equals r_i and r_l is the radius of the tumor r_T or the radius of the $T_{min,\ thera.}$ isotherm, whichever is smaller. For normal tissue, if r_T is smaller than the radius of the $T_{min,\ thera.}$ isotherm, then r_k equals r_T and r_l is the radius of the $T_{min,\ thera.}$ isotherm. Otherwise, r_T is larger than the radius of the $T_{min,\ thera.}$ isotherm and 100% of the normal tissue survived and $S_N = 1$ (Eq. 5.8).

With the fraction of cell survival $S_{Tissue\ Type}$ determined for normal and tumor tissues, $\Psi_{Tissue\ Type}$ can be computed with

$$\Psi_{Tissue\ Type} = \frac{\left(1 - S_{Tissue\ Type} \right) V_{Tissue\ Type}}{V_T} \tag{5.9}$$

Equation 5.9 is used for determining $\Psi_{Tissue\ Type}$ for tumor and normal tissues. In Eq. 5.9, $V_{Tissue\ Type}$ is the volume of tissue above $T_{min,\ thera.}$. Equation 5.9 can now be used to evaluate Eq. 5.6 for the objective function F.

Since the temperature function θ inside the integral in Eq. 5.8 contains several Bessel functions (recall Eq. 3.4), the integration of Eq. 5.8 was evaluated with Mathematica (Wolfram 1988). The input data for the Mathematica program to perform the integration of Eq. 5.8 is in Appendix C.1.

5.3.2 Numerically Computed Objective Function

Unlike the analytically-computed fractional cell survival $S_{Tissue\ Type}$ where one integration was performed over a continuum of tissue (Eq. 5.8), the numerical solution will require an integration over each finite element in the mesh.

Let the temperature within a triangular-shaped, finite element e be $T^{(e)}$ and equal to

$$T^{(e)} = \xi_i T_i^{(e)} + \xi_j T_j^{(e)} + \xi_k T_k^{(e)} \tag{5.10}$$

In Eq. 5.10, ξ_i, ξ_j and ξ_k are interpolating functions and $T_i^{(e)}$, $T_j^{(e)}$ and $T_k^{(e)}$ are the temperatures at vertices i, j and k of finite element e. Substituting Eq. 5.10 into Eq. 5.4b gives

$$S_{A^{(e)},\,Tissue\ Type} = \frac{1}{A^{(e)}} \int_{A^{(e)}} 10^{\,b\ [(\xi_i T_i^{(e)} + \xi_j T_j^{(e)} + \xi_k T_k^{(e)}) - T_{min,\,thera.}]}\, dA \tag{5.11}$$

From Myers (1989), it is known that

$$\xi_i = \frac{1}{b_{ijk}} [\,(x_j y_k - x_k y_j) - y_{jk} x + x_{jk} y\,] \tag{5.12a}$$

$$\xi_j = \frac{1}{b_{ijk}} [\,(x_k y_i - x_i y_k) + y_{ik} x - x_{ik} y\,] \tag{5.12b}$$

$$\xi_k = \frac{1}{b_{ijk}} [\,(x_i y_j - x_j y_i) - y_{ij} x + x_{ij} y\,] \tag{5.12c}$$

where $b_{ijk} = x_{ij} y_{jk} - x_{jk} y_{ij}$ and $x_{ij} = x_j - x_i$. Substituting Eq. 5.12 into 5.11 and rearranging terms gives

$$S_{A^{(e)},\,Tissue\ Type} = \frac{1}{A^{(e)}} \int_{A^{(e)}} 10^{\,b\ [(a_1 + a_2 x + a_3 y) - T_{min,\,thera.}]}\, dA \tag{5.13}$$

where

$$a_1 = \frac{1}{b_{ijk}} [\, (x_j y_k - x_k y_j)\, T_i^{(e)} + (x_k y_i - x_i y_k)\, T_j^{(e)} + (x_i y_j - x_j y_i)\, T_k^{(e)} \,]$$

$$a_2 = \frac{1}{b_{ijk}} (-y_{jk} T_i^{(e)} + y_{ik} T_j^{(e)} - y_{ij} T_k^{(e)})$$

$$a_3 = \frac{1}{b_{ijk}} (x_{jk} T_i^{(e)} - x_{ik} T_j^{(e)} + x_{ij} T_k^{(e)})$$

The integration in Eq. 5.13 is over the area in finite element e. An example of finite element e is shown in Fig. 5.4.

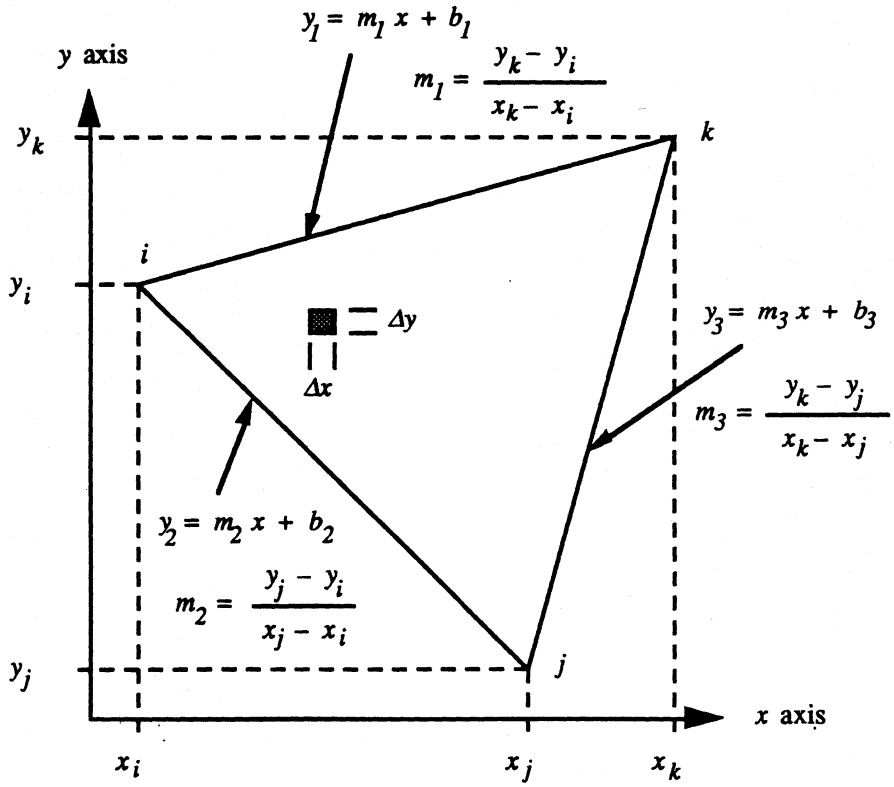

Figure 5.4 Example of finite element in which integration in Eqs. 5.13 and 5.14 are performed. The finite element has vertices i, j and k. The general (linear) equation fit for the three element lines connecting the vertices are shown. The slopes of the element lines are designated by m_1, m_2 and m_3.

With a change in the limits of integration, Eq. 5.13 becomes

$$S_{A^{(e)},\,Tissue\ Type} = \frac{2}{b_{ijk}} \int_{y_2}^{y_1} \int_{x_i}^{x_j} 10^{\,b\ [(a_1 + a_2x + a_3y) - T_{min,\,thera.}]}\, dx\, dy + \frac{2}{b_{ijk}} \int_{y_3}^{y_1} \int_{x_j}^{x_k} 10^{\,b\ [(a_1 + a_2x + a_3y) - T_{min,\,thera.}]}\, dx\, dy \qquad (5.14)$$

In Eq. 5.14, x_i, x_j, x_k, y_1, y_2 and y_3 are shown in Fig. 5.4. The term b_{ijk} can be shown to equal $2A^{(e)}$ (Myers 1989). The integration of Eq. 5.14 was performed symbolically with the aid Mathematica to obtain a general form of the solution. The general form of the solution is listed in Appendix C (Sec. C.2). Equation 5.14 can now be used to evaluate Eqs. 5.5 and 5.6 for the surviving fraction Ψ and the objective function F.

An analysis of the general solution to Eq. 5.14 revealed that the surviving fraction of tissue $S_{A^{(e)},\,Tissue\ Type}$ does not depend on the size of the triangular-shaped finite element (Appendix C.3). Instead the surviving fraction is a function only of the temperatures T_i, T_j and T_k at the vertices of the triangular element, the slope b of the survival curve, and the minimum therapeutic temperature $T_{min,\,thera.}$. The general solution to Eq. 5.14 was placed in FEHT as an algorithm.

5.3.3 Objective Function: Numerical vs. Analytical Solutions

The accuracy of the numerical solutions depends on an adequate choice of the finite element mesh. Simulations were performed with the dodecagonal thermoseed model and with uniform blood flow rates of m = 0.01, 0.1 and 1 l/min-kg. Although the dodecagon was selected as the preferred thermoseed model (Sec. 3.3), simulations were also performed for the hexagonal thermoseed model.

The numerical method requires the use of an adequate mesh size to obtain accurate solutions. A finite element mesh of 387 elements in the simulated tissue (Fig. 3.5) was reduced systematically in size to obtain meshes of 411, 507 and 603 elements. Element discretization was concentrated in the tumor near the thermoseed. The percentages of tumor and normal tissues greater than $T_{min,\ thera.}$ (= 42 C), Ψ_T, Ψ_N and F are in Table 5.2. As evident from Table 5.2, a finite element mesh of 603 elements was sufficient for convergence of the numerical solutions of the dodecagonal and hexagonal thermoseed models.

Simulations were performed on the tumor and normal tissue model with one thermoseed centrally located (Fig. 3.5). The objective function F was determined using the methods discussed in Secs. 5.3.1 and 5.3.2. The simulations were performed with uniform blood flow rates in tumor and normal tissues of m = 0.05, 0.1, 0.25, 0.5 and 1 l/min-kg. The energy absorption rates ($g_s''' = P'/A_s$) of the analytical and numerical thermoseed models were determined at each blood flow rate so that the thermoseed temperature T_s was 60 C. Unlike Sec. 3.3 where the thermoseed model was constrained by power P', the thermoseed model is constrained here, by temperature. In Sec. 3.3, the thermoseed model was constrained by power P' so that the thermoseed and tissue temperatures predicted by the numerical thermoseed models could be compared with those of the analytical model. In this section, however, the thermoseed temperature T_s is constrained so that the calculation of the objective function by the numerical method could be compared with the that of the analytical method. If, in this section, the thermoseed was constrained by power P', then the error in the numerically computed objective function would be confounded with the error in the numerical thermoseed models.

The percentages of tumor and normal tissues greater than $T_{min,\ thera.}$, Ψ_T, Ψ_N and F for $T_{min,\ thera.}$ = 42 C are in Table 5.3. The predicted fraction of tissue killed $\Psi_{Tissue\ Type}$

Table 5.2 Finite Element Mesh Reduction Study
$T_{min,\ thera.}$ = 42 C

(a) Uniform blood flow, m = 0.01 l/min-kg

Seed Model	Number of Finite Elements	% Tumor Tissue > 42 C	% Normal Tissue > 42 C	Ψ_T Tumor (Eq. 5.5)	Ψ_N Normal (Eq. 5.5)	Objective Function, F (γ = 0.8)
Hexagon	387	100	1.17	1	3.64	0.07
	411	100	1.18	1	3.65	0.07
	507	100	1.15	1	3.54	0.09
	603	100	1.08	1	3.55	0.09
Dodecagon	387	100	1.18	1	3.66	0.07
	412	100	1.18	1	3.66	0.07
	508	100	1.16	1	3.56	0.09
	603	100	1.09	1	3.56	0.09

(b) Uniform blood flow, m = 0.1 l/min-kg

Seed Model	Number of Finite Elements	% Tumor Tissue > 42 C	% Normal Tissue > 42 C	Ψ_T Tumor (Eq. 5.5)	Ψ_N Normal (Eq. 5.5)	Objective Function, F (γ = 0.8)
Hexagon	387	100	0.20	0.99	0.51	0.69
	411	100	0.20	0.99	0.52	0.69
	507	100	0.15	1.00	0.40	0.72
	603	100	0.17	1.00	0.47	0.70
Dodecagon	387	100	0.20	0.99	0.52	0.69
	412	100	0.20	0.99	0.52	0.69
	508	100	0.15	1.00	0.41	0.72
	603	100	0.17	1.00	0.48	0.70

(c) Uniform blood flow, m = 1 l/min-kg

Seed Model	Number of Finite Elements	% Tumor Tissue > 42 C	% Normal Tissue > 42 C	Ψ_T Tumor (Eq. 5.5)	Ψ_N Normal (Eq. 5.5)	Objective Function, F (γ = 0.8)
Hexagon	387	33.4	0	0.30	0	0.24
	411	33.4	0	0.30	0	0.24
	507	34.5	0	0.31	0	0.25
	603	34.6	0	0.31	0	0.25
Dodecagon	387	33.6	0	0.30	0	0.24
	412	33.5	0	0.30	0	0.24
	508	34.7	0	0.31	0	0.25
	603	34.7	0	0.31	0	0.25

Table 5.3 Numerically and Analytically Computed Objective Function
$T_{min,\ thera.} = 42$ C

Blood Flow, m (l/min-kg)	Seed Model*	% Tumor Tissue > 42 C	% Normal Tissue > 42 C	Ψ_T (Eq. 5.5)	Ψ_N (Eq. 5.5)	Objective Function, F ($\gamma = 0.8$)
0.05	H	100	0.44	1	1.37	0.53
	D	100	0.45	1	1.40	0.52
	A	100	0.40	1	1.25	0.55
0.1	H	100	0.17	1.00	0.47	0.70
	D	100	0.18	1.00	0.49	0.70
	A	100	0.15	0.99	0.38	0.72
0.25	H	89.0	0	0.78	0	0.62
	D	89.5	0	0.78	0	0.63
	A	83.4	0	0.78	0	0.62
0.5	H	55.4	0	0.49	0	0.39
	D	55.7	0	0.49	0	0.39
	A	51.6	0	0.48	0	0.39
1	H	34.7	0	0.31	0	0.25
	D	34.7	0	0.31	0	0.25
	A	32.2	0	0.30	0	0.24

*H - Hexagonal model; D - Dodecagonal model; A - Analytical model

in the tumor and normal tissues and the objective function F as a function of blood flow are shown in Fig. 5.5. It is concluded that the calculation of the fraction of tissue killed $\Psi_{Tissue\ Type}$ and the objective function F for the numerical hexagonal and dodecagonal thermoseed models adequately match the analytical solution.

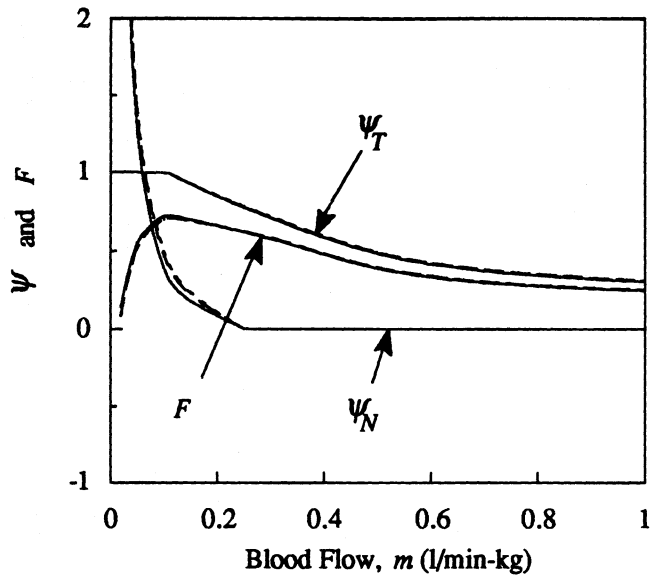

Figure 5.5 The fraction of tissue killed $\Psi_{Tissue\ Type}$ and the objective function F versus blood flow rate. The analytical solutions (solid lines) were determined with Eqs. 5.6 and 5.9. The solutions predicted by FEHT with the hexagonal (long dashes) and dodecagonal (short dashes) thermoseed models were computed with Eqs. 5.5, 5.6 and 5.14. In the simulations, $T_{min,\ thera.}$ = 42 C.

5.4 Concluding Remarks

In this chapter an objective function F was developed that can be used to optimize hyperthermia treatments. There are several salient features of the objective function. First, the objective function has a physiological basis and considers increased cell killing at temperatures above 42 to 43 C (= $T_{min,\ thera.}$). Second, there is a (penalty) term, Ψ_N, in the objective function to account for heating of normal tissues above $T_{min,\ thera.}$. Third, because normal tissues below $T_{min,\ thera.}$ are eliminated in the determination of the fraction of normal tissue killed (Ψ_N), the objective function is independent of normal tissue size and shape, subject to a known outer-surface, thermal boundary condition (*e.g.*, $T_{outer\ surface} = T_b$). Next, by dividing by the volume of the tumor V_T in Eq. 5.5, Ψ_T can be compared with tumors of different shapes and sizes. Last, since there is a scalar

weighting factor γ in the objective function that has treatment implications, the oncologist becomes an active participant in pretreatment planning.

The objective function was computed numerically with FEHT and shown to compare favorably with analytically computed values for simple tissue geometries.

Chapter 6

Performance of Objective Function with an Idealized Tissue Model

In this chapter simulations are performed on a square tissue model. The simulations are conducted to assess the performance of the objective function (see Chapter 5) in an idealized tissue model. Although any geometrically shaped tissue model could have been used (*e.g.*, triangle, rectangle, etc.), a square thermoseed array in a square tissue model has symmetry conditions that simplify the model. The description of the simulations is presented in Sec. 6.1.

In Sec. 6.2, the objective function is used to aid in selecting optimal thermoseed temperatures and seed spacings *a priori*. The effects of tumor survival models, weighting factors, blood flow rates, and thermoseed operating temperatures on the objective function are studied independently. Criteria that will be used to assess the performance of the objective function include: (1) sensitivity to the tumor survival model (Sec. 6.2.1), (2) presence of a unique maximum of the objective function (Sec. 6.2); (3) sensitivity of the objective function to interseed spacing between thermoseeds (Sec. 6.2); (4) sensitivity of the objective function to the weighting factor (Sec. 6.2.2); (5) sensitivity of the objective function to variations in blood flow in the tumor and normal tissues (Sec. 6.2.3); and (6) sensitivity of objective function to thermoseed operating temperatures (Sec. 6.2.4).

In this chapter, two methods are used to choose optimum[12] thermoseed configurations *a priori*. One method is based on maximizing the minimum tumor temperature ($T_{min,\ tumor}$) and the other method is based on maximizing the objective function F (Eq. 5.6). The suitability of the objective function is assessed by determining if the fraction of tumor killed, Ψ_T, using the objective function is larger than Ψ_T using temperature descriptors (Sec. 6.3). The performance of the objective function is also characterized by how well the optimum thermoseed configurations satisfy temperature-based therapeutic criteria (Sec. 6.3). The major results from the simulations are summarized in Sec. 6.4.

6.1 Description of Simulations

Simulations were performed on the tissue model shown in Fig. 4.6 which is implanted with a square 4x4 array of thermoseeds. The simulated tumor was implanted with thermoseeds of uniform operating temperature of 48.1, 54.1 or 60.1 C (Table 4.1). An array of 48.1 C-type thermoseeds consisted of 16 thermoseeds with operating temperatures of 48.1 C. Similarly, arrays of 54.1 C- and 60.1 C-type thermoseeds consisted only of thermoseeds with operating temperatures of 54.1 and 60.1 C, respectively. The preceding three thermoseed configurations are considered *uniformly-loaded* arrays. To study the effect of placing thermoseeds with higher operating temperatures near the tumor periphery and lower operating temperatures near the center of the thermoseed array, simulations were performed with a *differentially-loaded* thermoseed array. The differentially-loaded thermoseed array consisted of a combination of four

---

[12]Prior to the study of these two methods to choose optimum thermoseed configurations, optimization studies in ferromagnetic hyperthermia pretreatment planning have been limited to a few theoretical and a few *in-vitro* and *in-vivo* investigations (Sec. 1.5). None of these previous studies have proposed either of the two methods discussed in this chapter to plan ferromagnetic hyperthermia treatments.

48.1-type, eight 54.1-type and four 60.1-type thermoseeds. The 54.1 C-, 60.1 C- and 48.1 C-type thermoseeds were located at seed positions 1, 2 and 3, respectively, in Figs. 4.6 and 4.7.

Simulations were conducted with arrays of bare thermoseeds that were spaced uniformly in the x and y directions with an interseed spacing l between 9 and 15 mm. All simulations were performed with a mesh of 1530 finite elements (Sec. 4.2.1.1). The Newton-Raphson technique[13] was used to determine thermoseed temperature (Sec. 4.1.1.1). The dodecagonal thermoseed model was used in the simulations (Sec. 3.2.3).

Seven blood flow models are used in simulations in this chapter (Table 6.1). The numerical values of the blood flow cover the range of blood flow models found in reviewed journal papers. The various blood flow models are investigated to study the influence of changes in tumor blood flow m_t and normal tissue blood flow m_n on the objective function. Blood flow models 1, 2 and 3 assume there is uniform, moderate rate of blood flow in the tumor (0.1 l/min-kg) while models 4, 5 and 6 use a higher, uniform tumor blood flow (0.25 l/min-kg). Blood flow model 7 is a nonuniform tumor blood

Table 6.1 Blood Flow Models used in Simulations

Blood Flow Model	Blood Flow (l/min-kg)	
	Tumor, mt	Normal, mn
1	0.1	0.1
2	**0.1**	**0.25**
3	0.1	0.5
4	0.25	0.25
5	**0.25**	**0.5**
6	0.25	1
7	**0.1(c); 0.75(p)**	**0.5**

[13]An alternative method for determining thermoseed temperatures is the use of the variable-property routine in FEHT (Sec. 4.3.2.1).

flow model where the blood flow in the tumor periphery ((p) in Table 6.1) is 7.5 times greater than the tumor core ((c) in Table 6.1) and 1.5 times greater than the normal tissue[14]. Blood flow models 2, 5 and 7 are considered the models which closely represent the actual blood flow in a real tissue system[15].

6.2 Optimum Thermoseed Spacing and Operating Temperatures

Several figures in this section are plots of the objective function F versus thermoseed spacing l. The figures in each subsection consist of curves of the variable under independent investigation. For example, Sec. 6.2.1 investigates the effect of tumor survival models on the objective function; Sec. 6.2.2 studies the effect of the weighting factor γ; Sec. 6.2.3 looks at the effect of blood flow; and Sec. 6.2.4 investigates the effect of thermoseed operating temperature on the objective function. The results are presented in this manner to elucidate the influence of each variable on the objective function. The optimum thermoseed designs based on the objective function are discussed in Sec. 6.2.5.

6.2.1 Effect of Tumor Survival Model

The fraction of tumor killed and the objective function versus thermoseed spacing for the two models simulating the survival of tumor tissue is shown in Fig. 6.1. Since tumor survival model A has a steeper slope ($b = -2$) than model B ($b = -1$) (Fig. 5.2), more tumor will be killed in simulations using tumor model A versus model B at the same

---

[14]Earlier studies and clinical experience have shown that often, the inner core of the tumor is a tough, fibrous tissue and may have a blood flow that differs vastly from the outer periphery of the tumor. Thus the tumor was modeled as two distinct regions consisting of an inner core and an outer periphery.

[15]Blood flow models 2, 5 and 7 will appear in bold type in the remainder of this chapter. Furthermore, of blood flow models 2, 5 and 7, model 7 is considered the model which most *closely* represents the blood flow in real tissue since it contains a necrotic tumor core and well-perfused tumor periphery.

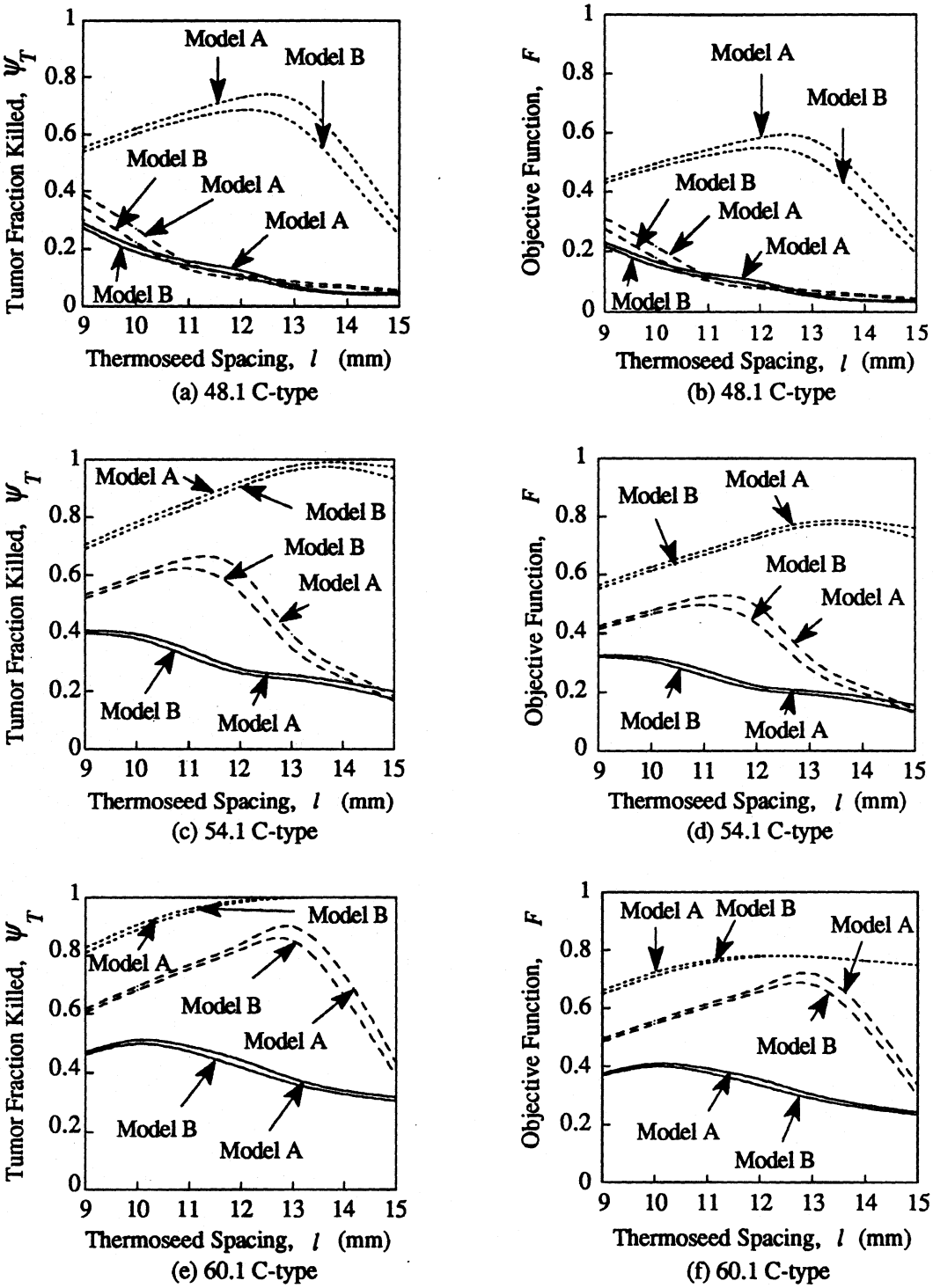

Figure 6.1 Effect of tumor survival models A and B (Fig. 5.2) on the fraction of tumor killed ψ_T and on the objective function F. Simulations were performed with $T_{min,\ thera.}$ = 42 C, γ = 0.8 and with an array of bare thermoseeds with operating temperatures of (a, b) 48.1 C, (c, d) 54.1 C and (e, f) 60.1 C. Curves are shown for blood flow models 2 (short dashed lines), 5 (long dashed lines) and 7 (solid line).

temperature. In all simulations, therefore, Ψ_T and F were larger with tumor survival model A than model B at the same temperature.

Percent differences, averaged over all thermoseed spacings, between the objective function with tumor survival model A and model B are 8.6, 2.3 and 0.8% for the 48.1 C-, 54.1 C- and 60.1 C-type thermoseed arrays and with blood flow model 2 (Table 6.2).

Table 6.2 Tumor Survival Model Influence on Objective Function

Seed Spacing, l (mm)	Percent difference in objective function between tumor models A and B								
	Operating temperature of thermoseeds in array								
	48.1 C-type			54.1 C-type			60.1 C-type		
	Blood flow model			Blood flow model			Blood flow model		
	2	5	7	2	5	7	2	5	7
9	2.9	11.2	5.2	2.3	2.4	2.1	2.0	2.0	1.6
10	3.0	18.0	9.0	2.1	2.7	3.8	1.8	2.0	2.4
11	3.7	14.2	9.5	2.0	5.3	6.9	1.2	1.9	3.6
12	6.0	12.5	16.0	1.9	12.3	5.4	0.4	2.2	5.6
13	11.4	12.9	12.1	1.7	12.3	5.9	0.1	5.3	4.6
14	16.3	10.3	12.4	1.8	10.1	7.5	0.0	8.4	4.3
15	16.8	11.1	12.8	4.2	9.3	12.9	0.0	10.8	4.1
Ave:	8.6	12.9	11.0	2.3	7.8	6.4	0.8	4.7	3.7

There was a 12.9, 7.8 and 4.7% difference for the same three thermoseed arrays and blood flow model 5, and a 11.0, 6.4, 3.7% difference with blood flow model 7. The largest percent difference with an array of 48.1 C-type thermoseeds was 18% (l = 10 mm and blood flow model 5), while the maximum percent difference in the objective function in simulations with arrays of 54.1 C- and 60.1 C-type thermoseeds was 12.3% (l = 13 mm and blood flow model 5) and 10.8% (l = 15 mm and blood flow model 5).

The curves in Fig. 6.1 and Table 6.2 reveal that the objective function is weakly dependent on differences between tumor survival models A and B. Thus the first criteria (in second paragraph of this chapter) on the sensitivity of the objective function to the

tumor survival model has been established. It is concluded that since the hyperthermia cell survival of the tumor can only be approximated, differences, similar to the two models used herein, between the actual and the model of tumor cell survival should have a minimal influence on the fraction of tumor killed and the objective function. Thus the simulations in the remainder of Sec. 6.2 were performed with tumor survival model B.

6.2.2 Effect of Weighting Factor

The objective function F versus thermoseed spacing l for weighting factors γ of 0.2, 0.5, 0.8 and 1 are shown in Figs. 6.2 through 6.8 for all four types of thermoseed arrays. Figures. 6.2 through 6.8 are the results from simulations with blood flow models 1 through 7, respectively. In Figs. 6.2 through 6.8, the objective function increases at all interseed spacings with increasing weighting factors because of the linear dependence between the weighting factor and the objective function (Eq. 5.6). The optimum thermoseed spacing for several weighting factors γ, blood flow rates m and thermoseed operating temperatures are compiled in Table 6.3.

6.2.2.1 Moderate Tumor Blood Flow

The weighting factor had a negligible effect on altering the location of the optimum thermoseed spacing when tumor blood flow m_t was 0.1 l/min-kg (blood flow models 1, 2 and 3) and with an array of 48.1 C-type thermoseeds (Table 6.3 and Figs. 6.2a, 6.3a and 6.4a). The optimum thermoseed spacing did decrease though with increasing normal tissue blood flow. For a five-fold increase in normal tissue blood flow m_n from 0.1 to 0.5 l/min-kg, the optimum thermoseed spacing decreased from about 12.8 to 11.7 mm.

The weighting factor can alter the optimum thermoseed spacing when tumor blood flow m_t is 0.1 l/min-kg with arrays of 54.1 C- and 60.1 C-type thermoseeds and with the

Effect of Weighting Factor – Blood Flow Model 1

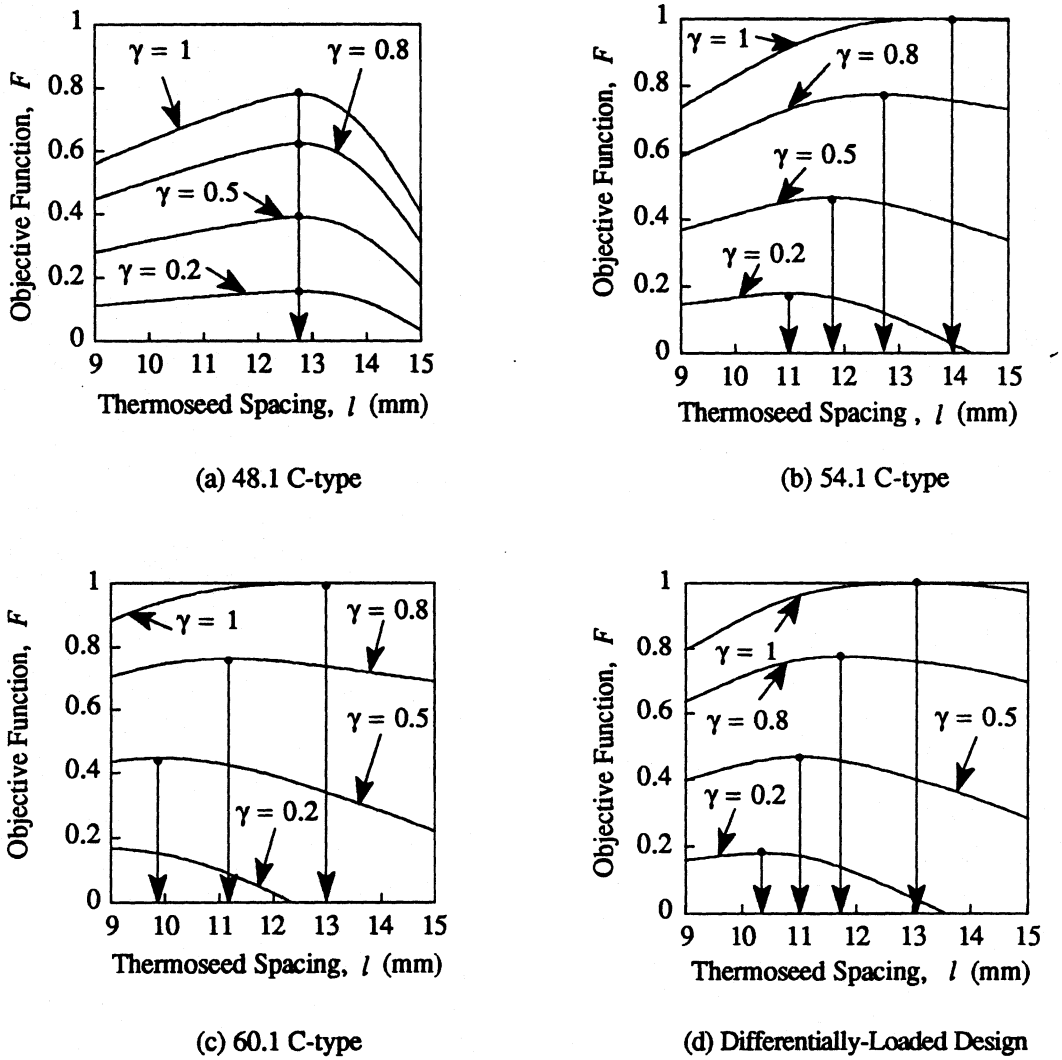

Figure 6.2 Objective function F versus thermoseed spacing l with weighting factors γ of 0.2, 0.5, 0.8 and 1. Simulations were performed with blood flow model 1 (Table 6.1) and with arrays of (a) 48.1 C-type, (b) 54.1 C-type, and (c) 60.1 C-type thermoseeds and (d) the differentially-loaded thermoseed design. Simulations were performed with tumor survival model B (Fig. 5.2), $T_{min,\ thera.}$ = 42 C. Maximums of the objective function are shown with black dots and vertical arrows.

Effect of Weighting Factor – Blood Flow Model 2

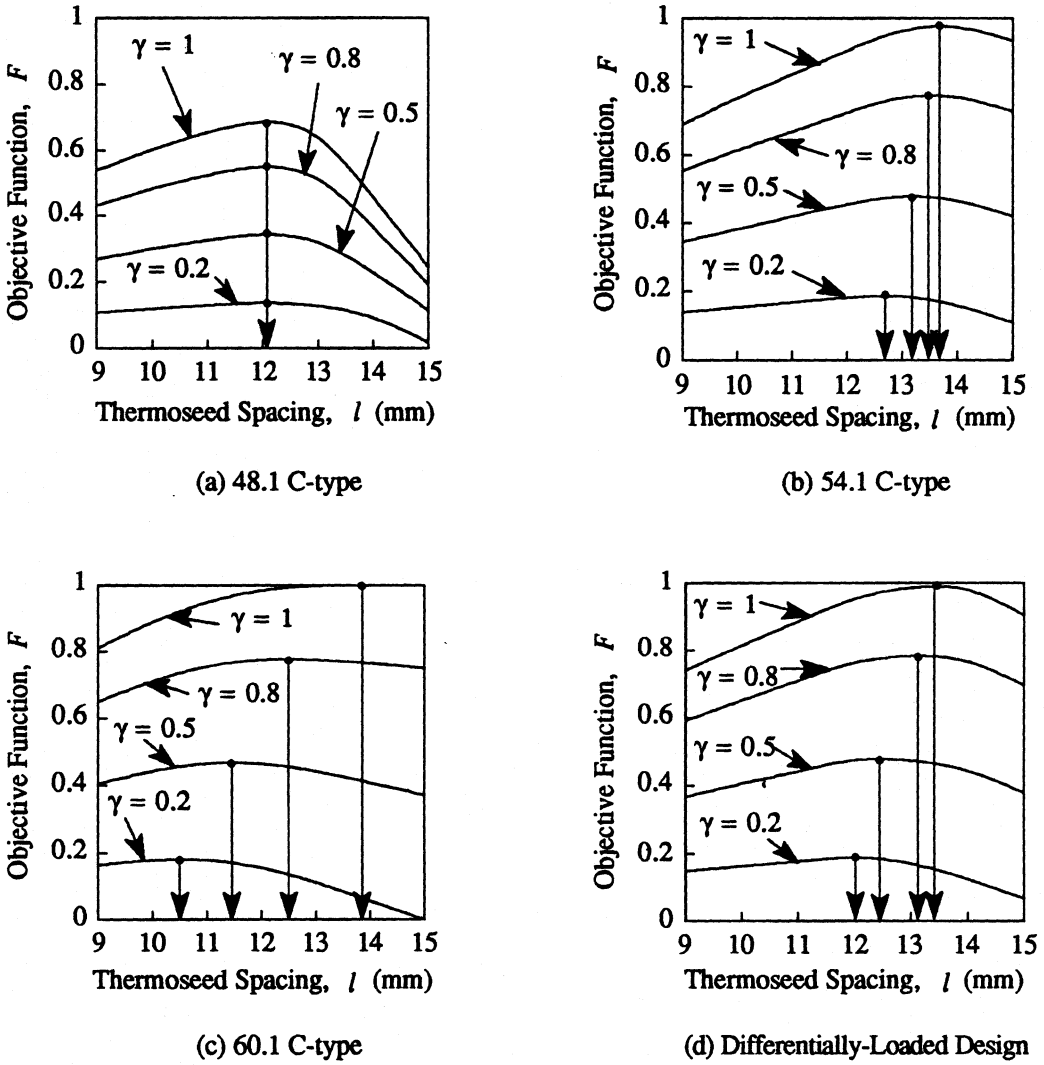

Figure 6.3 Objective function F versus thermoseed spacing l with weighting factors γ of 0.2, 0.5, 0.8 and 1. Simulations were performed with blood flow model 2 (Table 6.1) and with arrays of (a) 48.1 C-type, (b) 54.1 C-type, and (c) 60.1 C-type thermoseeds and (d) the differentially-loaded thermoseed design. Simulations were performed with tumor survival model B (Fig. 5.2), $T_{min,\ thera.}$ = 42 C. Maximums of the objective function are shown with black dots and vertical arrows.

Effect of Weighting Factor – Blood Flow Model 3

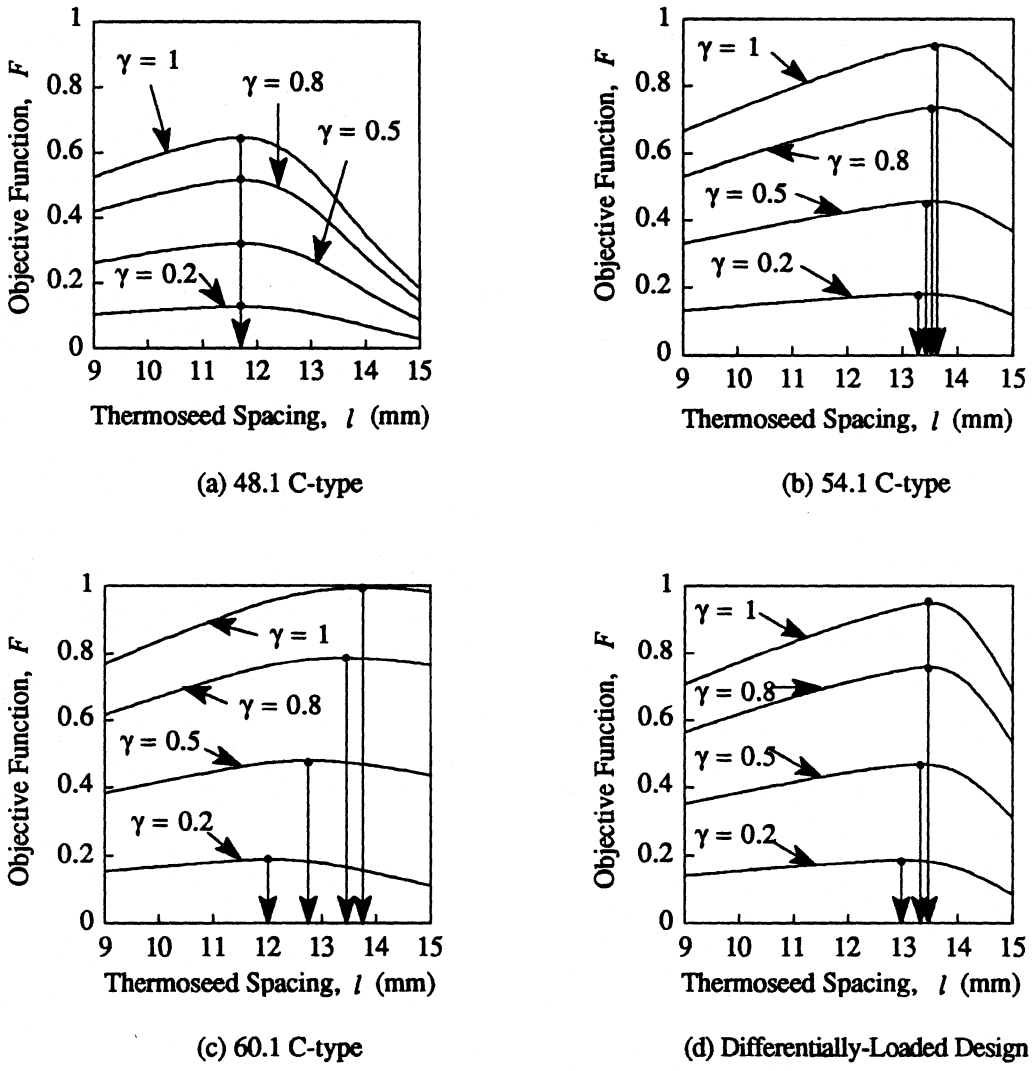

Figure 6.4 Objective function F versus thermoseed spacing l with weighting factors γ of 0.2, 0.5, 0.8 and 1. Simulations were performed with blood flow model 3 (Table 6.1) and with arrays of (a) 48.1 C-type, (b) 54.1 C-type, and (c) 60.1 C-type thermoseeds and (d) the differentially-loaded thermoseed design. Simulations were performed with tumor survival model B (Fig. 5.2), $T_{min,\ thera.}$ = 42 C. Maximums of the objective function are shown with black dots and vertical arrows.

Effect of Weighting Factor – Blood Flow Model 4

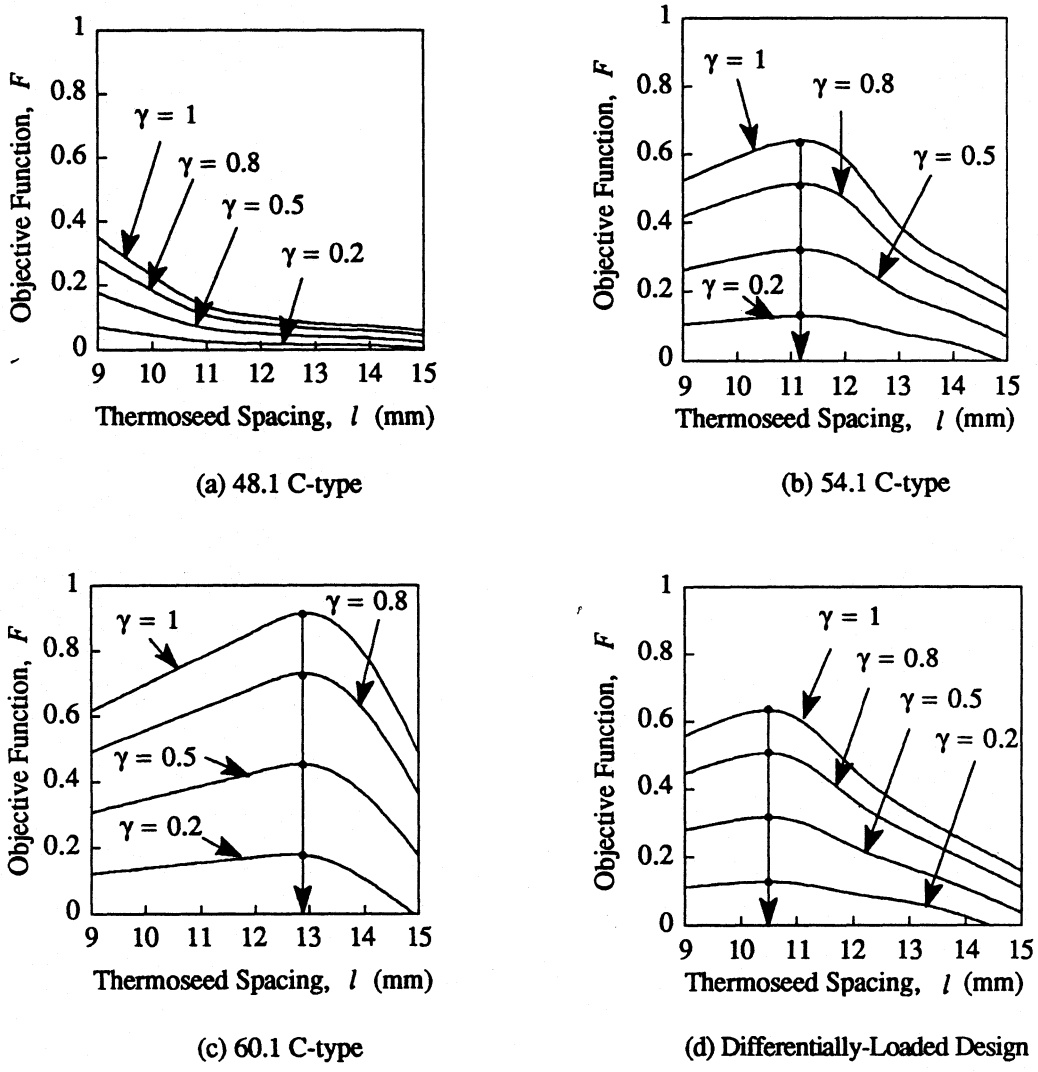

Figure 6.5 Objective function F versus thermoseed spacing l with weighting factors γ of 0.2, 0.5, 0.8 and 1. Simulations were performed with blood flow model 4 (Table 6.1) and with arrays of (a) 48.1 C-type, (b) 54.1 C-type, and (c) 60.1 C-type thermoseeds and (d) the differentially-loaded thermoseed design. Simulations were performed with tumor survival model B (Fig. 5.2), $T_{min,\ thera.}$ = 42 C. Maximums of the objective function are shown with black dots and vertical arrows.

Effect of Weighting Factor – Blood Flow Model 5

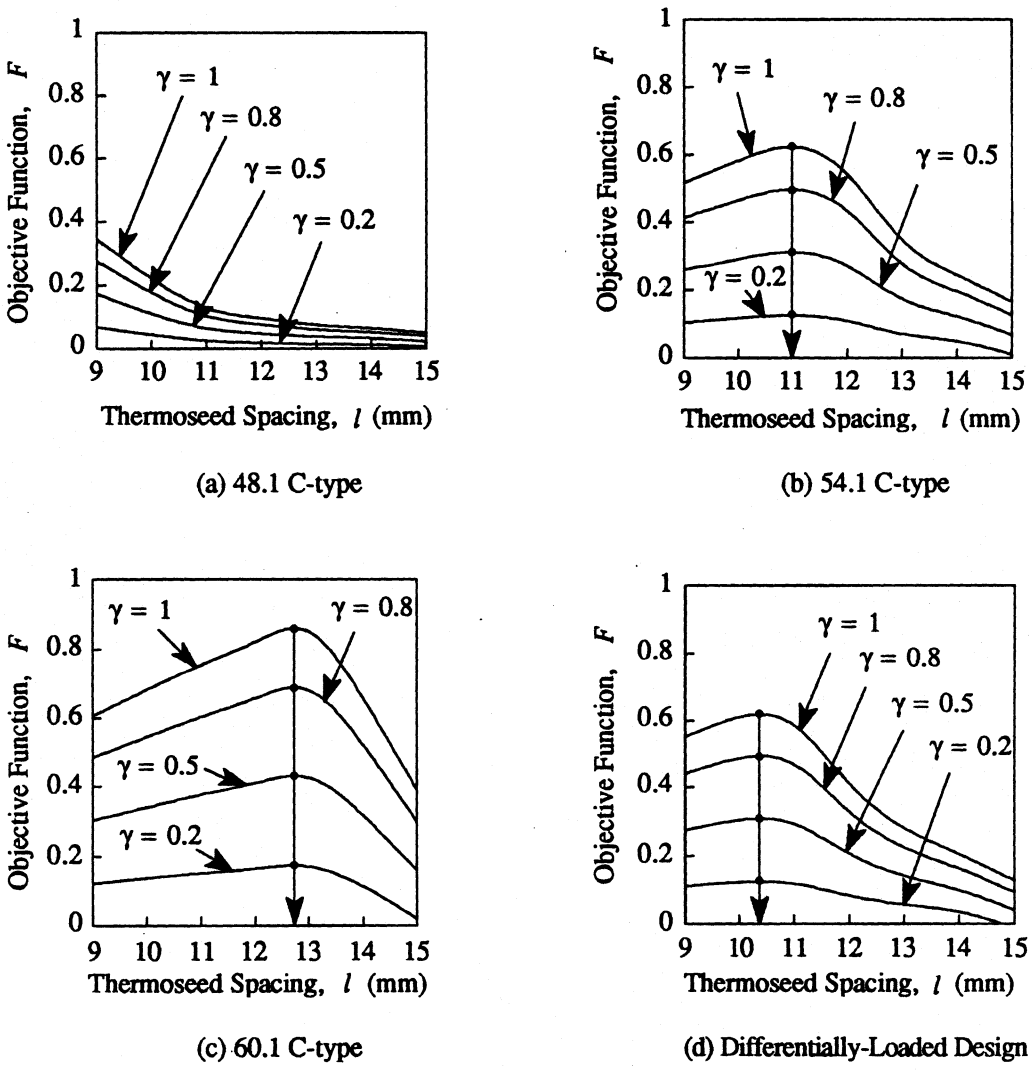

Figure 6.6 Objective function F versus thermoseed spacing l with weighting factors γ of 0.2, 0.5, 0.8 and 1. Simulations were performed with blood flow model 5 (Table 6.1) and with arrays of (a) 48.1 C-type, (b) 54.1 C-type, and (c) 60.1 C-type thermoseeds and (d) the differentially-loaded thermoseed design. Simulations were performed with tumor survival model B (Fig. 5.2), $T_{min,\ thera.}$ = 42 C. Maximums of the objective function are shown with black dots and vertical arrows.

Effect of Weighting Factor – Blood Flow Model 6

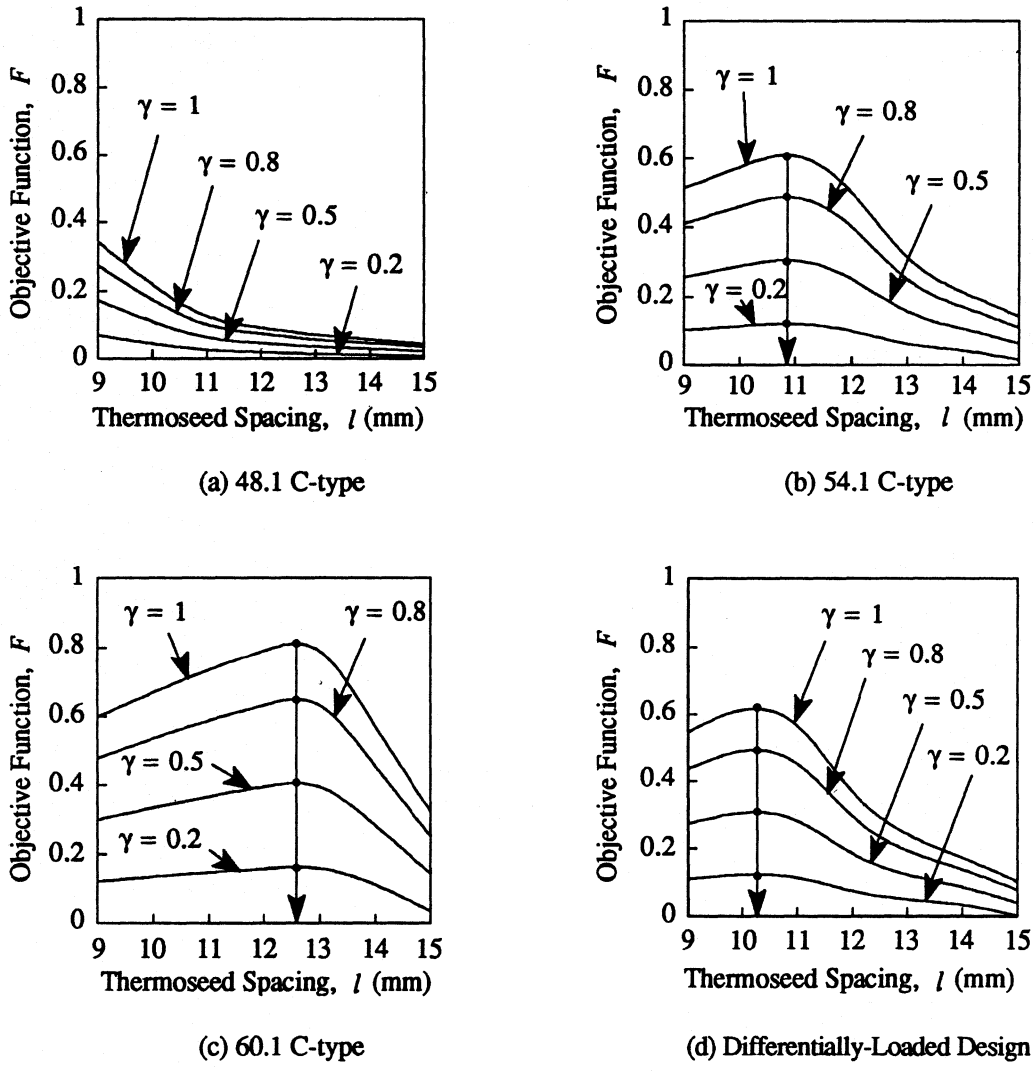

Figure 6.7 Objective function F versus thermoseed spacing l with weighting factors γ of 0.2, 0.5, 0.8 and 1. Simulations were performed with blood flow model 6 (Table 6.1) and with arrays of (a) 48.1 C-type, (b) 54.1 C-type, and (c) 60.1 C-type thermoseeds and (d) the differentially-loaded thermoseed design. Simulations were performed with tumor survival model B (Fig. 5.2), $T_{min,\ thera.}$ = 42 C. Maximums of the objective function are shown with black dots and vertical arrows.

Effect of Weighting Factor - Blood Flow Model 7

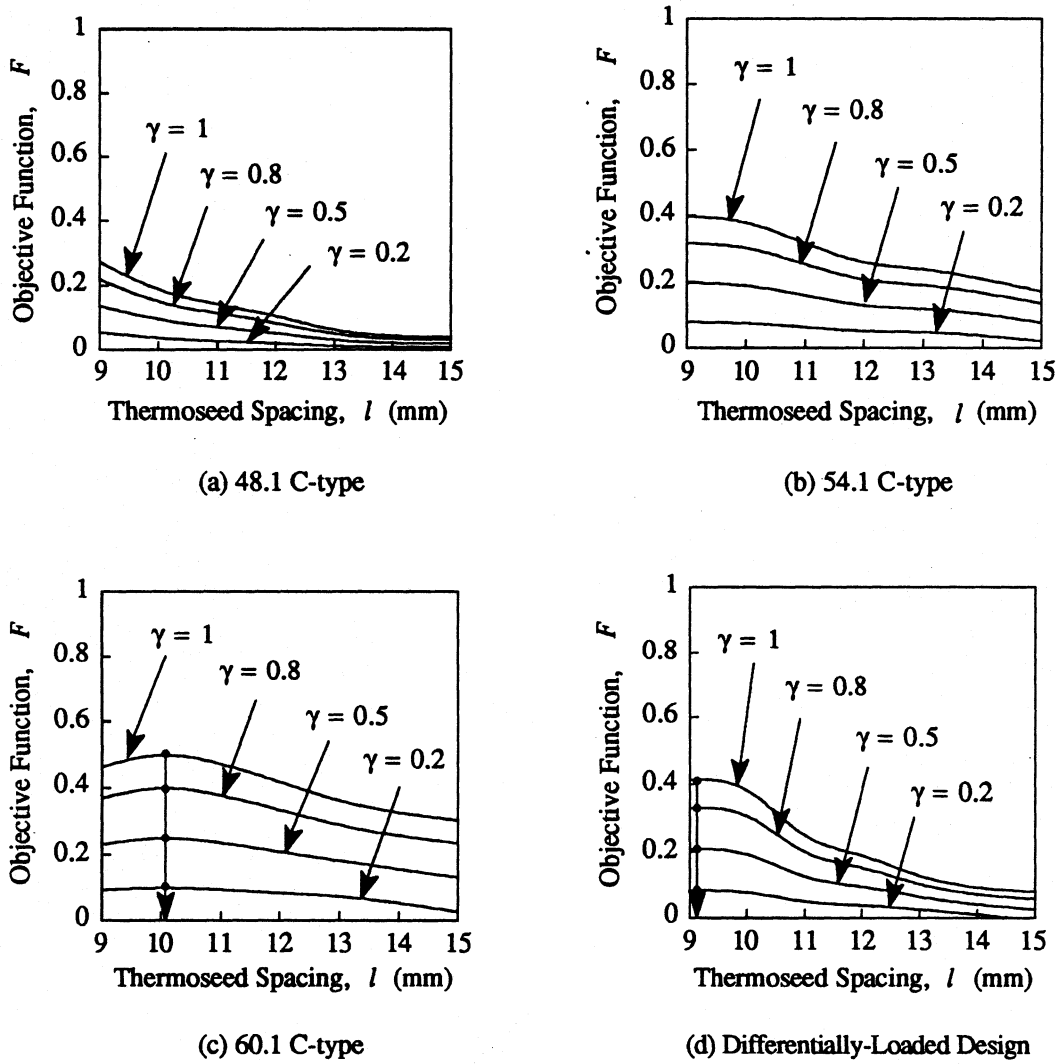

Figure 6.8 Objective function F versus thermoseed spacing l with weighting factors γ of 0.2, 0.5, 0.8 and 1. Simulations were performed with blood flow model 7 (Table 6.1) and with arrays of (a) 48.1 C-type, (b) 54.1 C-type, and (c) 60.1 C-type thermoseeds and (d) the differentially-loaded thermoseed design. Simulations were performed with tumor survival model B (Fig. 5.2), $T_{min,\ thera.}$ = 42 C. Maximums of the objective function are shown with black dots and vertical arrows.

Table 6.3 Optimum Thermoseed Spacing
(See Table 6.1 for description of blood flow models.)

(a) 48.1 C-type design

Blood Flow Model	Optimum Thermoseed Spacing, l_{opt} (mm)			
	$\gamma = 0.2$	$\gamma = 0.5$	$\gamma = 0.8$	$\gamma = 1$
1	12.8	12.8	12.8	12.8
2	**12.1**	**12.1**	**12.1**	**12.1**
3	11.7	11.7	11.7	11.7
4	< 9	< 9	< 9	< 9
5	**< 9**	**< 9**	**< 9**	**< 9**
6	< 9	< 9	< 9	< 9
7	**< 9**	**< 9**	**< 9**	**< 9**

(b) 54.1 C-type design

Blood Flow Model	Optimum Thermoseed Spacing, l_{opt} (mm)			
	$\gamma = 0.2$	$\gamma = 0.5$	$\gamma = 0.8$	$\gamma = 1$
1	11.0	11.8	12.7	14.0
2	**12.7**	**13.2**	**13.4**	**13.6**
3	13.3	13.4	13.5	13.6
4	11.2	11.2	11.2	11.2
5	**11.0**	**11.0**	**11.0**	**11.0**
6	10.8	10.8	10.8	10.8
7	**< 9**	**< 9**	**< 9**	**< 9**

(c) 60.1 C-type design

Blood Flow Model	Optimum Thermoseed Spacing, l_{opt} (mm)			
	$\gamma = 0.2$	$\gamma = 0.5$	$\gamma = 0.8$	$\gamma = 1$
1	< 9	9.8	11.2	13.0
2	**10.5**	**11.5**	**12.5**	**13.8**
3	12.0	12.8	13.5	13.8
4	12.9	12.9	12.9	12.9
5	**12.7**	**12.7**	**12.7**	**12.7**
6	12.5	12.5	12.5	12.5
7	**10.1**	**10.1**	**10.1**	**10.1**

(d) Differentially-Loaded design

Blood Flow Model	Optimum Thermoseed Spacing, l_{opt} (mm)			
	$\gamma = 0.2$	$\gamma = 0.5$	$\gamma = 0.8$	$\gamma = 1$
1	10.3	11.0	11.7	13.1
2	**12.0**	**12.4**	**13.1**	**13.4**
3	13.0	13.4	13.5	13.5
4	10.4	10.4	10.4	10.4
5	**10.3**	**10.3**	**10.3**	**10.3**
6	10.2	10.2	10.2	10.2
7	**9.1**	**9.1**	**9.1**	**9.1**

differentially-loaded array. For example, when γ increased from 0.2 to 1, the optimum spacing in an array of 54.1 C-type thermoseeds increased from 11 to 14 mm (Fig. 6.2b), from 12.7 to 13.6 mm (Fig. 6.3b) and from 13.3 to 13.6 mm (Fig. 6.4b) for normal tissue blood flow rates m_n of 0.1, 0.25 and 0.5 l/min-kg, respectively.

The optimum thermoseed spacing generally decreased, while maintaining approximately the same value for the objective function, with an array of 60.1 C-type thermoseeds versus that of 54.1 C-type thermoseeds. The decrease in thermoseed spacing is evident by comparing Figs. 6.2c with 6.2b, Fig. 6.3c with 6.3b, Figs. 6.4c with 6.4b. For instance, when $\gamma = 0.8$ and normal tissue blood flow m_n is 0.25 l/min-kg, the maximum of the objective function for arrays of 54.1 C- and 60.1 C-type thermoseeds is 0.77. This maximum occurs at an interseed spacing of 13.4 mm for the array of 54.1 C-type thermoseeds and at 12.5 mm for the array of 60.1 C-type thermoseeds (Table 6.3).

The maximums of the objective function with the differentially-loaded design for all γs studied were close to those of the 54.1 C- and 60.1 C-type arrays (Figs. 6.2d, 6.3d and 6.4d). The optimum thermoseed spacings of the differentially-loaded design were close or slightly less than those of the 54.1 C-type thermoseed design (Table 6.3d).

6.2.2.2 High Tumor Blood Flow

The objective function was maximized with an interseed spacing less than 9 mm when tumor blood flow m_t was 0.25 l/min-kg and with an array of 48.1 C-type thermoseeds (Figs. 6.5a, 6.6a and 6.7a and Table 6.3a). The objective function was also maximized with arrays of 54.1 C- and 60.1 C-type thermoseeds. The optimum spacing in an array of 54.1 C-type thermoseeds was about 11.2, 11 and 10.8 mm with normal tissue blood flow rates m_n of 0.25, 0.5 and 1 l/min-kg, respectively (Figs. 6.5b, 6.6b

and 6.7b and Table 6.3b). The optimum spacing in the array of 60.1 C-type thermoseeds was 12.9, 12.7 and 12.5 mm for the same four-fold increase in normal tissue blood flow from 0.25 to 1 l/min-kg. Similarly, the optimum spacing in the differentially-loaded array was 10.4, 10.3 and 10.2 mm for the same four-fold increase in m_n.

The maximum of the objective function with $\gamma = 1$ increased by approximately 0.27, 0.2 and 0.18 with the array of 60.1 C-type thermoseeds versus that of 54.1 C-type thermoseeds at normal tissue blood flows m_n of 0.25, 0.5 and 1 l/min-kg, respectively (compare Figs. 6.5c and 6.5b, Figs. 6.6c with 6.6b and Figs. 6.7c with 6.7b). The maximum of the objective function with the array of 54.1 C-type thermoseeds occurred with an interseed spacing of about 11 mm, averaged over normal tissue blood flows m_n of 0.25, 0.5 and 1 l/min-kg. Similarly, the maximum of the objective function with the array of 60.1 C-type thermoseeds occurred with an interseed spacing of about 12.7 mm, averaged over normal tissue blood flows studied. Thus at higher rates of tumor blood flow, wider interseed spacing can be used with higher operating temperature thermoseeds to attain an equal or higher value of the objective function.

The differentially-loaded thermoseed design attained maximum objective functions that were similar to those of the 54.1 C-type thermoseed array (Figs. 6.5d, 6.6d and 6.7d). The maximum of the objective function in the differentially-loaded array occurred with an interseed spacing of about 10.3 mm, averaged over normal tissue blood flow of 0.25, 0.5 and 1 l/min-kg. Thus the differentially-loaded array heated the tumor and normal tissues close to that of the 54.1 C-type array, but l_{opt} was between 0.6 and 0.8 mm tighter in the differentially-loaded design than in the 54.1 C-type design (Table 6.3d and 6.3b).

6.2.2.3 Compartmentalized Tumor Blood Flow Model

Optimum spacings in the arrays of 48.1 C and 54. C-type seeds were less than 9 mm (Figs. 6.8a and 6.8b). Optimum seed spacings in the 60.1 C-type and the differentially-loaded arrays were 10.1 and 9.1 mm, respectively (Fig. 6.8c and 6.8d). In both the 60.1 C- and differentially-loaded arrays, however, the weighting factor had a negligible influence on optimum spacing.

In conclusion, criteria's (2), (3) and (4) discussed in the second paragraph in this chapter have been established. Unique maximums of the objective function are obtained, and the weighting factor alters the optimum thermoseed spacing in simulations with some blood flow models.

6.2.3 Effect of Blood Flow Rate

The objective function versus thermoseed spacing for several normal and tumor blood flow rates are shown in Fig. 6.9 for $\gamma = 0.8$. At a moderate rate of tumor blood flow $m_t = 0.1$ l/min-kg, optimum spacing in the array of 48.1 C-type thermoseeds decreased from 12.8 to 11.7 mm (Table 6.3) as normal tissue blood flow m_n increased from 0.1 to 0.5 l/min-kg (Fig. 6.9a). However, at the same rate of tumor blood flow (m_t = 0.1 l/min-kg), optimum spacing of 54.1 C-type thermoseeds increased slightly from 12.7 to 13.5 mm as normal tissue blood flow increased from 0.1 to 0.5 l/min-kg. Likewise, optimum spacing of 60.1 C-type thermoseeds increased from 11.2 to 13.5 mm over an increase in normal tissue blood flow m_n from 0.1 to 0.5 l/min-kg. Similarly, the optimum spacing of thermoseeds in the differentially-loaded design increased from 11.7 to 13.5 mm.

The optimum spacing in the array of 48.1 C-type thermoseeds at a high rate of tumor blood flow m_t of 0.25 l/min-kg was below 9 mm for normal tissue blood flow

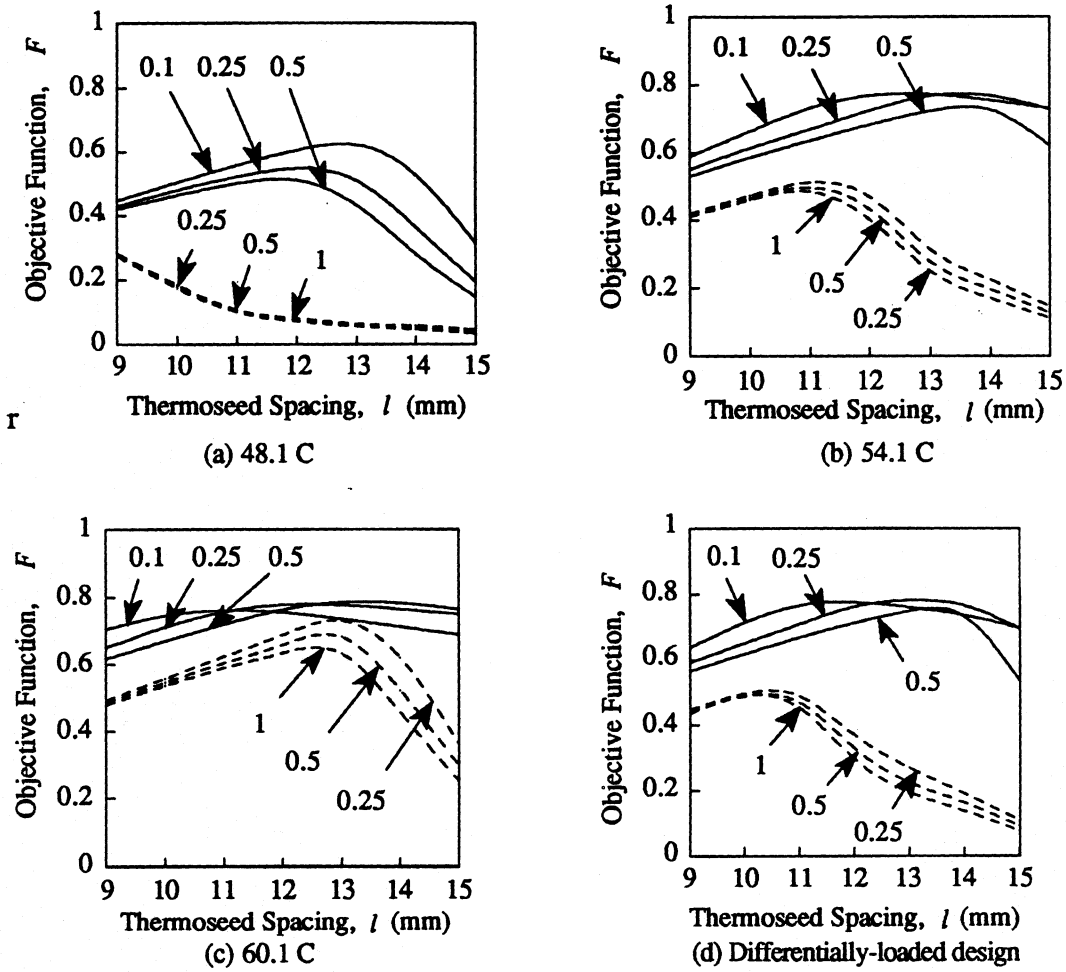

Figure 6.9 Effect of blood flow on objective function F with $\gamma = 0.8$ and tumor survival model B. Simulations were performed with an array of bare thermoseeds with operating temperatures of (a) 48.1 C, (b) 54.1 C, and (c) 60.1 C and (d) for the differentially-loaded thermoseed design. Curves are shown for blood flow models 1 through 6 where m_n (l/min-kg) is labeled and with tumor blood flow of m_t = 0.1 l/min-kg (solid lines) and m_t = 0.25 l/min-kg (dashed lines).

rates of 0.25 to 1 l/min-kg (Figs. 6.5a, 6.6a and 6.7a). However, in arrays of 54.1 C- and 60.1 C-type thermoseeds and in the differentially-loaded design, the optimum seed spacing was approximately 11, 12.7 and 10.3 mm, respectively, over normal tissue blood flows between 0.25 and 1 l/min-kg.

Several conclusions can be made from the effect of blood flow on the objective function. First, smaller objective functions are associated with higher tumor blood flow

rates. Second, high tumor blood flow rates (m_t = 0.25 l/min-kg) generally yield optimum thermoseed spacings that (1) increase with arrays of higher operating temperature thermoseeds and (2) are somewhat independent of normal tissue blood flow rates. Last, lower tumor blood flow rates (m_t = 0.1 l/min-kg) generally yield optimum thermoseed spacings that decrease with arrays of lower operating temperature thermoseeds and increasing normal tissue blood flow.

6.2.4 Effect of Thermoseed Operating Temperature

The objective function F versus thermoseed spacing l for square arrays of 48.1 C-, 54.1 C-, 60.1 C-type thermoseeds are shown in Fig. 6.10. Larger objective functions correlate with arrays containing higher operating temperature thermoseeds. Wide variations in thermoseed spacing (between 11 and 14 mm) give optimal values of the objective function for an array of 60.1 C-type thermoseeds (Fig. 6.10a). There is uniqueness of the optimal value of F in the curves in Fig. 6.10b where clearly-defined maximums of the objective function are achieved with all four types of arrays in a tumor blood flow of m_t = 0.25 l/min-kg. With blood flow model 7, there are unique values of the optimal F with the 60.1 C-type array and the differentially-loaded array (Fig. 6.10c).

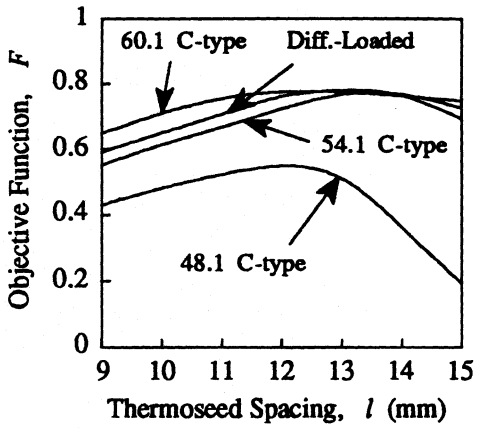

(a) **Blood flow model 2**

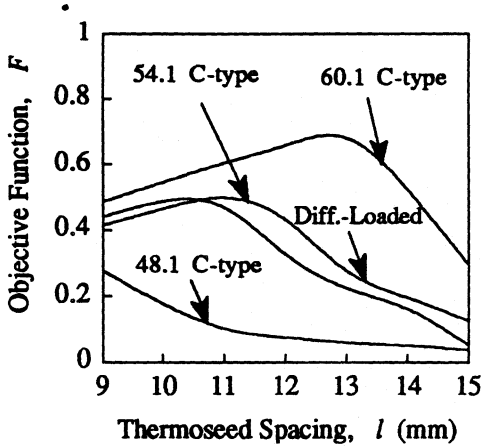

(b) **Blood flow model 5**

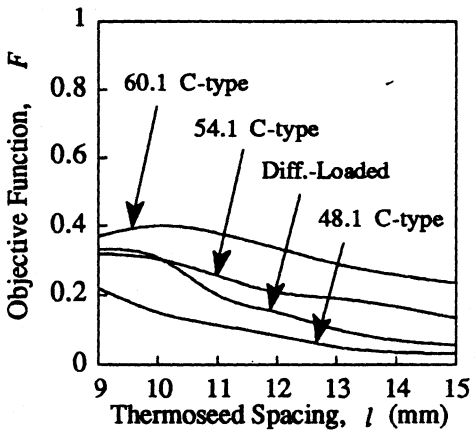

(c) **Blood flow model 7**

Figure 6.10 Objective function F versus thermoseed spacing l for arrays of thermoseeds with operating temperatures of 48.1 C, 54.1 C and 60.1 C and the differentially-loaded array. Objective functions were computed with tumor survival model B and with $\gamma = 0.8$. Simulations were performed with (a) blood flow model 2, (b) blood flow model 5 and (c) blood flow model 7 (see Table 6.1).

6.2.5 Optimum Thermoseed Designs based on Objective Function

The optimum thermoseed designs based on maximizing the objective function are in Table 6.4. The array of 60.1 C-type thermoseeds maximized the objective function for all γ's with blood flow models 3 through 7. Although the differentially-loaded design was the optimum design in five simulations (Table 6.4), the objective function of the 54.1 C-

type design was close to the differentially-loaded design in these five simulations. Thus the optimum thermoseed design is somewhat dependent on the blood flow model. It is therefore critical that the blood flow model approximate the actual blood flow as close as possible.

Table 6.4 Optimum Thermoseed Design based on Objective Function

Blood Flow Model	Optimum Thermoseed Design			
	$\gamma = 0.2$	$\gamma = 0.5$	$\gamma = 0.8$	$\gamma = 1$
1	54.1	Diff-Load	Diff-Load	60.1
2	**Diff-Load**	**Diff-Load**	**Diff-Load**	**60.1**
3	60.1	60.1	60.1	60.1
4	60.1	60.1	60.1	60.1
5	**60.1**	**60.1**	**60.1**	**60.1**
6	60.1	60.1	60.1	60.1
7	**60.1**	**60.1**	**60.1**	**60.1**

6.3 Therapeutic Assessment of Objective Function

This section discusses the performance of the objective function relative to temperature-based criteria including (1) the percentage of tumor between lower and upper temperature limits (Sec. 6.3.1); and (2) the minimum tumor temperature ($T_{min,\ tumor}$) and the maximum normal tissue temperature ($T_{max,\ normal}$) (Sec. 6.3.2). The suitability if the objective function is assessed by determining if the fraction of tumor killed, Ψ_T, using the objective function is larger than Ψ_T using temperature descriptors.

6.3.1 Percentage of Tumor Between Lower & Upper Temperature Limits

The percentage of tumor between lower and upper temperature limits for all four types of thermoseed designs are in Figs. 6.11 through 6.17. Figures 6.11 through 6.17 contain the results from the simulations with the seven blood flow models.

The temperature range where the maximum percentage of tumor is heated in simulations with the optimum thermoseed designs (see Table 6.4) are in Table 6.5. Notice that for tumor blood flow rates of m_t = 0.25 l/min-kg, the largest percentage of tumor is heated between 43 and 44 C.

Table 6.5 Temperature Range where Maximum Percentage of Tumor is Between for Optimum Thermoseed Configuration (see Table 6.3)

Blood Flow Model	Temperature Range (C)			
	$\gamma = 0.2$	$\gamma = 0.5$	$\gamma = 0.8$	$\gamma = 1$
1	47 - 48	46 - 47	45 - 46	> 48
2	**45 - 46**	**45 - 46**	**44 - 45**	**> 48**
3	> 48	> 48	> 48	> 48
4	43 - 44	43 - 44	43 - 44	43 - 44
5	**43 - 44**	**43 - 44**	**43 - 44**	**43 - 44**
6	43 - 44	43 - 44	43 - 44	43 - 44
7	**< 42**	**< 42**	**< 42**	**< 42**

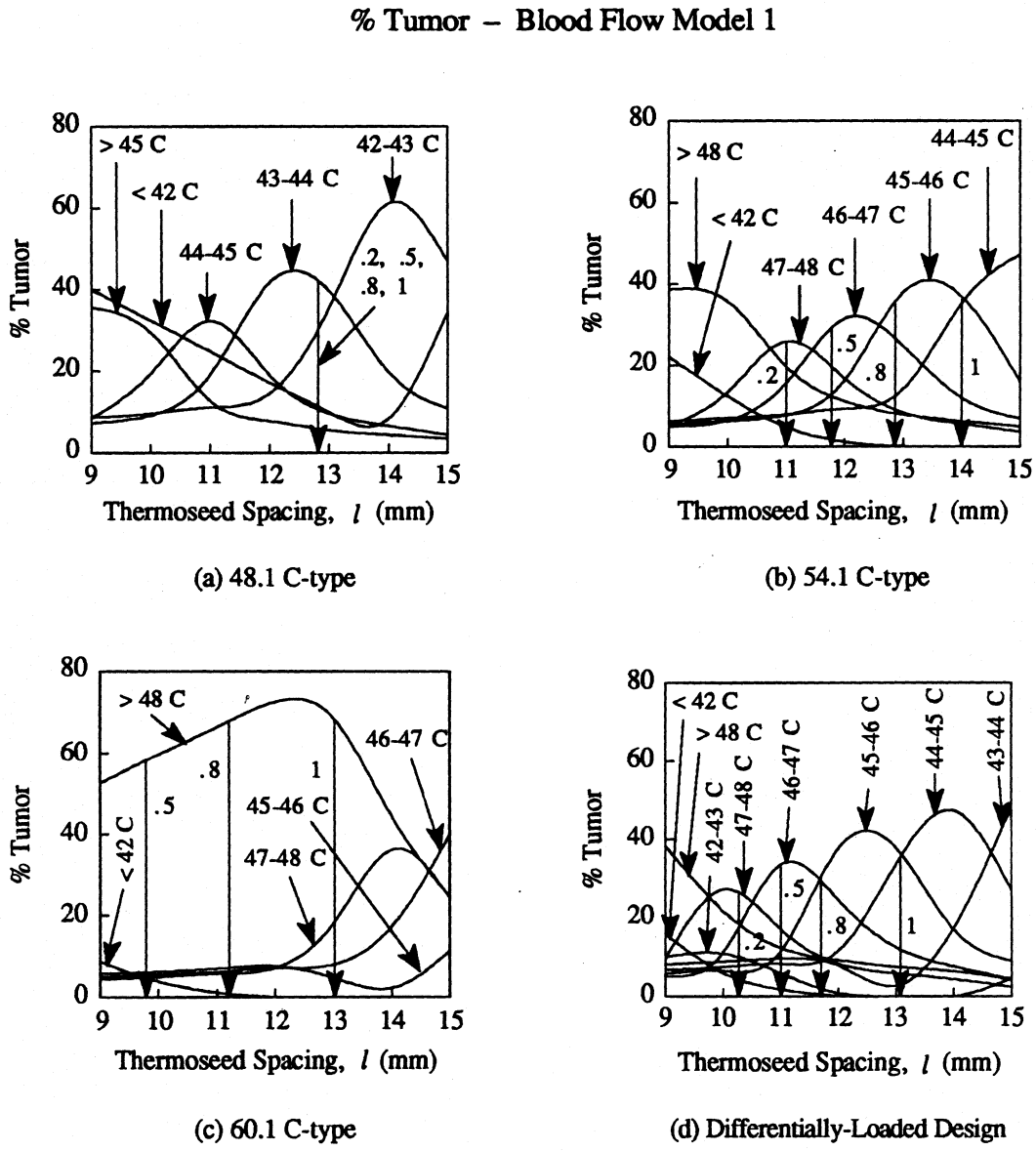

Figure 6.11 Percentage of tumor between lower and upper temperature limits versus thermoseed spacing l for arrays of thermoseeds with (a) 48.1 C-type, (b) 54.1 C-type, (c) 60.1 C-type thermoseeds and (d) for the differentially-loaded thermoseed design. Simulations were performed with blood flow model 1 (Table 6.1) and with tumor survival model B (Fig. 5.2). The optimum thermoseed spacing as determined by the objective function for $\gamma = 0.2, 0.5, 0.8$ and 1 are labeled in each figure.

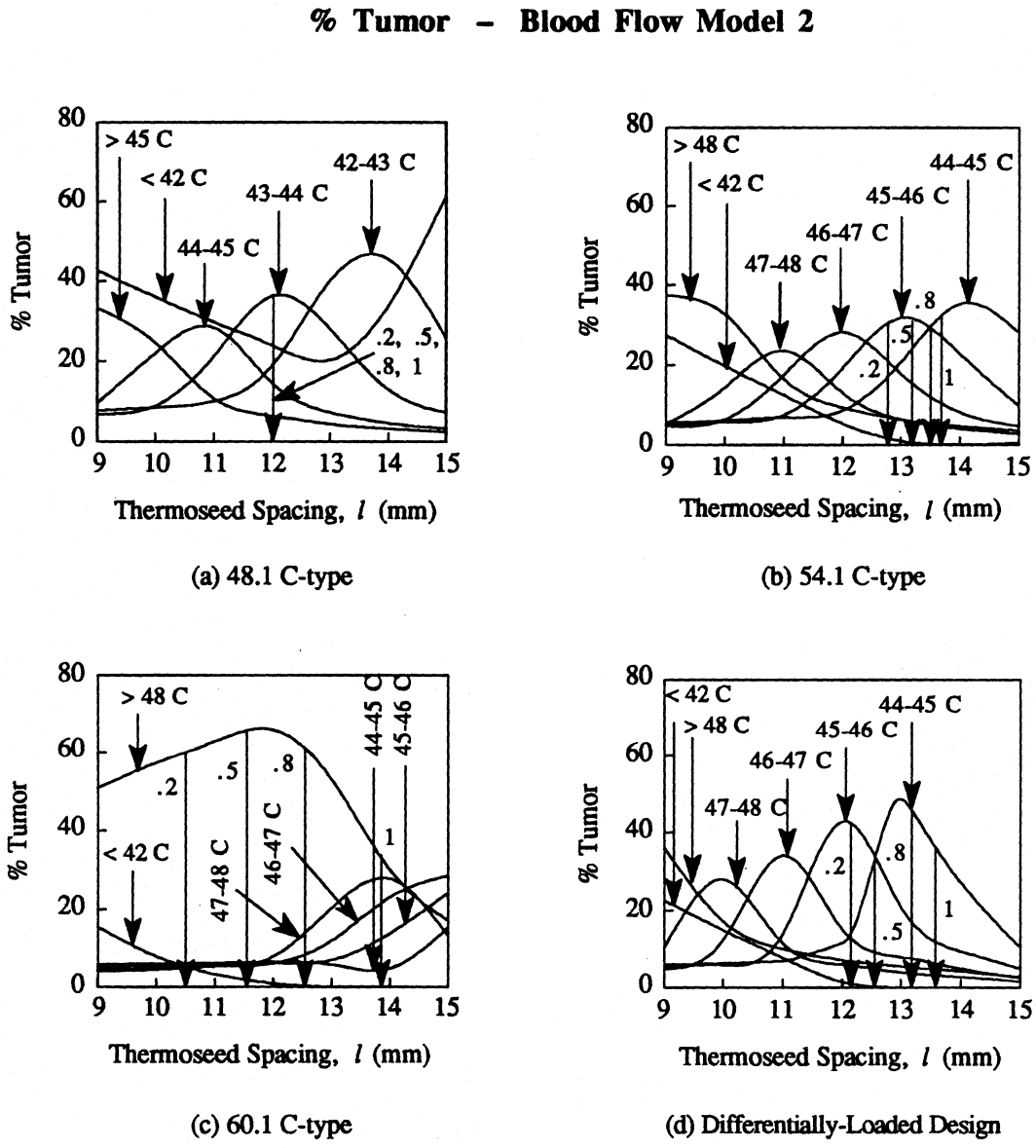

Figure 6.12 Percentage of tumor between lower and upper temperature limits versus thermoseed spacing l for arrays of thermoseeds with (a) 48.1 C-type, (b) 54.1 C-type, (c) 60.1 C-type thermoseeds and (d) for the differentially-loaded thermoseed design. Simulations were performed with blood flow model 2 (Table 6.1) and with tumor survival model B (Fig. 5.2). The optimum thermoseed spacing as determined by the objective function for $\gamma = 0.2, 0.5, 0.8$ and 1 are labeled in each figure.

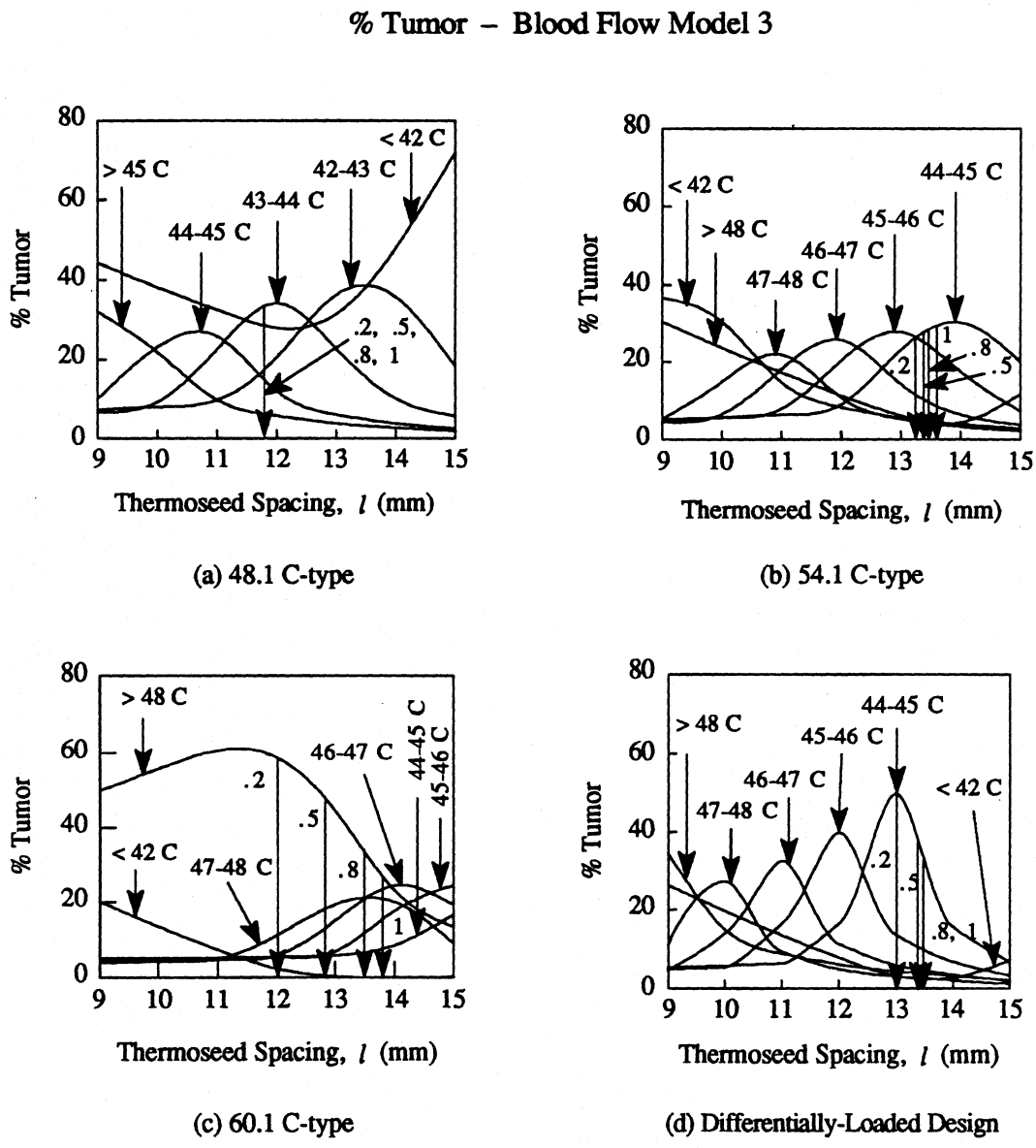

Figure 6.13 Percentage of tumor between lower and upper temperature limits versus thermoseed spacing l for arrays of thermoseeds with (a) 48.1 C-type, (b) 54.1 C-type, (c) 60.1 C-type thermoseeds and (d) for the differentially-loaded thermoseed design. Simulations were performed with blood flow model 3 (Table 6.1) and with tumor survival model B (Fig. 5.2). The optimum thermoseed spacing as determined by the objective function for γ= 0.2, 0.5, 0.8 and 1 are labeled in each figure.

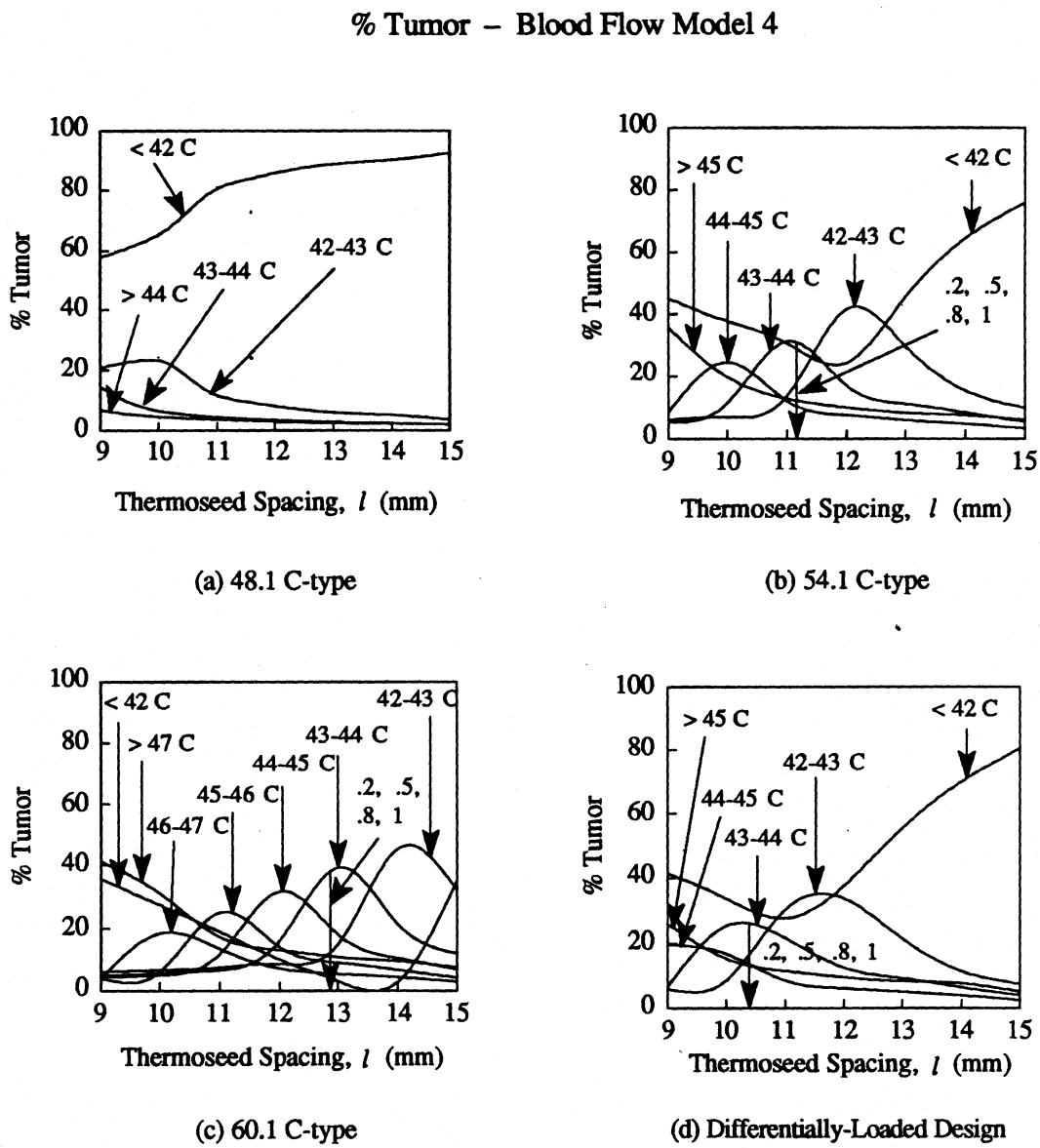

Figure 6.14 Percentage of tumor between lower and upper temperature limits versus thermoseed spacing l for arrays of thermoseeds with (a) 48.1 C-type, (b) 54.1 C-type, (c) 60.1 C-type thermoseeds and (d) for the differentially-loaded thermoseed design. Simulations were performed with blood flow model 4 (Table 6.1) and with tumor survival model B (Fig. 5.2). The optimum thermoseed spacing as determined by the objective function for $\gamma = 0.2, 0.5, 0.8$ and 1 are labeled in each figure.

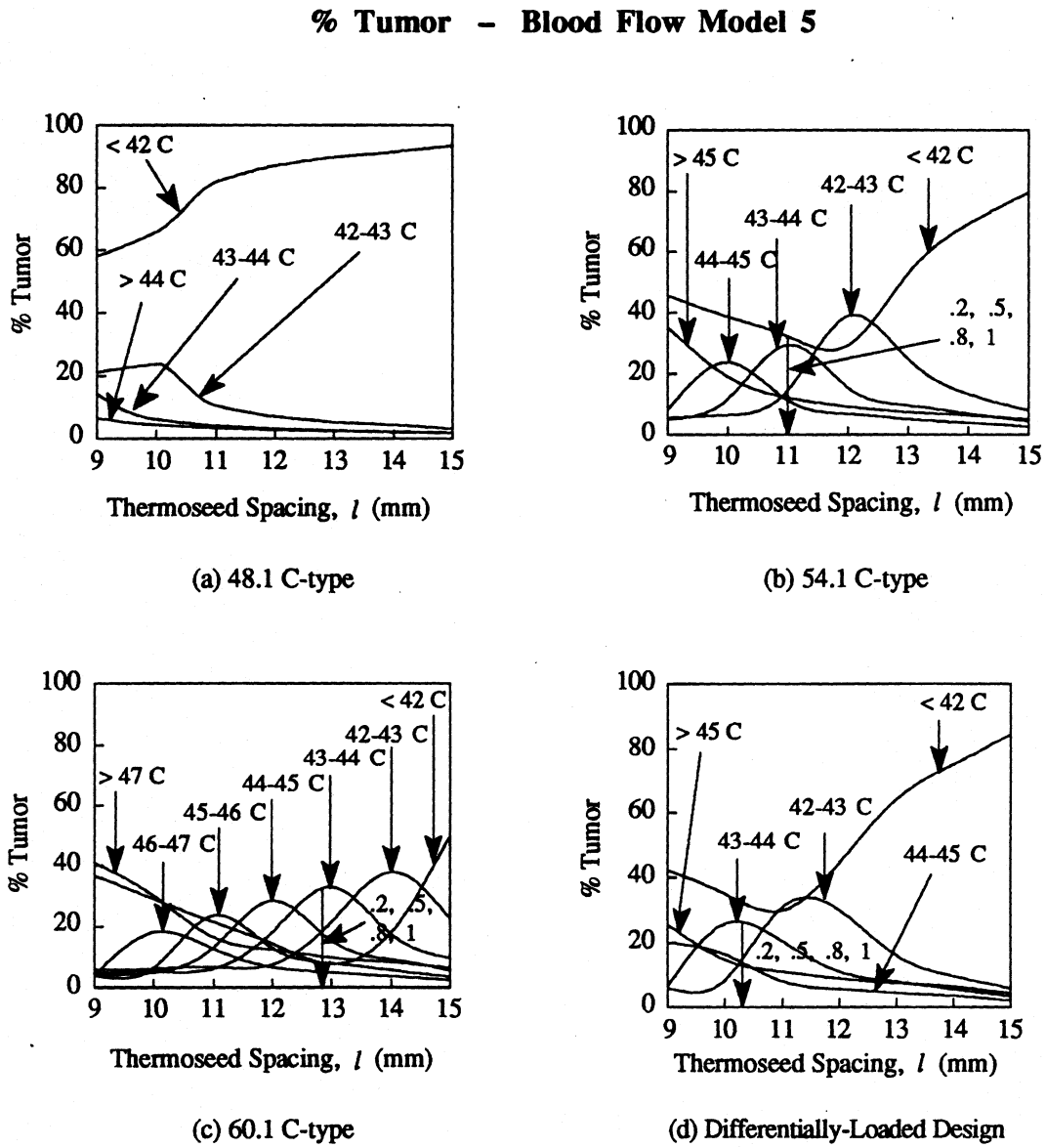

Figure 6.15 Percentage of tumor between lower and upper temperature limits versus thermoseed spacing l for arrays of thermoseeds with (a) 48.1 C-type, (b) 54.1 C-type, (c) 60.1 C-type thermoseeds and (d) for the differentially-loaded thermoseed design. Simulations were performed with blood flow model 5 (Table 6.1) and with tumor survival model B (Fig. 5.2). The optimum thermoseed spacing as determined by the objective function for γ= 0.2, 0.5, 0.8 and 1 are labeled in each figure.

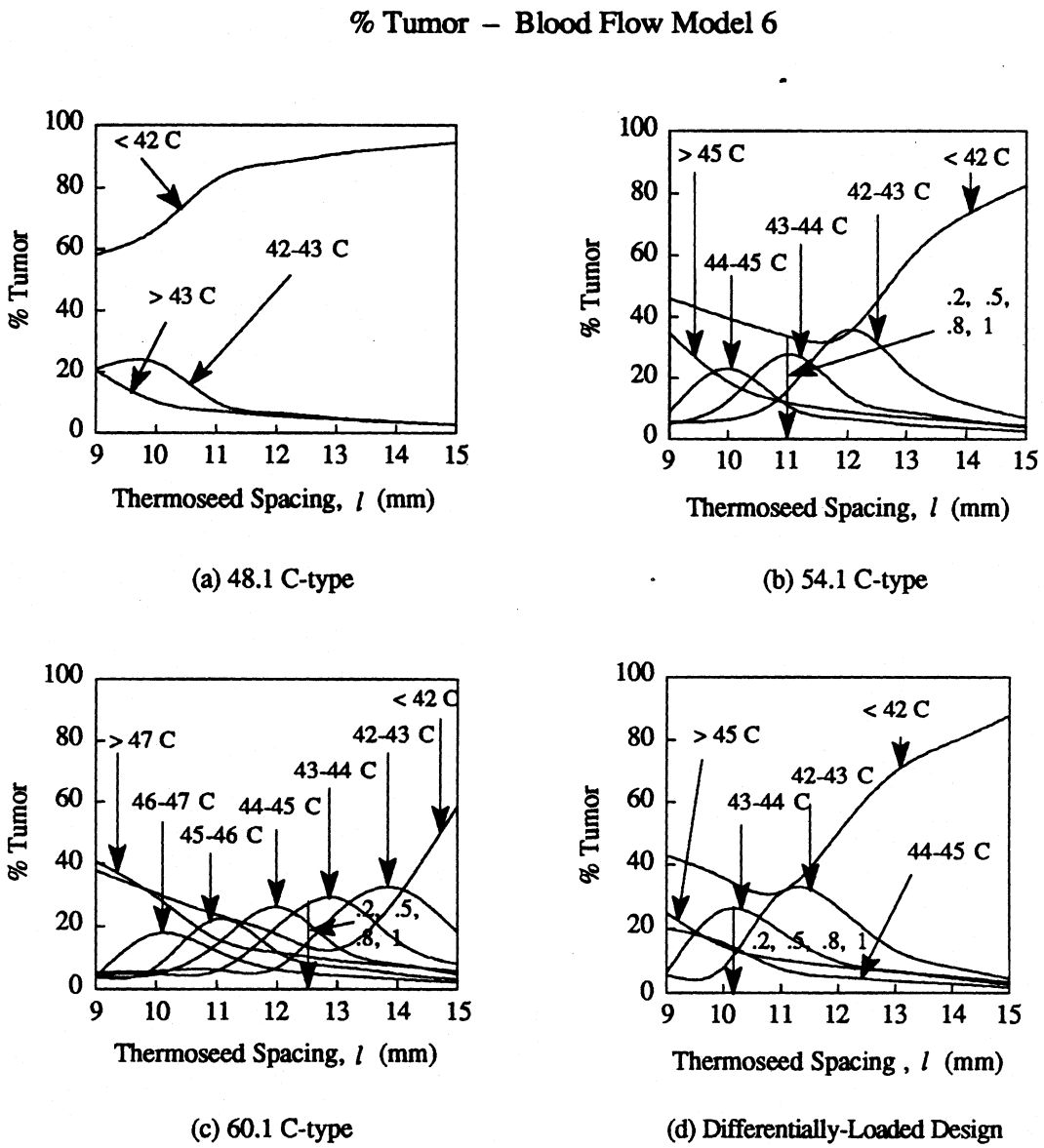

Figure 6.16 Percentage of tumor between lower and upper temperature limits versus thermoseed spacing l for arrays of thermoseeds with (a) 48.1 C-type, (b) 54.1 C-type, (c) 60.1 C-type thermoseeds and (d) for the differentially-loaded thermoseed design. Simulations were performed with blood flow model 6 (Table 6.1) and with tumor survival model B (Fig. 5.2). The optimum thermoseed spacing as determined by the objective function for $\gamma = 0.2, 0.5, 0.8$ and 1 are labeled in each figure.

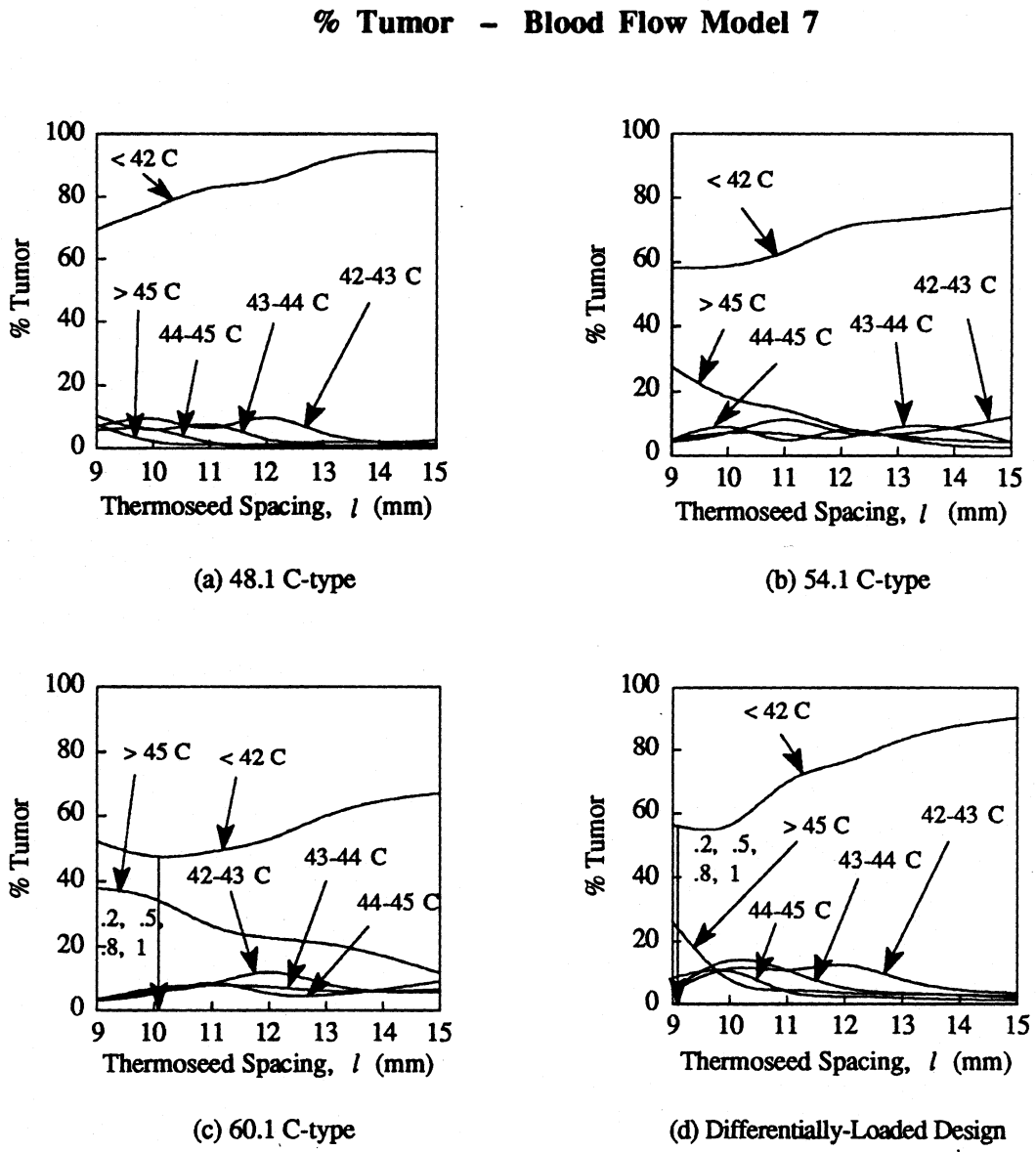

Figure 6.17 Percentage of tumor between lower and upper temperature limits versus thermoseed spacing l for arrays of thermoseeds with (a) 48.1 C-type, (b) 54.1 C-type, (c) 60.1 C-type thermoseeds and (d) for the differentially-loaded thermoseed design. Simulations were performed with blood flow model 7 (Table 6.1) and with tumor survival model B (Fig. 5.2). The optimum thermoseed spacing as determined by the objective function for γ= 0.2, 0.5, 0.8 and 1 are labeled in each figure.

6.3.2 Temperature Descriptors

Several temperature descriptors including the maximum tumor temperature ($T_{max,\ tumor}$), the minimum tumor temperature ($T_{min,\ tumor}$), the maximum normal tissue temperature ($T_{max,\ normal}$), and the average temperature on the boundary of the tumor and normal tissue ($T_{ave,\ boundary}$) are plotted in Figs. 6.18 through 6.24 for blood flow models 1 through 7. Notice that since the simulations were performed with bare thermoseeds, $T_{max,\ tumor}$ is a plot of the warmest thermoseed in the array. In Figs. 6.18 through 6.24, $T_{max,\ tumor}$ decreases with increasing thermoseed spacing because of the reduced heating effect that thermoseeds have on each other with increasing thermoseed spacing l. In Figs. 6.18 through 6.24, the slopes of $T_{max,\ normal}$ and $T_{ave,\ boundary}$ are small at narrow l's and then increase at an l between 13 and 14 mm. The modest increase in the slopes of $T_{max,\ normal}$ and $T_{ave,\ boundary}$ at a seed spacing of about 13 or 14 mm was due to the close proximity of the thermoseed array to the boundary of the tumor and normal tissue. The slopes of $T_{min,\ tumor}$ were fairly small at l's between 9 and 12 mm, increased at l's between 12 and 14 mm and then became somewhat flat between l's of 14 and 15 mm.

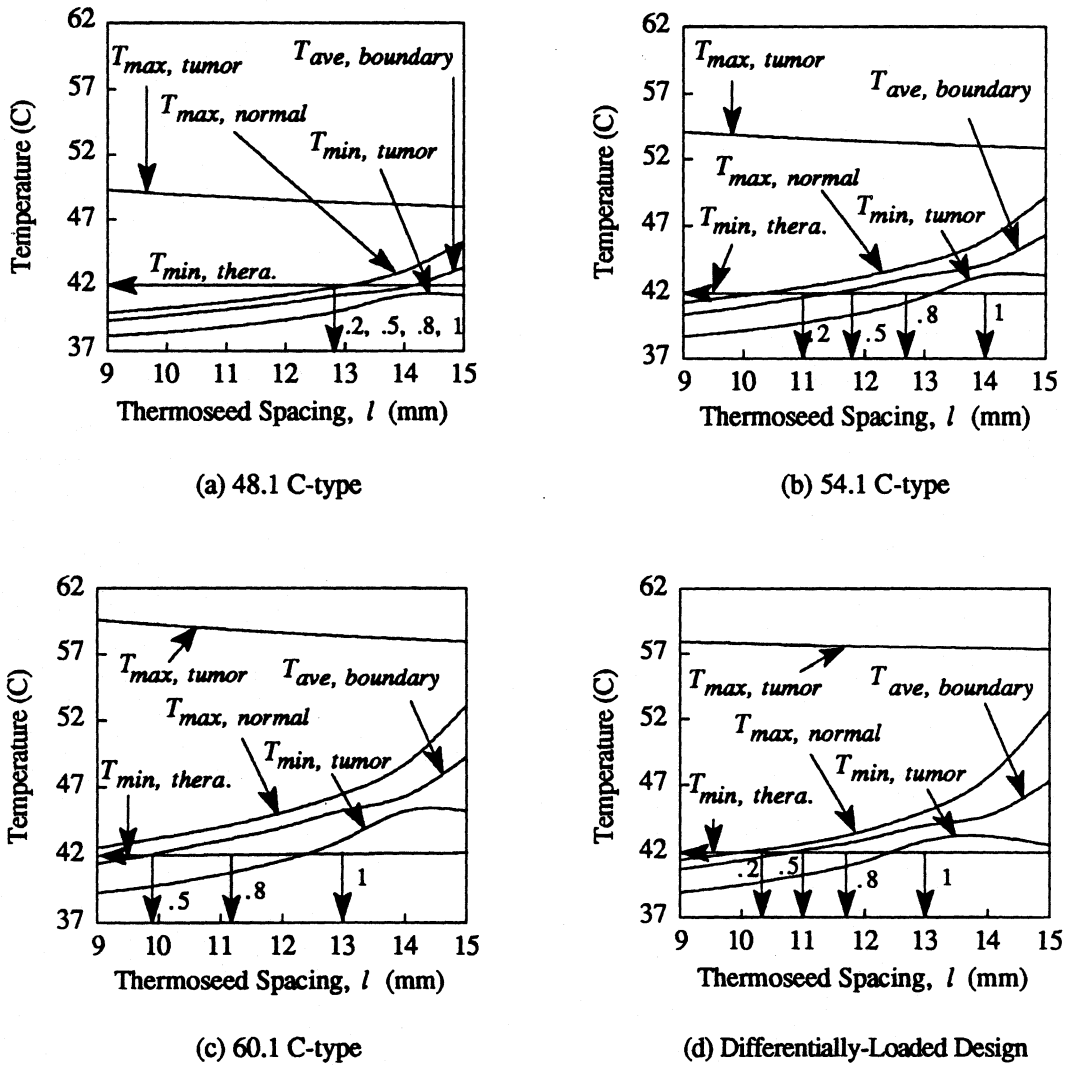

Figure 6.18 Temperature descriptors in tumor and normal tissue versus thermoseed spacing l for arrays of thermoseeds with (a) 48.1 C-type, (b) 54.1 C-type, (c) 60.1 C-type thermoseeds and (d) for the differentially-loaded thermoseed design. Simulations were performed with blood flow model 1 (Table 6.1). The optimum thermoseed spacing as determined by the objective function with $\gamma = 0.2, 0.5, 0.8$ and 1 are labeled in each figure.

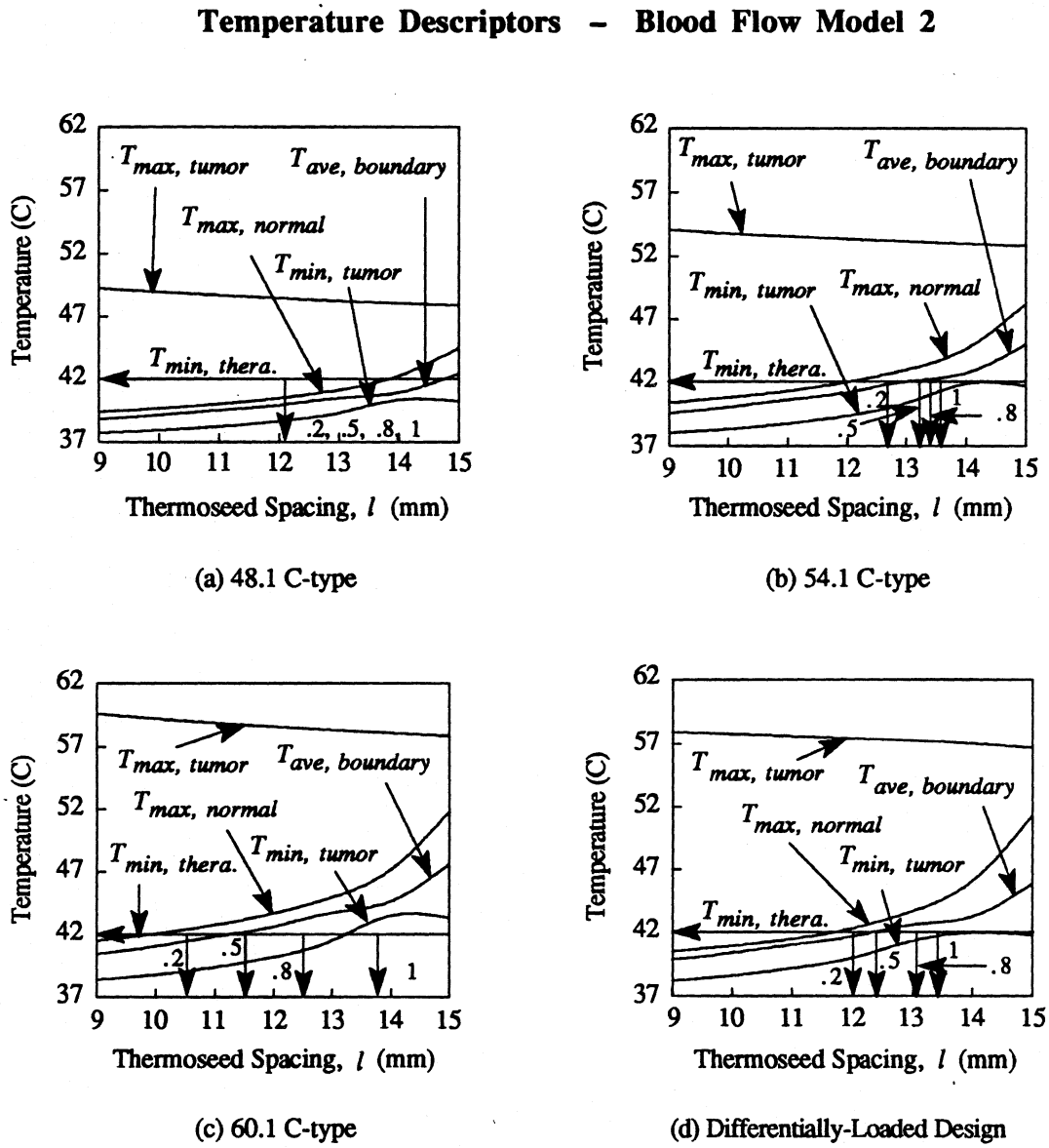

Figure 6.19 Temperature descriptors in tumor and normal tissue versus thermoseed spacing l for arrays of thermoseeds with (a) 48.1 C-type, (b) 54.1 C-type, (c) 60.1 C-type thermoseeds and (d) for the differentially-loaded thermoseed design. Simulations were performed with blood flow model 2 (Table 6.1). The optimum thermoseed spacing as determined by the objective function with $\gamma = 0.2, 0.5, 0.8$ and 1 are labeled in each figure.

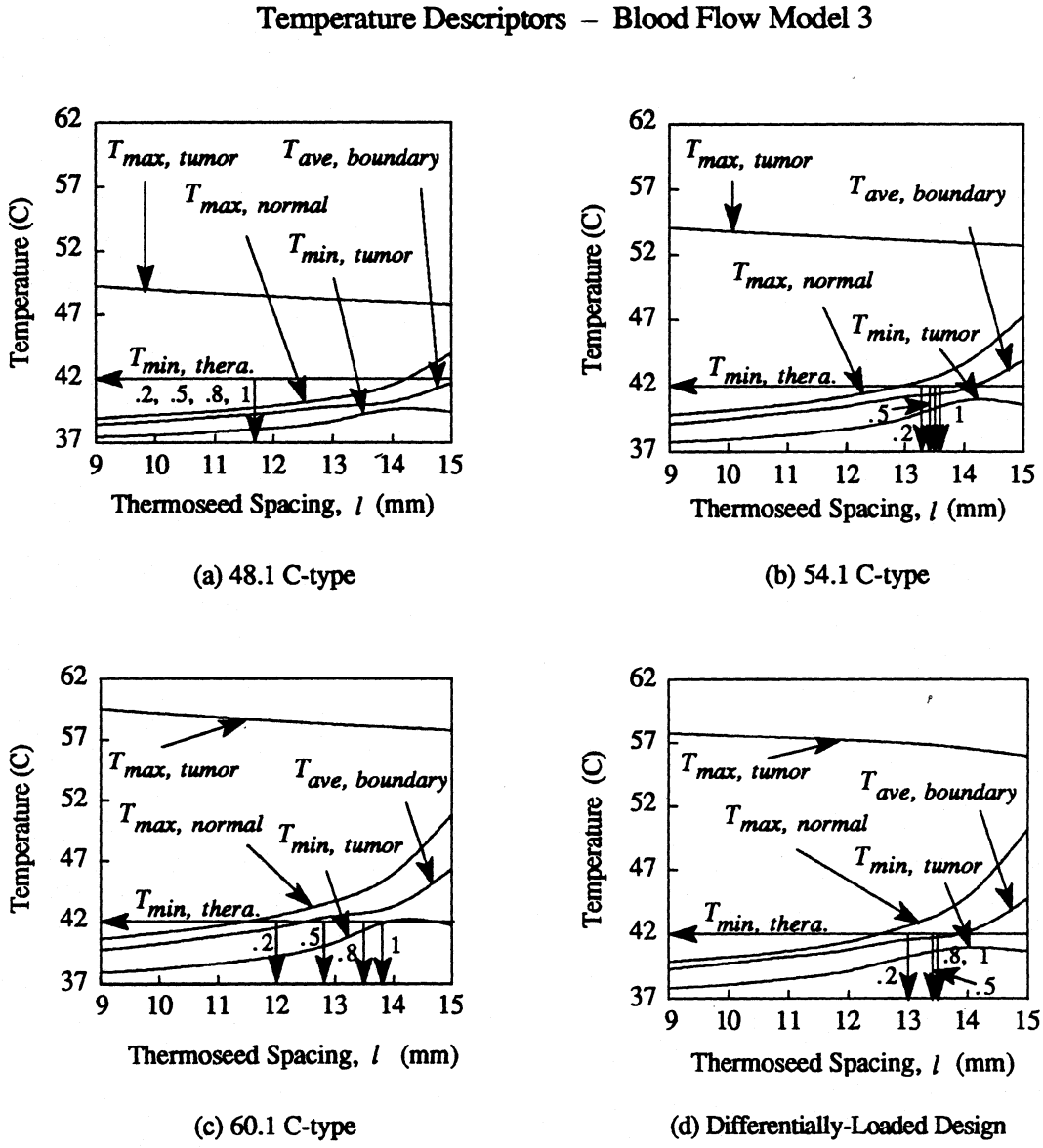

Figure 6.20 Temperature descriptors in tumor and normal tissue versus thermoseed spacing l for arrays of thermoseeds with (a) 48.1 C-type, (b) 54.1 C-type, (c) 60.1 C-type thermoseeds and (d) for the differentially-loaded thermoseed design. Simulations were performed with blood flow model 3 (Table 6.1). The optimum thermoseed spacing as determined by the objective function with $\gamma = 0.2, 0.5, 0.8$ and 1 are labeled in each figure.

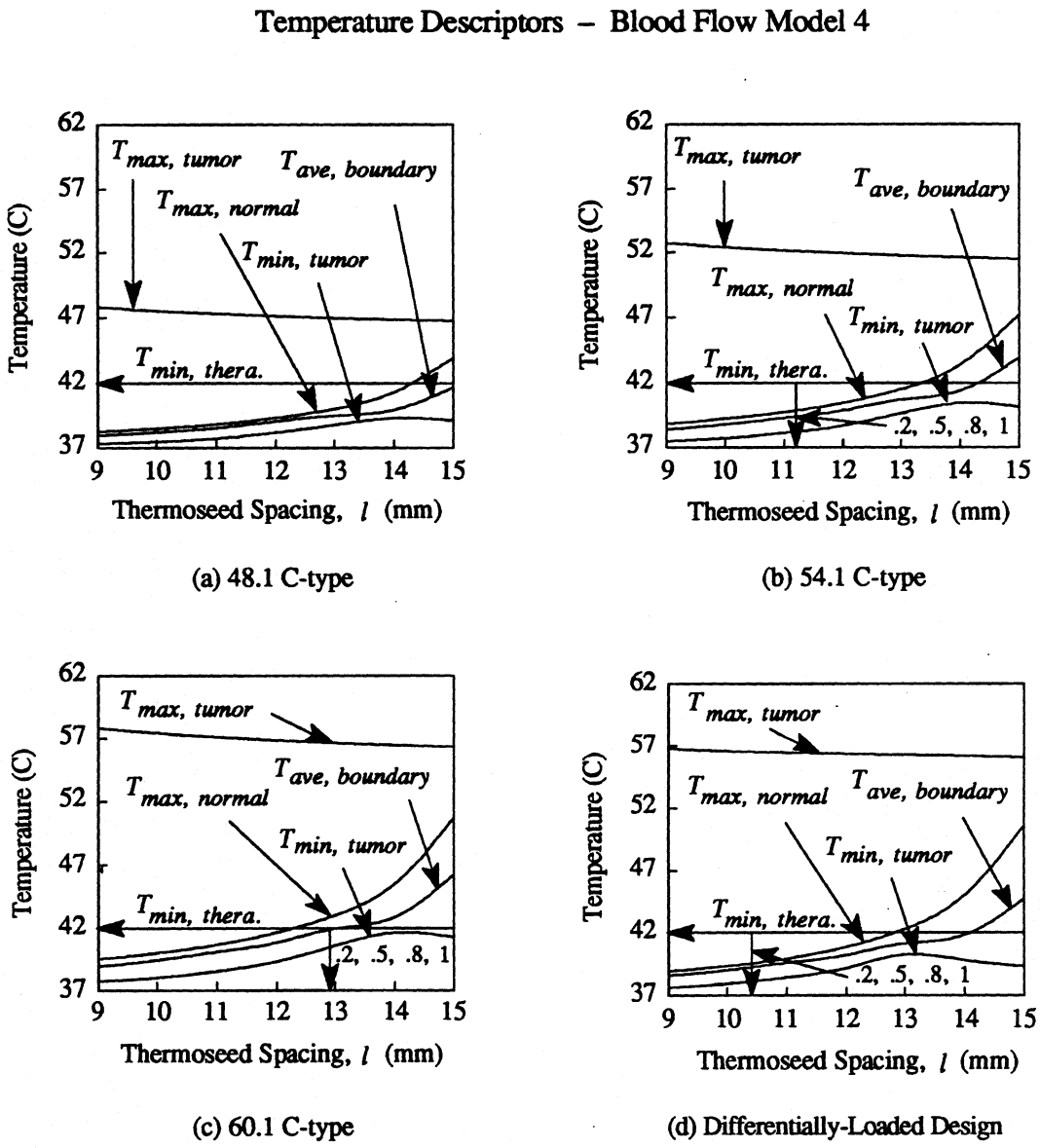

Figure 6.21 Temperature descriptors in tumor and normal tissue versus thermoseed spacing l for arrays of thermoseeds with (a) 48.1 C-type, (b) 54.1 C-type, (c) 60.1 C-type thermoseeds and (d) for the differentially-loaded thermoseed design. Simulations were performed with blood flow model 4 (Table 6.1). The optimum thermoseed spacing as determined by the objective function with $\gamma = 0.2$, 0.5, 0.8 and 1 are labeled in each figure.

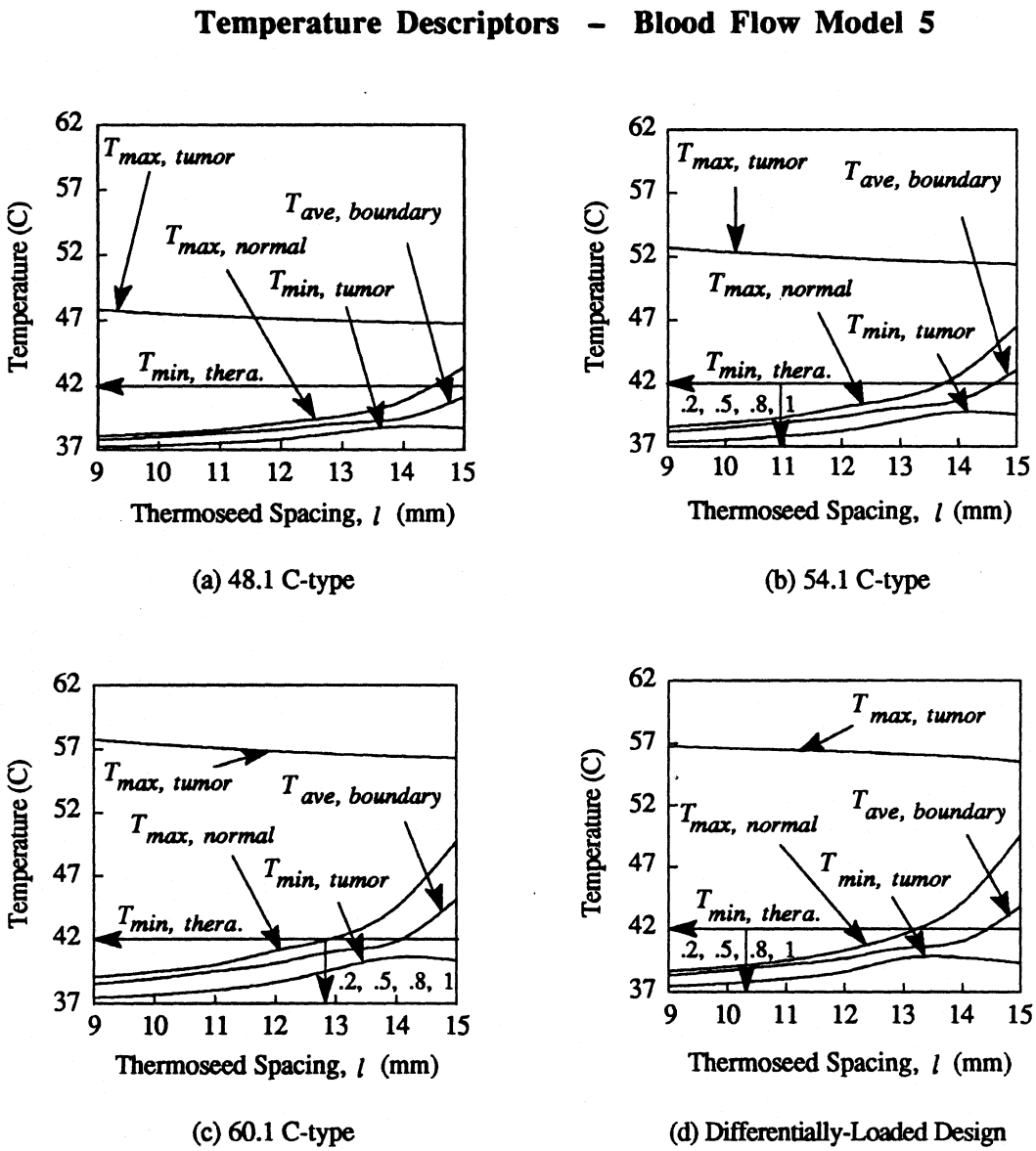

Figure 6.22 Temperature descriptors in tumor and normal tissue versus thermoseed spacing l for arrays of thermoseeds with (a) 48.1 C-type, (b) 54.1 C-type, (c) 60.1 C-type thermoseeds and (d) for the differentially-loaded thermoseed design. Simulations were performed with blood flow model 5 (Table 6.1). The optimum thermoseed spacing as determined by the objective function with $\gamma = 0.2, 0.5, 0.8$ and 1 are labeled in each figure.

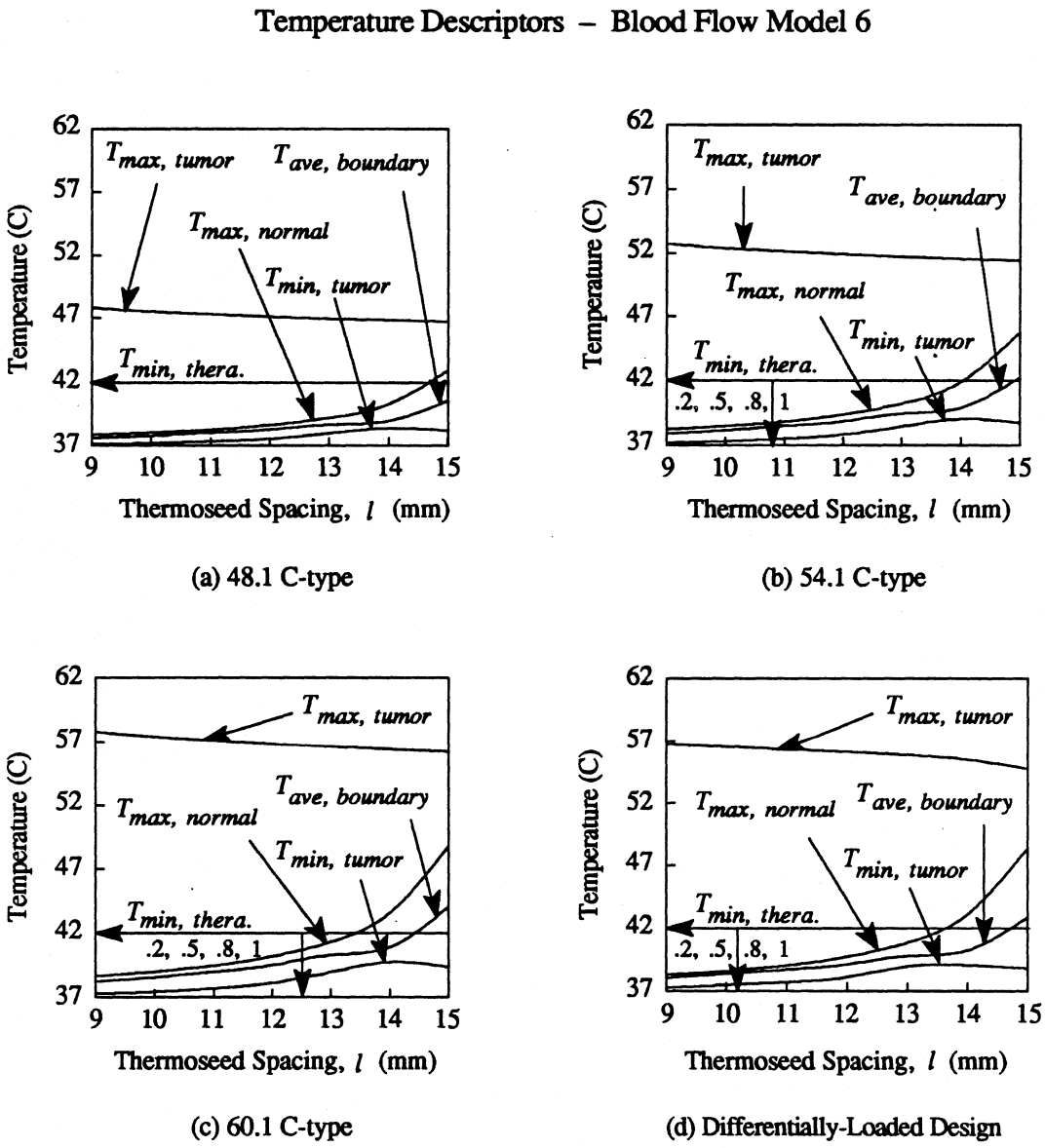

Figure 6.23 Temperature descriptors in tumor and normal tissue versus thermoseed spacing l for arrays of thermoseeds with (a) 48.1 C-type, (b) 54.1 C-type, (c) 60.1 C-type thermoseeds and (d) for the differentially-loaded thermoseed design. Simulations were performed with blood flow model 6 (Table 6.1). The optimum thermoseed spacing as determined by the objective function with $\gamma = 0.2, 0.5, 0.8$ and 1 are labeled in each figure.

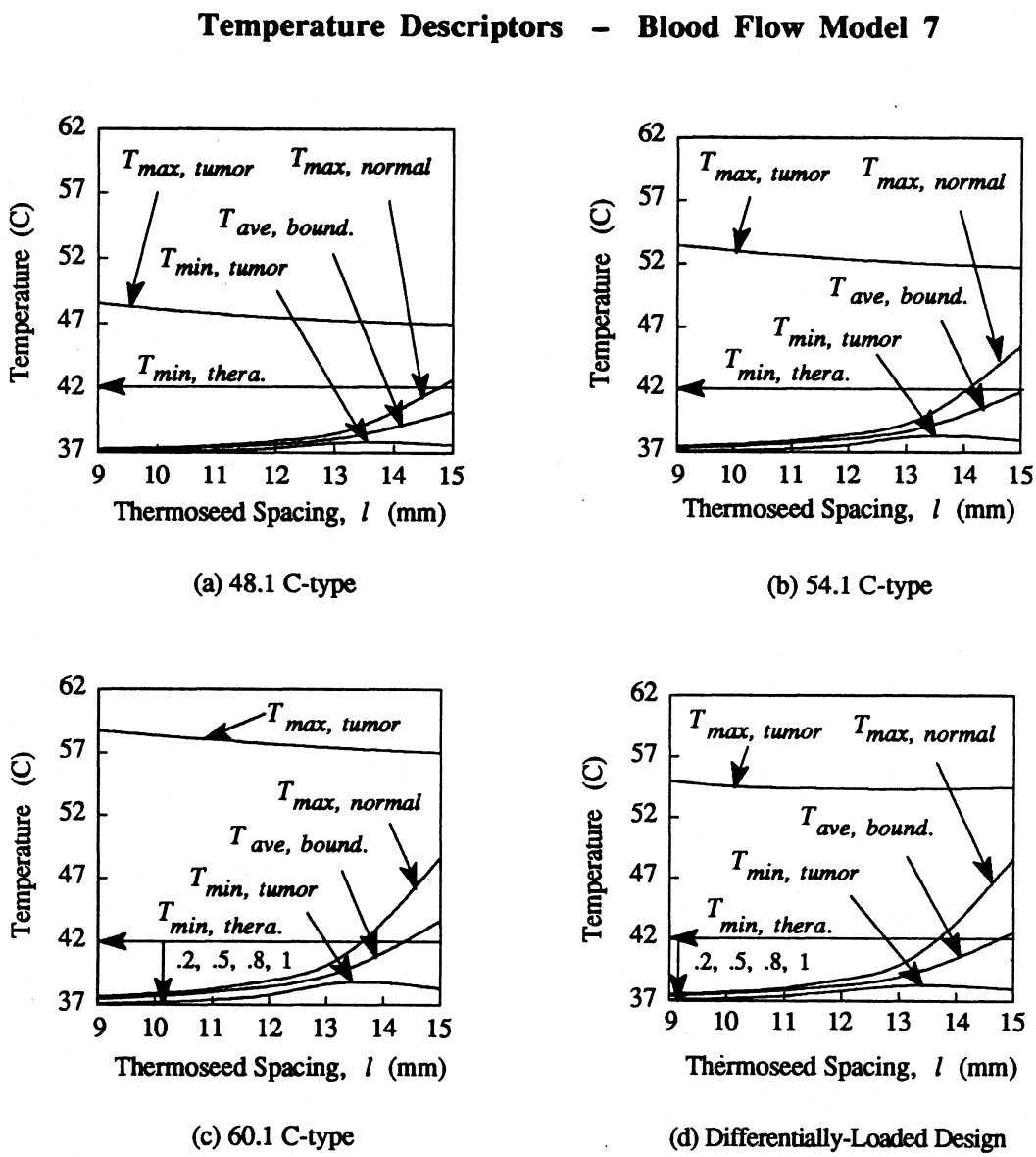

Figure 6.24 Temperature descriptors in tumor and normal tissue versus thermoseed spacing l for arrays of thermoseeds with (a) 48.1 C-type, (b) 54.1 C-type, (c) 60.1 C-type thermoseeds and (d) for the differentially-loaded thermoseed design. Simulations were performed with blood flow model 7 (Table 6.1). The optimum thermoseed spacing as determined by the objective function with $\gamma = 0.2, 0.5, 0.8$ and 1 are labeled in each figure.

6.3.3 Performance of Objective Function

The suitability of the objective function is assessed by determining if the fraction of tumor killed, Ψ_T, using the objective function is larger than Ψ_T using temperature descriptors. Optimal values of thermoseed spacing l in the 60.1 C-type thermoseed design based on maximizing $T_{min,\,tumor}$ and attaining $T_{max,\,normal}$ = 45 C and based on the objective function are shown in Fig. 6.25 for blood flow models 2, 5 and 7. The tumor

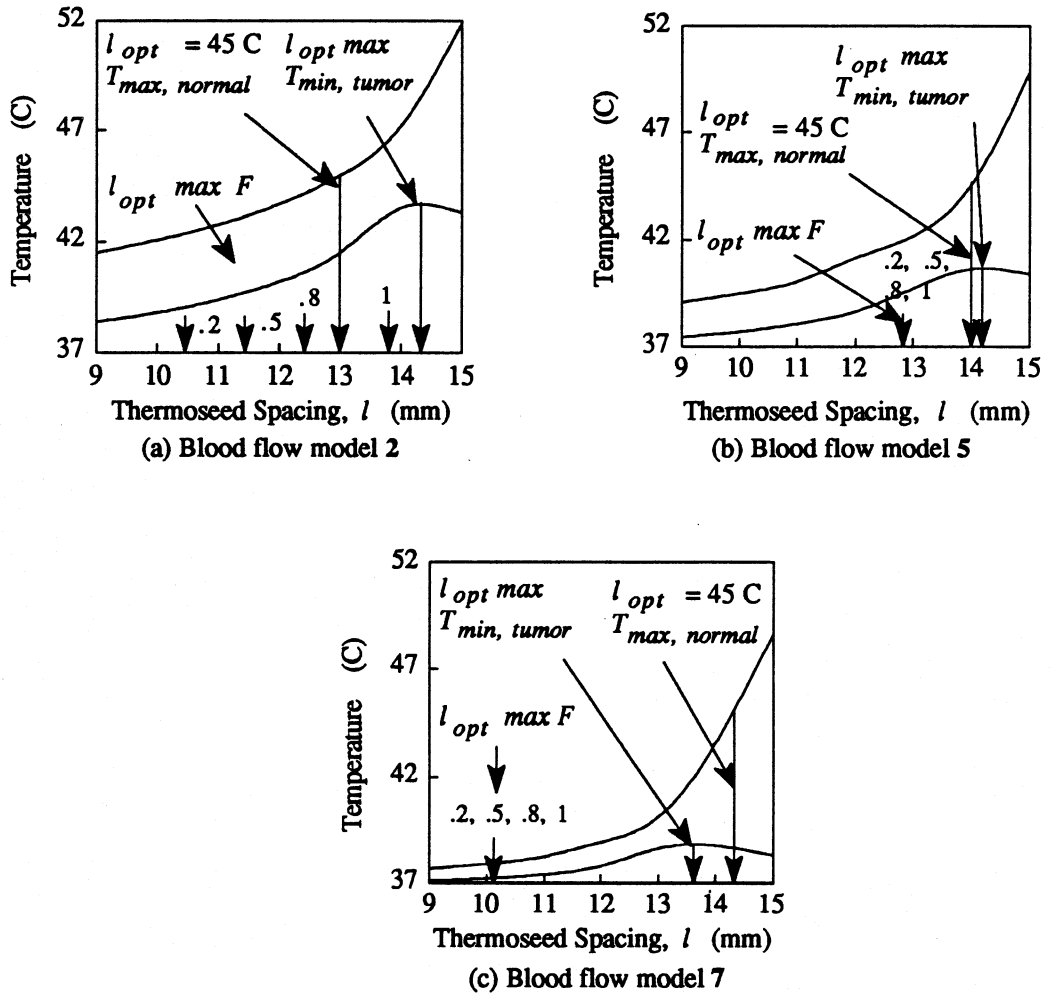

Figure 6.25 Optimum thermoseed spacing l_{opt} of 60.1 C-type thermoseed design based on maximizing $T_{min,\,tumor}$, attaining $T_{max,\,normal}$ = 45 C and based on maximizing the objective function for blood flow models (a) 2, (b) 5 and (c) 7.

fraction killed (Ψ_T) versus thermoseed spacing for the 60.1 C-type design is shown in Fig. 6.26. The optimum seed spacings l_{opt} using the objective function F, maximizing the $T_{min,\ tumor}$ and attaining $T_{max,\ normal}$ = 45 C are shown. With blood flow models 2, 5 and 7, Ψ_T is equal to or higher with l_{opt} using the objective function than with l_{opt} using the temperature descriptors. Indeed, with blood flow model 7, Ψ_T with $l_{opt,\ F}$ is 32% higher than with l_{opt} based on maximizing $T_{min,\ tumor}$ and attaining $T_{max,\ normal}$ = 45 C.

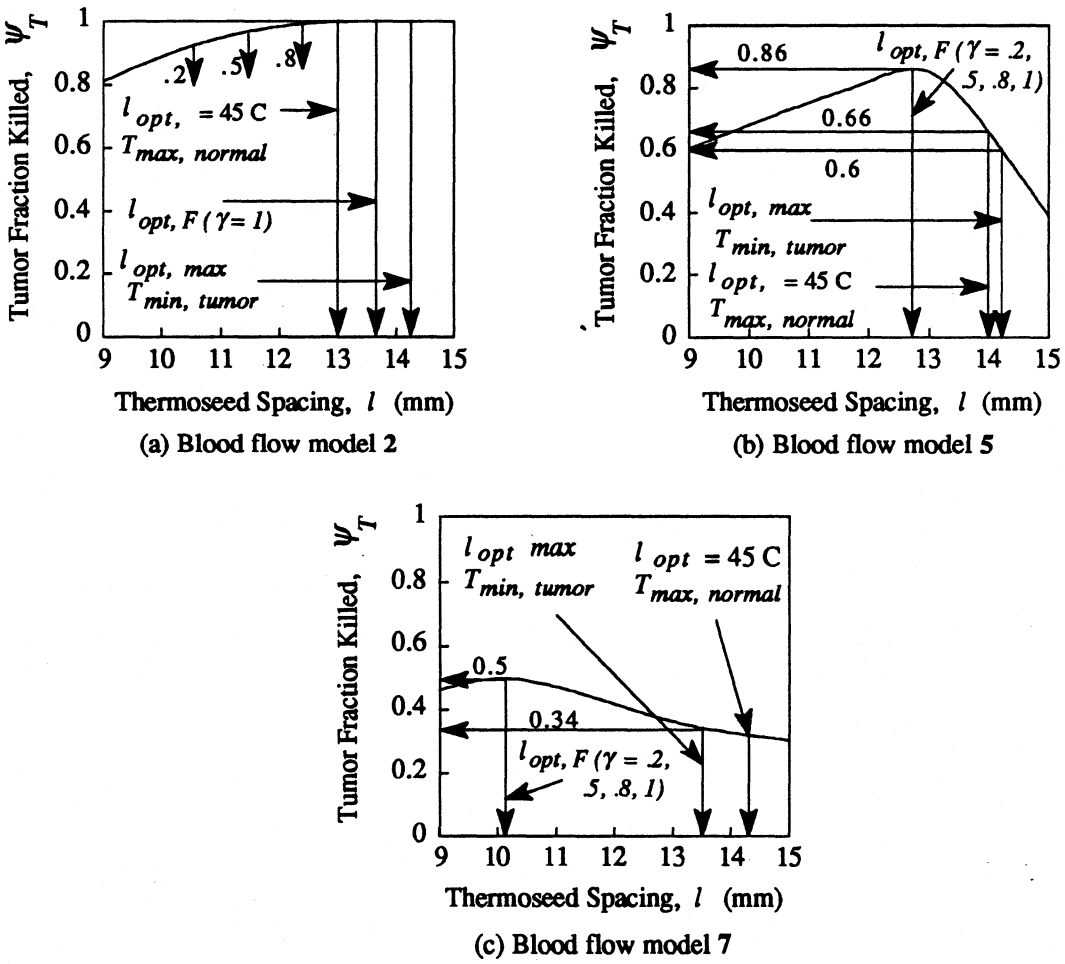

Figure 6.26 Fraction of tumor killed (Ψ_T) versus thermoseed spacing l for the 60.1 C-type thermoseed design with blood flow models (a) 2, (b) 5 and (c) 7. The optimum thermoseed spacing as determined by the objective function with γ = .2, .5, .8 and 1 ($l_{opt,\ F}$), the $T_{min,\ tumor}$ and $T_{max,\ normal}$ ($l_{opt,\ max}$ $T_{min,\ tumor}$ and $l_{opt,\ T_{max,\ normal}}$ = 45 C) temperature descriptors are labeled in each figure.

The results in Fig. 6.26 are *quite* significant. They indicate that the objective function with $\gamma = 1$ selects the thermoseed spacing that maximizes the fraction of tumor killed. Moreover, the objective function out performs the method of choosing optimum thermoseed spacings based on the $T_{min,\ tumor}$ temperature descriptor. In other words, smaller (than the maximum) fractions of tumor would be killed if the pretreatment plan were based on maximizing $T_{min,\ tumor}$ than if the pretreatment plan were based on seed spacings that maximize F with $\gamma = 1$.

The performance of the objective function is also assessed by how well optimum thermoseed designs satisfy $T_{min,\ tumor} > T_{min,\ thera.}$ and $T_{max,\ normal} < 45$ C temperature criteria. The result of whether $T_{min,\ tumor}$ was greater than $T_{min,\ thera.} = 42$ C for the optimum thermoseed designs are in Table 6.6. (The results in Table 6.6 are also valid for $T_{min,\ thera.} = 43$ C, except for blood flow model 3 and $\gamma = 1$.)

Table 6.6 Optimum Thermoseed Designs' Heating of Tumor

Blood Flow Model	$T_{min,\ tumor} > T_{min,\ thera.}$ (= 42 C) ?			
	$\gamma = 0.2$	$\gamma = 0.5$	$\gamma = 0.8$	$\gamma = 1$
1	No	No	No	Yes
2	No	No	No	Yes
3	No	No	No	Yes
4	No	No	No	No
5	No	No	No	No
6	No	No	No	No
7	No	No	No	No

The results in Table 6.6 revealed that if the ferromagnetic hyperthermia treatment plan were designed to maximize Ψ_T ($\gamma = 1$), then the optimum thermoseed design satisfied the $T_{min,\ tumor} > T_{min,\ thera.} = 42$ and 43 C temperature criteria in tumors considered to have a moderate rate of blood flow (models 4 through 7). The $T_{min,\ tumor} > T_{min,\ thera.}$

temperature criteria was not satisfied in tumors considered to have a high rate of blood flow (m_t = 0.25 l/min-kg). However, *none* of the four thermoseed designs with blood flow model 4 through 7 heated the tumor sufficiently to satisfy the $T_{min,\ tumor} > T_{min,\ thera.}$ temperature criteria (recall Figs. 6.21 through 6.24). Recall that in simulations with tumors which had a high rate of blood flow, the weighting factor had no influence on the optimum thermoseed design since F was not near 1. In still other simulations, the $T_{min,\ tumor} > T_{min,\ thera.}$ temperature criteria was not satisfied with any thermoseed spacing and an array of 48.1 C-type thermoseeds with a moderate rate of tumor blood flow (see Figs. 6.18a, 6.19a and 6.20a). Further, recall that F was not near 1 in simulations with arrays of 48.1 C-type thermoseeds (see Figs. 6.2a, 6.3a and 6.4a). Thus it is concluded that the $T_{min,\ tumor} > T_{min,\ thera.}$ temperature criteria can be satisfied with the optimum thermoseed configuration provided that the objective function with γ= 1 is near 1.

The results in Table 6.7 revealed that if the pretreatment plan were designed to minimize Ψ_N (γ = 0.2), then the optimum thermoseed design would satisfy the $T_{max,\ normal} < 45$ C temperature criteria.

Table 6.7 Optimum Thermoseed Designs' Heating of Normal Tissue

Blood Flow Model	$T_{max,\ normal} < 45$ C ?			
	γ = 0.2	γ = 0.5	γ = 0.8	γ = 1
1	Yes	Yes	Yes	No
2	**Yes**	**Yes**	**Yes**	**No**
3	Yes	Yes	Yes	No
4	Yes	Yes	Yes	Yes
5	**Yes**	**Yes**	**Yes**	**Yes**
6	Yes	Yes	Yes	Yes
7	**Yes**	**Yes**	**Yes**	**Yes**

6.4 Summary

Several conclusions are made from the simulations in this chapter. The effect of the tumor survival model (Sec. 6.4.1), the sensitivity of the objective function to weighting factors and blood flow models (Sec. 6.4.2) and the therapeutic assessment of the objective function (Sec. 6.4.3) are discussed.

6.4.1 Tumor Survival Model

The difference between the two tumor survival models had a small effect on the fraction of tumor killed and on the objective function. Average differences in the objective function over thermoseed spacings between 9 and 15 mm with tumor survival models A and B were between 0.8 to 12.9% in simulations over all blood flow models and thermoseed array types. It is concluded that since the hyperthermia cell survival of the tumor can only be approximated, differences, similar to the two models used herein, between the actual and the model of tumor cell survival should have a minimal influence on the objective function.

6.4.2 Sensitivity of Objective Function

Unique and optimal values of the objective function were obtained in the simulations (Figs. 6.2 through 6.8). The weighting factor had some influence on optimum thermoseed spacing (Figs. 6.2, 6.3 and 6.4). The weighting factor had an influence on optimum *l*'s with the 54.1 C- and 60.1 C-type thermoseed designs and the differentially-loaded design and with blood flow models 1, 2 and 3. With higher blood flow models (models 4 through 6), and the compartmentalized tumor blood flow model (model 7), however, the weighting factor had a negligible influence on altering optimum *l*'s.

The optimum thermoseed design is somewhat dependent on the blood flow model (Table 6.4). The optimum thermoseed design for blood flow models 4 through 7 was the 60.1 C-type design, while the 54.1 C-type design and the differentially-loaded designs were optimum with blood flow models 1 and 2. It is therefore critical that the blood flow model be as accurate as possible.

6.4.3 Therapeutic Assessment of Objective Function

It was shown that the objective function was an effective method of choosing optimum thermoseed spacings (Fig. 6.26). It was predicted that smaller (than the maximum) fractions of tumor would be killed if the pretreatment plan were based on maximizing $T_{min,\ tumor}$ or maintaining $T_{max,\ normal}$ = 45 C than if the pretreatment plan were based on maximizing F with γ= 1.

The $T_{min,\ tumor} > T_{min,\ thera.}$ temperature criteria was satisfied by the optimum thermoseed designs in simulations with γ= 1 and where the blood flow in the tumor was low (Table 6.6). The $T_{min,\ tumor} > T_{min,\ thera.}$ temperature criteria was not met, though, by the optimum thermoseed design with γ= 1 and with a high tumor blood flow of m_t = 0.25 l/min-kg. However, in simulations with m_t = 0.25 l/min-kg, the configurations of thermoseeds were inadequate to heat the tumor sufficiently to result in F near 1 when γ= 1. Thus it is concluded that the $T_{min,\ tumor} > T_{min,\ thera.}$ temperature criteria can be satisfied with the optimum thermoseed configuration provided that the objective function F with γ= 1 is near 1. The results in Table 6.7 revealed that if the pretreatment plan were designed to minimize Ψ_N (*i.e.*, maximize F with γ= 0.2), then the optimum thermoseed design would satisfy the $T_{max,\ normal} < 45$ C temperature criteria.

Since the maximum of the objective function selects seed spacings that maximize Ψ_T, it is concluded from the simulations on the simple tissue model that the objective

function is an effective method of selecting optimum thermoseed configurations. Moreover, in addition to the salient features of the objective function summarized in Sec. 5.4, the objective function may have an *advantage* over the method of choosing optimum seed configurations based on $T_{min,\ tumor}$ and $T_{max,\ normal}$ temperature descriptors. That is, since the objective function is a *single-valued* number which can be used to select an optimum seed configuration, one avoids having to decide on the therapeutic trade-off between maximizing $T_{min,\ tumor}$ and minimizing $T_{max,\ normal}$ in order to identify an optimum seed design.

Chapter 7

Performance of Objective Function with Patient-Specific Tissue Model

In this chapter a ferromagnetic hyperthermia treatment plan of a tumor in the human prostate is presented. The finite element software program (FEHT) is used with a human tissue model (Sec. 7.1) to determine temperature distributions and predict the minimum tumor temperature ($T_{min,\ tumor}$) and maximum normal tissue temperatures ($T_{max,\ normal}$). Simulations are performed with several thermoseed combinations and with several constant and temperature-dependent blood flow models (Sec. 7.2). The simulations are performed using a model of a tumor in the prostate since this type of tumor is often treated with brachytherapy. It is shown how the two temperature descriptors ($T_{min,\ tumor}$ and $T_{max,\ normal}$) can be used to identify an optimum combination of thermoseeds *a priori* (Sec. 7.3). Additionally, the objective function (see Chapter 5) is computed, and it is shown how the objective function can be used to replace the temperature descriptor method of identifying the optimum combination of thermoseeds (Sec. 7.3). Some general comments on the temperatures achieved in tissues with constant and temperature-dependent blood flow models are discussed in Sec. 7.4. Concluding remarks are made in Sec. 7.5.

Hyperthermia is usually combined with other forms of cancer therapy. Sometimes hyperthermia is given with brachytherapy. Brachytherapy uses radioactive implants such

as ^{125}I (iodine-125) to kill the malignant tissues. A combined brachytherapy and hyperthermia treatment might proceed as follows. Initially, catheters are placed surgically into the tumor. When the ferromagnetic hyperthermia treatment is given prior to brachytherapy, thermoseeds are placed into catheters and heated thereafter via the inductive heating method described earlier (Sec. 1.5). Since 60 min of heating at steady-state temperatures is the normal treatment time, the ideal hyperthermia treatment usually lasts about 1.17 hours, allowing for 10 min of transient heating at the beginning of the treatment. After the hyperthermia treatment, the thermoseeds are removed from the catheters and replaced by radioactive implants. The brachytherapy treatment can last from several hours to several days depending on the amount of radiation to be delivered.

7.1 Tissue Model Description

A description of the tissue model used in the simulations is described in Sec. 7.1.1. The thermal conductivities and blood flows in the tissue model are discussed in Sec. 7.1.2.

7.1.1 Tissue Model

Several two-dimensional, transverse plane, computerized-tomography (CT) images of the prostate and surrounding normal tissues are shown in Fig. 7.1. Each CT image in Fig. 7.1 is separated by four millimeters in the z-direction. The z-axis is parallel with the long axis of the body. Slices 9 through 16 in Fig. 7.1 proceed in a cephalic (toward the head) to caudal (toward the trunk) direction. The simulations in this chapter are performed on the cross-section shown by the CT image in Fig. 7.2, which is slice 13 in Fig. 7.1, a slice near the midpoint of the prostate.

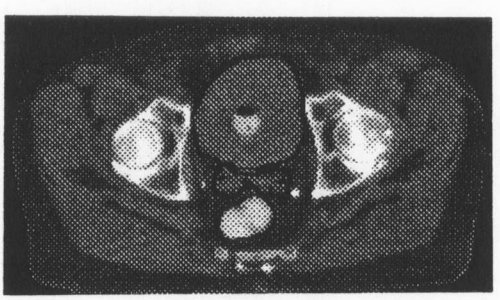

(a) Slice 9

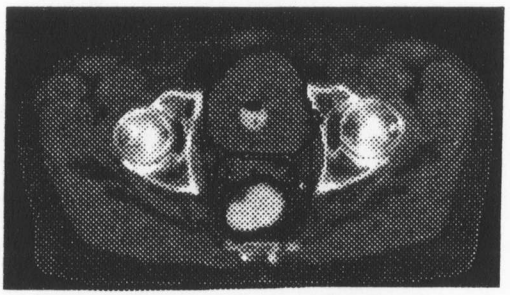

(b) Slice 10

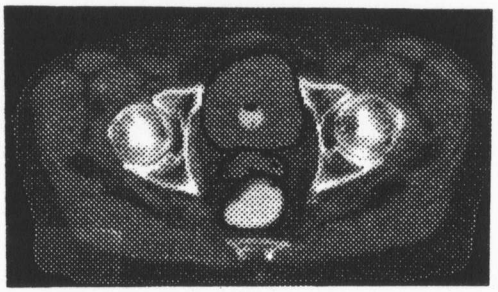

(c) Slice 11

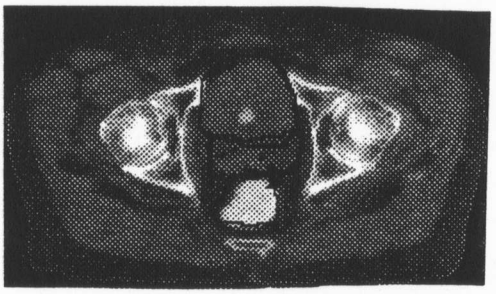

(d) Slice 12

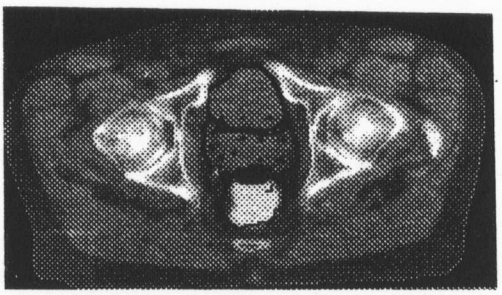

(c) Slice 13

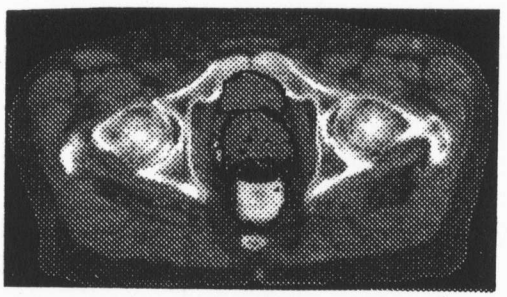

(f) Slice 14

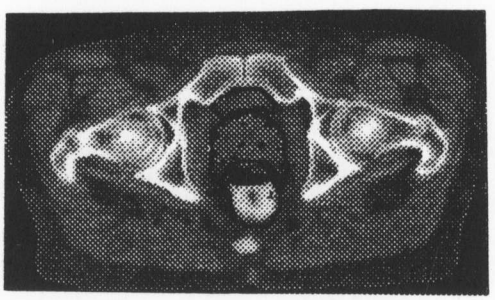

(g) Slice 15

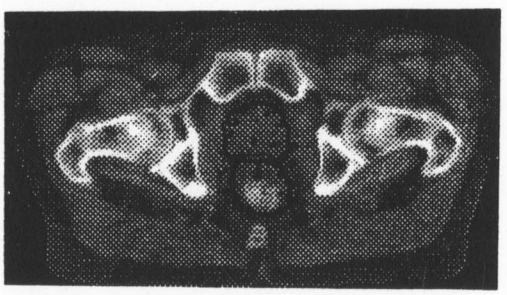

(h) Slice 16

Figure 7.1 Eight computerized tomography (CT) images of a human pelvic region. Slices 9 through 16 are shown in Fig. 7.1a through 7.1h. Each slice is separated by 4 mm in the z-direction. The red-colored contour is the location of the prostate. Cross-hairs designate locations of catheters.

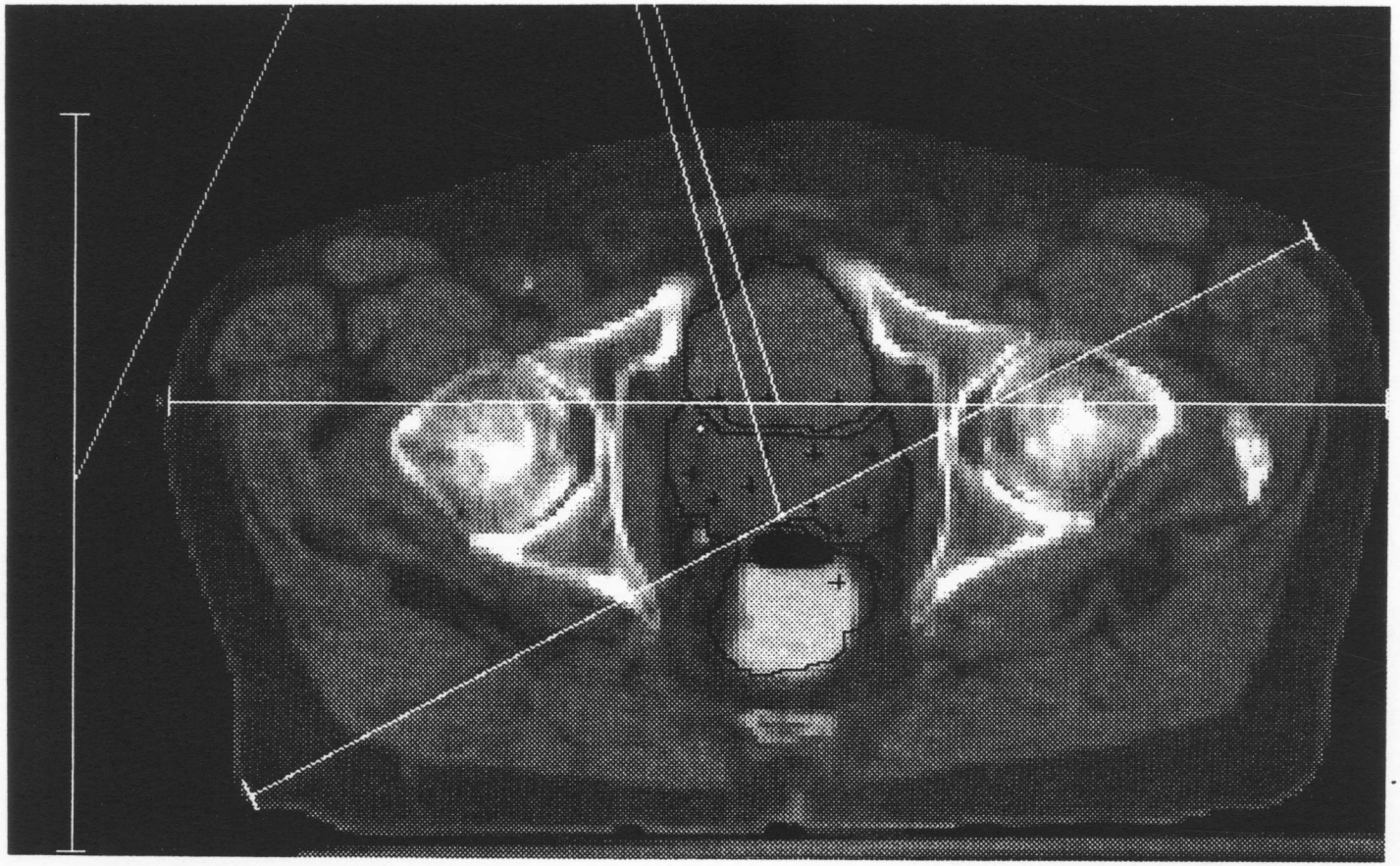

Figure 7.2 Computerized tomography image of slice 13 in Fig. 7.1e. The red-colored contour is the location of the prostate and is contour nearest the center of the image. The green-colored contour defines the bladder and is anterior to (or up from) the prostate. The blue-colored contour defines the rectum and is posterior to (or down from) the prostate. The red-, green- and magenta-colored cross-hairs are locations of catheters. The white-colored lines are length scales. For copies of this figure which appear in black and white, see Fig. 7.3 for tissue identification.

The cross-section in Fig. 7.2 was selected because it had the largest cross-sectional area of the prostate. In addition, it has been suggested that two-dimensional (versus three-dimensional) modeling of ferromagnetic hyperthermia tissue models is adequate so long as the cross-section which is modeled is further than 10 mm from the ends of the thermoseeds (Chin and Stauffer 1991). Also, two-dimensional modeling is justified so long as the thermoseeds are longer than 30 mm and the cross-section is the centrally-located plane (Chen *et al.* 1991). The cross-section in Fig. 7.2 and thermoseed lengths used in this study satisfy these requirements.

In Figs. 7.1 and 7.2, the red-colored contour defines the tumor-containing prostate. The red-colored contour is the contour closest to the center of the image. The bladder is anterior to the prostate (or up from the prostate in Figs. 7.1 and 7.2) and is defined by the green-colored contour. The rectum is posterior to the prostate (or below the prostate in Figs. 7.1 and 7.2) and is outlined by the blue-colored contour. The black-colored area within the bladder is the location of the *in-dwelling* catheter (see slices 9 through 11 in Fig. 7.1). The in-dwelling catheter is placed into the bladder via the urethra prior to treatment for urinary drainage. Since the bladder in Fig. 7.2 is devoid of black- or white-colored areas, the in-dwelling catheter has exited the body superior to the cross section in Fig. 7.2. During the CT scan, the bladder in slices 9 though 13 is filled with liquid. During treatment, however, the bladder will drain due to gravity and will be smaller and will have no urine inside. Thus the bladder region will be modeled as a region of muscle tissue.

The black-colored area near the center of Fig. 7.2 is the location of an air pocket in the rectum (*i.e.*, gas). This air pocket is small relative to the cross-sectional area of the rectum and other tissues. The air pocket is approximately 10 mm in length (z-direction) as evident by CT slices 13, 14 and 15 in Fig. 7.1. In the simulations the air pocket will

be assumed to be rectum and will have thermal properties identical to those of the rectum. By modeling the air pocket as rectal material, the predicted temperature distributions will be lower than they would have been had the air pocket been modeled as a distinct region. In other words, air pockets behave thermally as insulators.

The cross-hairs in Figs. 7.1 and 7.2 are locations of catheters. The red-colored cross-hairs designate catheters which are approximately parallel to the z-axis, the magenta-colored cross-hair designates the *center* catheter which is used as a reference in brachytherapy treatment planning, and the green-colored cross-hairs are catheters that have been *angled* appropriately so as to follow the boundary of the prostate in the third dimension (or z-direction). The locations of 19 catheters are shown in Fig. 7.2. The catheter locations were chosen by medical physicists and the oncologist to obtain an adequate iso-dose distribution of radiation in the prostate. Ten of these catheters are located within the prostate and nine are located within the surrounding normal tissues. Of the catheters in the normal tissues, three are in the bladder and six are located in the rectum and surrounding fatty tissue which is posterior to the prostate. Usually at least two catheters are used for measuring temperatures during the hyperthermia treatment. One of these two catheters is typically located near the center of the prostate, while the other is in the prostate and located near the boundary of the prostate and normal tissues. The maximum number of catheters, therefore, which could be *loaded* with thermoseeds is 17. In the simulations in this chapter, however, the nine catheters in the normal tissues will not be loaded with thermoseeds. Thus a study of the two-dimensional temperature distributions produced by thermoseeds located only within the prostate is possible. In the remainder of this chapter, the tumor-containing prostate will be referred to simply as the *tumor*.

Several steps were performed to transfer the tissue contours and catheter locations shown in Fig. 7.2 into the FEHT program. First, the CT image was scanned digitally with DeskScan (Hewlett-Packard Co., Palo Alto, CA) and a Macintosh II computer. DeskScan created a PICT file which was later *opened* within the software drawing program McDraw Pro (Claris Corp., Santa Clara, CA). Within McDraw Pro, the polygon feature was used to trace the tissue contours, catheter locations and the vertical length scale shown in Fig. 7.2. These tracings were then transferred into FEHT via the Macintosh clipboard feature.

Using the traces created by McDraw Pro as a template, the scale of the tissue model was specified and the contours of the tissues were drawn with FEHT (recall Sec. 2.3) (Fig. 7.3). Earlier studies and clinical experience have shown that often, the inner core of the tumor is a tough, fibrous tissue and may have a blood flow that differs vastly from the outer periphery of the tumor. Thus the tumor was modeled as two distinct regions consisting of an inner core and an outer periphery. The boundary between the core and periphery was arbitrarily chosen. A finite element mesh in the normal tissues was then created using algorithms and menu items within FEHT (Sec. 2.3).

Using the 'Add Seed' pull-down menu item in FEHT (Sec. 3.4), models of eight thermoseeds within catheters (0.35 mm-wall) (Sec. 3.2.3) were placed within the tumor at the location of the cross-hairs. The locations of the eight thermoseeds are the black-colored circles 1 through 5, 7, 9 and 10 in Fig. 7.3. The locations of the two temperature-monitoring catheters are shown by circle 6 in the tumor periphery and circle 8 in the tumor core (Fig. 7.3). The finite element mesh in the tumor was created thereby completing the entire finite element mesh of the tissue model. The complete finite element mesh of the tissue model and thermoseeds is shown in Fig. 7.4.

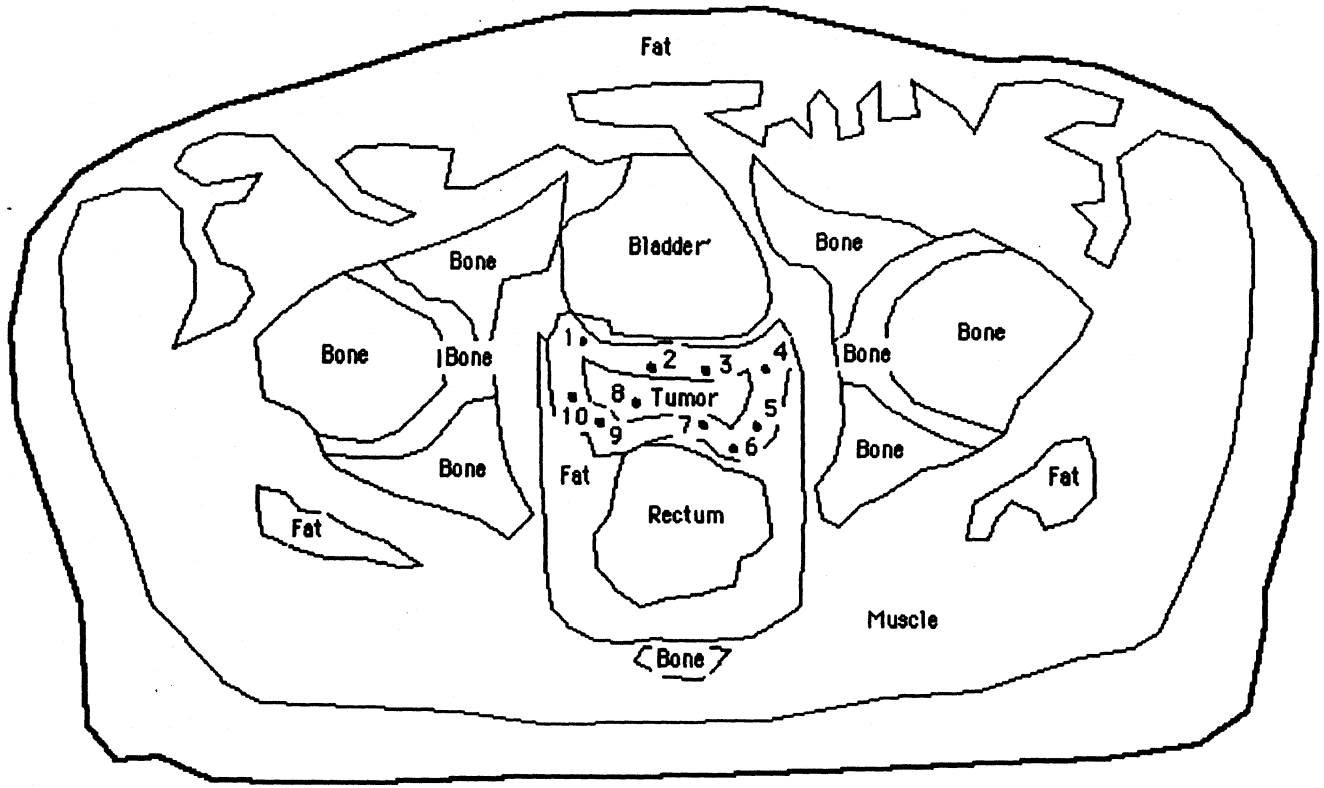

Figure 7.3 Contours of tissues and locations of thermoseeds used in simulations. The tumor (*i.e.*, prostate) is modeled as two distinct regions consisting of an inner core and an outer periphery. The black-colored circles 1-5, 7, 9 and 10 in the outer periphery of the tumor are the locations of the thermoseeds. Circles 6 and 8 are the locations of the catheters used for temperature measurements. The tissue contours and simulated thermoseeds were created with FEHT using the CT image of Fig. 7.2 as a template.

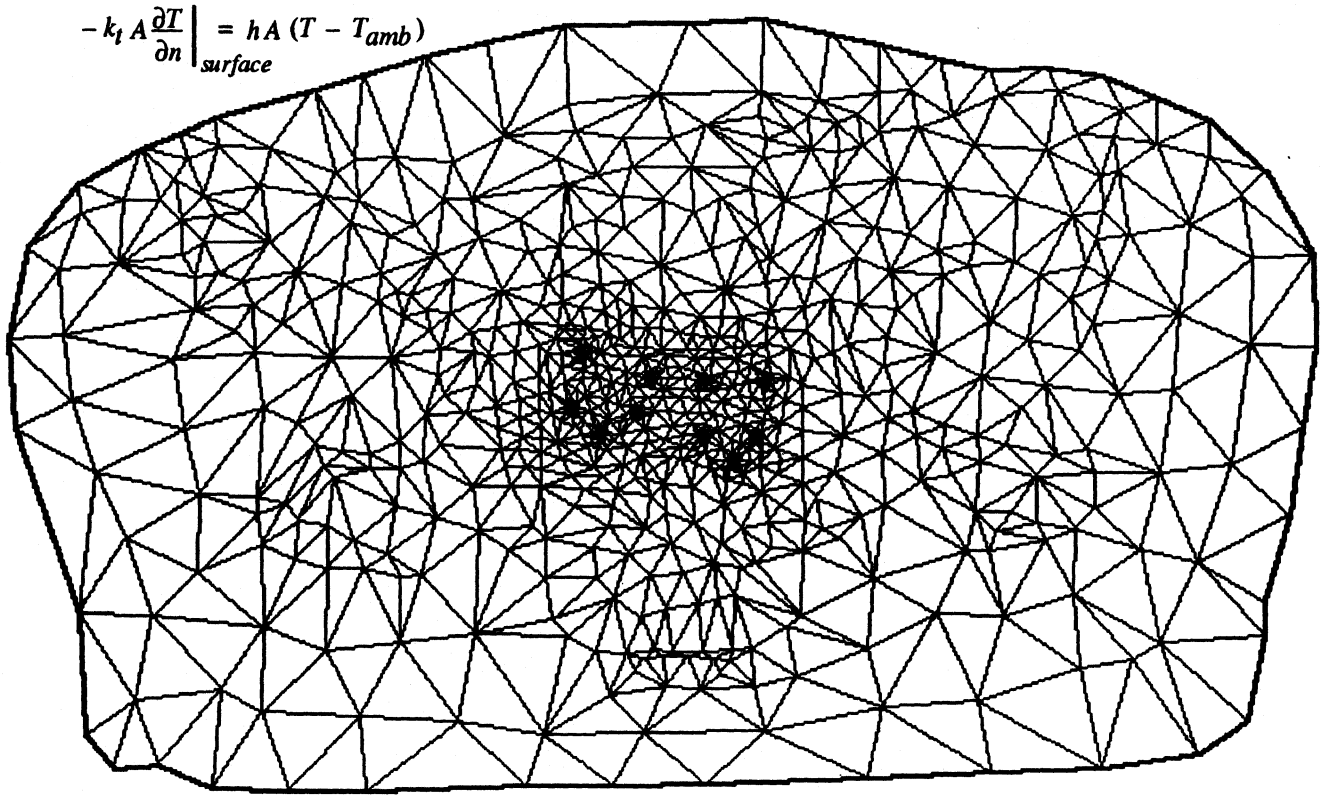

Figure 7.4 The finite element mesh of the tissue system shown in Fig. 7.3. The finite element mesh was created with FEHT. The mesh contains models of eight thermoseeds and two catheters for thermometry. There is a convection boundary condition on the outer surface with $h = 5$ W/m^2-C and $T_{amb} = 25$ C. The thermoseeds have a heat flow P' at their boundaries as described earlier (Fig. 3.5).

FEHT was used to solve Eqs. 2.2 and 5.6 to predict the temperature distribution and compute the objective function. The dodecagonal thermoseed model was used in the simulations (Sec. 3.2.3). The eight simulated thermoseeds had a heat flow P' at their boundaries as described earlier (Fig. 3.5 and Eq. 4.5d). The two simulated catheters used for monitoring temperatures were modeled as thermoseeds without energy generation. Boundary conditions for the tissue model included a convection boundary on the outer surface with h = 5 W/m^2-C and T_{amb} = 25 C. All tissues in the model were perfused by blood at T_b = 37 C. The thermal conductivities and blood flows of all tissues in the model are discussed in Sec. 7.1.2.

7.1.2 Thermal Conductivity and Blood Flow

The thermal conductivities of tumors have been measured. Jain *et al.* (1979) measured the thermal conductivity of a tumor of mammary origin-Walker 256 carcinoma using a noninvasive probe technique. Bowman (1980) has also measured thermal conductivity of tumors using invasive-probe techniques. These thermal conductivities are compiled in Table 7.1.

Blood flow rates of various animal and human tumors at normal body temperature are given in Table 7.2. In general, the average perfusion rates of tumors are less than those of normal tissues, with the exception of a canine lymphosarcoma.

Table 7.1 Thermal Conductivity of Various Animal & Human Tumors
(A reprint of Table 3 in Chapter 16 of *Heat Transfer in Medicine & Biology*, Shitzer & Eberhart, eds., Plenum Press, 1985.)

Species	Tumor Type	Thermal Conductivity, k_t (W/m-C)
Rat	Walker 256 carcinoma	0.32
Human	Breast	
	Normal atrophic tissue	0.499
	Scirrhous carcinoma	0.397
	Mucinous (colloid) carcinoma	0.527
	Colon	
	Normal	0.556
	Metastatic colonic carcinoma	0.556
	Liver	
	Normal	0.572
	Metastatic colonic carcinoma	0.52
	Normal	0.508
	Metastatic pancreatic cancer	0.562
	Lung	
	Normal	0.518
	Squamous cell	0.666
	Pancreas	
	Normal	0.345
	Metastatic carcinoma	0.478
	Normal	0.468
	Metastatic gastric cancer	0.492
	Other	
	Acoustic Schwannoma	0.581

Table 7.2 Blood Flow Rates of Animal & Human Tumors
(A reprint of Table 4 in Chapter 16 of *Heat Transfer in Medicine & Biology*, Shitzer & Eberhart, eds., Plenum Press, 1985.)

Tumor	Species	Blood Flow, m (l/min-kg)
Hepatoma 5123	Rat	0.1 - 0.17
Novikoff hepatoma	Rat	0.02 - 0.05
Walker 256 carcinoma	Rat	0.03 - 0.1
Walker 256 carcinoma	Rat	0.16 - 0.48
Sarcoma	Rat	0.04 - 0.21
Sarcoma	Rat	0.22 - 0.58
DS-carsinosarcoma	Rat	0.07 - 0.32
Yoshida sarcoma	Rat	0.07
Nerve and brain tumors	Rat	0.44 - 0.79
Guerin carcinoma	Rat	0.20 - 0.21
DMBA-induced adenocarcinoma	Rat	0.025
Melanoma	Hamster	0.6
Cervical carcinoma	Hamster	0.22
Sarcoma	Mouse	0.01 - 0.22
Sarcoma	Mouse	0.04 - 0.19
Sarcoma	Mouse	0.07 - 0.14
Mammary carcinoma	Mouse	0.01 - 0.17
VX-2 carcinoma	Rabbit	0.24 - 1.13
Lymphosarcoma	Dog	0.63 - 3.4
Lymphoma	Human	0.34
Anaplastic carcinoma	Human	0.15
Differentiated tumors	Human	0.23
Liver carcinoma	Human	0.12

The numerical values of tissue thermal conductivity and blood flow used in the simulations are shown in Table 7.3. The thermal conductivities of the tissues are assumed to be independent of temperature over the hyperthermia temperature range. The thermal conductivity of the tumor (k_t = 0.64 W/m-C) was assumed to be equal to muscle tissue (Appendix 2 in Shitzer and Eberhart 1986) and is near that of the squamous cell of the lung (Table 7.1).

Table 7.3 Thermal Conductivity and Blood Flow of Tissues

Tissue/Material Type	Thermal Conductivity, k_t (W/m-C)	Volumetric Blood Flow, m (l/min-kg)	Tissue Density, ρ_t (kg/m^3)	Perfusion, $w_b c_b$ (W/m^3-C)
Bladder* (empty) (muscle tissue)	0.64	Table 7.4	1080	Fig. 7.6a
Rectum*	0.64	–	-	–
Bone	1.16 (1)	6.7e-3 (5)	1500 (1)	690
Fat	0.19 (2)	1.84e-2 (6)	850 (1)	1078
Muscle	0.64 (3)	Table 7.4	1080 (1)	Fig. 7.6a
Tumor*				
Core	0.64	Table 7.4	1080	Fig. 7.6b
Periphery	0.64	Table 7.4	1080	Fig. 7.6c
Catheter	0.34 (4)	–	–	–

*Assumed to have the properties of muscle tissue.

1 - Gordon *et al.* 1976
2 - Cooper and Trezek 1971
3 - Nevins and Darwish 1970
4 - Clay Adams Co. 1991
5 - Root 1963
6 - Nielsen 1972

It is known that blood flow in tissues can depend strongly on temperature. Song *et al.* (1984) has plotted the *relative* change in blood flow in the muscle of rats and that in animal tumors after heating for 30 to 40 min at various temperatures (Fig. 7.5). The *relative* change in blood flow is the ratio of blood flow at elevated temperatures to the blood flow before heating.

The relative change in blood flow (Fig. 7.5) was transformed into blood flow with dimensional units by assuming that the volumetric flow rate of blood per unit mass, m in Eq. 2.1, in muscle before heating is 0.027 l/min-kg (Lassen *et al.*, 1964). The mass flow rate of blood per unit volume multiplied by the specific heat of blood, $w_b c_b$ in Eq. 2.2, was then determined by multiplying m by the density ρ_t of muscle tissue (1080 kg/m^3), the density ρ_b of blood (1060 kg/m^3) and the specific heat c_b of blood (3900 J/kg-C).

Calculations like this were performed to determine tissue perfusion values $w_b c_b$ in the last column of Table 7.3. As will be seen, similar calculations were performed to determine the tissue perfusion values in Fig. 7.6 from the data in Fig. 7.5.

Models of temperature-dependent blood flow rates in the muscle and tumor were obtained from approximations of the data in Fig. 7.5. The core of a tumor is generally believed to be a *necrotic* region and thus to have a low rate of blood flow. Since the periphery of a tumor usually has more blood vessels than the core, the tumor periphery is generally considered to have a higher rate of blood flow than the tumor core. Thus the

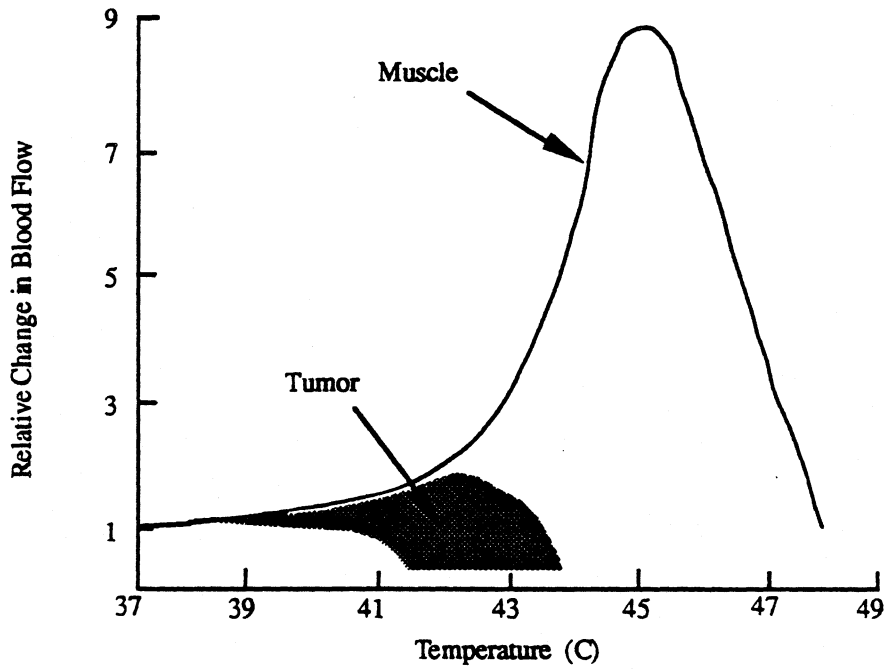

Figure 7.5 Temperature-dependent changes in the relative blood flow rates for muscle and animal tumors (A reprint of Fig. 3 in Song *et al.* 1984).

temperature-dependent blood flow model for the core of the tumor was obtained by approximating the lower edge of the shaded region in Fig. 7.5 and is shown in Fig. 7.6b. The temperature-dependent, *low*-rate blood flow model of the tumor periphery was ob-

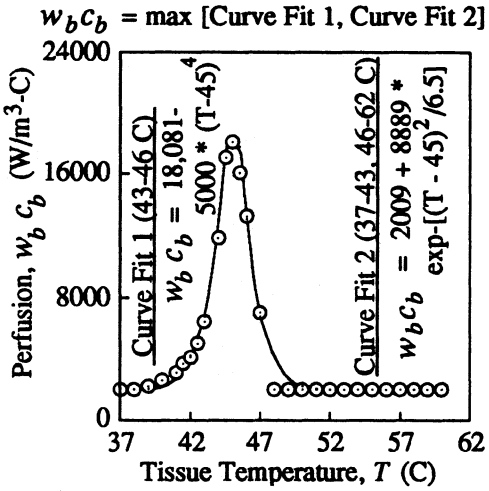

(a) Muscle tissue and *high*-rate blood flow model of tumor periphery

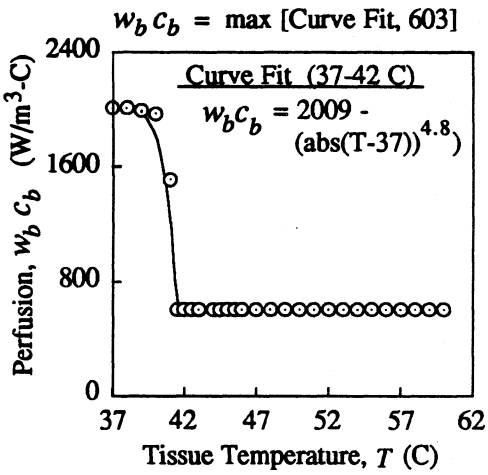

(b) Tumor core

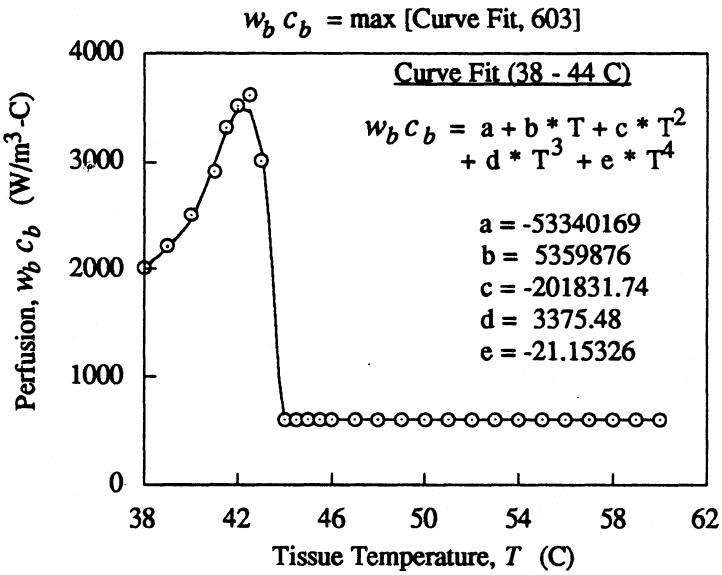

(c) *Low*-rate blood flow model of tumor periphery

Figure 7.6 Models of temperature-dependent perfusion for (a) muscle tissue and the *high*-rate blood flow of the tumor periphery, (b) the tumor core and (c) *low*-rate blood flow of the tumor periphery. The circles are data from the curves in Fig. 7.5 and the solid lines are approximations of that data. The perfusion $w_b c_b$ was obtained by determining the maximum of (a) two curve fits or (b and c) a curve fit and a constant as shown above each figure.

tained by approximating the upper edge of the shaded region in Fig. 7.5 and is shown in Fig. 7.6c. The temperature-dependent blood flow model for normal muscle tissue and the temperature-dependent, *high*-rate blood flow model of the tumor periphery were determined by approximating the curve for muscle tissue in Fig. 7.5 as shown in Fig. 7.6a. The numerical values of the blood flow in the tumor core and periphery are within the range of the blood flows shown in Table 7.2.

The data in Figs. 7.6a, b and c are approximated by curve fits. The perfusion term $w_b c_b$ for muscle tissue was obtained by determining the maximum of two curve fits. The perfusion term for the tumor was obtained by determining the maximum of a curve fit and a constant. The expressions for evaluating the perfusion term are shown above Figs. 7.6a, b and c. These expressions are used in an algorithm within FEHT (Klein *et al.* 1988) to evaluate the local blood flow as a function of temperature.

7.2 Simulations

A study was performed to determine an adequate choice for the discretization of the finite element mesh. Results from the discretization study are discussed in Sec. 7.2.1. Simulations were performed on the tissue model shown in Fig. 7.3 for six blood flow models and seven thermoseed combinations. The blood flow models are discussed in Sec. 7.2.2, and the thermoseed combinations are presented in Sec. 7.2.3.

7.2.1 Finite Element Mesh Discretization

The temperature distribution computed with the finite element technique will depend on the level of discretization of the finite element mesh. An adequate discretization of the finite element mesh shown in Fig. 7.4 was determined by studying the effect of successively smaller discretizations. The smaller discretizations were

concentrated in the vicinity of the thermoseeds, the tumor, and the boundary between the tumor and normal tissues. Simulations were performed with meshes of 1680, 1804 and 1904 finite elements. Simulations were conducted with uniform blood flow rates of m = 0.027 and 0.27 l/min-kg in the muscle and tumor. All eight thermoseeds (1-5, 7, 9 and 10 in Fig. 7.3) had operating temperatures of 54.1 C in simulations with the blood flow of 0.027 l/min-kg and 60.1 C in simulations with the blood flow of 0.27 l/min-kg.

The effect of finite element discretization on the solution was evaluated. The percentage of tumor above temperatures between 42 and 50 C is shown in Fig. 7.7. The maximum and minimum tumor temperature ($T_{max,\ tumor}$ and $T_{min,\ tumor}$), the maximum normal tissue temperature ($T_{max,\ normal}$), and the average temperature of the tumor ($T_{ave,\ tumor}$) and the average temperature on the boundary between the tumor and normal tissues ($T_{ave,\ boundary}$) are illustrated in Fig. 7.8. Last, the objective function is displayed in Fig. 7.9. A mesh of 1904 elements satisfies the requirement for convergence of the numerical

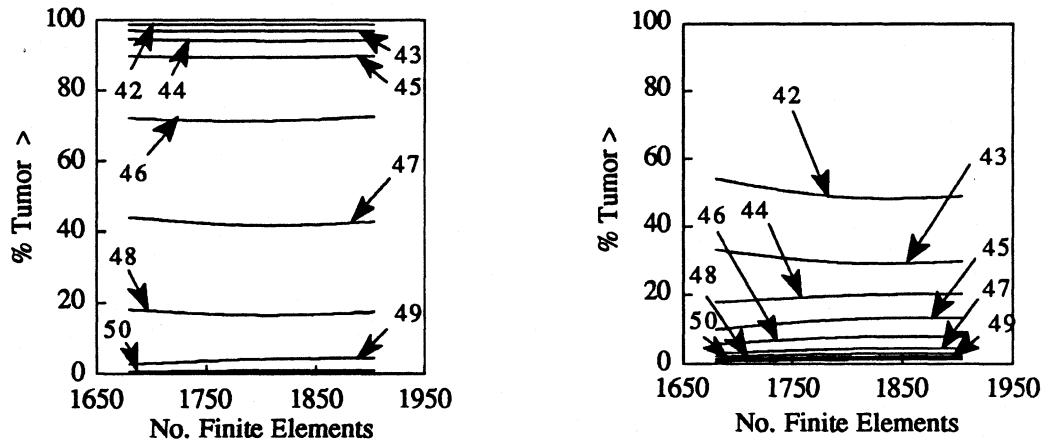

(a) m = 0.027 l/min-kg (b) m = 0.27 l/min-kg

Figure 7.7 Effect of finite element mesh discretization on percentage of tumor greater than temperatures between 42 and 50 C. The simulations were performed with a uniform blood flow rate in the tumor and muscle tissue of (a) 0.027 l/min-kg and (b) 0.27 l/min-kg. Thermal conductivity and blood flow in other tissues are in Table 7.3. Operating temperatures of all thermoseeds were (a) 54.1 C and (b) 60.1 C.

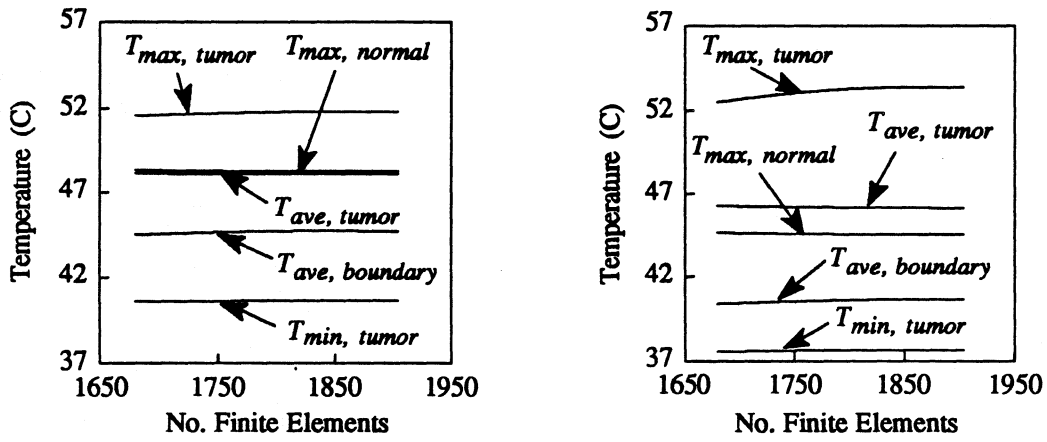

(a) m = 0.027 l/min-kg (b) m = 0.27 l/min-kg

Figure 7.8 Effect of finite element mesh discretization on several temperature descriptors including $T_{max,\ tumor}$, $T_{max,\ normal}$, $T_{ave,\ tumor}$, $T_{ave,\ boundary}$ and $T_{min,\ tumor}$. The simulations were performed with a uniform blood flow rate m in the tumor and muscle of (a) 0.027 l/min-kg and (b) 0.27 l/min-kg. Thermal conductivity and blood flow in other tissues are in Table 7.3. Operating temperatures of all thermoseeds were (a) 54.1 C and (b) 60.1 C.

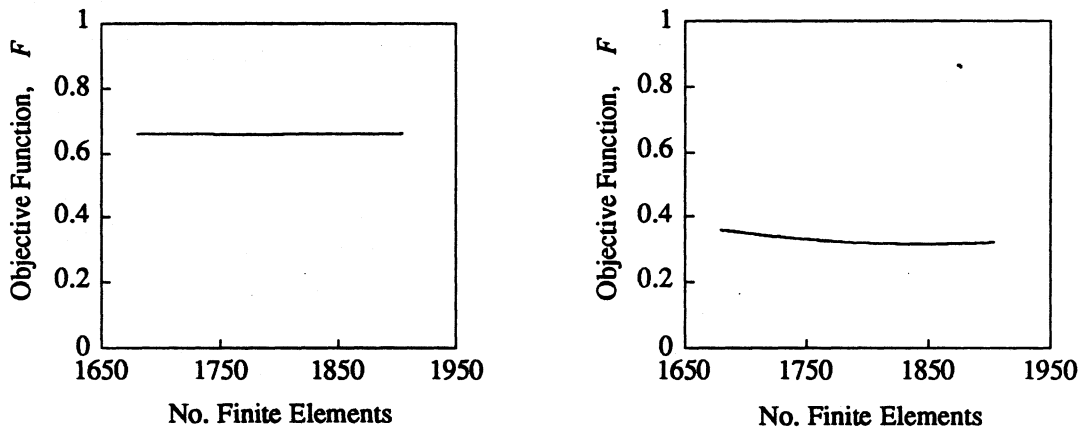

(a) m = 0.027 l/min-kg (b) m = 0.27 l/min-kg

Figure 7.9 Effect of finite element mesh discretization on objective function. In the simulations, $T_{min,\ thera.}$ = 42 C, γ = 0.8 and the uniform blood flow rate m in the tumor and muscle tissue was (a) 0.027 l/min-kg and (b) 0.27 l/min-kg. Thermal conductivity and blood flow in other tissues are in Table 7.3. Operating temperatures of all thermoseeds were (a) 54.1 C and (b) 60.1 C.

solution, since, at this discretization, all curves in Figs. 7.7, 7.8 and 7.9 are flat. The simulations in this chapter are, therefore, performed with a mesh of 1904 finite elements.

In contrast to the finite element mesh in Fig. 7.4, it would have been possible to perform the simulations in this chapter with an outer-edge boundary just a few millimeters greater than the T_b contour. Isotherms are shown in Fig. 7.10 for a simulation with 60.1 C-type thermoseeds and a constant blood flow model (seed blood flow model 2 in Sec. 7.2.2). The T_b (= 37 C) contour is approximately 70 mm from the outer edge of the tumor. If the simulation had been performed with an outer edge slightly larger than the T_b contour, the outer-edge boundary condition would have been $T_{outer\ surface} = T_b$.

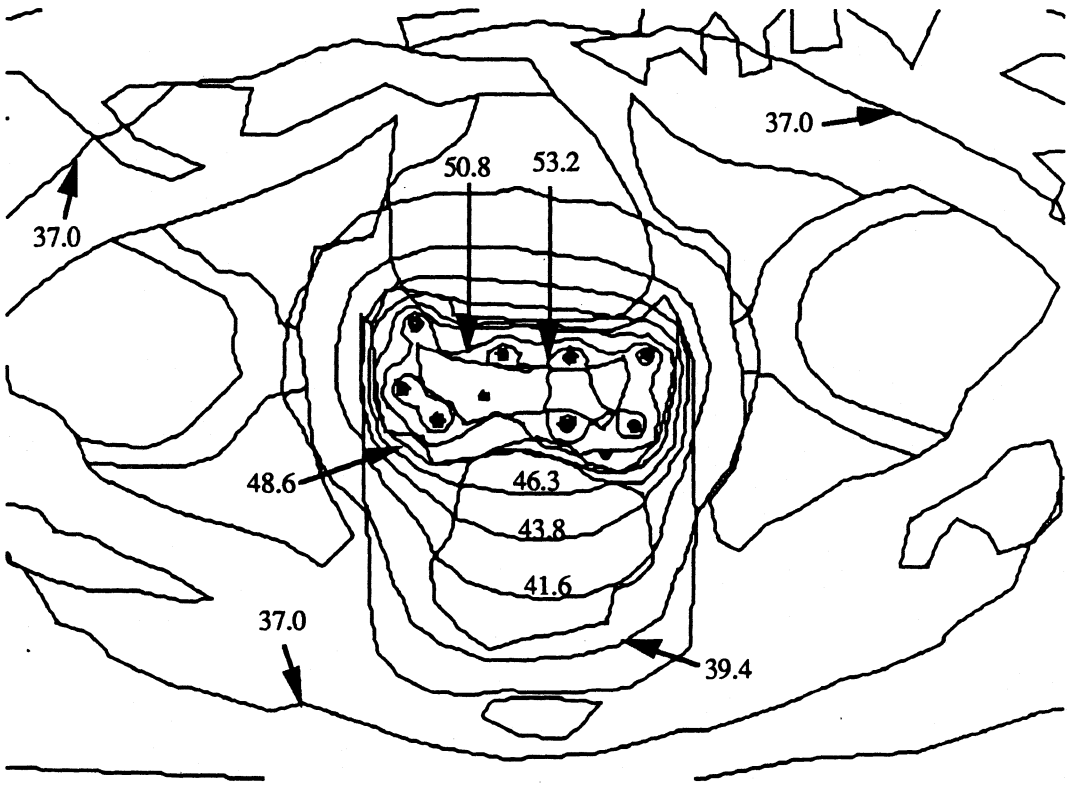

Figure 7.10 Isotherms (C) from a simulation with 60.1 C-type thermoseeds and blood flow model 2 (see Sec. 7.2.2). Thermal conductivity and blood flow in other tissues are in Table 7.3. The isotherms were created with FEHT. The mesh contains eight simulated thermoseeds and two catheter models for thermometry. There is a convection boundary condition on the outer surface with h = 5 W/m^2-C and T_{amb} = 25 C (see Fig. 7.4). The thermoseeds had a heat flow P' at their boundaries as described earlier (Fig. 3.5 and Eq. 4.5d).

7.2.2 Blood Flow Models

Simulations were performed with six blood flow models[16]. Blood flow models 1 through 4 assume that blood flow is independent of temperature while blood flow models 5 and 6 are temperature-dependent (Table 7.4). Blood flow model descriptions are:

Blood flow model 1

Assumes the blood flow in the tumor is a constant m_t = 0.027 l/min-kg (which is equivalent[17] to $w_b c_b$ = 2009 W/m^3-C) and equal to the blood flow in normal muscle tissue at body temperature of T_b (= 37 C).

Blood flow model 2

Studies the effect of a necrotic tumor core. The blood flow in the tumor core is a constant m_t = 0.008 l/min-kg (equivalent to $w_b c_b$ = 600 W/m^3-C) which is equal to the flat, lower portion of the curve in Fig. 7.6b.

Blood flow model 3

Studies the influence of highly perfused, constant blood flow in normal muscle tissue. The blood flow in the muscle tissue is nine times higher than in the tumor and is equal to the maximum of the curve in Fig. 7.6a (m_{muscle} = 0.243 l/min-kg which is equivalent to $w_b c_b$ = 18,081 W/m^3-C).

Blood flow model 4

Investigates the effect of highly perfused muscle tissue *and* tumor periphery. The blood flow in the tumor periphery is a constant $m_{t,\,periphery}$ = 0.243 l/min-kg and assumed equal to that in the muscle tissue.

Blood flow model 5

The blood flows in the tumor core, tumor periphery and normal muscle tissue are *temperature-dependent.* Models for the blood flow are shown in Fig. 7.6a, b, and c. The tumor periphery has a *low*-rate blood flow model (Fig. 7.6c)

Blood flow model 6

The blood flows in the tumor core, tumor periphery and normal muscle tissue are *temperature-dependent.* Models for the blood flow are shown in Fig. 7.6a and b. The tumor periphery has a *high*-rate blood flow model and is identical to that of the normal muscle tissue (Fig. 7.6a).

---

[16]The blood flow models used in simulations in this chapter differ from the seven blood flow models used previously in Chapter 6.

[17]Assuming that ρ_t = 1080 kg/m^3, ρ_b = 1060 kg/m^3 and c_b = 3900 J/kg-C.

Table 7.4 Tumor and Normal Muscle Blood Flow Models Used in Simulations (The blood flow in all other tissues is given in Table 7.3.)

Blood Flow Model	Temperature Dependent?	Blood Flow Rate (l/min-kg)		
		Tumor		Normal Muscle
		Core, $m_{t,\ core}$	Per., $m_{t,\ periph.}$	Tissue*, m_n
1	No	0.027	0.027	0.027
2	No	0.008	0.027	0.027
3	No	0.027	0.027	0.243
4	No	0.027	0.243	0.243
5	Yes	Fig. 7.6b	Fig. 7.6c	Fig. 7.6a
6	Yes	Fig. 7.6b	Fig. 7.6a	Fig. 7.6a

* The blood flow rate in muscle was taken from Lassen *et al.*, 1964.

Blood flow models 1 through 6 were designed to study the influence of blood flow on temperature distributions and the objective function. The blood flow in model 1 is constant and assumed equal to the blood flow at normal body temperature. Results from simulations with blood flow model 2 will be compared with those of model 1 to study the effect of modeling the tumor core with a blood flow rate that is lower than the tumor periphery (Sec. 7.4.1). The blood flow in normal muscle tissue of model 3 is constant and equal to the maximum of the temperature-dependent blood flow rate in normal muscle tissue of model 5. Results from the simulations of blood flow model 3 will, therefore, provide an upper limit of the cooling effect expected from a constant, high rate of blood flow. Results from simulations with model 5 will be compared with those of model 3 to assess the influence of temperature-dependent versus constant, highly-perfused normal muscle tissue (Sec. 7.4.2.1). The blood flow in the normal muscle *and* tumor periphery of blood flow model 4 is equal to the maximum of the temperature-dependent blood flow in normal muscle tissue. Results from simulations with model 6 will be compared with

those of model 4 to study the effect of modeling temperature-dependent blood flow versus constant, highly-perfused blood flow in normal muscle tissue *and* the tumor periphery (Sec. 7.4.2.2).

The results from the simulations with the six blood flow models are studied independently and comparatively to elucidate the effects of various blood flow models on temperature distributions and the objective function. However, the blood flow in real tissue systems is generally believed to be temperature-dependent. Thus blood flow models 5 and 6 are considered the models which most closely represent the blood flow in real tissue systems[18].

7.2.3 Thermoseed Combinations

Simulations were performed with seven combinations of thermoseeds (Table 7.5). Combinations 1, 4 and 7 have thermoseeds with operating temperatures of 48.1, 54.1 and 60.1 C, respectively. Combination 2 contains four 48.1 C-type thermoseeds and four 54.1 C-type thermoseeds. Combination 2 is considered the *differentially-loaded* design because it has thermoseeds with different operating temperatures. The four 54.1 C-type thermoseeds in combination 2 were placed in catheters near the four corners of the tumor periphery (locations 1, 4, 5 and 9 in Fig. 7.3). Placing high-temperature versus low-temperature thermoseeds in the corners of the tumor may increase tumor temperatures beyond the outer edge of the thermoseed array. Combination 3 is studied to determine whether a design of thermoseeds at one temperature, the average temperature of thermoseeds in combination 2, performs better than the differentially-loaded design of

[18]Blood flow models 5 and 6 will appear in bold type in the remainder of this chapter as they are considered the models which most closely represent the blood flow in real tissues.

Table 7.5 Thermoseed Combinations used in Simulations

Thermoseed Combination	Thermoseed Operating Temperature*							
	1	2	3	4	5	7	9	10
1	48.1	48.1	48.1	48.1	48.1	48.1	48.1	48.1
2	54.1	48.1	48.1	54.1	54.1	48.1	54.1	48.1
3	Average temperature of seed combination # 2							
4	54.1	54.1	54.1	54.1	54.1	54.1	54.1	54.1
5	60.1	54.1	54.1	60.1	60.1	54.1	60.1	54.1
6	Average temperature of seed combination # 5							
7	60.1	60.1	60.1	60.1	60.1	60.1	60.1	60.1

* Refer to Fig. 7.3 for thermoseed location.

combination 2. Combination 5 is another differentially-loaded design which has four 54.1 C-type thermoseeds and four 60.1 C-type thermoseeds. As with combination 2, the four higher operating temperature thermoseeds (60.1 C-type) of combination 5 were placed in catheters near the four corners of the tumor periphery. Thermoseed combination 6 is studied to determine whether a design of thermoseeds at an one temperature, the average temperature of thermoseeds in combination 5, performs better than the differentially-loaded design of combination 5. The temperatures of the thermoseeds in all combinations were obtained with the Newton-Raphson technique[19] (Sec. 4.1.1.1).

7.3 Performance of the Objective Function

This section is divided into two subsections. Section 7.3.1 discusses the effect of the tumor survival model on the objective function while Sec. 7.3.2 describes the influence of the weighting factor on the objective function. The effects of the blood flow

[19]An alternative method for determining thermoseed temperatures is the use of the variable-property routine in FEHT (Sec. 4.3.2.1).

models and thermoseed combinations on the objective function are provided in both subsections. A therapeutic assessment of the objective function is discussed in Sec. 7.3.3. The effect of blood flow models on the choice of an optimum thermoseed combination is presented in Sec. 7.3.4.

7.3.1 Effect of Tumor Survival Model

The influence of the tumor survival model on the objective function is shown in Fig. 7.11. Since tumor survival model A is assumed to kill more tissue than model B at the same temperature, the objective function will be greater for model A than for model B at the same temperature.

There was little difference in the objective functions determined with tumor survival models A and B for all blood flow models and thermoseed combinations (Fig. 7.11). The largest difference was 12.7% and occurred with seed combination 1 and blood flow model 6 (Fig. 7.11f) Differences in the objective function between tumor survival models A and B were caused by thermoseed combinations that heated a small percentage (or fraction) of tumor to high temperatures. Conversely, in simulations where there was little difference in the objective function between tumor models A and B, a large percentage of tumor was heated to high temperatures.

To illustrate the conclusion that differences in the objective function between tumor survival models A and B arise only with thermoseed combinations that heat a small fraction of tumor to high temperatures, the result of a simulation is discussed. There was a 1.8% difference in the objective function between tumor survival models A and B in the simulation with blood flow model 1 and thermoseed combination 1 (Fig. 7.11a). The 1.8% difference was the largest difference among all seven combinations and blood flow

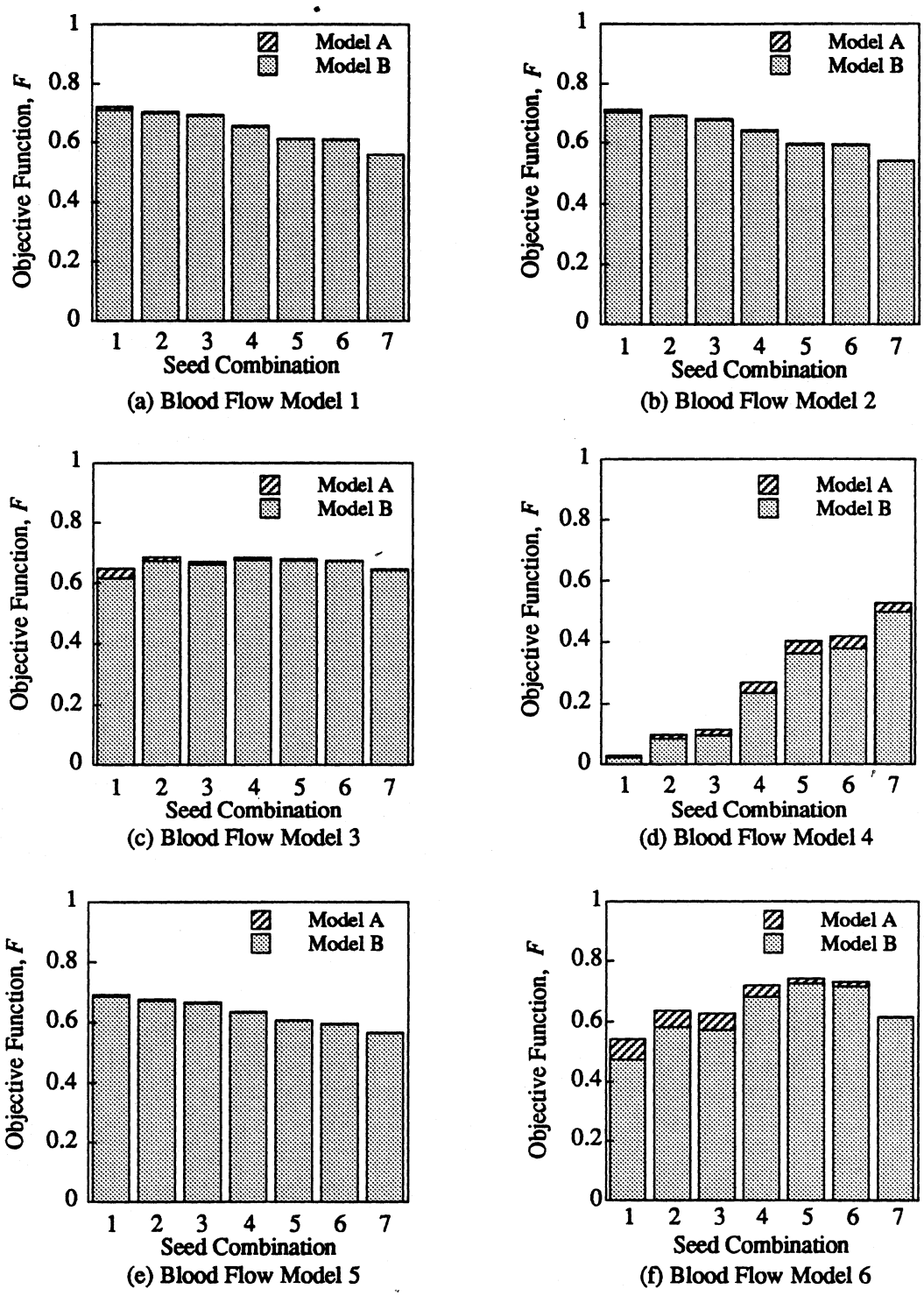

Figure 7.11 Effect of tumor survival models A and B (Fig. 5.2) on objective function for blood flow models 1 through 6 (Table 7.2). The objective function was computed with $\gamma = 0.8$.

model 1. A plot of the percentage of tumor greater than temperatures between 42 and 50 C is shown in Fig. 7.12b for blood flow model 1. The percentage of tumor greater than 46 C was approximately 4, 42, 48, 84, 95, 95 and 97% for thermoseed combinations 1 through 7, respectively. It is evident that the largest percent difference in the objective function between tumor models A and B occurred with combination 1 which heated the smallest percentage (4%) of the tumor above 46 C versus combinations 2 through 7 which heated 42 to 97% of the tumor above 46 C. By similar examinations of the objective function (Figs. 7.11b through 11f) and percentages of tumor greater than 46 C for blood flow models 2 through 6 (figure (b) in Figs. 7.13 through 7.17), it can be shown that differences in the objective function between tumor survival models A and B arise only with thermoseed combinations that heat a small fraction of tumor to high temperatures.

The reason for larger differences in the objective function F between tumor survival models A and B for combinations of thermoseeds that heat a significant fraction of tumor to low temperatures can be explained. The slope of the tumor survival curve for model A is $b = -2$ and has a fractional cell survival as shown in Table 7.6. Alternatively, the slope of the tumor survival curve for model B is $b = -1$ and has a fractional cell survival greater than that of model A (Table 7.6). Thus differences between fractional cell survival of

Table 7.6 Differences in Fractional Cell Survival

Tissue Temperature, T (C)	Fractional Cell Survival, S_{Tumor} (Fig. 5.2)		Difference in Survival Model (Model B – Model A)
	Model A	Model B	
42	1	1	0
43	10^{-2}	10^{-1}	10^{-1}
44	10^{-4}	10^{-2}	10^{-2}
.	.	.	.
.	.	.	.
.	.	.	.
50	10^{-16}	10^{-8}	10^{-8}

models A and B are larger at lower temperatures, especially between 42 and 44 C, than at higher temperatures. Therefore differences in the objective function between tumor survival models A and B increase with thermoseed combinations that heat a large fraction of tumor to low temperatures.

In general there was little difference in the objective functions determined with tumor survival models A and B. It is concluded that since the hyperthermia cell survival of the tumor can only be approximated, differences, similar to the two models used herein, between the actual and the model of tumor cell survival should have a minimal influence on the objective function. Thus the results from simulations in the remainder of this chapter will be shown for tumor survival model B.

7.3.2 Effect of Weighting Factor

Results of the simulations are illustrated in Figs. 7.12 through 7.17 for blood flow models 1 through 6, respectively. Figures 7.12 through 7.17 contain the effect of the weighting factor on the objective function and the percentage of normal and tumor tissues above temperatures between 42 and 50 C. In addition, Figs. 7.12 through 7.17 contain four temperature descriptors including the (1) maximum tumor temperature ($T_{max,\ tumor}$), (2) maximum normal tissue temperature ($T_{max,\ normal}$), (3) average temperature on the boundary of the tumor and normal tissues ($T_{ave,\ boundary}$), and (4) minimum tumor temperature ($T_{min,\ tumor}$). Figures 7.12 through 7.17 also contain a table of $T_{min,\ tumor}$ and $T_{max,\ normal}$ and indicate if $T_{min,\ tumor}$ was greater than $T_{min,\ thera.}$ = 42 and 43 C and if $T_{max,normal}$ was less than 45 C. The last four columns in Figs. 7.12e through 7.17e

tabulate the objective function for $\gamma = 0.2, 0.5, 0.8$ and 1 and indicate by bold type which thermoseed combination maximizes the objective function[20].

The results of the simulations are discussed in Secs. 7.3.2.1 through 7.3.2.6 for blood flow models 1 through 6, respectively. Results are discussed for all blood flow models for completeness of the presentation. Recall that blood flow models 5 and 6 are considered the models which most closely represent the blood flow in reality (see last paragraph in Sec. 7.2.2). The reader can, therefore, limit his/her reading to Secs. 7.3.2.4 through 7.3.2.6 without losing the context of the discussion. (The results from simulations with blood flow model 4 in Sec. 7.3.2.4 are interesting and are not observed with blood flow models 5 and 6).

7.3.2.1 Blood Flow Model 1

The objective function was maximized by thermoseed combination 1 (the array of 48.1 C-type thermoseeds) at $\gamma = 0.2$, 0.5 and 0.8 (Fig. 7.12c and e). Thermoseed combination 7 maximized the objective function with $\gamma = 1$. Notice that as γ increases from 0.2 to 1, the objective function becomes flatter over all thermoseed combinations. Indeed the objective functions with $\gamma = 1$ for thermoseed combinations 5 and 6 were only 0.1 and 0.2% lower, respectively, than that of combination 7. Also, the objective functions with $\gamma = 0.8$ for combinations 2 and 3 were 1.3 and 2.8% lower, respectively, than that for combination 1. Nonetheless, lower objective functions correspond to survival of some fraction of tumor. Thus small differences in the objective function can be significant.

---

[20]In simulations where values of the objective function differ by a small amount, log F can be used to expand the scale. After all, when considering the survival of tumor cells, even *small* differences in F can be significant

Blood Flow Model 1

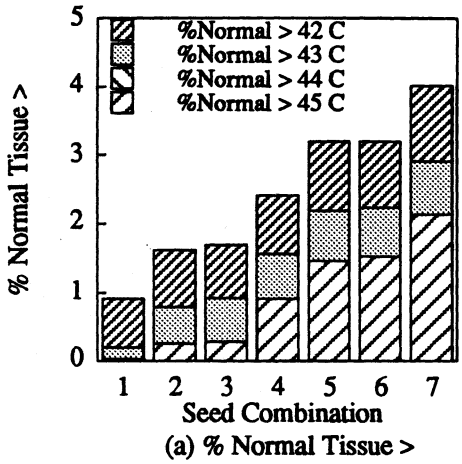

(a) % Normal Tissue >

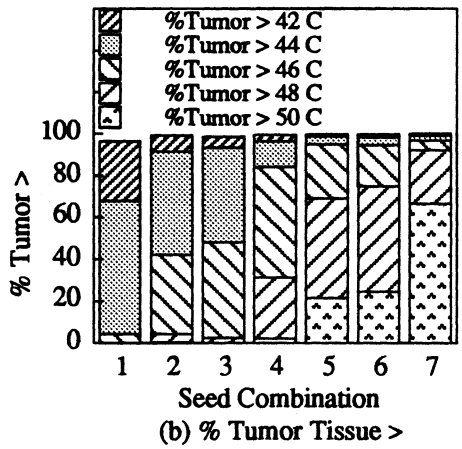

(b) % Tumor Tissue >

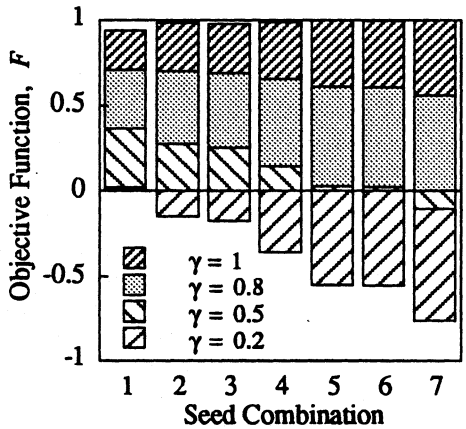

(c) Effect of Weighting Factor

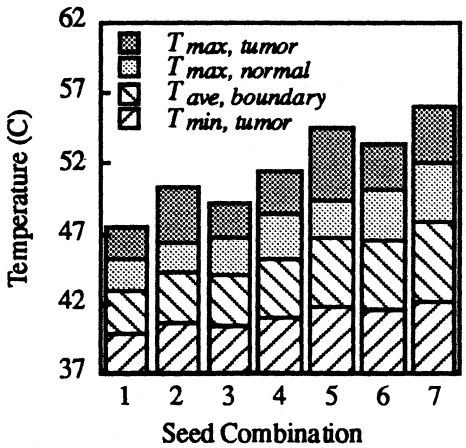

(d) Temperature Descriptors

Seed Combination	$T_{min,\ tumor}$			$T_{max,\ normal}$		Objective Function, F			
	(C)	> 42 C	> 43 C	(C)	< 45 C	$\gamma = 0.2$	$\gamma = 0.5$	$\gamma = 0.8$	$\gamma = 1$
1	39.8	No	No	45.2	No	**0.023**	**0.366**	**0.709**	0.937
2	40.6	No	No	46.4	No	-0.148	0.276	0.700	0.983
3	40.4	No	No	46.7	No	-0.174	0.258	0.689	0.977
4	41.0	No	No	48.4	No	-0.358	0.147	0.652	0.989
5	41.8	No	No	49.5	No	-0.554	0.028	0.610	0.998
6	41.6	No	No	50.1	No	-0.558	0.025	0.608	0.997
7	42.2	Yes	No	52.1	No	-0.764	-0.103	0.558	**0.999**

(e) Summary of Results

Figure 7.12 Results of simulation with blood flow model 1. Results are presented as (a) % normal tissue above 42, 43, 44 and 45 C, (b) % tumor tissue above 42, 44, 46, 48 and 50 C, (c) effect of weighting factor on objective function, (d) maximum, minimum and average temperatures achieved, and (e) a table comparing the optimum thermoseed combination based on temperature descriptors and the objective function shown in bold type.

Blood Flow Model 2

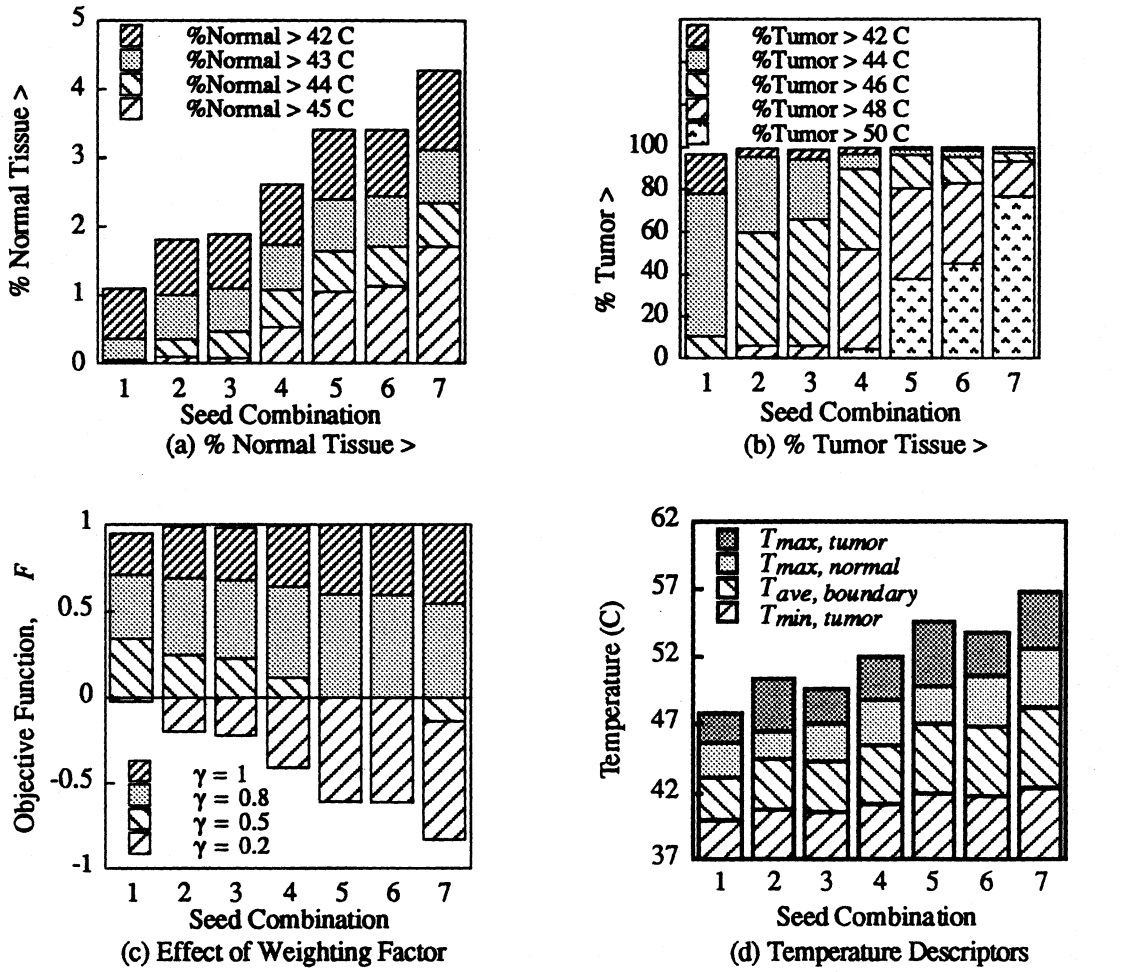

Seed Combination	$T_{min,\ tumor}$			$T_{max,\ normal}$		Objective Function, F			
	(C)	> 42 C	> 43 C	(C)	< 45 C	$\gamma = 0.2$	$\gamma = 0.5$	$\gamma = 0.8$	$\gamma = 1$
1	39.9	No	No	45.6	No	**-0.025**	**0.339**	**0.704**	0.947
2	40.7	No	No	46.6	No	-0.201	0.244	0.689	0.986
3	40.5	No	No	47.1	No	-0.225	0.227	0.678	0.980
4	41.1	No	No	48.9	No	-0.411	0.114	0.640	0.991
5	41.9	No	No	49.8	No	-0.611	-0.007	0.596	0.997
6	41.7	No	No	50.6	No	-0.615	-0.010	0.594	0.997
7	42.4	Yes	No	52.7	No	-0.829	-0.143	0.542	**0.999**

(e) Summary of Results

Figure 7.13 Results of simulation with blood flow model 2. Results are presented as (a) % normal tissue above 42, 43, 44 and 45 C, (b) % tumor tissue above 42, 44, 46, 48 and 50 C, (c) effect of weighting factor on objective function, (d) maximum, minimum and average temperatures achieved, and (e) a table comparing the optimum thermoseed combination based on temperature descriptors and the objective function shown in bold type.

Blood Flow Model 3

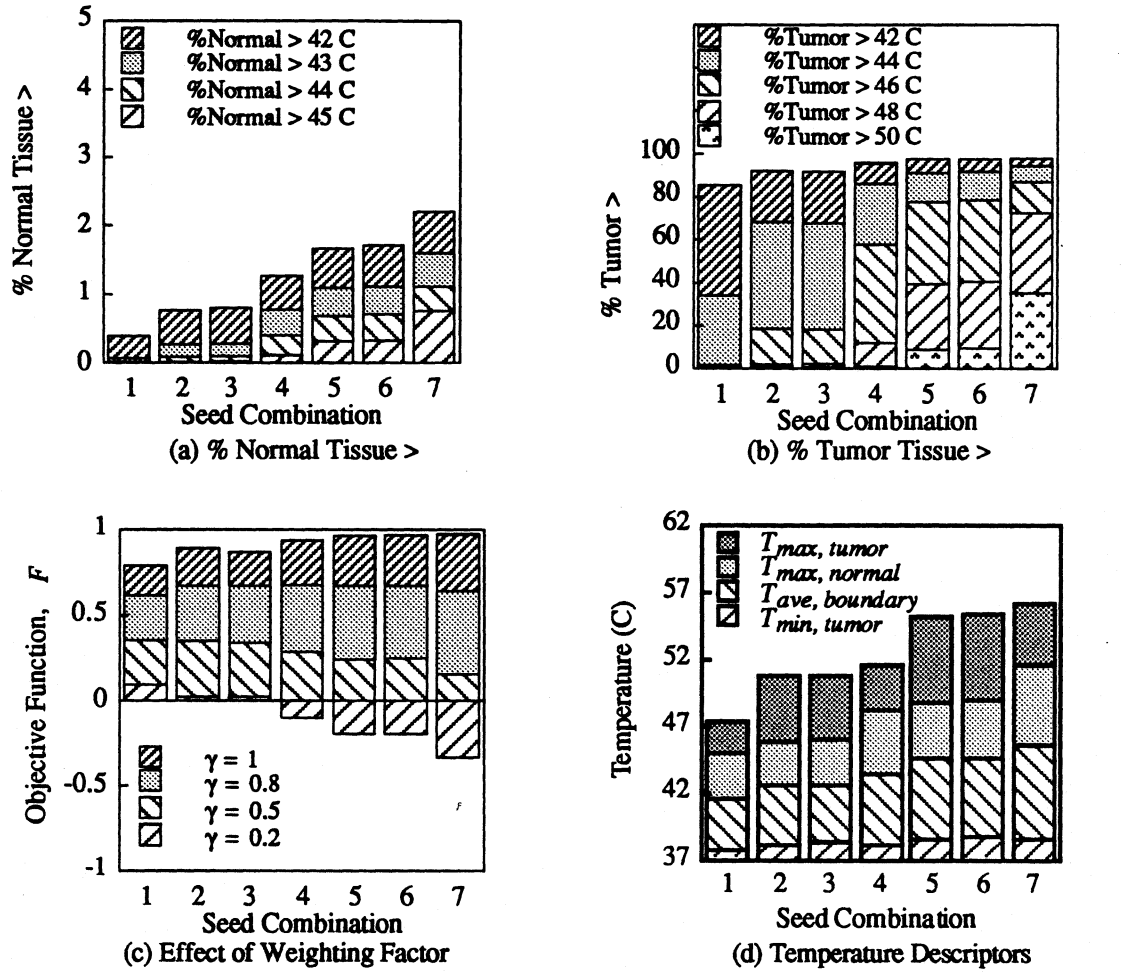

Seed Combination	$T_{min,\ tumor}$			$T_{max,\ normal}$		Objective Function, F			
	(C)	> 42 C	> 43 C	(C)	< 45 C	$\gamma = 0.2$	$\gamma = 0.5$	$\gamma = 0.8$	$\gamma = 1$
1	37.9	No	No	44.9	Yes	**0.097**	**0.357**	0.616	0.789
2	38.2	No	No	45.8	No	0.027	0.350	0.673	0.888
3	38.3	No	No	45.9	No	0.025	0.340	0.672	0.870
4	38.3	No	No	48.1	No	-0.101	0.287	**0.676**	0.936
5	38.6	No	No	48.8	No	-0.193	0.241	0.675	0.965
6	38.7	No	No	48.9	No	-0.195	0.250	0.674	0.967
7	38.7	No	No	51.6	No	-0.337	0.153	0.644	**0.970**

(e) Summary of Results

Figure 7.14 Results of simulation with blood flow model 3. Results are presented as (a) % normal tissue above 42, 43, 44 and 45 C, (b) % tumor tissue above 42, 44, 46, 48 and 50 C, (c) effect of weighting factor on objective function, (d) maximum, minimum and average temperatures achieved, and (e) a table comparing the optimum thermoseed combination based on temperature descriptors and the objective function shown in bold type.

Blood Flow Model 4

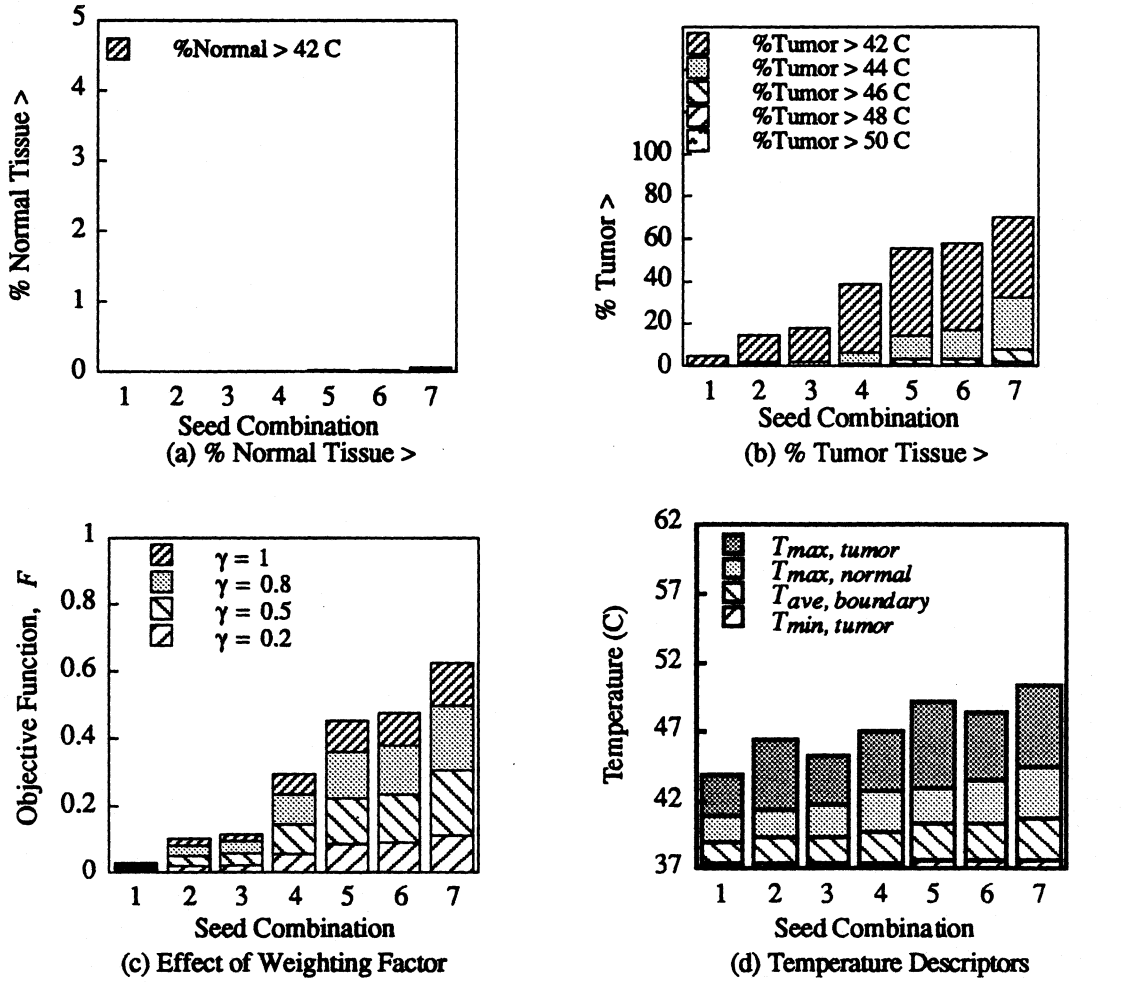

Seed Combination	$T_{min,\ tumor}$			$T_{max,\ normal}$		Objective Function, F			
	(C)	> 42 C	> 43 C	(C)	< 45 C	$\gamma = 0.2$	$\gamma = 0.5$	$\gamma = 0.8$	$\gamma = 1$
1	37.4	No	No	40.9	Yes	0.006	0.015	0.024	0.031
2	37.5	No	No	41.5	Yes	0.021	0.052	0.083	0.104
3	37.4	No	No	41.7	Yes	0.024	0.059	0.095	0.118
4	37.5	No	No	42.7	Yes	0.058	0.146	0.235	0.294
5	37.7	No	No	43.0	Yes	0.088	0.225	0.362	0.454
6	37.7	No	No	43.5	Yes	0.092	0.235	0.379	0.475
7	37.7	No	No	44.6	Yes	**0.115**	**0.306**	**0.497**	**0.624**

(e) Summary of Results

Figure 7.15 Results of simulation with blood flow model 4. Results are presented as (a) % normal tissue above 42, 43, 44 and 45 C, (b) % tumor tissue above 42, 44, 46, 48 and 50 C, (c) effect of weighting factor on objective function, (d) maximum, minimum and average temperatures achieved, and (e) a table comparing the optimum thermoseed combination based on temperature descriptors and the objective function shown in bold type.

Blood Flow Model 5

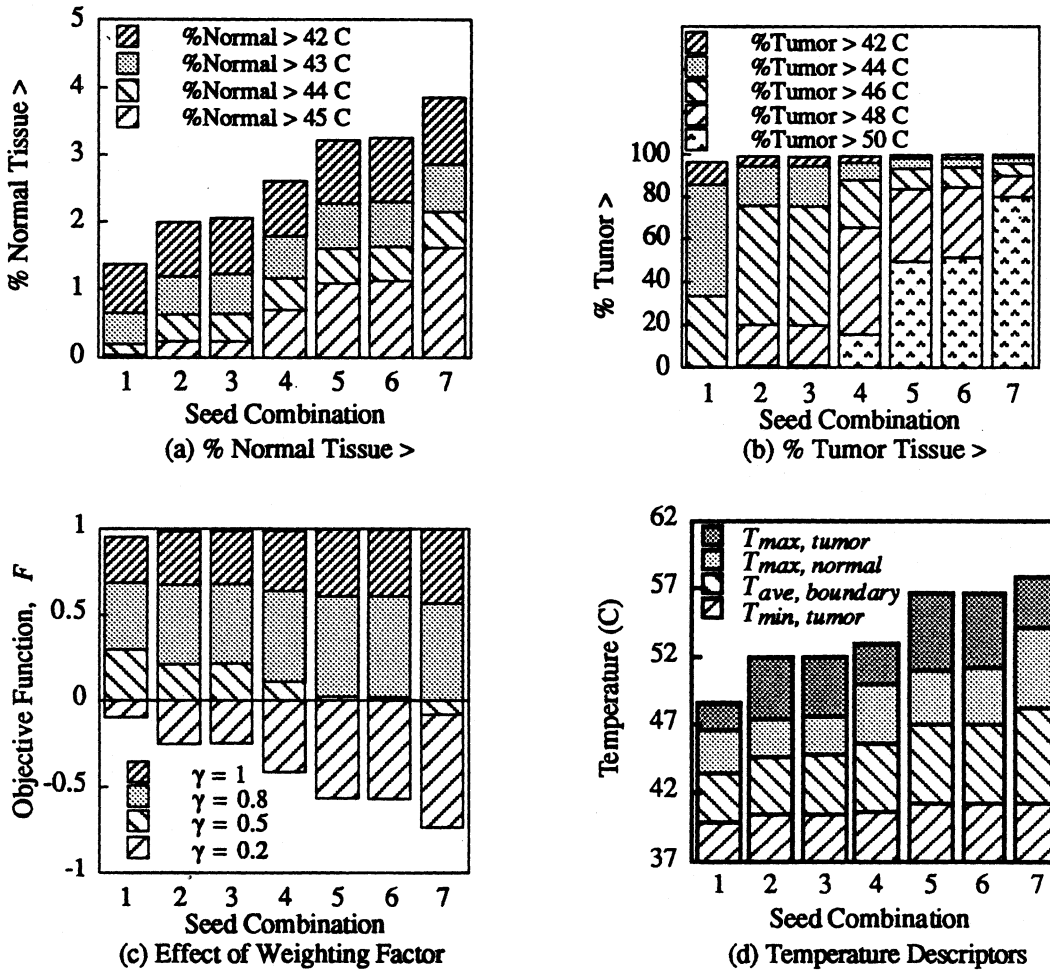

Seed Combination	$T_{min,\ tumor}$			$T_{max,\ normal}$		Objective Function, F			
	(C)	> 42 C	> 43 C	(C)	< 45 C	$\gamma = 0.2$	$\gamma = 0.5$	$\gamma = 0.8$	$\gamma = 1$
1	39.8	No	No	46.5	No	**-0.100**	**0.294**	**0.687**	0.950
2	40.5	No	No	47.5	No	-0.251	0.211	0.674	0.983
3	40.4	No	No	47.4	No	-0.248	0.213	0.677	0.986
4	40.7	No	No	50.0	No	-0.417	-0.235	0.635	0.985
5	41.2	No	No	51.0	No	-0.563	-0.362	0.606	0.995
6	41.1	No	No	50.9	No	-0.567	0.019	0.603	0.995
7	41.4	No	No	54.1	No	-0.733	-0.085	0.564	**0.996**

(e) Summary of Results

Figure 7.16 Results of simulation with blood flow model 5. Results are presented as (a) % normal tissue above 42, 43, 44 and 45 C, (b) % tumor tissue above 42, 44, 46, 48 and 50 C, (c) effect of weighting factor on objective function, (d) maximum, minimum and average temperatures achieved, and (e) a table comparing the optimum thermoseed combination based on temperature descriptors and the objective function shown in bold type.

Blood Flow Model 6

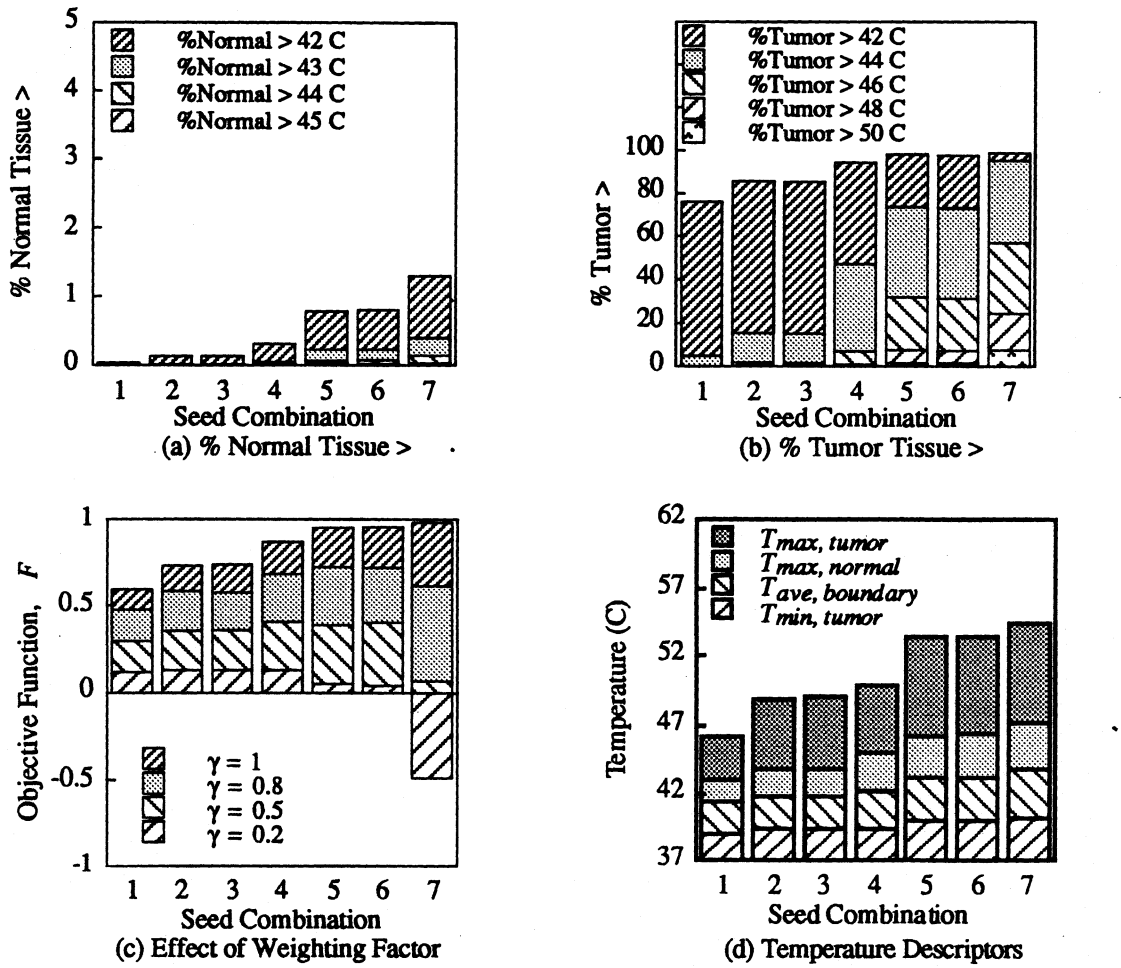

Seed Combination	$T_{min,\ tumor}$			$T_{max,\ normal}$		Objective Function, F			
	(C)	> 42 C	> 43 C	(C)	< 45 C	$\gamma = 0.2$	$\gamma = 0.5$	$\gamma = 0.8$	$\gamma = 1$
1	39.1	No	No	43.0	Yes	0.114	0.294	0.474	0.593
2	39.4	No	No	43.8	Yes	0.127	0.355	0.582	0.734
3	39.5	No	No	43.8	Yes	0.126	0.360	0.575	0.740
4	39.5	No	No	44.9	Yes	**0.128**	**0.406**	0.683	0.869
5	40.0	No	No	46.2	No	0.050	0.388	**0.726**	0.951
6	40.0	No	No	46.3	No	0.040	0.400	0.722	0.955
7	40.3	No	No	47.1	No	-0.486	0.064	0.614	**0.980**

(e) Summary of Results

Figure 7.17 Results of simulation with blood flow model 6. Results are presented as (a) % normal tissue above 42, 43, 44 and 45 C, (b) % tumor tissue above 42, 44, 46, 48 and 50 C, (c) effect of weighting factor on objective function, (d) maximum, minimum and average temperatures achieved, and (e) a table comparing the optimum thermoseed combination based on temperature descriptors and the objective function shown in bold type.

For thermoseed combinations containing seeds with higher operating temperatures, the objective function decreased in value for $\gamma = 0.2$, 0.5 and 0.8 (Fig. 7.12c). The decline of the objective function with combinations of thermoseeds with higher operating temperatures is due to an increasing percentage (or fraction) of normal tissue death (Fig. 7.12a). The increase in normal tissue damage with combinations of higher temperature thermoseeds is also evident by the increase in the maximum temperature of the normal tissue and average boundary temperature (Fig. 12d).

Optimum thermoseed combinations as selected by the objective function agree with choices based on $T_{min,\ tumor}$ and $T_{max,\ normal}$ temperature descriptors. For example, if a hyperthermia pretreatment plan were designed to maximize the fraction of tumor killed Ψ_T, then the combination of thermoseeds which maximizes the objective function with γ near 1 would be selected as the optimum combination (recall Table 5.1). Notice that thermoseed combination 7 maximizes the objective function with $\gamma = 1$ and achieves the highest $T_{min,\ tumor}$ (= 42.2 C) of all the thermoseed combinations (Fig. 7.12d and e). Therefore, the same combination of thermoseeds, combination 7, would have been selected if the goal was to maximize $T_{min,\ tumor}$. If, on the other hand, a pretreatment plan were designed to minimize the fraction of normal tissue damage Ψ_N, then the combination of thermoseeds which maximizes the objective function with $\gamma = 0.2$ or 0.5 would be selected as the optimum combination. The optimum combination of thermoseeds with $\gamma =$ 0.2 or 0.5 is combination 1. Coincidentally, $T_{max,\ normal}$ in the simulations with thermoseed combination 1 is 45.2 C which is above 45 C, but is, nonetheless, the lowest $T_{max,\ normal}$ in simulations with all seven thermoseed combinations. Furthermore, the percentage (or fraction) of normal tissue above temperatures between 42 and 45 C is minimized with combination 1 versus combinations 2 through 7 (Fig. 7.12a).

7.3.2.2 Blood Flow Model 2

The results from simulations performed with blood flow model 2 closely resemble those of blood flow model 1. The objective function with $\gamma = 0.2$, 0.5 and 0.8 was maximized by combination 1 (Fig. 7.13c and e). The objective function with $\gamma = 1$ was maximized with thermoseed combination 7.

Optimum thermoseed combinations as selected by the objective function agree with choices based on $T_{min,\ tumor}$ and $T_{max,\ normal}$ temperature descriptors. In other words, combination 7 would have been selected if a hyperthermia pretreatment plan were designed to maximize Ψ_T or maximize $T_{min,\ tumor}$. Thermoseed combination 1 would be the best design if the pretreatment goal was to minimize Ψ_N or minimize $T_{max,\ normal}$ (Fig. 7.13e).

7.3.2.3 Blood Flow Model 3

With the assumption that a constant blood flow in the muscle tissue is nine times higher than at normal body temperature, the objective function with $\gamma = 1$ was maximized with thermoseed combination 7. The objective function with $\gamma = 0.8$ was maximized by combination 4, and with $\gamma = 0.2$ and 0.5, F was maximized by combination 1 (Fig. 7.14c and e). The condition of a unique maximum for the objective function is just met with $\gamma =$ 0.5, 0.8 and 1.

Optimum thermoseed combinations as selected by the objective function agree with choices based on $T_{max,\ normal}$ and $T_{min,\ tumor}$ temperature descriptors. For instance, thermoseed combination 1 is the only combination which satisfies the $T_{max,\ normal}$ temperature criteria (< 45 C) (Fig. 7.14e). Combination 1 also minimizes the the percent of normal tissue above temperatures between 42 and 45 C (Fig. 7.14a). Coincidentally, combination 1 would be selected on the basis of minimizing Ψ_N by choosing an optimum

thermoseed combination with the objective function and $\gamma = 0.2$ (or 0.5) (Fig. 7.14e). If, on the other hand, the pretreatment plan were designed to maximize Ψ_T, combination 7 is the optimum design (Fig. 7.14e). Although combination 7 does not meet the $T_{min,\ tumor}$ temperature criteria ($> T_{min,\ thera.} = 42$ or 43 C), combination 7 does maximize $T_{min,\ tumor}$ for all seven combinations. If the treatment plan were designed to achieve some balance between maximizing Ψ_T and minimizing Ψ_N, then combination 4 which maximizes the objective function with $\gamma = 0.8$ is the optimum design.

7.3.2.4 Blood Flow Model 4

In simulations where the blood flow rate in the tumor periphery was assumed to be constant and approximately nine times higher than the tumor core and equal to the blood flow in muscle tissue, the objective function was maximized for all γ's by thermoseed combination 7 (Fig. 7.15c and e). The condition of a unique maximum for the objective function was achieved with all γ 's, but the uniqueness over all combinations diminished as γ decreased.

Optimum thermoseed combinations as selected by the objective function agree with choices based on $T_{min,\ tumor}$ and $T_{max,\ normal}$ temperature descriptors. For example, $T_{max,\ normal}$ is less than 45 C with all seven thermoseed combinations (Fig. 7.15d and e). Further, the percentage of normal tissue greater than 42 C is negligible for all seven combinations (Fig. 7.15a). Therefore, the optimum thermoseed combination based on maximizing Ψ_T *and/or* minimizing Ψ_N is combination 7. Thus the optimum thermoseed combination is independent of γ in simulations with blood flow model 4.

It is interesting to note that if the pretreatment plan were based on minimizing $T_{max,\ normal}$, then combination 1 would have been selected as the preferred design. However, because the percentage (or fraction) of normal tissue greater than 42 C was negligible for

thermoseed combinations 2 through 7, combination 7 was the optimum design for $\gamma = 0.2$ and 0.5.

7.3.2.5 Blood Flow Model 5

In simulations where the blood flow in the tumor and normal muscle tissue depended on temperature, the optimum thermoseed design based on maximizing F with $\gamma = 1$ is combination 7, and with $\gamma = 0.2$, 0.5 and 0.8, the optimum is combination 1 (Fig. 7.16c and e). The condition of a unique maximum for the objective function, however, was barely met with $\gamma = 0.8$ and 1.

Optimum thermoseed combinations as selected by the objective function agree with choices based on maximizing $T_{min,\ tumor}$ and minimizing $T_{max,\ normal}$. If a pretreatment plan were designed to minimize Ψ_N ($\gamma = 0.2$) or maximize Ψ_T ($\gamma = 1$), thermoseed combinations 1 and 7, respectively, would be the best choices. Coincidentally, the optimum thermoseed combinations based on minimizing $T_{max,\ normal}$ or maximizing $T_{min,\ tumor}$ would be combinations 1 and 7, respectively.

7.3.2.6 Blood Flow Model 6

In simulations where the blood flow in the tumor and normal tissues depended on temperature and where the blood flow in the tumor periphery was assumed equal to that of muscle, the objective function with $\gamma = 0.2$ and 0.5 was maximized with combination 4. Maximum F's with $\gamma = 0.8$ and 1 were achieved with combinations 5 and 7, respectively (Fig. 7.17c and e). The condition of a unique maximum of the objective function is met with $\gamma = 1$.

Optimum thermoseed combinations as selected by the objective function agree with choices based on $T_{max,\ normal}$ and $T_{min,\ tumor}$ temperature descriptors. For instance, if a

pretreatment plan were designed to minimize Ψ_N, then the combination of thermoseeds which maximizes the objective function for $\gamma = 0.2$ (or 0.5) would be chosen as the optimum design. For this design, combination 4 would have been selected since the objective function was maximized with $\gamma = 0.2$ and 0.5. Also, the percentage of normal tissue above temperatures between 42 and 45 C is small (Fig. 7.17a) and $T_{max,\ normal}$ is below 45 C for combination 4 (Fig. 7.17d). If instead, the pretreatment plan were designed to maximize Ψ_T ($\gamma = 1$), then thermoseed combination 7 was the optimum design. Although all thermoseed combinations achieved a $T_{min,\ tumor}$ less than $T_{min,\ thera.}$ (= 42 and 43 C), $T_{min,\ tumor}$ was maximized with thermoseed combination 7. If some therapeutic balance between Ψ_T and Ψ_N was the desired pretreatment plan, then the optimum thermoseed combination would be based on maximizing the objective function for a γ between 0.6 and 0.8. In this case, thermoseed combination 5 would be the optimum design.

7.3.3 Therapeutic Assessment of Objective Function

The suitability of the objective function is assessed by determining if the fraction of tumor killed (Ψ_T) using the objective function is larger than Ψ_T using temperature descriptors. The tumor fraction killed for all thermoseed combinations and blood flow models 5 and 6 are in Fig. 7.18. In simulations with blood flow model 5, optimum seed combinations based on achieving $T_{max,\ normal} \sim 45$ C and maximizing $T_{min,\ tumor}$ are combinations 1 and 7, respectively. Likewise, combinations 1 and 7 are optimum based on maximizing the objective function with $\gamma = 0.2$ and 1, respectively. In simulations with blood flow model 6, combination 7 is still the optimum based on maximizing $T_{min,\ tumor}$ and F with $\gamma = 1$. Seed combination 4 is optimum based on achieving $T_{max,\ normal} \sim$ 45 C and maximizing F with $\gamma = 0.2$. Thus for these two blood flow models the temper-

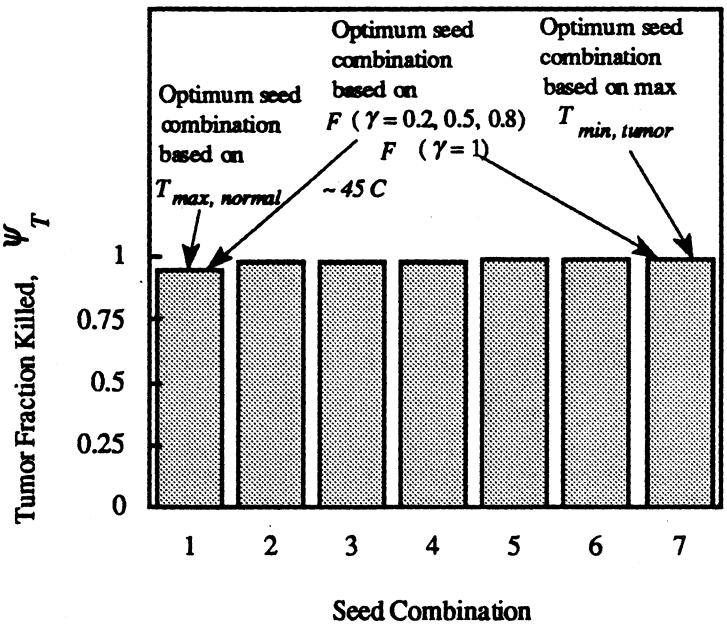

(a) Blood flow model 5

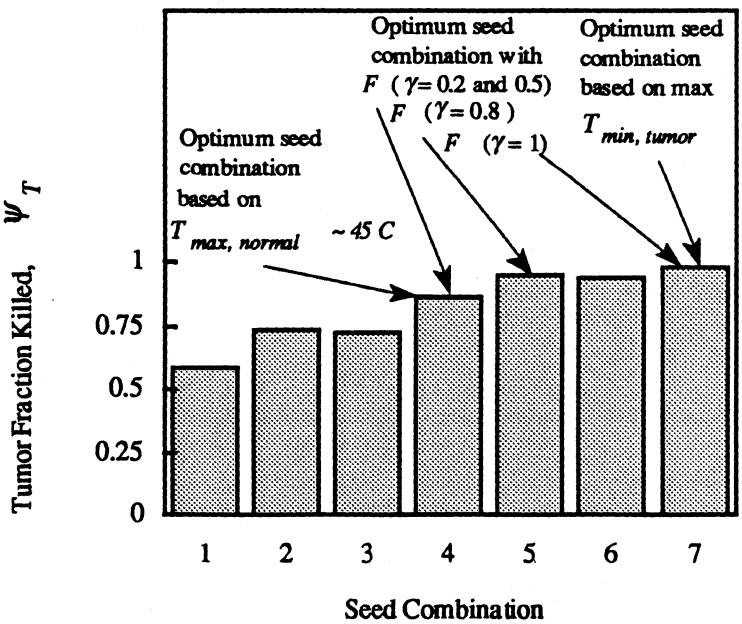

(b) Blood flow model 6

Figure 7.18 Fraction of tumor killed, ψ_T, versus thermoseed combination for blood flow models (a) 5 and (b) 6. Optimum seed combinations as identified by the objective function F, maximizing $T_{min, tumor}$ and achieving $T_{max, normal}$ ~ 45 C are labeled in each figure.

ature descriptor method and the objective function predict optimum seed combinations that kill the same fraction of tumor.

The *advantage* of the objective function over the temperature-descriptor method in selecting an optimum seed combination is with pretreatment plans that desire to achieve a balance between maximizing the tumor fraction killed and minimizing normal tissue complications. This type of treatment plan is likely to be the most frequently occurring treatment goal. It would be difficult to select an optimum seed combination based on achieving a balance between maximizing $T_{min,\,tumor}$ and minimizing $T_{max,\,normal}$, short of an educated guess and intuition. Fortunately, though, the objective function could be used to select the optimum combination. Instead of basing the optimum combination on a therapeutic trade-off between maximizing $T_{min,\,tumor}$ and attaining $T_{max,\,normal} \sim 45$ C, the *single-valued*, maximum of the objective function with $\gamma = 0.8$ (or close to 0.8) would provide an optimum combination. For example, in the simulations with blood flow model 6, seed combination *5* is the *optimum* design based on maximizing F with $\gamma = 0.8$. Notice that seed combination 5 kills 8.6% more tumor than does combination 4 which was the optimum design with the criteria that $T_{max,\,normal} \sim 45$ C.

In summary, the objective function was an effective method to aid in selecting optimum combinations of thermoseeds. Moreover, under the assumptions of the model, use of the objective function in pretreatment planning will ensure that, of all the possible combinations of thermoseed temperatures, the combination which maximizes the fraction of tumor killed will be selected as the optimum combination based on the desired treatment goal.

7.3.4 Blood Flow Effect on Optimum Thermoseed Combination

The variable which is least known in hyperthermia pretreatment planning is the blood flow in the tumor and surrounding normal tissues. Six blood flow models were, therefore, investigated to study the influence of blood flow on optimum thermoseed combinations. Recall that blood flow models 1 through 4 are constant blood flow models, while blood flow models 5 and 6, the temperature-dependent models, are considered the models which most closely represent the blood flow in real tissue systems (Sec. 7.2.2). The constant blood flow models were studied to compare temperature distributions in the tissues with those of the temperature-dependent models (Secs. 7.4.1 and 7.4.2).

The optimum thermoseed combinations based on the objective function for all blood flow models are shown in Table 7.7. Ideally, the optimum thermoseed combination would be independent of the blood flow model. Discussion in this section will be limited primarily to $\gamma = 0.8$ which would be used if the pretreatment plan were designed to achieve some balance between maximizing Ψ_T and minimizing Ψ_N.

Table 7.7 Blood Flow Effect on Optimum Thermoseed Combination

Blood Flow Model	Optimum Thermoseed Combination			
	$\gamma = 0.2$	$\gamma = 0.5$	$\gamma = 0.8$	$\gamma = 1$
1	1	1	1	7
2	1	1	1	7
3	1	1	4	7
4	7	7	7	7
5	1	1	1	7
6	4	4	5	7

Thermoseed combination 1 is the optimum design with $\gamma = 0.8$ for blood flow models 1, 2 and 5, while combinations 4, 7 and 5 are the optimum designs for blood flow

models 3, 4 and 6, respectively. Notice that for blood flow model 4, thermoseed combination 7 is the optimum design for all γs. The optimum thermoseed design with γ = 1 for all blood flow models is combination 7. Unfortunately, the optimum thermoseed combination with γ= 0.2, 0.5 and 0.8 is dependent on the blood flow model as evident by blood flow models 5 and 6. It is therefore critical that the most accurate blood flow model be used in determining the optimum thermoseed combination.

7.4 General Comments on Results from Simulations

Discussion on the results from several simulations are presented in this section. The discussion will be limited mainly to the effect of various blood flow modeling assumptions on temperatures achieved in the tumor and surrounding normal tissues. A study of the temperature distributions in simulations with the necrotic tumor core blood flow model are presented in Sec. 7.4.1. A comparison is made in Sec. 7.4.2 between the temperature distributions from simulations with temperature-dependent versus constant blood flow models. Temperature distributions from simulations with the differentially-loaded thermoseed designs are compared with those from simulations with combinations of thermoseeds at uniform temperatures (Sec. 7.4.3). The calculation times required to identify the optimum thermoseed designs are presented in Sec. 7.4.4.

7.4.1 Modeling the Tumor Core as a Region of Low Blood Flow

Modeling the tumor core as a (necrotic) region of constant, low blood flow (blood flow model 2) versus modeling the tumor with a uniform blood flow equal to normal muscle tissue at body temperature (blood flow model 1) had a small influence on temperature predictions. The $T_{min,\,tumor}$ was only 0.1 C higher in simulations with blood flow model 2 versus model 1 for all thermoseed combinations (Fig. 7.19c). The $T_{max,}$

normal and $T_{max,\ tumor}$ were between 0.2 and 0.6 C higher with model 2 compared with model 1 (Fig. 7.19c). The maximum difference in the percentage of normal tissue above temperatures between 42 and 45 C for model 2 versus model 1 was 0.25% (Fig. 7.19a). The maximum difference in the percentage of tumor above temperatures between 42 and 50 C for model 2 versus model 1 was 20% (Fig. 7.19b).

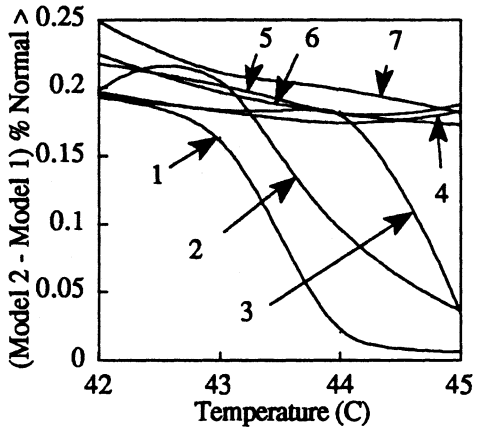

(a) Difference in % Normal Tissue >

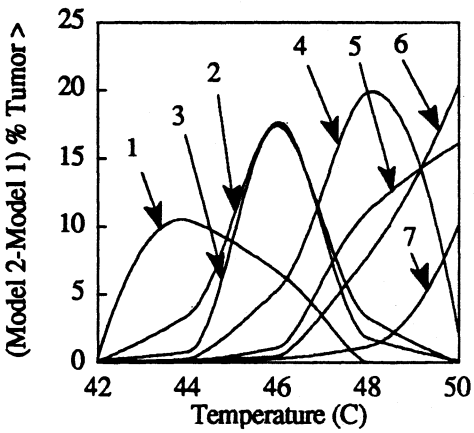

(b) Difference in % Tumor >

Thermoseed Combination	Temperature differences between blood flow model 2 and model 1		
	$T_{max,\ tumor}$	$T_{min,\ tumor}$	$T_{max,\ normal}$
1	0.4	0.1	0.4
2	0.2	0.1	0.2
3	0.4	0.1	0.4
4	0.5	0.1	0.5
5	0.3	0.1	0.3
6	0.4	0.1	0.5
7	0.6	0.1	0.6

(c) Difference in Temperature Descriptors

Figure 7.19 Effect of modeling the tumor core with a constant, low rate of blood flow (model 2) versus modeling with a blood flow rate at normal body temperature (model 1). The blood flow in model 1 is constant and uniform in the tumor and surrounding normal muscle (m = 0.027 l/min-kg). The blood flow in model 2 is constant and equal to 0.008 l/min-kg in the tumor core and 0.027 l/min-kg in the tumor periphery and normal muscle tissue. The results are presented as (a) the difference in the % of normal tissue greater than temperatures between 42 and 45 C, (b) the difference in the % of tumor greater than temperatures between 42 and 50 C and (c) the difference in the $T_{max,\ tumor}$, $T_{min,\ tumor}$ and $T_{max,\ normal}$. Thermoseed combinations 1 through 7 are labeled in figures (a) and (b).

The thermoseed placement in the present study was limited to the tumor periphery. In other tumors, it is possible that thermoseed(s) would be placed in the tumor periphery *and* the tumor core. Simulations performed on a thermoseed combination consisting of thermoseed(s) in the tumor periphery *and* core may have a greater effect on the temperature distribution than those achieved with thermoseeds only in the tumor periphery.

7.4.2 Constant versus Temperature-Dependent Blood Flow Modeling

Temperature distributions from simulations with constant blood flow models are compared with those where the blood flow depended on temperature. Comparisons of the temperature distributions from simulations where the blood flow in normal muscle tissue was higher than normal body temperature are discussed in Sec. 7.4.2.1. Similarly, comparisons of the temperature distributions from simulations where the blood flow in normal muscle tissue *and* the tumor periphery were assumed equal and higher than normal body temperature are presented in Sec. 7.4.2.2.

7.4.2.1 High Blood Flow in Normal Muscle Tissue

Temperature distributions from simulations with blood flow model 3 are compared with those of blood flow model 5. The blood flow in the tumor of model 3 was constant and uniform at m_t = 0.027 l/min-kg and the blood flow in the normal muscle tissue was constant and nine times higher than in the tumor (0.243 l/min-kg). The blood flow in model 5 depended on temperature (Sec. 7.2.2).

The temperature descriptors in the tumor and normal tissues are higher with the temperature-dependent model than the constant blood flow model (Fig. 7.20c). The $T_{max,\ tumor}$ is between 1.2 and 1.7 C higher over all thermoseed combinations with the

temperature-dependent blood flow model. The $T_{min,\ tumor}$ is between 1.9 and 2.7 C higher, and the $T_{max,\ normal}$ is between 1.6 and 2.4 C higher with the temperature-dependent blood flow model.

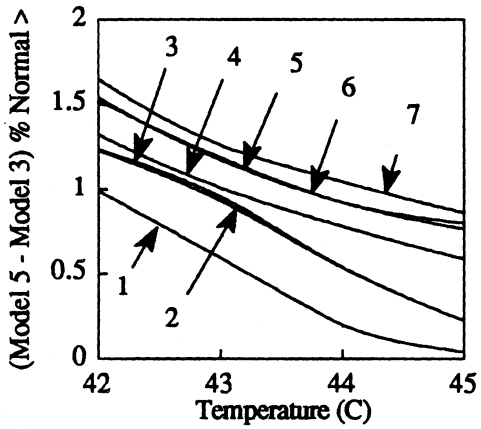

(a) Difference in % Normal Tissue >

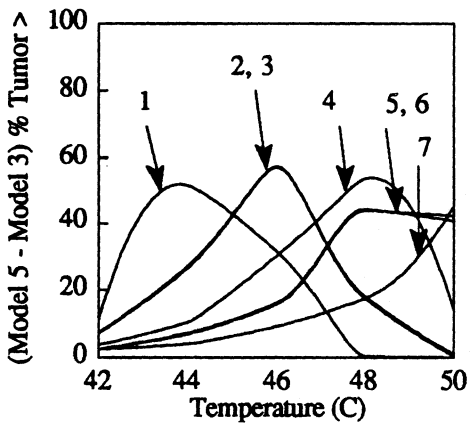

(b) Difference in % Tumor Tissue >

Thermoseed Combination	Temperature differences between blood flow model 5 and model 3		
	$T_{max,\ tumor}$	$T_{min,\ tumor}$	$T_{max,\ normal}$
1	1.3	1.9	1.6
2	1.2	2.3	1.7
3	1.2	2.2	1.6
4	1.4	2.4	1.9
5	1.4	2.6	2.1
6	1.4	2.5	2.2
7	1.7	2.7	2.4

(c) Difference in Temperature Descriptors

Figure 7.20 Effect of the temperature-dependent blood flow model 5 versus the constant blood flow model 3. The constant blood flow model has a uniform flow in the tumor (m_t = 0.027 l/min-kg) and a blood flow in surrounding muscle tissue which is nine times higher than the tumor (model 3). The temperature-dependent blood flow model has a uniform blood flow in the tumor and surrounding normal muscle tissue at normal body temperature, but increases with temperature to a maximum of 0.047 l/min-kg in the tumor periphery and to a maximum of 0.243 l/min-kg in the muscle tissue (model 5). Results are presented as (a) the difference in the % of normal tissue greater than temperatures between 42 and 45 C, (b) the difference in the % of tumor greater than temperatures between 42 and 50 C and (c) the difference in the $T_{max,\ tumor}$, $T_{min,\ tumor}$ and $T_{max,\ normal}$. Thermoseed combinations 1 through 7 are labeled in figures (a) and (b).

The differences in the percentage of normal and tumor tissues above temperatures between 42 and 50 C between the temperature-dependent and constant blood flow models are shown in Figs. 7.20a and b, respectively. The differences in the percentage of normal tissue above temperatures between 42 and 45 C are between 0.1 and 1.6% higher over all thermoseed combinations with the temperature-dependent model versus the constant blood flow model. The differences in the percentage of tumor above temperatures between 42 and 50 C are between 0 and 60% higher in the temperature-dependent blood flow model.

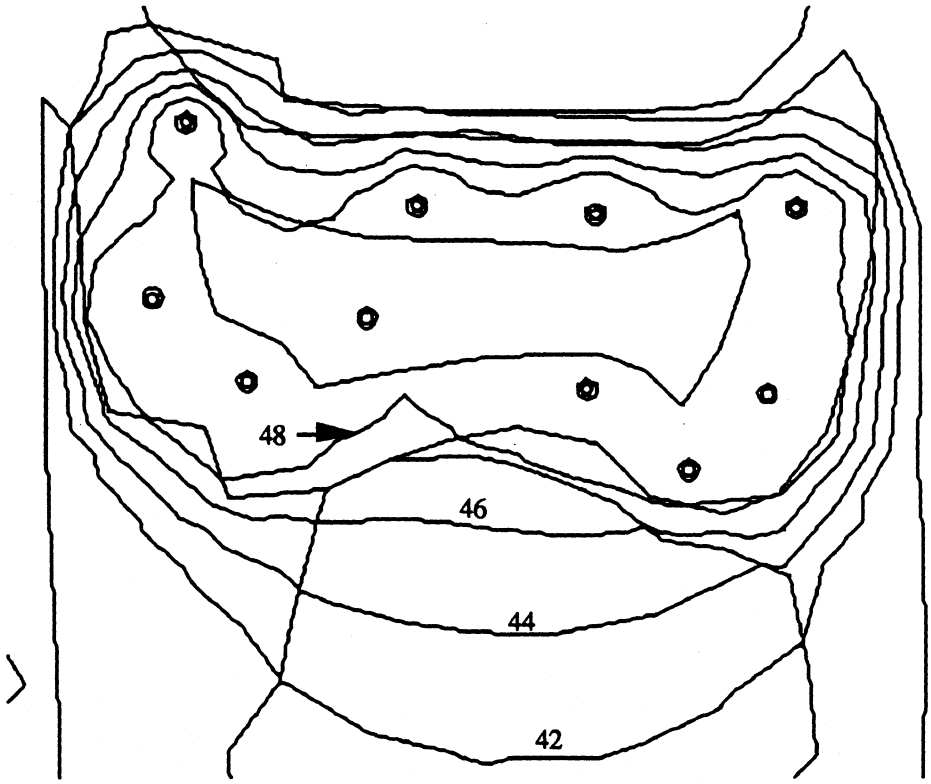

(a) Blood flow model 3

Figure 7.21a The 42, 44, 46 and 48 C isotherms in and near the tumor for simulations with (a) the constant, higher blood flow model 3 and (b) the temperature-dependent blood flow model 5. The simulations were performed with a combination of 60.1 C-type thermoseeds (combination 7). The eight thermoseed and two catheter models for measuring temperatures are shown by the 10 innermost circles.

Isotherms in and near the tumor from simulations with the constant and temperature-dependent blood flow models are shown in Fig. 7.21. The simulation was performed with combination 7 consisting of 60.1 C-type thermoseeds. Larger fractions of the tumor and surrounding normal tissues are at higher temperatures with the temperature-dependent blood flow model.

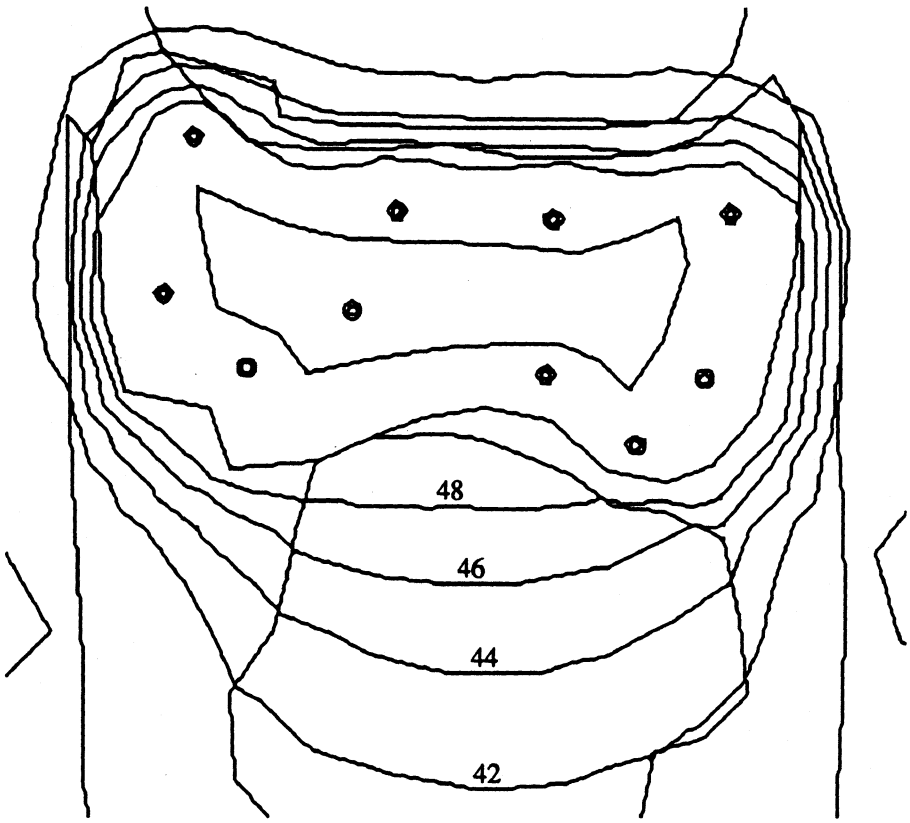

(b) Blood flow model 5

Figure 7.21b The 42, 44, 46 and 48 C isotherms in and near the tumor for simulations with (a) the constant, higher blood flow model 3 and (b) the temperature-dependent blood flow model 5. The simulations were performed with a combination of 60.1 C-type thermoseeds (combination 7). The eight thermoseed and two catheter models for measuring temperatures are shown by the 10 innermost circles.

7.4.2.2 High Blood Flow in Tumor Periphery and Normal Muscle Tissue

Temperature distributions from simulations with blood flow model 4 are compared with the results with blood flow model 6. The blood flow in the tumor core of model 4 was constant at 0.027 l/min-kg and the blood flow in the tumor periphery and normal muscle tissue was constant and nine times higher than the tumor core (0.243 l/min-kg). The blood flow in model 6 depended on temperature (Sec. 7.2.2).

The temperature descriptors in the tumor and normal tissues are higher with the temperature-dependent blood flow model than the constant blood flow model (Fig. 7.22c). The $T_{max,\ tumor}$ is between 1.3 and 3.5 C higher over all thermoseed combinations with the temperature-dependent blood flow model. Likewise, the $T_{min,\ tumor}$ is between 1.7 and 2.6 C higher and the $T_{max,\ normal}$ is between 2.1 and 3.3 C higher with the temperature-dependent blood flow model.

The differences in the percentage of normal tissue above temperatures between 42 and 45 C between the temperature-dependent model and the constant blood flow model vary between 0 to 1.25% (Fig. 7.22a). The differences in the percentage of tumor above temperatures between 42 and 50 C are between 0 and about 65% higher over all thermoseed combinations with the temperature-dependent blood flow model.

Isotherms in and near the tumor from simulations with the constant and temperature-dependent blood flow models are shown in Fig. 7.23. The simulation was performed with combination 7 consisting of 60.1 C-type thermoseeds. *Significantly* larger fractions of the tumor and surrounding normal tissues are at higher temperatures with the temperature-dependent blood flow model.

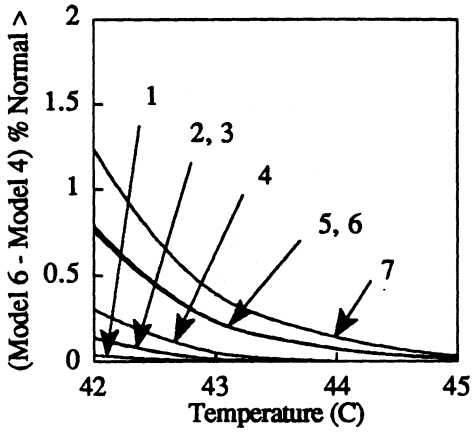

(a) Difference in % Normal Tissue >

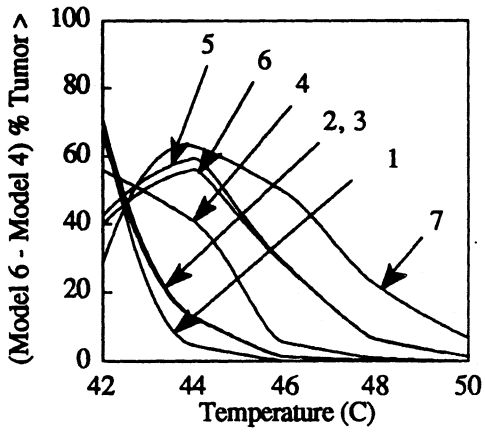

(b) Difference in % Tumor Tissue >

Thermoseed Combination	Temperature differences between blood flow model 6 and model 4		
	$T_{max,\ tumor}$	$T_{min,\ tumor}$	$T_{max,\ normal}$
1	1.4	1.7	2.1
2	1.3	1.9	2.3
3	2.7	2.1	2.1
4	1.6	2.0	2.2
5	2.1	2.3	3.3
6	3.5	2.3	2.8
7	2.5	2.6	2.5

(c) Difference in Temperature Descriptors

Figure 7.22 Effect of the temperature-dependent blood flow model 6 versus the constant blood flow model 4. The constant blood flow model has a blood flow in the tumor core of 0.027 l/min-kg and a uniform blood flow in the tumor periphery and surrounding muscle tissue which is nine times higher than the tumor (0.243 l/min-kg). The temperature-dependent blood flow model has a uniform blood flow in the tumor and surrounding normal muscle tissue at normal body temperature, but increases with temperature to a maximum of 0.243 l/min-kg in the tumor periphery and normal muscle tissue (model 6). Results are presented as (a) the difference in the % of normal tissue greater than temperatures between 42 and 45 C, (b) the difference in the % of tumor greater than temperatures between 42 and 50 C and (c) the difference in the $T_{max,\ tumor}$, $T_{min,\ tumor}$ and $T_{max,\ normal}$. Thermoseed combinations 1 through 7 are labeled in figures (a) and (b).

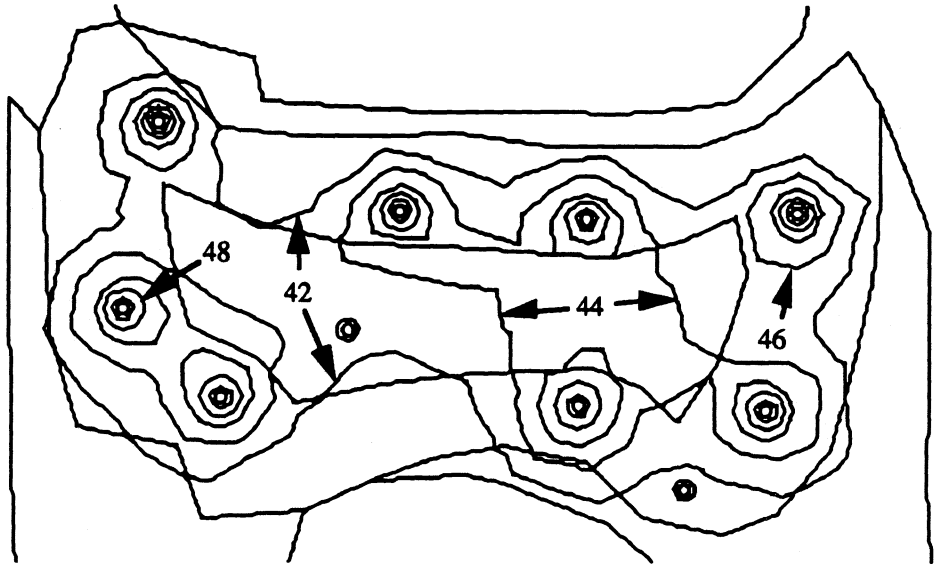

(a) Blood flow model 4

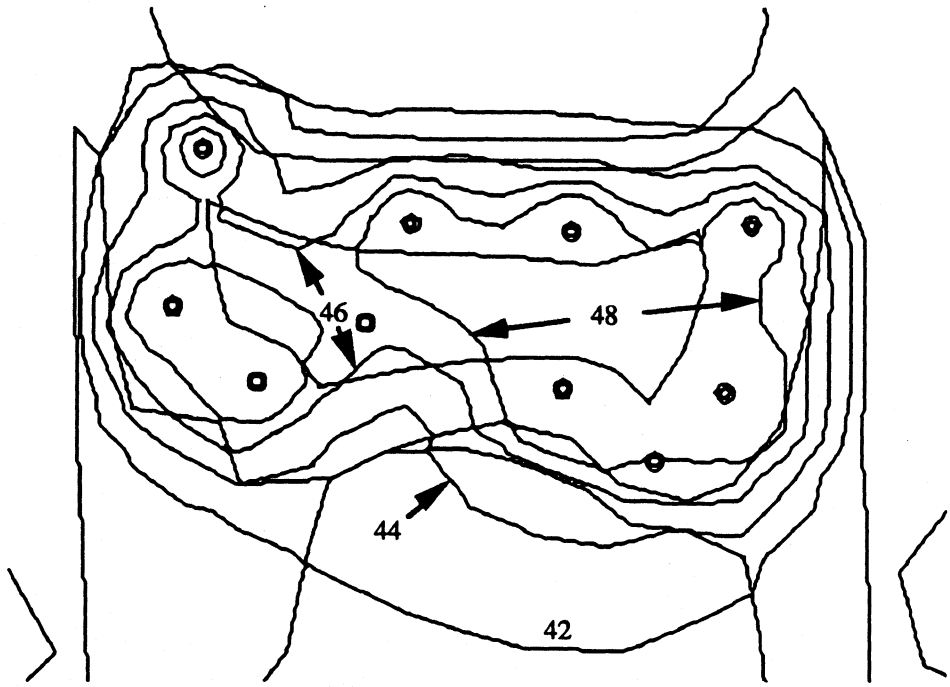

(b) Blood flow model 6

Figure 7.23 The 42, 44, 46 and 48 C isotherms in and near the tumor for simulations with (a) the constant, higher blood flow model 4 and (b) the temperature-dependent blood flow model 6. The simulations were performed with a combination of 60.1 C-type thermoseeds (combination 7). The eight thermoseed and two catheter models for measuring temperatures are shown by the 10 innermost circles.

7.4.3 Differentially-Loaded Thermoseed Design

The temperature distributions achieved with differentially-loaded thermoseed combinations 2 and 5 were similar to those of uniformly-loaded seed combinations 3 and 6, respectively. Recall that the temperature of the thermoseeds in combinations 3 and 6 are fixed at the average temperature of the differentially-loaded thermoseeds in combinations 2 and 5, respectively. Comparisons between combinations 2 and 3 and between combinations 5 and 6 in Figs. 7.12 through 7.17 revealed that there was little difference in the objective function and in the percentage of normal and tumor tissues above 42 C. Absolute temperature differences in $T_{min,\ tumor}$ and $T_{max,\ normal}$ between combinations 2 and 3 and between combinations 5 and 6 are shown in Table 7.8. The difference in $T_{min,\ tumor}$ was between 0 and 0.2 C while the difference in $T_{max,\ normal}$ was between 0 and 0.8 C.

Table 7.8 Effect of Differentially-Loaded Thermoseed Design on Temperature Descriptors

Blood Flow Model	Absolute Temperature Difference between Thermoseed Combinations			
	$T_{min,\ tumor}$		$T_{max,\ normal}$	
	|Com. 2 – Com. 3|	|Com. 5 – Com. 6|	|Com. 2 – Com. 3|	|Com. 5 – Com. 6|
1	0.2	0.2	0.3	0.6
2	0.2	0.2	0.5	0.8
3	0.1	0.1	0.1	0.1
4	0.1	0	0.2	0.5
5	**0.1**	**0.1**	**0.1**	**0.1**
6	**0.1**	**0**	**0**	**0.1**

Isotherms in and near the tumor from simulations with the uniformly-loaded design 5 and the differentially-loaded design 6 are shown in Fig. 7.24. The simulations were performed with blood flow model 2 (Sec. 7.2.2) since the differences in the temperature descriptors were the largest with this blood flow model (see Table 7.8). Notice that the isotherms for both combinations are similar.

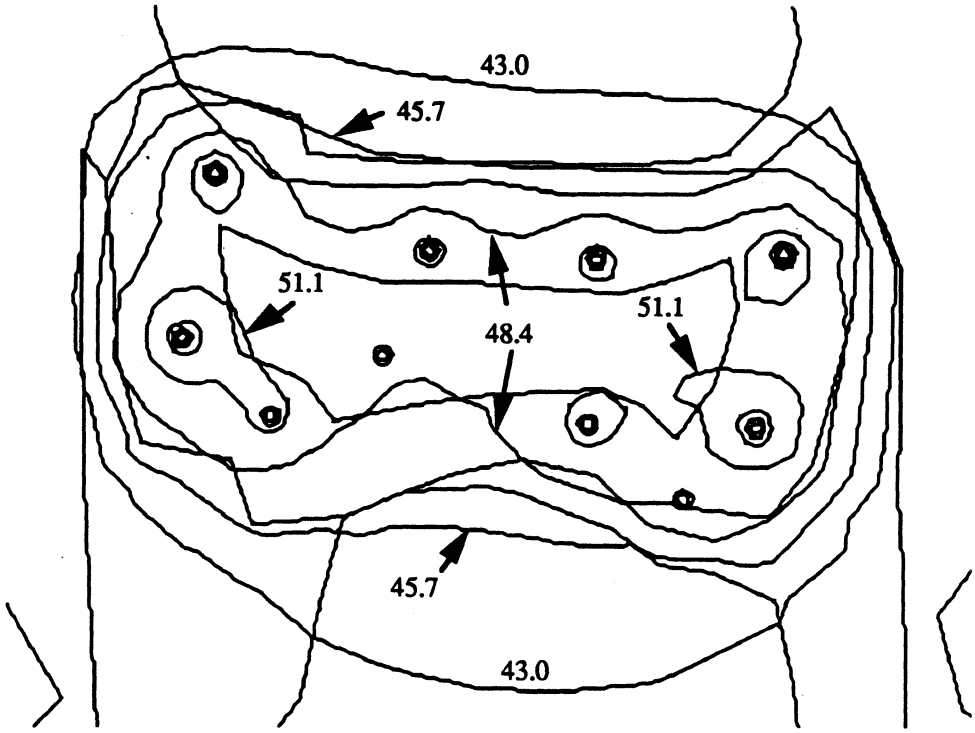

(a) Uniformly-loaded combination 5

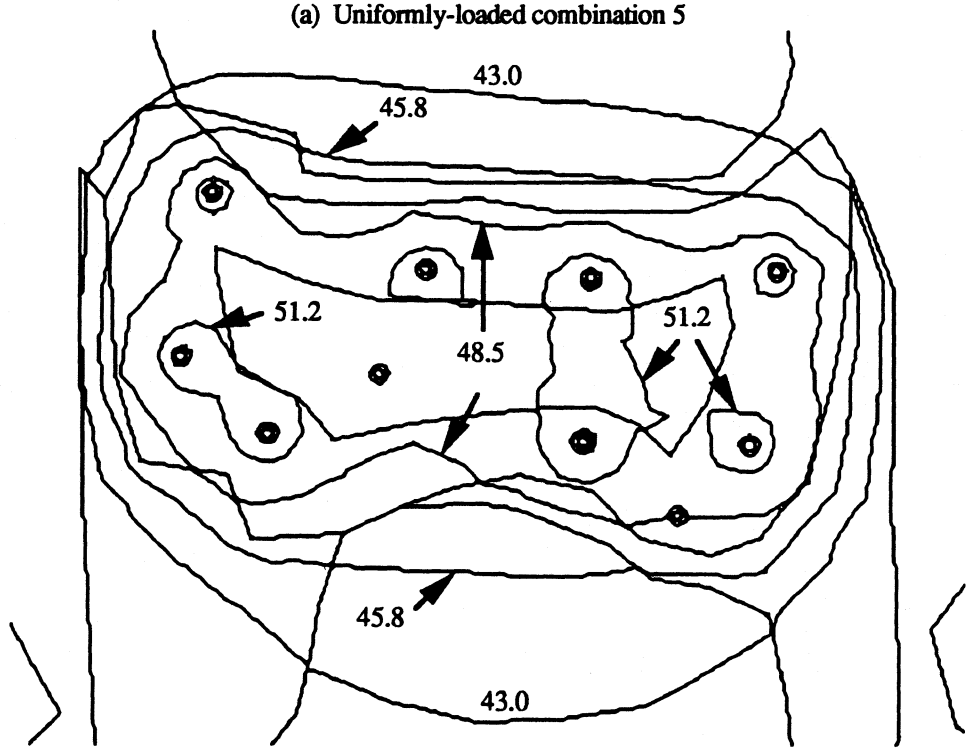

(b) Differentially-loaded combination 6

Figure 7.24 Isotherms (C) in and near the tumor from simulations with (a) uniformly-loaded design 5 and (b) differentially-loaded design 6. The simulations were performed with blood flow model 2 (Sec. 7.2.2).

7.4.4 Computation Time

The calculation times of FEHT that were required to identify optimum thermoseed combinations with blood flow models 1 through 6 are in Table 7.9. The calculations were performed with a Macintosh II fx which has a clock-speed of 40 MHz and a 68030 microprocessor running on System 7.01. (The calculation times for simulations with ther-

Table 7.9 Computation Time Required to Determine Optimum Seed Combinations (Newton-Raphson iteration tolerance, Tol = 5e-3 (Sec. 4.1.1.1))

Thermoseed Combination	Calculations in Real Time (hrs) Blood Flow Model					
	1	2	3	4	5	6
1	1.3	1.3	0.7	1.3	**6.2**	**4.7**
2	1.2	1.3	0.7	1.2	**3.3**	**6.4**
4	0.9	1.2	0.7	1.2	**5.7**	**8.5**
5	1.3	1.2	1.0	1.3	**5.0**	**8.3**
7	1.3	2.5	0.7	1.3	**6.5**	**3.3**
Total =	6.0	7.5	3.8	6.3	**26.7**	**31.2**

moseed combinations 3 and 6 are not shown in Table 7.9 since the Newton-Raphson method (Sec. 4.1.1.1) was not used with these uniformly-loaded designs (see Sec. 7.2.3).) The simulations with the constant blood flow models required between 3.8 and 7.5 hr while the simulations with the temperature-dependent blood flow models required between 26.7 and 31.2 hr. Although simulations with the temperature-dependent models took substantially longer than that for the constant blood flow models, the complete pretreatment planning process including finite element mesh creation should take no longer than 1.5 days in the worst case with this software and using the Newton-Raphson scheme. Based on the discussion in Sec. 4.3.2.1, however, the variable-property routine in FEHT (Klein *et al.* 1988) should *significantly* reduce these calculation times. With the

frequent release of new and faster computers, running the software on higher speed computers will further reduce the computational time. Thus pretreatment planning should require only about 0.5 days in the near future.

7.5 Concluding Remarks

The main ideas which will be summarized in this concluding section include: (1) modeling of a tumor in the prostate is an example of the pretreatment planning approach; (2) normally, the physician observes a few measured temperatures during treatment to determine if a treatment was good, however, with FEHT, the pretreatment planning approach considers temperatures *throughout* the tumor and surrounding normal tissues and therefore should give a better indication of the *goodness* of the treatment *a priori*; (3) the objective function is the *best* way to plan a treatment if all modeling assumptions (*e.g.*, $w_b c_b$ and k_t in the tumor and surrounding normal tissues and the cell survival models) approximated closely the actual conditions during treatment; (4) the objective function was an effective method to optimize the treatment plan particularly when only an educated guess can be made of the therapeutic trade-off between $T_{min,\ tumor}$ and $T_{max,\ normal}$.

A ferromagnetic hyperthermia pretreatment plan of a tumor in the human prostate was developed in this chapter. A CT scan containing the largest cross-section of the prostate and located near the midpoint of the prostate in the z-direction was used in the simulations (Figs. 7.1 and 7.2). Contours of the boundaries of the organs and other tissues in the model were obtained from the CT scan and transferred into FEHT using standard Macintosh application programs and desktop features (Sec. 7.1.1). The numerical values of thermal conductivity and blood flow were obtained from published data (Sec. 7.1.2). The complete finite element mesh of the tissue model with eight

simulated thermoseeds and two catheter models (used for monitoring temperatures during treatment) was created with FEHT (see Fig. 7.3). About 1.5 to 2 hrs were required to create the entire finite element mesh. A mesh consisting of 1904 finite elements was adequate for sufficient accuracy of the numerical solutions (Sec. 7.2.1). Six blood flow models were studied including two temperature-dependent models (Sec. 7.2.2). Seven thermoseed designs, consisting of combinations of 48.1 C-, 54.1 C- and 60.1 C-type thermoseeds, were used in simulations (Sec. 7.2.3). A Newton-Raphson technique was used to determine the temperature of each thermoseed for the power absorbed (Sec. 4.1.1).

7.5.1 Tumor Survival Model

The differences between fractional cell-survival models A and B are larger at lower temperatures, especially between 42 and 44 C, than at higher temperatures. Thus the difference in the objective function between tumor survival models A and B increased with thermoseed combinations that heated a small fraction of tumor to high temperatures. In general, there was little difference in the objective functions computed with tumor survival models A and B. It is concluded that since the hyperthermia cell survival of the tumor can only be approximated, differences, similar to the two models used herein, between the actual and the model of tumor cell survival will have a minimal influence on the objective function.

7.5.2 Influence of Blood Flow Models on Temperature Distributions

Modeling the tumor core as a necrotic region of constant, low blood flow versus modeling the tumor with a uniform, blood flow equal to normal muscle tissue at body temperature had a small influence on temperature predictions. The $T_{min,\,tumor}$ was only

0.1 C higher in simulations with the necrotic tumor-core model. The $T_{max,\ normal}$ and $T_{max,\ tumor}$ were between 0.2 and 0.6 C higher with the necrotic tumor-core model. Thus it is concluded that temperatures predicted with a necrotic tumor-core model will be slightly higher than the temperatures predicted with a uniform blood flow model in the tumor. However, this conclusion may not hold in simulations where thermoseeds are implanted within the tumor core or in simulations with higher blood flow rates in the tumor periphery.

Modeling the blood flow as constant and nine times higher in normal muscle tissue and the tumor periphery resulted in significantly lower temperatures than that of modeling the blood flow with a temperature-dependent model. In simulations, $T_{max,\ tumor}$ was between 1.3 and 3.5 C lower, $T_{min,\ tumor}$ was between 1.7 and 2.6 C lower and $T_{max,\ normal}$ was between 2.1 and 3.3 C lower with the constant blood flow model than the temperature-dependent model. The percentage of tumor tissue greater than temperatures between 42 and 50 C is between 0 and 65% higher over all thermoseed combinations with the temperature-dependent blood flow model.

7.5.3 Differentially-Loaded Thermoseed Designs

The temperature distributions achieved with differentially-loaded thermoseed designs were close to those of designs where thermoseed temperatures were fixed at the average temperature of the differentially-loaded designs. Absolute temperature differences between the differentially-loaded and uniformly-loaded designs were less than 0.8 C for $T_{min,\ tumor}$ and $T_{max,\ normal}$. Isotherms from simulations with a differentially-loaded design were similar to the uniformly-loaded design.

7.5.4 Objective Function

It is possible to use a patient-specific model and show that the objective function can assist in selecting an optimum thermoseed combination among several possible designs. The numerical value of the scalar weighting factor γ had some influence on the optimum design (Table 7.7). Ideally, the optimum thermoseed combination would be independent of the blood flow model since blood flow can never be known exactly. The optimum thermoseed combination was independent of the blood flow models with $\gamma = 1$. The optimum thermoseed combination did, however, depend on blood flow models when $\gamma = 0.2$, 0.5 and 0.8 (see Table 7.7). Therefore, it is critical that blood flow models simulate the actual blood flow as best as possible.

This study has developed two methods, the temperature descriptor method and the objective function method, to optimize hyperthermia treatments *a priori*. Without the objective function, the optimum ferromagnetic hyperthermia pretreatment plan would mostly likely be selected on the basis of two temperature descriptors, the $T_{min,\ tumor}$ and $T_{max,\ normal}$ temperatures. If the pretreatment plan were designed to maximize $T_{min,\ tumor}$ among all thermoseed combinations regardless of $T_{max,\ normal}$, then the combination with the highest operating temperature thermoseeds (combination 7) would maximize $T_{min,\ tumor}$. If the pretreatment plan were designed to minimize $T_{max,\ normal}$ regardless of $T_{min,\ tumor}$, then the combination with the lowest operating temperature thermoseeds (combination 1) would minimize $T_{max,\ normal}$. (The $T_{max,\ normal}$ was, however, lower than 45 C with seed combinations 4 and 6 which were warmer than combination 1 (see Figs. 7.15e and 7.17e).) If instead the pretreatment plan were designed to achieve a balance between maximizing $T_{min,\ tumor}$ and minimizing $T_{max,\ normal}$, which is the most frequently occurring design consideration, then selecting an optimum thermoseed combination is somewhat more difficult. For example, recall that blood flow models 5

and 6 are considered the models which most closely represent the blood flow in real tissue (last paragraph in Sec. 7.2.2). It would be difficult to select an optimum thermoseed combination based on achieving a balance between maximizing $T_{min,\ tumor}$ and minimizing $T_{max,\ normal}$, short of an educated guess and intuition (see the first six columns in Figs. 7.16e and 7.17e). Fortunately, though, the objective function identifies the optimum thermoseed combination. Instead of basing the optimum combination on a therapeutic trade-off between $T_{min,\ tumor}$ and $T_{max,\ normal}$, the *single-valued*, maximum of the objective function with $\gamma = 0.8$ would identify the optimum thermoseed combination. As such, the objective function may have an *advantage* over the method of selecting an optimum treatment plan based on maximizing $T_{min,\ tumor}$ or minimizing $T_{max,\ normal}$. The thermoseed combination which maximized $T_{min,\ tumor}$ also maximized the objective function with $\gamma = 1$ for every blood flow model (Figs. 7.12 through 7.17). Similarly, the thermoseed combination which minimized $T_{max,\ normal}$ and/or resulted in $T_{max,\ normal} < 45$ C also maximized the objective function with $\gamma = 0.2$ and 0.5.

In conclusion, the objective function was an effective method to aid in selecting optimum combinations of thermoseeds. Moreover, under the assumptions of the model, use of the objective function in pretreatment planning will ensure that, of all the possible combinations of thermoseed temperatures, the combination which *maximizes* the fraction of tumor killed will be selected as the optimum combination based on the desired treatment goal.

7.5.5 Tumor Site

In this chapter, a patient-specific, ferromagnetic hyperthermia pretreatment plan was developed for a tumor in the prostate. The objective function could also be used in pretreatment plans for other tumors that will receive brachytherapy. The sites of these

other tumors may include the brain, cervix and ocular tissues, among others. Based on the performance of the objective function to identify an optimum combination of thermoseed temperatures for a tumor in the prostate, it is likely that the objective function can identify an optimum seed combination which maximizes the fraction of tumor killed in these other tumor sites .

7.5.6 Discrete versus Continuous Search for Optimum Thermoseed Combination

The optimum thermoseed combinations identified by the objective function were based on *discrete* values in the operating temperature of the thermoseeds (*e.g.*, 48.1, 54. 1 and 60.1 C). The 48.1 C-, 54. 1 C- and 60.1 C-type thermoseeds were used in the present study because 48.1 and 54.1 C-type, Ni-Cu thermoseeds are ready-made and available for treatments (Brezovich 1991). It is possible, though, that the objective function could be maximized with thermoseed operating temperatures between 48.1 and 60.1 C. Thus the objective function could have been maximized by performing a *continuous* search for the optimum temperature of the thermoseeds.

Thermoseed locations in this chapter were fixed at catheter sites which were established by the oncologist and brachytherapy pretreatment considerations. It is possible and probably likely, however, that these catheter sites were not the optimal locations of thermoseeds required to achieve the best temperature distribution in the tumor and surrounding normal tissues. Again, the objective function could have been maximized by performing a continuous search for the optimal locations of the thermoseeds. The search for the optimal locations could have been performed simultaneously with the search for the operating temperature of the thermoseeds to obtain the *global* maximum of the objective function.

The 43 C isotherm in simulations with thermoseed combinations 5 and 6 encloses all but the upper right corner of the prostate and a significant amount of the bladder and rectum (Fig. 7.24). Thus it is expected that the global maximum of the objective function would be achieved with low-temperature thermoseeds at locations 2, 3, 7 and 9 (Fig. 7.3) and higher-temperature thermoseeds at sites 1, 4, 5 and 10. In addition, the objective function would probably be maximized globally if the high-temperature thermoseeds at sites 1, 4 and 5 were placed closer to the upper left, upper right, and lower right corners, respectively, in the prostate than that shown in Fig.7.3.

Chapter 8

Summary and Recommendations

A summary of this study and some concluding remarks and recommendations are presented in Sec. 8.1. Recommendations for further research and development of the work presented herein are discussed in Sec. 8.2.

8.1 Summary

This section contains a summary of ferromagnetic thermoseed and catheter models, the implementation of the power-versus-temperature dependence of thermoseeds, the physiologically-based objective function, and the performance of the objective function to identify a *best* set of thermoseed temperatures and interseed spacings in ferromagnetic hyperthermia.

8.1.1 Ferromagnetic Thermoseed Model

Analytical and numerical thermoseed models were developed in tissue models where the heat flow was assumed one-dimensional. Results from the point-source numerical thermoseed model showed that the thermoseed power P' goes to zero as the nodal area around the seed, over which the energy balance is performed, approached zero. In this case, the temperature gradient at the *surface* of the thermoseed would be infinite. Thus the point-source model is an invalid model.

The two finite-sized numerical thermoseed models had the shapes of a regular hexagon and a dodecagon (12-sided polygon) in radial cross-section. The temperature distributions determined with the hexagonal and dodecagonal thermoseed models match equally well with the analytically-determined temperature distribution. The dodecagonal thermoseed model was the preferred model because its cross-section more closely resembles a thermoseed.

Although the dodecagonal and hexagonal thermoseed models were developed in a symmetrical tissue model in which the temperature distribution was one-dimensional, both models are, however, general in their design. Thus the numerical models can be used in two-dimensional simulations. The complete three-dimensional model was not investigated.

8.1.2 Power-versus-Temperature Dependence of Thermoseed

Several simulations showed that fractions of tumor greater than 43 C are smaller in simulations when thermoseed temperatures depend on power versus models which assume a constant thermoseed temperature such as the Curie or operating temperature. Fractions of tumor greater than 43 C were between 8 and 40% lower when thermoseed temperatures depended on power versus models which assumed a constant temperature equal to the operating temperature. Fractions of tumor greater than 43 C were even larger than those achieved with the constant operating-temperature assumption if the Curie temperature was used as the assumed constant temperature. By using the iteration technique to determine thermoseed temperature for the power absorbed, it was shown that over an order-of-magnitude change in normal tissue blood flow and a 2.5-fold change in tumor blood flow, the temperature of thermoseeds changed by 1 to 2 C.

The location of a thermoseed in a square array combination can also alter thermoseed temperature. Thermoseeds furthest from the center of the square array had the highest power absorption and the lowest temperature, while thermoseeds closest to the center of the array had the lowest power absorption and the highest temperature. The difference in temperature between the furthest and closest thermoseeds to the center of the square array was between 0.4 and 2 C over thermoseed spacings between 9 and 15 mm.

The modeling of catheters around thermoseeds was shown to decrease the absorbed power of thermoseeds and increase their temperature versus modeling thermoseeds without catheters. The drops in temperature through the catheter walls were significant. The temperatures at the outer surface of catheters were between 1.7 and 6.8 C below the temperatures at the inner surface over a wide range of blood flow models and thermoseed types. Because of the temperature drop through the catheters, the fraction of tumor greater than 42 C in simulations using thermoseed and catheter models were between 1 and 45.3% lower over all blood flow models and thermoseed array types studied than in simulations with bare thermoseeds. In summary, because of the modest to dramatic temperature drops through catheter walls and the smaller fractions of tumor above 42 C for models of thermoseeds within catheters versus bare thermoseeds, more realistic temperature distributions will be obtained if catheter models are included in computer simulations.

The Implant-Biot number is a dimensionless variable that results from nondimensionalizing a tissue model which has implants separated by a uniform distance. The Implant-Biot number Bi_I ($= w_b c_b l^2/k_t$) is proportional to tissue perfusion $w_b c_b$ and to the square of thermoseed spacing l and inversely proportional to tissue thermal conductivity k_t. It was shown that for ferromagnetic hyperthermia treatment planning, changes in thermoseed spacing are more critical (*i.e.*, detrimental) than for the same

relative changes in tissue perfusion. It was also shown that the use of higher operating temperature thermoseeds more than off-sets the decrease in thermoseed temperatures caused by wider interseed spacing or higher tissue perfusion rates.

8.1.3 Physiologically-Based Objective Function

The objective function is a mathematical equation which was formulated to optimize hyperthermia treatments. Within the limits of the model, the maximum of the objective function identifies thermoseed temperatures and interseed spacings that deliver a *best* heat treatment. There are several important features of the objective function. First, the objective function has a physiological basis and considers increased cell killing at temperatures above 42 to 43 C (= $T_{min,\ thera.}$). Second, there is a (penalty) term, Ψ_N, in the objective function to account for heating of normal tissues above $T_{min,\ thera.}$. Third, because normal tissues below $T_{min,\ thera}$ are eliminated in the determination of the fraction of normal tissue killed (Ψ_N), the objective function is independent of normal tissue size and shape. Next, it was shown how Ψ_T can be compared with tumors of different shapes and sizes. Last, since there is a scalar weighting factor γ in the objective function that has treatment implications, the oncologist becomes an active participant in treatment planning. A guide for selecting γ was provided. The value of γ depends on hyperthermia pretreatment design considerations including the therapeutic goal and the thermal tolerance of normal tissues on the boundary of the tumor and normal tissues.

8.1.4 Performance of Objective Function with Ideal Tissue Model

The difference between the two tumor survival models had a small effect on the fraction of tumor killed and on the objective function. It was concluded that since the hyperthermia cell survival of the tumor can only be approximated, differences, similar to

the two models used herein, between the actual and the model of tumor cell survival should have a minimal influence on the objective function.

It was shown that the objective function was an effective method in identifying optimum thermoseed spacings. In several simulations, smaller (than the maximum) fractions of tumor would be killed if the pretreatment plan were based on maximizing $T_{min,\ tumor}$ and maintaining $T_{max,\ normal}$ = 45 C than if the pretreatment plan were based on maximizing F with $\gamma = 1$. Indeed, maximizing F with $\gamma = 1$ yielded thermoseed temperatures and interseed spacings that maximized the fraction of tumor killed in all blood flow models studied. Therefore, it is concluded from simulations on the simple tissue model that the objective function was an effective method in identifying optimum thermoseed configurations. In addition, the objective function may have an *advantage* over the method of selecting optimum seed configurations based on the $T_{min,\ tumor}$ and $T_{max,\ normal}$ temperature descriptors. That is, since the objective function is a *single-valued* number which can be used to select an optimum seed configuration, one avoids having to decide on the therapeutic trade-off between maximizing $T_{min,\ tumor}$ and minimizing $T_{max,\ normal}$ in order to identify an optimum seed design.

8.1.5 Performance of Objective Function with Patient-Specific Model

In general, there was little difference in the objective functions computed with tumor survival models A and B. It is concluded that since the hyperthermia cell survival of the tumor can only be approximated, differences, similar to the two models used herein, between the actual and the model of tumor cell survival will have a minimal influence on the objective function.

Two methods, the temperature descriptor method and the objective function method, were used to identify an optimum combination of thermoseed temperatures *a*

priori. It was shown that if the pretreatment plan were designed to achieve a balance between maximizing $T_{min,\ tumor}$ and minimizing $T_{max,\ normal}$, which is the most frequently encountered design consideration, then the objective function is the preferred method to choose the optimum combination.

In conclusion, the objective function can replace the temperature-descriptor method of selecting optimum combinations of thermoseeds. Under the assumptions of the model, use of the objective function in pretreatment planning will ensure that, of all the possible combinations of thermoseed temperatures, the combination which *maximizes* the fraction of tumor killed will be selected as the optimum combination based on the desired treatment goal.

8.1.6 Concluding Remarks

There were several important features in the objective function. The objective function was not, however, formulated to consider patient pain directly. In other words, there is no term in the objective function that accounts directly for pain. Indirectly, though, the weighting factor could be used to consider patient pain. A value for γ between 0.2 and 0.5 could be used in pretreatment planning of patients who have a low threshold of pain. Conversely, a value for γ between 0.8 and 1 could be used for patients with a high threshold of pain.

The objective function was shown in simulations to provide optimum thermoseed temperatures and spacings in square arrays that killed a greater fraction of tissue than thermoseed design choices that maximized $T_{min,\ tumor}$ and achieved $T_{max,\ normal} = 45$ C. Ultimately, though, the usefulness and adequacy of the objective function can only be validated through clinical trials. In a clinical trial, patients would be randomized to receive a ferromagnetic hyperthermia treatment where the thermoseed combination would be

based on temperature descriptors (*e.g.*, $T_{min,\ tumor}$ and $T_{max,\ normal}$) or to receive a treatment with a thermoseed combination that maximizes the objective function.

An issue of considerable interest in this study was blood flow modeling in the tumor and surrounding normal tissues. It was shown that temperature-dependent (versus constant) blood flow models had a significant effect on temperature distributions and optimum choices of thermoseed designs. Thus it is critical that models of blood flow approximate actual blood flow as closely as possible. However, the actual blood flow in several tissues at temperatures between 37 and 50 C is not known very well but is generally believed to be temperature dependent. As such, the temperature-dependent blood flow models used herein were based on published data (Song *et al.* 1984) from rat muscle and animal tumors. It is therefore concluded that temperature-dependent blood flow models similar to those used herein should be used in pretreatment planning. In the future, when other well-investigated, temperature-dependent, site-specific (*e.g.*, prostate, cervix, brain, etc.) blood flow data become available, these can be used in appropriate tissue models.

Presently the complete pretreatment planning process including finite element mesh creation should take no longer than 1.5 days in the worst case with this software and using a Newton-Raphson scheme. However, the variable-property routine in FEHT should *significantly* reduce the calculation time. Moreover, with the frequent release of new and faster computers, running the software on higher speed computers will further reduce the computational time. Therefore, complete two-dimensional, ferromagnetic hyperthermia pretreatment planning should require only about 0.5 days in the near future.

A major objective of this study was to develop a method that can be used to plan ferromagnetic hyperthermia treatments. The objective function was developed to provide a physiologically-based method with which hyperthermia treatments might be optimized *a*

priori. The objective function utilizes cell-survival curves. Critics of the objective function may argue that tumors are comprised of different cell types and each may be in a different phase of their cell cycle, with some phases being more resistant to heat than others. However, it was shown in this study that the fraction of tumor killed and the objective function was fairly insensitive between two different models of tumor cell survival. Still other critics may argue that the *use* of hyperthermia cell-survival curves to optimize ferromagnetic hyperthermia treatments may be *before its time*. After all, it is only recent, that some research has begun to focus on optimizing radiation therapy to cell cycle and proliferation rates. Nonetheless, the objective function developed herein is the first of its kind to incorporate the physiological response of tissue to heat into a pretreatment planning method. Under the assumptions of the models in the simulations investigated herein, the objective function was shown to identify optimal thermoseed temperatures and seed spacings by maximizing the fraction of tumor killed.

8.2 Recommendations & Further Research

Recommendations on how to use the objective function to plan ferromagnetic hyperthermia treatments is discussed in Sec. 8.2.1. Ideas for further research and development in ferromagnetic hyperthermia are presented in Sec. 8.2.2.

8.2.1 Recommendations

Recommendations on the use of the physiologically-based objective function to plan ferromagnetic hyperthermia treatments are presented below in a step-wise manner. The recommendations are subdivided into thermoseed designs using a square array and those using a combination of thermoseeds where seed location has been fixed previously by other considerations (*e.g.*, brachytherapy treatment planning).

Square Array of Thermoseeds

Step 1 Specify the temperature-dependent blood flow models in tumor and normal tissues.

Step 2 Specify the cell-survival model of normal tissue. Unless better data is available, assume the cell-survival model of tumor is equal to that of normal tissue.

Step 3 Compute the objective function for several weighting factors between 0.2 and 1 and arrays of thermoseeds with operating temperatures of 48.1, 54.1 and 60.1 C with interseed spacings between 8 to 15 mm.

Step 4 Determine the treatment goals and choose the weighting factor consistent with those goals.

Step 5 Select the operating temperatures and spacing of the thermoseeds in the array which maximizes the objective function for the chosen weighting factor.

Fixed Location of Thermoseeds

Step 1 Specify the temperature-dependent blood flow models in tumor and normal tissues.

Step 2 Specify the cell-survival model of normal tissue. Unless better data is available, assume the cell-survival model of tumor is equal to that of normal tissue.

Step 3 Compute the objective function for several weighting factors between 0.2 and 1 and arrays of thermoseeds with operating temperatures of 48.1, 54.1 and 60.1 C

Step 4 Determine the treatment goals and choose the weighting factor consistent with those goals.

Step 5 Select the operating temperatures of the thermoseeds in the array which maximizes the objective function for the chosen weighting factor.

8.2.2 Further Research

Areas of further research include: (1) the inclusion of treatment time into the model of cell kill in the objective function (Sec. 8.2.2.1) (2) assessing the applicability of the Pennes bioheat transfer equation to predict temperatures in a two-dimensional model which were measured previously in an *in vivo* model (Sec. 8.2.2.2), (3) theoretical and experimental studies on using ferromagnetic hyperthermia to treat choroidal melanomas (Sec. 8.2.2.3), (4) the development of general-purpose, two-dimensional ferromagnetic hyperthermia pretreatment planning software (Sec. 8.2.2.4), (5) the extension of the two-dimensional software (FEHT) to three dimensions (Sec. 8.2.2.5).

8.2.2.1 Hyperthermia Treatment Time

The inclusion of treatment time into the model of cell kill in the objective function could also be studied with computer models. Recall that hyperthermia cell-survival curves are a function of temperature *and* time, among others (Ch. 5). It may be possible to show with simulations that shorter treatment times are needed with higher temperature thermoseeds to kill the same fraction of tumor as that needed with lower temperature thermoseeds and longer treatment times. However, there may be practical limits to transferring these results to the clinic. After all, the objective function does not consider patient pain directly, and the use of higher temperature thermoseeds will most likely result increased patient pain.

8.2.2.2 Applicability of the Pennes Bioheat Transfer Equation

Tompkins *et al.* (1992a) studied the effect of several ferromagnetic hyperthermia treatment variables including generator power level, interseed spacing, thickness of catheter walls and orientation of a 3x3 array of thermoseeds. The effects of these

variables were studied both *in vitro* in tissue equivalent phantom material (*i.e.*, gel) and *in vivo* in the hindlimb of rabbits. Transient and steady-state temperatures were measured and recorded at several interseed locations. The accuracy of the dodecagonal thermoseed and catheter models developed in Chapters 3 and 4 could be assessed by comparing the experimental data from Tompkins *et al.* (1992a) to simulations using the thermoseed and catheter models. A study of this kind should reveal the applicability of using the Pennes bioheat equation to predict measured temperature response.

8.2.2.3 Choroidal Melanoma Study

A major effort is underway at the University of Wisconsin to treat choroidal melanomas (tumors originating subretinally in the inferior portion of the eye) with a combination of hyperthermia and radiation (Steeves *et al.* 1992). Current protocols allow for randomization of choroidal melanoma patients to enucleation (or removal) of the eye or to receive 100 Gy of ^{125}I radiation to the tumor apex (COMS or the Collaborative Ocular Melanoma Study). The radiation alone therapy is delivered with episcleral plaques (*i.e.*, small circular, silastic disks) that contain several (12-15) ^{125}I sources. The combined hyperthermia and brachytherapy treatment, however, uses 10 ^{125}I and four thermoseeds in a parallel, alternate arrangement on the surface of the plaque (Steeves *et al.* 1992). There is evidence that tumor control with the combined radiation-hyperthermia method can be achieved with (significantly) lower amounts of radiation than with radiation alone (Steeves *et al.* 1992). The lower amount of radiation may reduce the magnitude and frequency of normal tissue damage (*e.g.*, hemorrhaging, blindness, etc.) engendered by the radiation-only therapy.

Upon completion of the present study, research will focus on experiments to measure temperature distributions in the eye produced by heating of the combined

radiation-hyperthermia plaque. A computer model will be developed to predict the experimental results. It is possible, that the physiologically-based objective function may be used to optimize the heat treatments from the episcleral plaques.

8.2.2.4 General-Purpose Ferromagnetic Hyperthermia Pretreatment Planning Software

For the purpose of this research project, several ferromagnetic hyperthermia treatment variables were hard-wired (*i.e.*, placed within the source code) into FEHT. The treatment variables include the magnetization-versus-temperature dependence and the electrical conductivity of the thermoseeds, thermoseed and catheter wall thicknesses, and the frequency and strength of magnetic field. Since these variables are hard-wired, it is impossible to alter the values of these variables without access to the FEHT *source* code. General-purpose ferromagnetic hyperthermia pretreatment planning software would, however, allow users to alter variables with an *executable* version of FEHT. The following is a brief discussion of the modifications required to transform FEHT into a general-purpose, ferromagnetic hyperthermia treatment planning software. The discussion consists of three modifications. Each modification is depicted by a bold type **Current** which discusses the current features of FEHT and bold type **Modification** which describes the modification to FEHT.

Current

When the user selects 'Bio-Heat Transfer' from the Subject menu, the 'Blood Temperature' menu item appears at the bottom of the Setup menu.

Modification 1

Place a menu item entitled 'Hyper Treatment' below the 'Blood Temperature' menu item (Fig. 8.1). After selecting the 'Hyper Treatment' menu item, a dialog box could

appear as shown in Fig. 8.2. The dialog box would allow the user to specify the thermoseed radius and catheter wall thickness. Three different thermoseed types could be specified where the magnetization and electrical conductivity could depend on temperature. The strength and frequency of the magnetic field could be specified. The thickness, magnetization and electrical conductivity of the thermoseeds and the strength and frequency of the magnetic field would be used to evaluate the power absorption of thermoseeds (recall Eq. 4.2).

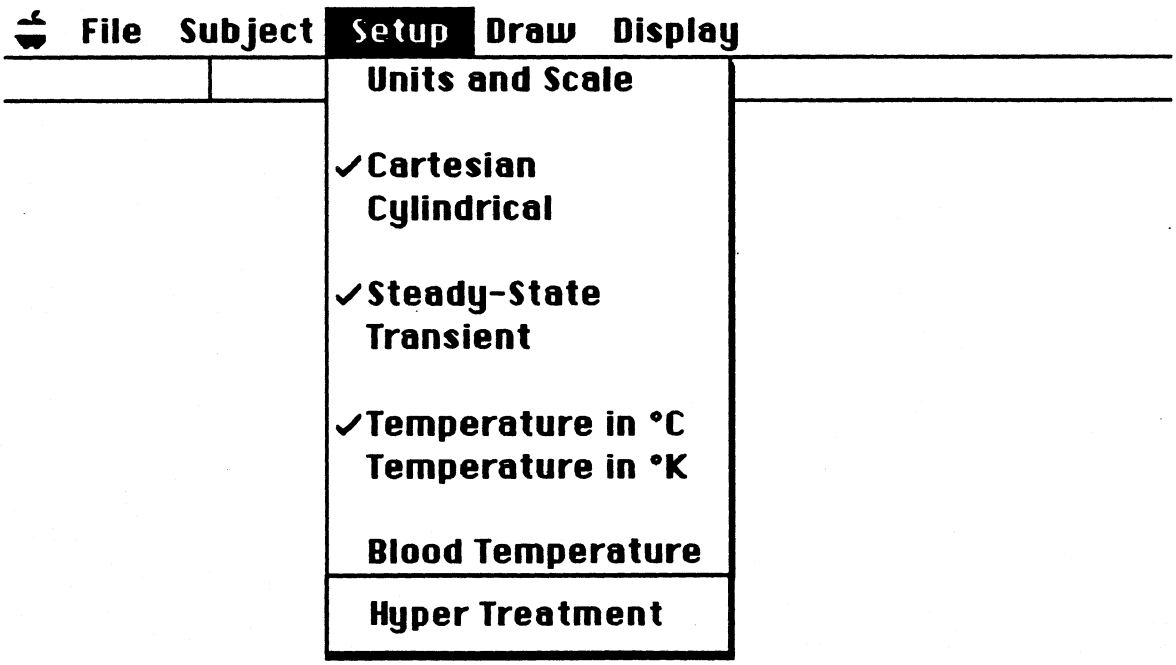

Figure 8.1 Modified 'Setup' Menu

Current

When the user selects 'Add Seed' from the Draw menu, the arrow head changes into a cross-hair and the user can place models of thermoseeds into the finite element mesh (recall Sec. 3.4).

Modification 2

Two sub-menu items entitled 'Catheter' and 'No Catheter' should be placed next to the 'Add Seed' menu item (Fig. 8.3). When the user selects 'Add Seed' from the Draw menu, the catheter option will be made available. By designating 'Catheter' as

the active option, the thermoseed model will include a catheter with the wall thickness as previously designated in the 'Hyper Treatment' dialog box. The thermal model of the catheter has been discussed (recall Sec. 3.4).

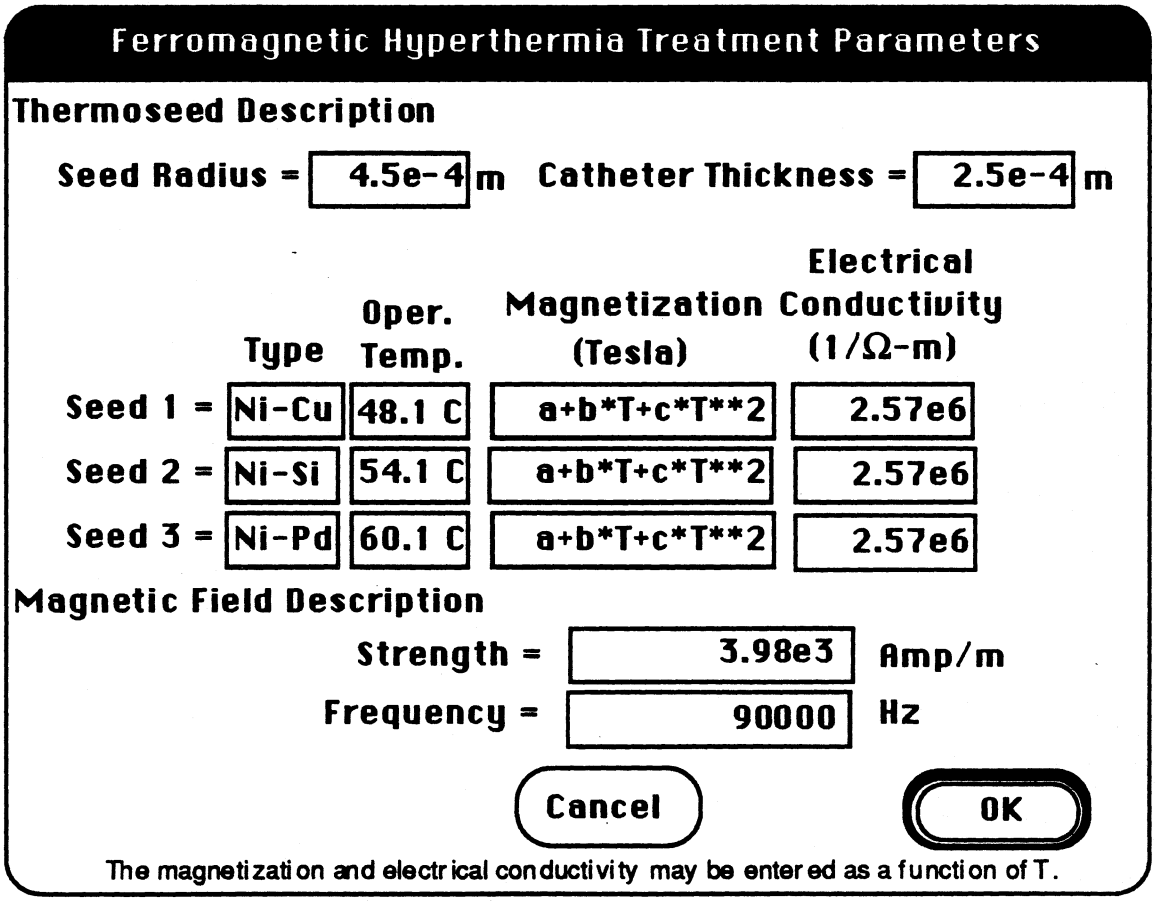

Figure 8.2 'Hyper Treatment' dialog box

Current

The 'Run' menu item contains options to perform a 'Check' of the finite element mesh, to 'Calculate' or determine the unknown temperatures, and to 'Continue' during specified break points during a transient calculation.

Modification 3

Place a menu item entitled 'Do Iteration' below the 'Continue' menu item (Fig. 8.4). By choosing the 'Do Iteration' option, thermoseed temperatures will be determined with the iteration technique described Sec. 4.1.1.1.

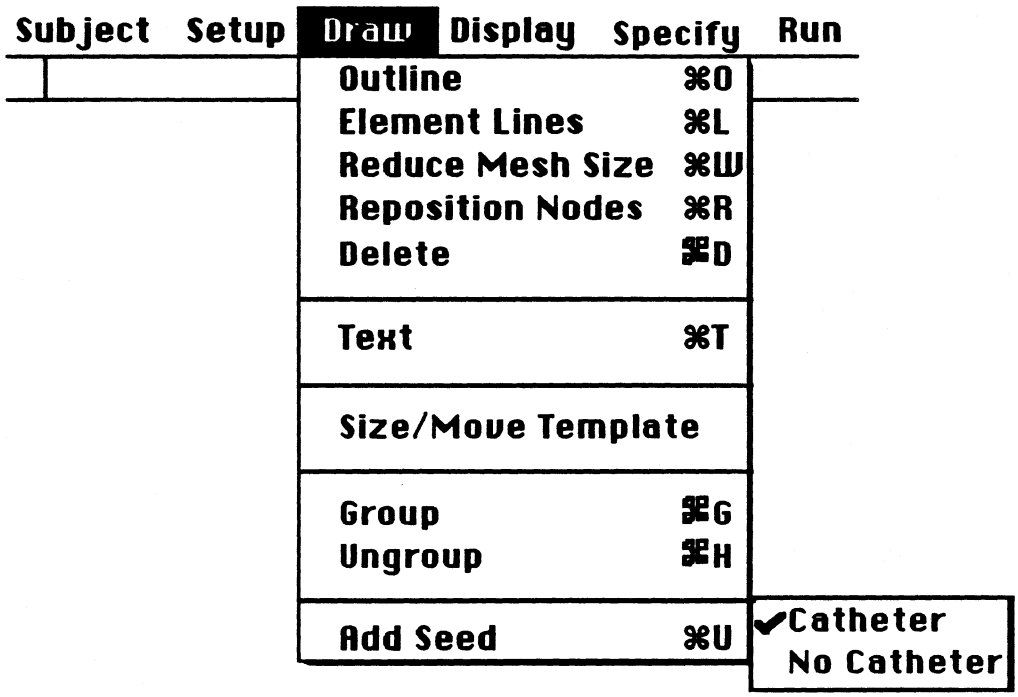

Figure 8.3 Modified 'Draw' Menu

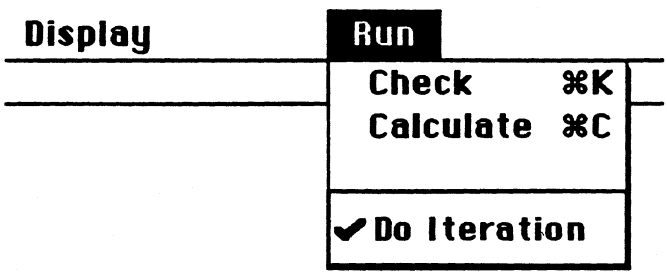

Figure 8.4 Modified 'Run' Menu

The development of general-purpose ferromagnetic hyperthermia pretreatment planning software could find use among several institutions currently administering this form of therapy to patients.

8.2.2.5 Three-Dimensional Treatment Planning Software

Ultimately, the two-dimensional treatment planning software (FEHT) should be extended to three-dimensions. Studies contrasting the temperature distributions from two- and three-dimensional models of ferromagnetic thermoseeds have shown that two-dimensional modeling is sufficient only under certain conditions. One condition is that the thermoseeds should be longer than 30 mm and that the plane modeled is perpendicular to the thermoseeds and centrally-located within the tumor (Chen *et al.* 1991). Another condition is that the plane modeled should be perpendicular to the thermoseeds and at a distance of at least 10 mm from the ends of the thermoseeds (Chin and Stauffer 1991). Since there is growing clinical interest at the UW (and elsewhere) in the use of combined brachytherapy and ferromagnetic hyperthermia by combining alternately, short (4 mm) radiation and ferromagnetic thermoseeds end-to-end in catheters, complete three-dimensional modeling will be necessary.

In the development of the three-dimensional software, consideration must be given to the order (or basis function) of the finite elements. In the case of linear elements, the three-dimensional extension of the two-dimensional, triangular finite element (used in FEHT) is the tetrahedron. Other linear elements include the pentahedral and hexahedral, among others. In the development of three-dimensional finite element software for an interstitial microwave hyperthermia system, it was shown that solutions obtained with tetrahedrons required longer (by a factor of two or three) CPU times than with pentahedrals and hexahedrals (Mechling 1990). Thus the use of pentahedrals and

hexahedrals over tetrahedrons should reduce the critically-important CPU time. For ease in development, the consideration of higher order elements will be limited to quadratics.

To reduce the time needed to create three-dimensional finite element meshes, consideration must be given to the use of auto-meshing techniques and the expedient transfer of CT/MRI data to the host computer. Here, there is a vast supply of techniques that can be used for expedient mesh generation.

REFERENCES

Abramowitz, M.B., and Stegun, I.A., eds., 1964. Handbook of mathematical functions with formulas, graphs, and mathematical tables. Dover Publications, Inc., N.Y.

Arcangeli, G., Lombardini, P.P., Lovisolo, G.A., Marsiglia, G., Piattelli, M., 1984. Focusing of 915 MHz electromagnetic power on deep human tissues: a mathematical model study. IEEE Transactions on Biomedical Engineering 31: 47- 52.

Astrahan, M.A., and Norman, A., 1982. A localized current field hyperthermia system for use with 192-iridium interstitial implants. Medical Physics 9: 419-424.

Atkinson, W.J., Brezovich, I.A., Chakraborty, D.P., 1984. Usable frequencies in hyperthermia with thermal seeds. IEEE Transactions in Biomedical Engineering 31: 70-75.

Barlogie, B., Corry, P.M., Yip, E., Lippman, L., Johnston, D.A., Khalil, K., Tenczynski, T.F., Reilly, E., Lawson, R., Dosik, G., Rigor, B., Hankenson, R., Freireich, E.J., 1979. Total-body hyperthermia with and without chemotherapy for advanced human neoplasms. Cancer Research 39: 1485-1493.

Ben-Hur, E., Elkind, M.M., Riklis, E., 1978. The combined effects of hyperthermia and radiation in cultured mammalian cells. In: Cancer Therapy by Hyperthermia and Radiation, Proceedings of the 2nd International Symposium, Essen, June 2-4, 1977, Streffer, C., van Beuningen, D., Dietzel, F., Rottinger, E., Robinson, J.E., Scherer, E., Seeber, S., Trott, K.R., eds., Baltimore, Munich, Urban & Schwarzenberg, pp. 29-36.

Beyer, W.H., ed., 1981. CRC standard mathematical tables. CRC Press, Inc., Boca Raton, FL, pg. 122.

Bowman, H.F., 1980. Heat transfer mechanisms and thermal dosimetry. 3rd International Symposium Cancer Therapy Hyperthermia, Drugs, and Radiation, Fort Collins, CO, June 22-26, 1980.

Bowman, H.F., Cravalho, E.C., Woods, M., 1975. Theory, measurement, and application of thermal properties of biomaterials. Annual Review of Biophysics and Bioengineering 4: 43-80.

Brezovich, I.A., 1991. Personal communication. Department of Medical Physics, University of Alabama, Birmingham, AL.

Brezovich, I.A., and Atkinson, W.J., 1984. Temperature distributions in tumor models heated by self-regulating nickel-copper alloy thermoseeds. Medical Physics 11: 145-152.

Brezovich, I.A., Lilly, M.B., Meredith, R.F., Weppelmann, B., Henderson, R.A., Brawner, W.R., Salter, M.M., 1990. Hyperthermia of pet animal tumors with self-regulating ferromagnetic thermoseeds. International Journal Hyperthermia 6: 117-130.

Brezovich, I.A., and Meredith, R.F., 1989. Practical aspects of ferromagnetic thermoseed hyperthermia. In: Steeves, R.A., ed., The Radiologic Clinics of North America. Philadelphia: W.B. Saunders Co., pp. 589-602.

Brezovich, I.A., Meredith, R.F., Henderson, R.A., Brawner, W.R., Weppelmann, B., Salter, M.M., 1989. Hyperthermia with water-perfused catheters. In: Overgaard, J., ed., Hyperthermic Oncology. London: Taylor and Francis, pp. 809-810.

Bronk, B.V., 1976. Thermal potentiation of mammalian cell killing: clues for understanding and potential for tumor therapy. In: Advances in Radiation Biology, vol. 6, Lett, J.T. and Adler, H., eds., New York, Academic Press, pp. 267-324.

Burnett, D.S., 1987. Finite element analysis: From concepts to applications. Addison-Wesley Publishing, Reading, MA, Ch. 9.

Burton, C.V., Hill, M., Walker, A.E., 1971. The RF thermoseed–A thermally self-regulating thermoseed. IEEE Transactions in Biomedical Engineering 18: 104-109.

Carslaw, H.S., and Jaeger, J.C., 1959. Conduction of heat in solids. 2nd edition, Fair Lawn, NJ: Oxford University Press.

Cavaliere, R., Ciocatto, E.C., Giovanella, B.C., Heidelberger, C., Johnson, R.O., Margottini, M., Mondovi, B., Moricca, G., Rossi-Fanelli, A., 1967. Selective heat sensitivity of cancer cells: Biochemical and clinical studies. Cancer 20: 1351-1381.

Chen, J.S., Poirier, D.R., Damento, M.A., Demer, L.J., Biencaniellow, F., Cetas, T.C., 1988. Development of Ni-4 weight percent Si thermoseeds for hyperthermia cancer treatment. Journal of Biomaterials Research 22: 303-319.

Chen, M.M., and Holmes, K.R., 1980. Microvascular contributions in tissue heat transfer. Annals of New York Academy of Science 355: 137-150.

Chen, Z.P., 1989. Three dimensional hyperthermia cancer treatment simulation. Ph.D. dissertation, Department of Aerospace and Mechanical Engineering, University of Arizona, Tucson, AZ.

Chen, Z.P., Roemer, R.B., Cetas, T.C., 1991. Errors in the two-dimensional simulation of ferromagnetic implant hyperthermia. International Journal of Hyperthermia 7: 735-739.

Chin, R.B., and Stauffer, P.R., 1991. Treatment planning for ferromagnetic seed heating. International Journal Radiation Oncology, Biology and Physics 21: 431-439.

Clay Adams Co., 1991. Thermophysical properties of polyethylene tubing (PE 200), Phone call to Clay Adams Co., Parisippany, NJ.

Coley, W.B., 1893. The treatment of malignant tumors by repeated inoculations of erysipelas: with a report of ten original cases. American Journal Medical Science, 105: 486-511.

Cooper, T.E., and Trezek, G.J., 1971. Correlation of thermal properties of some human tissues with water content. Aerospace Medicine 42: 24-27.

Coughlin, C.T., Wong, T.Z., Strohbehn, J.W., Colacchhio, T.A., Sutton, J.E., Belch, R.Z., Douple, E.B., 1985. Intraoperative interstitial microwave-induced hyperthermia and brachytherapy. International Journal Radiation Oncology, Biology and Physics 11: 1673-1678.

Crile, G., 1963. The effects of heat and radiation on cancers implanted on the feet of mice. Cancer Research 23: 372-380.

Daikuzono, N., Joffe, S.N., Tajiri, H., Suzuki, S., Tsunekawa, H., Ohyama, M., 1987. Laserthermia: a computer-controlled contact Nd:YAG system for interstitial local hyperthermia. Medical Instrumentation 21: 275-277.

Davies, E.J., and Simpson, P., 1979. Induction heating handbook. Maindenhead and Berkshire, England: McGraw-Hill.

De Wagter C., 1986. Optimization of simulated two-dimensional temperature distributions induced by multiple electromagnetic applicators. IEEE Transactions on Microwave Theory and Techniques 34: 589-596.

Dewey, W.C., Freeman, M.L., Raaphorst, G.P., Clark, E.P., Wong, R.S.L., Highfield, D.P., Spiro, I.J., Tomasovic, S.P., Denman, D.L., Coss, R.A., 1980. Cell biology of hyperthermia and radiation. In: Radiation Biology in Cancer Research. Meyn, R.E., Withers, H.R., eds., New York: Raven Press, pp. 589-621.

Dewey, W.C., Hopwood, L.E., Sapareto, S.A., Gerweck, L.E., 1977a. Cellular responses to combinations of hyperthermia and radiation. Radiology 123: 463-474.

Dewey, W.C., Thrall, D.E., Gillette, E.L., 1977b. Hyperthermia and radiation–A selective thermal effect on chronically hypoxic tumor cells *in vivo*, International Journal Radiation Oncology, Biology and Physics 2: 99-103.

Dewhirst, M.W., Sim, D.A., Sapareto, S.A., and Connor, W.G., 1984. Importance of minimum tumor temperature in determining early and long-term responses of spontaneous canine and feline tumors to heat and radiation. Cancer Research 44: 43-50.

Dickson, J.A., Shah, S.A., Waggott, D., Whalley, W.B., 1977. Tumor eradication in the rabbit by radiofrequency heating. Cancer Research 37: 2162-2169.

Emami, B., Myerson, R.J., Scott, C., Gibbs, R., Lee, C., Perez, C.A., 1991. Phase I/II study, combination of radiotherapy and hyperthermia in patients with deep-seated

malignant tumors: Report of a pilot study by the radiation therapy oncology group. International Journal Radiation Oncology, Biology, Physics 20: 73-79.

Emami, B., Perez, C.A., Leybovich, L., Straube, W., Vongerichten, D., 1987. Interstitial thermoradiotherapy in treatment of malignant tumours. International Journal of Hyperthermia 3: 107-118.

Fessenden, P., Lee, E.R., Anderson, T.L., Strohbehn, J.W., Meyer, J., Samulski, T.V., Marmor, J.B., 1984. Experience with a multitransducer ultrasound system for localized hyperthermia of deep tissues. IEEE Transactions on Biomedical Engineering 31: 126-135.

Fessenden, P., Meyer, J.L., Valdagni, R., Lee, E.R., Samulski, T.V., Kapp, D.S., Bagshaw, M.A., 1985. Analysis of deep hyperthermia treatments using six ultrasound transducers in a fixed frequency/fixed geometry configuration. Abstracts of Papers for the 33rd Annual Meeting of the Radiation Research Society, p. 15.

Freeman, M.L., Dewey, W.C., Hopwood, L.E., 1977. Effect of pH on hyperthermic cell survival: Brief communication. Journal National Cancer Institute 58: 1837-1839.

Ganong, W.C., 1967. Review of medical physiology. Lange Medical Publications, Los Altos. CA.

Gerweck, L.E., Gillette, E.L., Dewey, W.C., 1975. Effect of heat and radiation on synchronous Chinese hamster cells: Killing and repair. Radiation Research 64: 611-623.

Gerweck, L.E., Nygaard, T.G., Burlett, M., 1979. Response of cells to hyperthermia under acute and chronic hypoxic conditions. Cancer Research 39: 966-972.

Gibbs, F.A., 1984. Regional hyperthermia: a clinical appraisal of non-invasive deep-heating methods. Cancer Research 44 (suppl.): 4765-4770.

Gordon, R.B., Roemer, R.B., Howath, S.M., 1976. A mathematical model of the human temperature regulatory system - transient cold exposure response. IEEE Transactions in Biomedical Engineering 23: 434-444.

Hahn, G.M., 1974. Metabolic aspects of the role of hyperthermia in mammalian cell inactivation and their possible relevance to cancer treatment. Cancer Research 34: 3117-3123.

Hahn, G.M., Marmor, J.B., Pounds, D., 1981. Induction of hyperthermia by ultrasound. Bulletin Cancer, Paris, 68: 249-254.

Haider, S.A., Cetas, T.C., Wait, J.R., Chen, J.S., 1991. Power absorption in ferromagnetic implants from radiofrequency magnetic field and the problem of optimization. IEEE Transactions Microwave Theory and Techniques 39: 1817-1827.

Hall, E.J., 1988. Radiobiology for the radiologist, 3rd edition, Philadelphia, PA: J.B. Lippincott, Chapter 14.

Hand, J.W., Trembly, B.S., Prior, M.V., 1991. Physics of interstitial hyperthermia: radiofrequency and hot water techniques. In: Urano, M., Douple, E., eds., Hyperthermia and oncology. vol. 3, Interstitial hyperthermia, Zeist.

Hill, S.A., and Denekamp, J., 1978. The effect of vascular occlusion on the thermal sensitization of a mouse tumour. British Journal Radiology 51: 997-1002.

Hynynen, K., Roemer, R., Anhalt, D., Johnson, C., Xu, Z.X., Swindell, W., Cetas, T.C., 1987. A scanned focused, multiple transducer ultrasonic system for localized hyperthermia treatments. International Journal of Hyperthermia 3: 21-35.

Incropera, F.P., and DeWitt, D.P., 1985. Introduction to heat transfer. John Wiley Publishing, New York, NY, pg. 669.

Jain, R.K., 1983. Bioheat transfer: mathematical models of thermal systems. In: Storm, F.K., ed., Hyperthermia in cancer therapy. Boston, MA: G.K. Hall Medical Publishers, pp. 9-46.

Jain, R.K., Grantham, F.H., Gullino, P.M., 1979. Blood flow and heat transfer in Walker 256 mammary carcinoma. Journal of National Cancer Institute 62: 927-933.

Johnsen, M., 1989. Theoretical studies on the influence of blood vessels on bioheat transfer. M.S. Thesis, Thayer School of Engineering, Hanover, NH.

Kapp, D.S., Fessenden, P., Samulski, T.V., Bagshaw, M.A., Cox, R.S., Lee, E.R., Lohrbach, A.W., Meyer, J.L., Prionas, S.D., 1988. Stanford University institutional report: phase I evaluation of equipment for hyperthermia treatment of cancer. International Journal of Hyperthermia 4: 75-115.

Kapp, D.S., and Meyer, J.L., 1990. Clinical hyperthermic practice: non-invasive heating. In: Field, S.B., Hand, J.W., An introduction to the practical aspects of clinical hyperthermia, London: Taylor & Francis, pp. 143-171.

Klein, S.A., 1989. Personal communication. Mechanical Engineering Dept., University of Wisconsin, Madison, WI.

Klein, S.A., and Alvarado, F.L., 1989. EES: Engineering Equation Solver, Numerical equation solving software. Mechanical Engineering Dept., University of Wisconsin-Madison, Madison, WI.

Klein, S.A., Beckman, W.A., Myers, G.E., 1988. FEHT: Finite Element Heat Transfer software. Mechanical Engineering Dept., University of Wisconsin-Madison, Madison, WI.

Kobayashi, T., Kida, Y., Tanaka, T., Kageyama, N., Kobayashi, H., Amemiya, Y., 1986. Magnetic induction hyperthermia for brain tumor using ferromagnetic implant with low Curie temperature. Journal of Neuro-Oncology 4: 175-181.

Lagendijk, J.W., 1982. The influence of blood flow in large vessels on the temperature distribution in hyperthermia. Physics in Medicine and Biology 27: 17-23.

Lassen, N.A., Lindbjerg, J., Munck, O., 1964. Measurement of blood flow through skeletal muscle by intra muscular injection of Xenon-133. Lancet 1: 686-689.

Lele, P.P., 1983. Physical aspects and clinical studies with ultrasonic hyperthermia. In: Storm, F.K., ed., Hyperthermia in Cancer Therapy, Boston: Hall, pp. 333-367.

Leopold, K.A., Dewhirst, M., Samulski, T., Harrelson, J., Tucker, J.A., George, S.L., Dodge, R.K., Grant, W., Clegg, S., Prosnitz, L.R., Oleson, J.R., 1992. Relationships among tumor temperature, treatment time, and histopathological outcome using preoperative hyperthermia with radiation in soft tissue sarcomas. International Journal of Radiation Oncology, Biology and Physics 22: 989-998.

Lilly, M.B., Brezovich, I.A., Atkinson, W.J., 1985. Hyperthermia induction with thermally self-regulated ferromagnetic implants. Radiology 154: 243-244.

Marmor, J.B., Hahn, N., Hahn, G.M., 1977. Tumor cure and cell survival after localized radiofrequency heating, Cancer Research 37: 879-883.

Marmor, J.B., Hilerio, F.J., Hahn, G.M., 1979. Tumor eradication and cell survival after localized hyperthermia induced by ultrasound. Cancer Research 39: 2166-2171.

Matloubieh, A.Y., Roemer, R.B., Cetas, T.C., 1984. Numerical simulation of magnetic induction heating of tumors with ferromagnetic seed implants. IEEE Transactions in Biomedical Engineering 31: 227-234.

Mechling, J.A., 1990. Treatment planning software for the Dartmouth IMAAH system. Ph.D. thesis, Thayer School of Engineering, Dartmouth College, Dartmouth, NH.

Mechling, J.A., and Strohbehn, J.W., 1986. A theoretical comparison of the temperature distributions produced by three interstitial hyperthermia systems. International Journal Radiation Oncology, Biology and Physics 12: 2137-2149.

Mitchell, J.W., Galvez, T.L., Hengle, J., Myers, G.E., Siebecker, K.L., 1970. Thermal response of human legs during cooling. Journal of Applied Physiology 29: 859-865.

Moidel, R.A., Wolfson, S.K., Selker, R.G., Weiner, S.B., 1976. Materials for selective tissue heating in a radiofrequency electromagnetic field for the combined chemothermal treatment of brain tumors. Journal Biomedical Materials Research 10: 327-334.

Myers, G.E., 1987. Analytical methods in conduction heat transfer. Schenectady, NY: Genium Publishing Co.

Myers, G.E., 1989, Class notes from formal course in numerical methods of solving heat conduction equation (ME 764). Mechanical Engineering Dept., University of Wisconsin, Madison, WI.

Nauts, H.C., 1982. Bacterial products in the treatment of cancer: past, present and future. In: Jeljaszewics, J., Pulverer, G., Roskowski, W., eds., Bacteria and Cancer. London, New York: Academic Press, pp. 1-25.

Nevins, R.G., Darwish, M.A., 1970. Heat transfer through subcutaneous tissue as heat generating porous material. In: Hardy, J.D., Gagge, A.P., Stolwijk, J.A., eds., Physiological and Behavioral Temperature Regulation, Springfield, IL: Charles C. Thomas Publisher, Ch. 21, pp. 281-301.

Nielsen, S.L., 1972. Measurement of blood flow in adipose tissue from washout of Xenon-133 after atraumatic labelling. Acta Physiology Scandinavia 84: 187-196.

Ocheltree, K.B., and Frizzell, L.A., 1988. Determination of power deposition patterns for localized hyperthermia: a transient analysis. International Journal of Hyperthermia 4: 281-296.

Oleson, J.R., and Cetas, T.C., 1982. Clinical hyperthermia with RF currents. In: Nussbaum, G.H., ed., Physical aspects of hyperthermia. New York: American Institute of Physics, pp. 280-306.

Oleson, J.R., Sim, D.A., Conrad, J., Fletcher, A.M., Gross, E.J., 1986. Results of a phase I regional hyperthermia device evaluation: microwave annular array versus radiofrequency induction coil. International Journal of Hyperthermia 2: 327-336.

Overgaard, J., 1982. The design of clinical trials. In: Field, S.B., Franconi, C., eds., Hyperthermic Oncology, Physics and Technology of Hyperthermia, Amsterdam: Martinus Nijhuff Publishers.

Overgaard, J., 1978. The effect of local hyperthermia alone, and in combination with radiation, on solid tumors. In: Cancer Therapy by Hyperthermia and Radiation. Proceedings of the 2nd International Symposium, Essen, June 2-4, 1977, Streffer et al, eds., Baltimore, Munich, Urban & Schwarzenberg, pp. 49-61.

Overgaard, J., 1977. Effect of hyperthermia on malignant cells *in vivo*. A review and a hypothesis. Cancer 39: 2637-2646.

Overgaard, J., 1976. Influence of extracellular pH on the viability and morphology of tumor cells exposed to hyperthermia. Journal of National Cancer Institute 56: 1243-1250.

Overgaard, J., and Nielsen, O.S., 1980. The role of tissue environmental factors on the kinetics and morphology of tumor cells exposed to hyperthermia. Annals of New York Academy of Science 335: 254-278.

Overgaard, K., and Overgaard, J., 1972. Investigations on the possibility of a thermic tumour therapy–I. Short-wave treatment of a transplanted isologous mouse mammary carcinoma. European Journal of Cancer 8: 65-78.

Overgaard, J., and Suit, H.D., 1979. Time-temperature relation in hyperthermic treatment of malignant and normal tissue *in vivo*. Cancer Research 39: 3248-3253.

Parks, L.C., Minaberry, D., Simith, D.P., Neely, W.A., 1979. Treatment of far-advanced bronchogenic carcinoma by extracorporeally induced systemic hyperthermia. Journal of Thoracic Cardiovascular Surgery 78: 883-892.

Partington, B.P., Steeves, R.A., Su, S.L., Paliwal, B.R., Dubielzig, R.R., Wilson, J.W., Brezovich, I.A., 1989. Temperature distributions, microangiographic and histopathologic correlations in normal tissue heated by ferromagnetic needles. International Journal Hyperthermia 5: 319-327.

Pennes, H.H., 1948. Analysis of tissue and arterial blood temperatures in the resting human forearm. Journal of Applied Physiology 1: 93-122.

Perez, C.A. and Emami, B., 1989. Clinical trials with local (external and interstitial) irradiation and hyperthermia. Current and future perspectives. Radiologic Clinics of North America 27: 525-542.

Perl, W., 1965. Heat and matter distribution in body tissues and the determination of tissue blood flow by local clearance methods. Journal Theoretical Biology 2: 201-235.

Petrovich, Z., Langholz, B., Gibbs, F.A., Sapozink, M.D., Kapp, D.S., Stewart, R.J., Emami, B., Oleson, J., Senzer, N., Slater, J., Astrahan, M., 1989. Regional hyperthermia for advanced tumors: A clinical study of 353 patients. International Journal of Radiation Oncology, Biology, Physics 16: 601-607.

Pettigrew, R.T., Galt, J.M., Ludgate, C.M., Horn, D.N., Smith, A.N., 1974. Circulatory and biochemical effects of whole body hyperthermia, British Journal Surgery, 61: 727-730.

Priesching, A, 1976. Hyperthermie in der Krebsbehandlung. In: Prophylaxe und Therapie von Behandlungsfolgen bei Karzinomen der Frau; 2. Oberaudorger Gespräch, Oktober, 1975, Hrsg. von D. Schmähl, Stuttgart, Thieme Verlag, pp. 56-64.

Robins, H.I., Dennis, W.H., Neville, A.J., Shecterie, L.M., Marion, P.A., Grossman, J., Davis, T.E., Neville, S.R., Gillis, W.K., Rusy, B.F., 1985. A nontoxic system for 41.8 C whole-body hyperthermia: results of a phase I study using a radiant heat device. Cancer Research 45: 3937-3944.

Robins, H.I., Steeves, R.A., Clark, A.W., Martin, P.A., Miller, K., Dennis, W.H., 1983. Differential sensitivity of AKR murine leukemia and normal bone marrow cells to hyperthermia. Cancer Research 43: 4951-4955.

Roemer, R.B., 1988. Heat transfer in hyperthermia treatments: basic principles and applications. In: Paliwal, B.R., Hetzel, F.W., Dewhirst, M.W., eds., Biological, physical and clinical aspects of hyperthermia. New York, NY: American Institute of Physics, pp. 210-242.

Root, W.S., 1963. The flow of blood through bones and joints. Handbook of Physiology, Sec 2, vol. II, Washington, D.C., American Physiological Society.

Salcman, M., and Samaras, G.M., 1983. Interstitial microwave hyperthermia for brain tumours: results of phase-I clinical trial. Journal of Neuro-Oncology 1: 225-236.

Samulski, T.V., Kapp, D.S., Fessenden, P., Lohrbach, A., 1987. Heating deep seated eccentrically located tumors with an annular phased array system: a comparative clinical study using two annular array operating configurations. International Journal of Radiation Oncology, Biology and Physics 13: 83-94.

Satoh, T., and Stauffer, P.R., 1988. Implantable helical coil microwave antenna for interstitial hyperthermia. International Journal of Hyperthermia 4: 497-512.

Shimm, D.S., Hynynen, K.H., Anhalt, D.P., Roemer, R.B., Cassady, J.R., 1988. Scanned focused ultrasound hyperthermia: initial clinical results. International Journal of Radiation Oncology, Biology and Physics 15: 1703-1708.

Shitzer, A., and Eberhart, R.C., eds., 1985. Heat transfer in medicine and biology. Plenum Press, New York, NY.

Shoup, T.E., 1979. A practical guide to computer methods for engineers. Englewood Cliffs, NJ: Prentice Hall.

Song, C.W., 1978. Effect of hyperthermia on vascular functions of normal tissues and experimental tumors: Brief communication. Journal of National Cancer Institute 60: 711-713.

Song, C.W., Lokshina, A., Rhee, J.G., Patten, M., Levitt, S.H., 1984. Implication of blood flow in hyperthermic treatment of tumors. IEEE Transactions in Biomedical Engineering 31: 9-16.

Song, C.W., Rhee, J.G., Lee, C.K.K., Levitt, S.H., 1986. Capacitive heating of phantom and human tumors with an 8 MHz radiofrequency applicator (Thermotron RF-8). International Journal Radiation Oncology, Biology and Physics 12: 365-372.

Stauffer, P.R., 1990. Techniques for interstitial hyperthermia. In: Field, S.B., Hand, J.W., eds., Introduction to the practical aspects of clinical hyperthermia. Philadelphia, PA: Taylor and Francis; pp. 344-370.

Stauffer, P.R., 1984. Simple RF matching network for conversion of electrosurgical units or laboratory amplifiers to hyperthermia treatment devices. Medical Instrumentation 18: 326-328.

Stauffer, P.R., Cetas, T.C., Fletcher, A.M., DeYoung, D.W., Oleson, J.R., Roemer, R.B., 1984a. Observations in the use of ferromagnetic implants for inducing hyperthermia. IEEE Transactions Biomedical Engineering 31: 76-90.

Stauffer, P.R., Cetas, T.C., Jones, R.C., 1984b. Magnetic induction heating of ferromagnetic implants for inducing localized hyperthermia in deep-seated tumors. IEEE Transactions Biomedical Engineering 31: 235-251.

Steeves, R.A., Murray, T.G., Moros, E.G., Boldt, H.C., Mieler, W.F., Paliwal, B.R., 1992. Concurrent ferromagnetic hyperthermia and ^{125}I brachytherapy in a rabbit choroidal melanoma model. International Journal of Hyperthermia 8: 443-449.

Storm, F.K., Baker, H.W., Scanlon, E.F., Plenck, H.P., Meadows, P.M., Cohen, S.C., Olson, C.E., Thomson, J.W., Khandekar, J.D., Roe, D., Nizze, A., Morton, D.L., 1985. Magnetic-induction hyperthermia. Results of a 5-year multi-institutional national cooperative trial in advanced cancer patients. Cancer 55: 2677-2687.

Strikwerda, J., 1989. Finite Difference Schemes and Partial Differential Equations, Wadsworth & Brooks-Cole, Monterey, CA.

Strohbehn, J.W., 1983. Temperature distributions from interstitial RF electrode hyperthermia systems: theoretical predictions. International Journal of Radiation Oncology, Biology and Physics 9: 1655-1667.

Strohbehn, J.W., Bowers, E., Walsh, J., Douple, E.B., 1979. An invasive microwave antenna system for locally-induced hyperthermia for cancer therapy. Journal of Microwave Power 14: 339-350.

Strohbehn, J.W., Curtis, E.H., Paulsen, K.D., Lynch, D.R., 1989. Optimization of the absorbed power distribution for an annular phased array hyperthermia system. International Journal Radiation Oncology, Biology and Physics 16: 589-599.

Suit, H.D., 1977. Hyperthermic effects on animal tissues. Radiology 123: 483-487.

Suit, H.D., and Gerweck, L.E., 1979. Potential for hyperthermia and radiation therapy. Cancer Research 39: 2290-2298.

Swindell, W., Roemer, R.B., Clegg, S.T., 1982. Temperature distributions caused by dynamic scanning of focused ultrasound transducers. Proceedings of the Ultrasonics Symposium IEEE Group on Sonics and Ultrasonics, San Diego, 1982, vol. 2, pp. 750-753.

Tompkins, D.T., Partington, B.P., Steeves, R.A., Bartholow, S.D., Paliwal, B.R., 1992a. Effect of implant variables on temperatures achieved during ferromagnetic hyperthermia. International Journal Hyperthermia 8: 241-251.

Tompkins, D.T., Vanderby, R., Klein, S.A., Beckman, W.A., Paliwal, B.R., Steeves, R.A., 1992b. Effect of interseed spacing, tissue perfusion, thermoseed operating temperatures and catheters in ferromagnetic hyperthermia: results from simulations using finite element thermoseed and catheter models, IEEE Transactions in Biomedical Engineering, (to be submitted).

Turner, P.F., 1984. Regional hyperthermia with an annular phased array. IEEE Transactions on Biomedical Engineering 31: 106-115.

Van Der Zee, J., Van Putten, W.L.J., Van Den Berg, A.P., Van Rhoon, G.C., Wike Hooley, J.L., Broekmeyer-Reurink, M.P., Reinhold, H.S., 1986. Retrospective analysis of the response of tumors in patients treated with a combination of radiotherapy and hyperthermia. International Journal of Hyperthermia 2: 337-349.

Vanderby, R., Paliwal, B.R., Wakai, R.T., Belloli, D.M., Partington, B.P., Steeves, R.A., Heiner, J.P., 1988. A parametric study of temperature distributions in ferromagnetic hyperthermia. In: Spilker, R.L., Simon, B.R., eds., Computational Methods in Bioengineering. New York: American Society of Mechanical Engineering pp. 291-299.

Vora, N., Forell, B., Joseph, C., Lipsett, J., Archambeau, J., 1982. Interstitial implant with interstitial hyperthermia. Cancer 50: 2518-2523.

Weinbaum, S., and Jiji, L.M., 1985. A new simplified bioheat equation for the effect of blood flow on local average tissue temperature. Journal Biomechanical Engineering 107: 131-139.

Weinbaum, S., Jiji, L.M., Lemons, D.E., 1984. Theory and experiment for the effect of vascular microstructure on surface tissue heat transfer. Part 1: Anatomical foundation and model conceptualization. Journal Biomechanical Engineering 106: 321-330.

Westra, A., and Dewey, W.C., 1971. Variation in sensitivity to heat shock during the cell-cycle of Chinese hamster cells *in vitro*, International Journal Radiation Biology, 19: 467-477.

Win-Li, L., 1990. Scan parameter optimization and a temperature controller for scanned focussed ultrasound hyperthermia: a theoretical and experimental study. Ph.D. Thesis, University of Arizona, Tucson, AZ.

Wissler, E.H., 1963. An analysis of factors affecting temperature levels in the nude human. In: Hardy, J.D., ed., Temperature, its measurement and control in science and industry. New York: Reinhold, p. 603.

Wolfram, S., 1988. Mathematica: a system for doing mathematics by computer. Champaign, IL: Wolfram Research Inc.

Yuan, X., Strohbehn, J.W., Lynch, D.R., Johnsen, M., 1990. Theoretical investigation of a phased-array hyperthermia system with movable aperatures. International Journal of Hyperthermia 6: 227-240.

Zhu, X.L., and Gandhi, O.P., 1988. Design of RF needle applicators for optimum SAR distributions in irregularly shaped tumours. IEEE Transactions Biomedical Engineering 35: 382-388.

Appendix A

Development of Finite Element Equations

In Appendix A, the differential equation used for predicting temperature distributions in tissue is transformed into a system of equations which can be solved numerically. The differential equation is presented in Sec. A.1 and the transformation of the equation into a system of equations is discussed in Sec. A.2.

A.1 Governing Differential Equation

The governing partial differential equation for calculating the temperatures in two-dimensional tissue models is the bioheat transfer equation

$$\frac{\partial}{\partial x}(k_t T_x) + \frac{\partial}{\partial y}(k_t T_y) + g''' - \rho_t \rho_b c_b m (T - T_b) = \rho_t c_t \frac{\partial T}{\partial t} \qquad \text{(A.1)}$$

In Eq. A.1, $T_x = \partial T/\partial x$ and $T_y = \partial T/\partial y$; g''' is the energy rate associated with metabolic and/or absorption of applied energy; and all other variables were defined in Sec. 2.1. Setting the mass flow rate of blood per unit volume of tissue w_b [kg/s-m^3] equal to $\rho_t \rho_b m$, Eq. A.1 becomes

$$\frac{\partial}{\partial x}(k_t T_x) + \frac{\partial}{\partial y}(k_t T_y) + g''' - w_b c_b (T - T_b) = \rho_t c_t \frac{\partial T}{\partial t} \qquad \text{(A.2)}$$

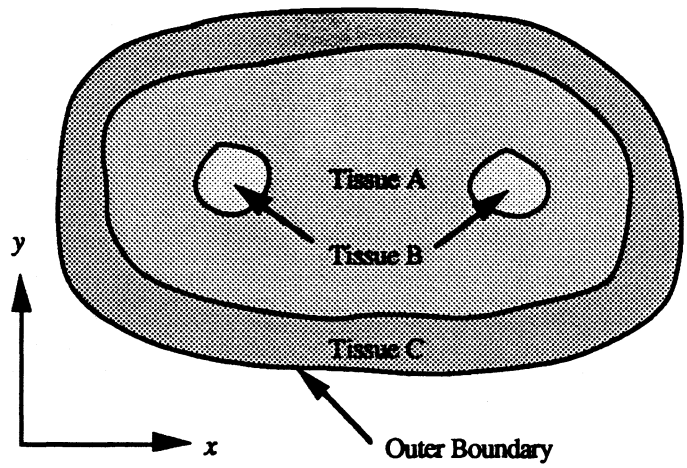

Figure A.1 General two-dimensional, transverse cross-section of tissue.

Equation A.2 can be solved for in the simulated tissue region shown in Fig. A.1.

The steady-state form of Eq. A.2, without energy dissipation due to metabolic processes and absorption due to applied energy, has exact analytical solutions when applied to a square domain with various boundary conditions (see Appendix B). However, the geometries of realistic normal and tumor tissues are irregular (see Chapter 7). Thus a numerical solution to Eq. A.2 will be required.

The finite element method using the Galerkin approach was used to transform Eq. A.2 into a system of equations which can be solved on a computer. The finite element method has been used to transform the two-dimensional heat conduction equation into a system of equations (Myers 1989). Since the bioheat transfer equation is similar to the heat conduction equation, several equations from Myers (1989) will be included in Appendix A for completeness of the presentation. Some of the notation in Appendix A will be consistent with that of Myers (1989).

A.2 Finite-Element Method

The complete transformation of Eq. A.2 into a system of equations which can be solved on a computer requires several steps. The method of weighted residuals is discussed in Sec. A.2.1. The tissue region is discretized and the matrices are developed in Sec. A.2.2. The numerical techniques used to determine temperatures are briefly presented in Sec. A.2.3, and the calculations of the heat flows and energy balances are mentioned in Sec. A.2.4.

A.2.1 Galerkin Weighted Residual Method

After rearranging and using the *method of weighted residuals*, Eq. A.2 is multiplied by a weighting function $f(x,y)$ and then integrated over the tissue region (Fig. A.1) to give

$$\iint_{Tissue} f(x,y) \left\{ \rho_t c_t \frac{\partial T}{\partial t} + \left[\frac{\partial}{\partial x}(-k_t T_x) + \frac{\partial}{\partial y}(-k_t T_y) \right] - g''' + w_b c_b (T - T_b) \right\} dx\, dy = 0 \quad \text{(A.3)}$$

The exact solution to Eq. A.3 will make the integrand (the portion of Eq. A.3 enclosed by brackets {}) identically zero in the tissue region. The *method of weighted residuals* finds an approximate solution that will make the integral (a weighted average of the residuals) equal to zero even though the integrand will not be zero. Thus the weighted average of the residual will be zero rather than the residual itself. After integrating the heat conduction terms in Eq. A.3 (the portion of Eq. A.3 enclosed by braces []) and evaluating the terms along the boundary, it may be shown

$$\iint_{Tissue} \rho_t c_t \frac{\partial T}{\partial t}\, dx\, dy + \iint_{Tissue} [f_x k_t T_x + f_y k_t T_y]\, dx\, dy - \iint_{Tissue} f\, g'''\, dx\, dy$$

$$+ \iint_{Tissue} f\, w_b c_b\, (T - T_b)\, dx\, dy = \int_{Boundary} f\, q_o''\, ds \qquad \text{(A.4)}$$

where q_o'' is the heat flux into the tissue along the boundary from outside the tissue.

Next, it is assumed that the temperature distribution can be approximated by N terms

$$T\ (x,y) = w_1(x,y)\, T_1 + w_2(x,y)\, T_2 + \cdots + w_i\,(x,y)\, T_i + \cdots + w_N\,(x,y)\, T_N$$

which can be written in matrix notation as

$$T\ (x,y) = \mathbf{w}^T(x,y)\, \mathbf{T} \qquad \text{(A.5)}$$

A set of N differential equations can be obtained by using N independent functions f_1 (x,y), ... , f_i (x,y), ... , f_N (x,y). The Galerkin technique requires that each $f_i\ (x,y) = w_i\ (x,y)$. After substituting Eq. A.5 into Eq. A.4 and upon replacing f by $\mathbf{f} = \mathbf{w}$, f_x by $\mathbf{f}_x = \mathbf{w}_x$, f_y by $\mathbf{f}_y = \mathbf{w}_y$, and letting $T_x = \mathbf{w}_x^T\, \mathbf{T}$, $T_y = \mathbf{w}_y^T\, \mathbf{T}$ and $\partial T/\partial t = \mathbf{w}^T\, \dot{\mathbf{T}}$, Eq. A.4 becomes

$$\left[\iint_{Tissue} \mathbf{w} \rho_t c_t \mathbf{w}^T\, dx\, dy\right] \dot{\mathbf{T}} + \left[\iint_{Tissue} \left(\mathbf{w}_x k_t \mathbf{w}_x^T + \mathbf{w}_y k_t \mathbf{w}_y^T\right) dx\, dy\right] \mathbf{T} - \iint_{Tissue} \mathbf{w}\, g'''\, dx\, dy$$

$$+ \left[\iint_{Tissue} \mathbf{w} w_b c_b \mathbf{w}^T\, dx\, dy\right] \mathbf{T} = \int_{Boundary} \mathbf{w} q_o''\, ds + \iint_{Tissue} \mathbf{w} w_b c_b T_b\, dx\, dy \qquad \text{(A.6)}$$

Equation A.6 is a system of N ordinary differential equations. After some rearranging, this system of ordinary differential equations can be written in matrix notation as

$$\mathbf{C}\dot{\mathbf{T}} + (\mathbf{K} + \mathbf{B})\mathbf{T} - \mathbf{g} = \mathbf{b} + \mathbf{q}_o \tag{A.7}$$

where

$$\mathbf{C} = \iint_{Tissue} \mathbf{w}\rho_t c_t \mathbf{w}^T \, dx \, dy \tag{A.8}$$

$$\mathbf{K} = \iint_{Tissue} \left(\mathbf{w}_x k_t \mathbf{w}_x^T + \mathbf{w}_y k_t \mathbf{w}_y^T\right) dx \, dy \tag{A.9}$$

$$\mathbf{B} = \iint_{Tissue} \mathbf{w} w_b c_b \mathbf{w}^T dx \, dy \tag{A.10}$$

$$\mathbf{g} = \iint_{Tissue} \mathbf{w} g''' dx \, dy \tag{A.11}$$

$$\mathbf{b} = \iint_{Tissue} \mathbf{w} w_b c_b T_b \, dx \, dy \tag{A.12}$$

$$\mathbf{q}_o = \int_{Boundary} \mathbf{w} q_o'' \, ds \tag{A.13}$$

Notation for the $\mathbf{C}$ and $\mathbf{K}$ matrices and the $\mathbf{T}$, $\dot{\mathbf{T}}$, $\mathbf{g}$ and $\mathbf{q_o}$ vectors were defined previously by Myers (1987).

A.2.2 Discretization of Tissue Region

A set of N nodal points will discretize the tissue model in Fig. A.1 (see Fig. A.2). Straight lines are used to connect the points thereby dividing the tissue into triangular elements. The function w_i (x,y) is used as an interpolating function to determine the

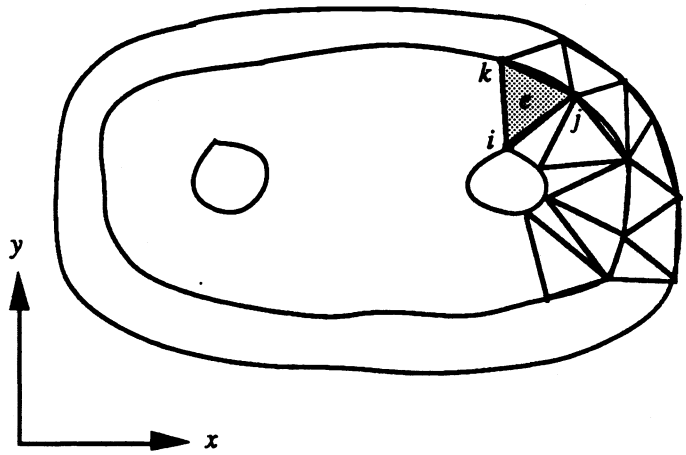

Figure A.2 Discretization of a portion of the tissue model in Fig. A.1 into triangular-shaped, finite elements. Vertices i, j and k are the nodes of finite element e.

temperature at locations inside the elements that surround node i. Therefore it is required that

$w_i\ (x,y) = 1$ at node i

and

$w_i\ (x,y) = 0$ at all other nodes.

It is assumed that $w_i\ (x,y)$ varies linearly from 1 at node i to 0 at nodes connected directly to node i and is 0 everywhere outside of the finite elements around node i.

A.2.2.1 Interior Elements

The next step in the finite element formulation is to evaluate **C**, **K**, **B**, **g** and **b** as given by Eqs. A.8, A.9, A.10, A.11 and A.12, respectively. Once the simulated tissue is discretized into triangular elements, the integral over the tissue area will equal the sum of the integrals over the elemental areas. An example of an elemental area is given by the shaded area in Fig. A.2. The formulation of **C**, **K**, **B**, **g** and **b** are given by

$$\mathbf{C} = \int\int_{Tissue} \mathbf{w}\rho_t c_t \mathbf{w}^T \, dx \, dy = \sum_{e=1}^{NE} \int\int_{Tissue(e)} \mathbf{w}\rho_t c_t \mathbf{w}^T \, dx \, dy \tag{A.14}$$

$$\mathbf{K} = \int\int_{Tissue} \left(\mathbf{w}_x k_t \mathbf{w}_x^T + \mathbf{w}_y k_t \mathbf{w}_y^T\right) dx \, dy = \sum_{e=1}^{NE} \int\int_{Tissue(e)} \left(\mathbf{w}_x k_t \mathbf{w}_x^T + \mathbf{w}_y k_t \mathbf{w}_y^T\right) dx \, dy \tag{A.15}$$

$$\mathbf{B} = \int\int_{Tissue} \mathbf{w} w_b c_b \mathbf{w}^T \, dx \, dy = \sum_{e=1}^{NE} \int\int_{Tissue(e)} \mathbf{w} w_b c_b \mathbf{w}^T dx \, dy \tag{A.16}$$

$$\mathbf{g} = \int\int_{Tissue} \mathbf{w} g''' dx \, dy = \sum_{e=1}^{NE} \int\int_{Tissue(e)} \mathbf{w} g''' dx \, dy \tag{A.17}$$

$$\mathbf{b} = \int\int_{Tissue} \mathbf{w} w_b c_b T_b \, dx \, dy = \sum_{e=1}^{NE} \int\int_{Tissue\,(e)} \mathbf{w} w_b c_b T_b \, dx \, dy \tag{A.18}$$

A.2.2.1.1 Uniform Element Properties

The values of ρ_t, c_t, k_t, w_b, c_b, and g''' will be assumed uniform within an element, while the blood temperature T_b will be uniform throughout the tissue. These values may be factored out of the element integrals to give

$$\mathbf{C} = \sum_{e=1}^{NE} \rho_t^{(e)} c_t^{(e)} \int_{Tissue(e)} \mathbf{w}\mathbf{w}^T \, dA \tag{A.19}$$

$$\mathbf{K} = \sum_{e=1}^{NE} k_t^{(e)} \int_{Tissue(e)} \left(\mathbf{w}_x \mathbf{w}_x^T + \mathbf{w}_y \mathbf{w}_y^T\right) dA \tag{A.20}$$

$$\mathbf{B} = \sum_{e=1}^{NE} w_b^{(e)} c_b^{(e)} \int_{Tissue(e)} \mathbf{w}\mathbf{w}^T dA \tag{A.21}$$

$$\mathbf{g} = \sum_{e=1}^{NE} g'''^{(e)} \int_{Tissue(e)} \mathbf{w}\, dA \tag{A.22}$$

$$\mathbf{b} = \sum_{e=1}^{NE} w_b^{(e)} c_b^{(e)} T_b \int_{Tissue(e)} \mathbf{w}\, dA \tag{A.23}$$

where $\rho_t^{(e)}$, $c_t^{(e)}$, $k_t^{(e)}$, $w_b^{(e)}$, $c_b^{(e)}$, and $g'''^{(e)}$ are the values of ρ_t, c_t, k_t, w_b, c_b, and g''', respectively, for element e. The differential area $dx\, dy$ has been written as dA.

Myers (1989) has defined an *element capacitance matrix* $\mathbf{C}^{(e)}$, an *element conduction matrix* $\mathbf{K}^{(e)}$ and an *element generation vector* $\mathbf{g}^{(e)}$ as

$$\mathbf{C}^{(e)} = \rho_t^{(e)} c_t^{(e)} \int_{Tissue(e)} \mathbf{w}\mathbf{w}^T\, dA \tag{A.24}$$

$$\mathbf{K}^{(e)} = k_t^{(e)} \int_{Tissue(e)} \left(\mathbf{w}_x \mathbf{w}_x^T + \mathbf{w}_y \mathbf{w}_y^T\right) dA \tag{A.25}$$

$$\mathbf{g}^{(e)} = g'''^{(e)} \int_{Tissue(e)} \mathbf{w}\, dA \tag{A.26}$$

Similarly it is convenient to define an *element perfusion matrix* $\mathbf{B}^{(e)}$ and an *element perfusion vector* $\mathbf{b}^{(e)}$ as

$$\mathbf{B}^{(e)} = w_b^{(e)} c_b^{(e)} \int_{Tissue(e)} \mathbf{w}\mathbf{w}^T dA \tag{A.27}$$

$$\mathbf{b}^{(e)} = w_b^{(e)} c_b^{(e)} T_b \int_{Tissue(e)} \mathbf{w}\, dA \tag{A.28}$$

The summation of $\mathbf{C}^{(e)}$, $\mathbf{K}^{(e)}$, $\mathbf{g}^{(e)}$, $\mathbf{B}^{(e)}$, and $\mathbf{b}^{(e)}$ over all the finite elements in the tissue model are given by the *global capacitance matrix* $\mathbf{C}$, the *global conduction matrix* $\mathbf{K}$, the

global generation vector **g** (Myers 1987), and the *global perfusion matrix* **B**, and the *global perfusion vector* **b**, respectively (Eq. A.7).

Capacitance Matrix

Myers (1989) shows that the *element capacitance matrix* $\mathbf{C}^{(e)}$ is given by

$$\mathbf{C}^{(e)} = \frac{\rho_t^{(e)} c_t^{(e)} A^{(e)}}{12} \begin{bmatrix} 2 & 1 & 1 \\ 1 & 2 & 1 \\ 1 & 1 & 2 \end{bmatrix}$$

Row i | Row j | Row k

Column i | Column j | Column k

where the area of an element $A^{(e)}$ is given by $A^{(e)} = \frac{1}{2}[x_{ij}y_{jk} - x_{jk}y_{ij}]$. Here, i, j and k are the nodes or vertices of element e and $x_{ij} = x_i - x_j$, $y_{jk} = y_k - y_j$, etc. The *element capacitance matrix* is an N by N matrix.

Conduction Matrix

Myers (1989) shows that the *element conduction matrix* $\mathbf{K}^{(e)}$ is given by

$$\mathbf{K}^{(e)} = \frac{k^{(e)}}{4A^{(e)}} \begin{bmatrix} \kappa_{ii} & \kappa_{ij} & \kappa_{ik} & \text{Row } i \\ \kappa_{ji} & \kappa_{jj} & \kappa_{jk} & \text{Row } j \\ \kappa_{ki} & \kappa_{kj} & \kappa_{kk} & \text{Row } k \\ \text{Column } i & \text{Column } j & \text{Column } k & \end{bmatrix} \tag{A.29}$$

where

$$\kappa_{ii} = x_{jk}x_{jk} + y_{jk}y_{jk} \qquad \kappa_{ij} = -(x_{jk}x_{ik} + y_{jk}y_{ik}) \qquad \kappa_{ik} = x_{jk}x_{ij} + y_{jk}y_{ij}$$

$$\kappa_{jj} = x_{ik}x_{ik} + y_{ik}y_{ik} \qquad \kappa_{jk} = -(x_{ik}x_{ij} + y_{ik}y_{ij})$$

$$\kappa_{kk} = x_{ij}x_{ij} + y_{ij}y_{ij}$$

The *element conduction matrix* is an N by N symmetric matrix.

Generation Vector

Myers (1989) also shows that the *element generation vector* $\mathbf{g}^{(e)}$ is given by

$$\mathbf{g}^{(e)} = \frac{g'''^{(e)} A^{(e)}}{3} \begin{bmatrix} 1 \\ 1 \\ \\ 1 \end{bmatrix} \begin{matrix} \text{Row } i \\ \text{Row } j \\ \\ \text{Row } k \end{matrix} \tag{A.30}$$

Perfusion Matrix

The *element perfusion matrix* $\mathbf{B}^{(e)}$ can be shown to be

$$\mathbf{B}^{(e)} = \frac{w_b^{(e)} c_b^{(e)} A^{(e)}}{12} \begin{bmatrix} 2 & 1 & 1 \\ 1 & 2 & 1 \\ 1 & 1 & 2 \end{bmatrix} \begin{matrix} \text{Row } i \\ \text{Row } j \\ \text{Row } k \end{matrix} \quad \begin{matrix} \text{Column } i & \text{Column } j & \text{Column } k \end{matrix} \tag{A.31}$$

Perfusion Vector

The *element perfusion vector* $\mathbf{b}^{(e)}$ was found to be

$$\mathbf{b}^{(e)} = \frac{w_b^{(e)} c_b^{(e)} T_b A^{(e)}}{3} \begin{bmatrix} 1 \\ 1 \\ \\ \\ 1 \end{bmatrix} \begin{matrix} \text{Row } i \\ \text{Row } j \\ \\ \\ \text{Row } k \end{matrix} \tag{A.32}$$

A.2.2.1.2 Variable Element Properties

The values of ρ_t, c_t, k_t, w_b, c_b, and g''' will be variable within an element. They are scalar values that are functions of x and y within an element.

Capacitance Matrix

The element capacitance matrix $\mathbf{C}^{(e)}$ is given by (Myers 1987)

$$\mathbf{C}^{(e)} = \int_{Tissue^{(e)}} \mathbf{w} \rho_t c_t \mathbf{w}^T \, dA \tag{A.33}$$

Let $\rho_t c_t$ be a linear function within an element as defined by

$$\rho_t c_t = \begin{bmatrix} (\rho_t c_t)_i & (\rho_t c_t)_j & (\rho_t c_t)_k \end{bmatrix} \begin{bmatrix} \delta_i \\ \delta_j \\ \delta_k \end{bmatrix} = \delta_i (\rho_t c_t)_i + \delta_j (\rho_t c_t)_j + \delta_k (\rho_t c_t)_k \tag{A.34}$$

In Eq. A.34, $(\rho_t c_t)_i$, $(\rho_t c_t)_j$ and $(\rho_t c_t)_k$ are the products of the densities and specific heats of the tissue at nodes i, j, and k, respectively. $\delta_i (x,y)$ is an interpolating function to help find the density and specific heat at points inside the elements that surround node i so that

$\delta_i (x,y) = 1$ at node i

and

$\delta_i (x,y) = 0$ at all other nodes.

Similarly, $\delta_j\,(x,y)$ and $\delta_k\,(x,y)$ are defined in the same manner. That is,

$\delta_j\,(x,y) = 1$ at node j

and

$\delta_j\,(x,y) = 0$ at all other nodes and

$\delta_k\,(x,y) = 1$ at node k

and

$\delta_k\,(x,y) = 0$ at all other nodes.

It is convenient to introduce a local coordinate system within the triangular-shaped finite elements. This coordinate system is based on the *area coordinates* ξ_i, ξ_j and ξ_k within each finite element (Myers 1989). Like $\delta_i\,(x,y)$, $\delta_j\,(x,y)$ and $\delta_k\,(x,y)$, area coordinates are equal to 1 at nodes i, j and k, respectively, and linearly decrease to zero at the side opposite to nodes i, j and k, respectively. The location of a point at (x, y) within the triangular element is fixed by specifying any two area coordinates. Area coordinates are useful for carrying out the integrations in Eq. A.33. Therefore within a triangle $\delta_i\,(x,y) = \xi_i$, $\delta_j\,(x,y) = \xi_j$, $\delta_k\,(x,y) = \xi_k$ and Eq. A.34 becomes

$$\rho_t c_t = \xi_i(\rho_t c_t)_i + \xi_j(\rho_t c_t)_j + \xi_k(\rho_t c_t)_k \tag{A.35}$$

A relation which will be made of use later is

$$\int_A \xi_i^a\,\xi_j^b\,\xi_k^c\,dA = \frac{a!b!c!}{(a+b+c+2)!}\,2A \tag{A.36}$$

The integrand in Eq. A.33 is given by

$$\mathbf{w}\,\rho_t\,c_t\,\mathbf{w}^T = \begin{bmatrix} \upsilon_{ii} & \upsilon_{ij} & \upsilon_{ik} & \text{Row } i \\ \upsilon_{ji} & \upsilon_{jj} & \upsilon_{jk} & \text{Row } j \\ \upsilon_{ki} & \upsilon_{kj} & \upsilon_{kk} & \text{Row } k \\ \text{Column } i & \text{Column } j & \text{Column } k & \end{bmatrix} \tag{A.37}$$

In Eq. A.37,

$$\upsilon_{ii} = \xi_i\ (\rho_t c_t)_i\ \xi_i\,\xi_i + \xi_i\ (\rho_t c_t)_j\ \xi_j\,\xi_i + \xi_i\ (\rho_t c_t)_k\ \xi_k\,\xi_i \tag{A.38}$$

$$\upsilon_{ij} = \xi_i\ (\rho_t c_t)_i\ \xi_i\,\xi_j + \xi_i\ (\rho_t c_t)_j\ \xi_j\,\xi_j + \xi_i\ (\rho_t c_t)_k\ \xi_k\,\xi_j \tag{A.39}$$

$$\upsilon_{ik} = \xi_i\ (\rho_t c_t)_i\ \xi_i\,\xi_k + \xi_i\ (\rho_t c_t)_j\ \xi_j\,\xi_k + \xi_i\ (\rho_t c_t)_k\ \xi_k\,\xi_k \tag{A.40}$$

$$\upsilon_{jj} = \xi_j\ (\rho_t c_t)_i\ \xi_i\,\xi_j + \xi_j\ (\rho_t c_t)_j\ \xi_j\,\xi_j + \xi_j\ (\rho_t c_t)_k\ \xi_k\,\xi_j \tag{A.41}$$

$$\upsilon_{jk} = \xi_j\ (\rho_t c_t)_i\ \xi_i\,\xi_k + \xi_j\ (\rho_t c_t)_j\ \xi_j\,\xi_k + \xi_j\ (\rho_t c_t)_k\ \xi_k\,\xi_k \tag{A.42}$$

$$\upsilon_{kk} = \xi_k\ (\rho_t c_t)_i\ \xi_i\,\xi_k + \xi_k\ (\rho_t c_t)_j\ \xi_j\,\xi_k + \xi_k\ (\rho_t c_t)_k\ \xi_k\,\xi_k \tag{A.43}$$

Equation A.37 is symmetric and must be integrated over the area of finite element *e*. Since $(\rho_t c_t)_i$, $(\rho_t c_t)_j$ and $(\rho_t c_t)_k$ are not functions of area (merely products of the density and specific heat at locations *i*, *j* and *k*), they can be taken outside the integrals. With the aid of Eq. A.36, the three (fundamental) solutions to integrations in Eqs. A.38 through A.43 are

$$\int_{Tissue^{(e)}} \xi_i^3 \, dA = \frac{3!0!0!}{(3+0+0+2)!} 2A^{(e)} = \frac{A^{(e)}}{10} \tag{A.44}$$

$$\int_{Tissue^{(e)}} \xi_i^2 \, \xi_j \, dA = \frac{2!1!0!}{(2+1+0+2)!} 2A^{(e)} = \frac{A^{(e)}}{30} \tag{A.45}$$

$$\int_{Tissue^{(e)}} \xi_i \, \xi_j \, \xi_k \, dA = \frac{1!1!1!}{(1+1+1+2)!} 2A^{(e)} = \frac{A^{(e)}}{60} \tag{A.46}$$

All other integrations in Eqs. A.38 through A.43 involve different combinations of ξ's than those appearing in Eqs. A.44, A.45 and A.46. The general result of these integrations, however, are given on the right-hand side of Eqs. A.44, A.45 and A.46. After all integrations in Eqs. A.38 through A.43 are evaluated, the element capacitance matrix $\mathbf{C}^{(e)}$ is given by

$$\mathbf{C}^{(e)} = \begin{bmatrix} \chi_{ii} & \chi_{ij} & \chi_{ik} & \text{Row } i \\ \chi_{ji} & \chi_{jj} & \chi_{jk} & \text{Row } j \\ \chi_{ki} & \chi_{kj} & \chi_{kk} & \text{Row } k \\ \text{Column } i & \text{Column } j & \text{Column } k & \end{bmatrix} \tag{A.47}$$

In Eq. A.47,

$$\chi_{ii} = [\ 3(\rho_t c_t)_i + (\rho_t c_t)_j + (\rho_t c_t)_k\ ]\ \frac{A^{(e)}}{30}$$

$$\chi_{ij} = [\ 2(\rho_t c_t)_i + 2(\rho_t c_t)_j + (\rho_t c_t)_k\ ]\ \frac{A^{(e)}}{60}$$

$$\chi_{ik} = [\ 2(\rho_t c_t)_i + (\rho_t c_t)_j + 2(\rho_t c_t)_k\ ]\ \frac{A^{(e)}}{60}$$

$$\chi_{jj} = [\ (\rho_t c_t)_i + 3(\rho_t c_t)_j + (\rho_t c_t)_k\ ]\ \frac{A^{(e)}}{30}$$

$$\chi_{jk} = [\ (\rho_t c_t)_i + 2(\rho_t c_t)_j + 2(\rho_t c_t)_k\ ]\ \frac{A^{(e)}}{60}$$

$$\chi_{kk} = [\ (\rho_t c_t)_i + (\rho_t c_t)_j + 3(\rho_t c_t)_k\ ]\ \frac{A^{(e)}}{30}$$

The *element capacitance matrix* $\mathbf{C}^{(e)}$ (Eq. A.47) is a symmetric matrix.

Conduction Matrix

The element conduction matrix $\mathbf{K}^{(e)}$ is given by (Myers 1987)

$$\mathbf{K}^{(e)} = \int_{Tissue(e)} \left(\mathbf{w}_x k_t \mathbf{w}_x^T + \mathbf{w}_y k_t \mathbf{w}_y^T\right) dA \tag{A.48}$$

Let k_t be a linear function within an element as defined by

$$k_t = \begin{bmatrix} k_{t\,i} & k_{t\,j} & k_{t\,k} \end{bmatrix} \begin{bmatrix} \delta_i \\ \delta_j \\ \delta_k \end{bmatrix} = \delta_i k_{t\,i} + \delta_j k_{t\,j} + \delta_k k_{t\,k} \tag{A.49}$$

In Eq. A.49, $k_{t\,i}$, $k_{t\,j}$, $k_{t\,k}$ are the thermal conductivities of the tissue at nodes i, j, and k. As in the development of the element capacitance matrix, $\delta_i\,(x,y) = \xi_i$, $\delta_j\,(x,y) = \xi_j$ and $\delta_k\,(x,y) = \xi_k$. The thermal conductivity at points inside the element can, therefore, be found by

$$k_t = \xi_i k_{t\,i} + \xi_j k_{t\,j} + \xi_k k_{t\,k} \tag{A.50}$$

where, again, ξ_i, ξ_j and ξ_k are the *area coordinates* for element *e*.

By using Eq. A.50, the first term on the fight-hand-side of Eq. A.48 ($\mathbf{w}_x\, k_t\, \mathbf{w}_x^T$) is

$$\mathbf{w}_x\, k_t\, \mathbf{w}_x^T = \frac{\left(\xi_i k_{t\,i} + \xi_j k_{t\,j} + \xi_k k_{t\,k}\right)}{b_{ijk}^{2(e)}} \begin{bmatrix} y_{jk}y_{jk} & -y_{jk}y_{ik} & y_{jk}y_{ij} \\ -y_{ik}y_{jk} & y_{ik}y_{ik} & -y_{ik}y_{ij} \\ y_{ij}y_{jk} & -y_{ij}y_{ik} & y_{ij}y_{ij} \end{bmatrix}$$

Row *i*, Row *j*, Row *k*

Column *i*, Column *j*, Column *k*

Here $b_{ijk}^{2(e)} = 4\,A^{(e)2}$ (Myers 1987). Similarly, the other integrand in Eq. A.48 ($\mathbf{w}_y\, k_t\, \mathbf{w}_y^T$) is given by

$$\mathbf{w}_y\, k_t\, \mathbf{w}_y^T = \frac{\left(\xi_i k_{t\,i} + \xi_j k_{t\,j} + \xi_k k_{t\,k}\right)}{b_{ijk}^{2\,(e)}} \begin{bmatrix} x_{jk}x_{jk} & -x_{jk}x_{ik} & x_{jk}x_{ij} & \text{Row } i \\ -x_{ik}x_{jk} & x_{ik}x_{ik} & -x_{ik}x_{ij} & \text{Row } j \\ x_{ij}x_{jk} & -x_{ij}x_{ik} & x_{ij}x_{ij} & \text{Row } k \\ \text{Column } i & \text{Column } j & \text{Column } k & \end{bmatrix}$$

Notice that both $\mathbf{w}_x\, k_t\, \mathbf{w}_x^T$ and $\mathbf{w}_y\, k_t\, \mathbf{w}_y^T$ are symmetric matrices. In addition, most of the entries in $\mathbf{w}_x\, k_t\, \mathbf{w}_x^T$ and $\mathbf{w}_y\, k_t\, \mathbf{w}_y^T$ are not functions of x or y and can be factored out of the integral in Eq. A.48. After factoring out the independent parts, three integrations remain to be performed for each entry in $\mathbf{w}_x\, k_t\, \mathbf{w}_x^T$ and $\mathbf{w}_y\, k_t\, \mathbf{w}_y^T$. With the aid of Eq. A.36, the three (general) solutions to the integrations in Eq. A.48 are

$$\int_{Tissue\,(e)} \xi_i \, dA = \frac{1!0!0!}{(1+0+0+2)!} 2A^{(e)} = \frac{A^{(e)}}{3} \tag{A.51}$$

$$\int_{Tissue\,(e)} \xi_j \, dA = \frac{0!1!0!}{(0+1+0+2)!} 2A^{(e)} = \frac{A^{(e)}}{3} \tag{A.52}$$

$$\int_{Tissue\,(e)} \xi_k \, dA = \frac{0!0!1!}{(0+0+1+2)!} 2A^{(e)} = \frac{A^{(e)}}{3} \tag{A.53}$$

Combining $\mathbf{w}_x\, k_t\, \mathbf{w}_x^T$ and $\mathbf{w}_y\, k_t\, \mathbf{w}_y^T$ with the result of Eqs. A.51, A.52 and A.53, the integration of Eq. A.48 becomes

$$\mathbf{K}^{(e)} = \frac{(k_{t\,i} + k_{t\,j} + k_{t\,k})\ A^{(e)}}{3\, b^{2\,(e)}_{ijk}} \begin{bmatrix} \kappa_{ii} & \kappa_{ij} & \kappa_{ik} & \text{Row } i \\ \kappa_{ji} & \kappa_{jj} & \kappa_{jk} & \text{Row } j \\ \kappa_{ki} & \kappa_{kj} & \kappa_{kk} & \text{Row } k \\ \text{Column } i & \text{Column } j & \text{Column } k & \end{bmatrix} \tag{A.54}$$

where κ_{ii}, κ_{ij}, ... , κ_{kk} are given in Eq. A.29. Since $b^{2\,(e)}_{ijk} = 4A^{(e)2}$, Eq. A.54 is equivalent to

$$\mathbf{K}^{(e)} = \frac{(k_{t\,i} + k_{t\,j} + k_{t\,k})}{12\ A^{(e)}} \begin{bmatrix} \kappa_{ii} & \kappa_{ij} & \kappa_{ik} & \text{Row } i \\ \kappa_{ji} & \kappa_{jj} & \kappa_{jk} & \text{Row } j \\ \kappa_{ki} & \kappa_{kj} & \kappa_{kk} & \text{Row } k \\ \text{Column } i & \text{Column } j & \text{Column } k & \end{bmatrix} \tag{A.55}$$

The *element conduction matrix* $\mathbf{K}^{(e)}$ is an N by N symmetric matrix.

Perfusion Matrix

The *element perfusion matrix* $\mathbf{B}^{(e)}$ is given by

$$\mathbf{B}^{(e)} = \int_{Tissue^{(e)}} \mathbf{w}\ w_b c_b\ \mathbf{w}^T\, dA \tag{A.56}$$

Let $w_b c_b$ be a linear function within an element as defined by

$$w_b c_b = \begin{bmatrix} (w_b c_b)_i & (w_b c_b)_j & (w_b c_b)_k \end{bmatrix} \begin{bmatrix} \delta_i \\ \delta_j \\ \delta_k \end{bmatrix} = \delta_i (w_b c_b)_i + \delta_j (s_b c_b)_j + \delta_k (w_b c_b)_k \tag{A.57}$$

where $(w_b c_b)_i$, $(w_b c_b)_j$, and $(w_b c_b)_k$ are tissue perfusion values at nodes i, j, and k. As designated earlier, $\delta_i(x,y)$, $\delta_j(x,y)$ and $\delta_k(x,y)$ are interpolating functions to help find the tissue perfusion at points inside the elements. As in the development of the element capacitance matrix $\mathbf{C}$ and thermal conduction matrix $\mathbf{K}$ with variable properties, $\delta_i\,(x,y) = \xi_i$, $\delta_j\,(x,y) = \xi_j$, $\delta_k\,(x,y) = \xi_k$. Thus Eq. A.57 becomes

$$w_b c_b = \xi_i (w_b c_b)_i + \xi_j (w_b c_b)_j + \xi_k (w_b c_b)_k \tag{A.58}$$

where ξ_i, ξ_j and ξ_k are the area coordinates for element e.

The integrand in Eq. A.56 is given by

$$\mathbf{w}\, w_b\, c_b\, \mathbf{w}^T = \begin{bmatrix} \omega_{ii} & \omega_{ij} & \omega_{ik} & \text{Row } i \\ \omega_{ji} & \omega_{jj} & \omega_{jk} & \text{Row } j \\ \omega_{ki} & \omega_{kj} & \omega_{kk} & \text{Row } k \\ \text{Column } i & \text{Column } j & \text{Column } k & \end{bmatrix} \tag{A.59}$$

In Eq. A.59,

$$\omega_{ii} = \xi_i\ (w_b c_b)_i\ \xi_i \xi_i + \xi_i\ (w_b c_b)_j\ \xi_j \xi_i + \xi_i\ (w_b c_b)_k\ \xi_k \xi_i \tag{A.60}$$

$$\omega_{ij} = \xi_i\ (w_b c_b)_i\ \xi_i \xi_j + \xi_i\ (w_b c_b)_j\ \xi_j \xi_j + \xi_i\ (w_b c_b)_k\ \xi_k \xi_j \tag{A.61}$$

$$\omega_{ik} = \xi_i\ (w_b c_b)_i\ \xi_i \xi_k + \xi_i\ (w_b c_b)_j\ \xi_j \xi_k + \xi_i\ (w_b c_b)_k\ \xi_k \xi_k \tag{A.62}$$

$$\omega_{jj} = \xi_j\ (w_b c_b)_i\ \xi_i \xi_j + \xi_j\ (w_b c_b)_j\ \xi_j \xi_j + \xi_j\ (w_b c_b)_k\ \xi_k \xi_j \tag{A.63}$$

$$\omega_{jk} = \xi_j\ (w_b c_b)_i\ \xi_i \xi_k + \xi_j\ (w_b c_b)_j\ \xi_j \xi_k + \xi_j\ (w_b c_b)_k\ \xi_k \xi_k \tag{A.64}$$

$$\omega_{kk} = \xi_k\ (w_b c_b)_i\ \xi_i \xi_k + \xi_k\ (w_b c_b)_j\ \xi_j \xi_k + \xi_k\ (w_b c_b)_k\ \xi_k \xi_k \tag{A.65}$$

Equation A.59 is symmetric and must be integrated over the area of finite element e. Since $(w_b c_b)_i$, $(w_b c_b)_j$, and $(w_b c_b)_k$ are not functions of area, they can be taken outside the integrals. With the aid of Eqs. A.36, A.44, A.45 and A.46, integrations in Eq. A.56 can be evaluated. The integration of Eq. A.56 gives the *element perfusion matrix* $\mathbf{B}^{(e)}$

$$\mathbf{B}^{(e)} = \begin{bmatrix} \beta_{ii} & \beta_{ij} & \beta_{ik} & \text{Row } i \\ \beta_{ji} & \beta_{jj} & \beta_{jk} & \text{Row } j \\ \beta_{ki} & \beta_{kj} & \beta_{kk} & \text{Row } k \\ \text{Column } i & \text{Column } j & \text{Column } k & \end{bmatrix} \tag{A.66}$$

In Eq. A.66,

$$\beta_{ii} = [\ 3(w_b c_b)_i + (w_b c_b)_j + (w_b c_b)_k\ ]\ \frac{A^{(e)}}{30}$$

$$\beta_{ij} = [\ 2(w_b c_b)_i + 2(w_b c_b)_j + (w_b c_b)_k\ ]\ \frac{A^{(e)}}{60}$$

$$\beta_{ik} = [\ 2(w_b c_b)_i + (w_b c_b)_j + 2(w_b c_b)_k\ ]\ \frac{A^{(e)}}{60}$$

$$\beta_{jj} = [\ (w_b c_b)_i + 3(w_b c_b)_j + (w_b c_b)_k\ ]\ \frac{A^{(e)}}{30}$$

$$\beta_{jk} = [\ (w_b c_b)_i + 2(w_b c_b)_j + 2(w_b c_b)_k\ ]\ \frac{A^{(e)}}{60}$$

$$\beta_{kk} = [\ (w_b c_b)_i + (w_b c_b)_j + 3(w_b c_b)_k\ ]\ \frac{A^{(e)}}{30}$$

The *element perfusion matrix* $\mathbf{B}^{(e)}$ is also a symmetric matrix.

Generation Vector

The *element generation vector* $\mathbf{g}^{(e)}$ is given by (Myers 1987)

$$\mathbf{g}^{(e)} = \int_{Tissue(e)} \mathbf{w}\, g'''\, dA \tag{A.67}$$

Let the energy rate (of dissipation and/or absorption) g''' be a linear function within finite element e as defined by

$$g''' = \begin{bmatrix} g_i''' & g_j''' & g_k''' \end{bmatrix} \begin{bmatrix} \delta_i \\ \delta_j \\ \delta_k \end{bmatrix} = \delta_i g_i''' + \delta_j g_j''' + \delta_k g_k''' \tag{A.68}$$

In Eq. A.68, g_i''', g_j''', and g_k''' are the energy rates per unit volume at nodes i, j, and k, respectively. As in Eq. A.34, A.49 and A.57, $\delta_i\,(x,y)$, $\delta_j\,(x,y)$, and $\delta_k\,(x,y)$ are interpolating functions to help find the energy rates at points inside the elements. As in the development of the element capacitance matrix **C**, thermal conduction matrix **K** and tissue perfusion matrix **B** with variable properties, $\delta_i\,(x,y) = \xi_i$, $\delta_j\,(x,y) = \xi_j$, $\delta_k\,(x,y) = \xi_k$. Therefore Eq. A.68 becomes

$$g''' = \xi_i g_i''' + \xi_j g_j''' + \xi_k g_k''' \tag{A.69}$$

where ξ_i, ξ_j, and ξ_k are the area coordinates for element e.

Substituting Eq. A.69 into Eq. A.67 gives

$$\mathbf{g}^{(e)} = \int_{A^{(e)}} \begin{bmatrix} \xi_i^2 g_i''' + \xi_i\xi_j g_j''' + \xi_i\xi_k g_k''' & \text{Row } i \\ \xi_i\xi_j g_i''' + \xi_j^2 g_j''' + \xi_j\xi_k g_k''' & \text{Row } j \\ \xi_i\xi_k g_i''' + \xi_j\xi_k g_j''' + \xi_k^2 g_k''' & \text{Row } k \end{bmatrix} dA \tag{A.70}$$

The integrations in Eq. A.70 can be evaluated using the relation given in Eq. A.36. The energy generation vector is then given by

$$\mathbf{g}^{(e)} = \frac{A^{(e)}}{12} \begin{bmatrix} 2g_i''' + g_j''' + g_k''' & \text{Row } i \\ g_i''' + 2g_j''' + g_k''' & \text{Row } j \\ g_i''' + g_j''' + 2g_k''' & \text{Row } k \end{bmatrix} \tag{A.71}$$

Perfusion Vector

The *element perfusion vector* $\mathbf{b}^{(e)}$ is given by

$$\mathbf{b}^{(e)} = \int_{Tissue^{(e)}} \mathbf{w} w_b c_b T_b \; dA \tag{A.72}$$

As in Eq. A.57, let $w_b c_b$ be a linear function within an element. The blood temperature T_b can be taken outside the integral as it will be held uniform over the region. After substitution of Eq. A.57 into Eq. A.72, the integration of Eq. A.72 is similar to the integration of Eq. A.70 with the tissue perfusion parameter $w_b c_b$ taking the place of energy rate per unit volume g'''. The tissue perfusion vector is given by

$$\mathbf{b}^{(e)} = \frac{T_b A^{(e)}}{12} \begin{bmatrix} 2(w_b c_b)_i + (w_b c_b)_j + (w_b c_b)_k & \text{Row } i \\ (w_b c_b)_i + 2(w_b c_b)_j + (w_b c_b)_k & \text{Row } j \\ \\ (w_b c_b)_i + (w_b c_b)_j + 2(w_b c_b)_k & \text{Row } k \end{bmatrix} \quad \text{(A.73)}$$

A.2.2.2 Boundary Segments

The next step in the finite element formulation is to evaluate $\mathbf{q}_o$ in Eq. A.7 as given by Eq. A.13. Myers (1989) has shown that the boundary segments can be broken up into specified heat-flux boundaries for segments having a specified heat flux and convective boundary segments that have a convection boundary. Thus Eq. A.13 can be given by

$$\mathbf{q}_o = \sum_{b_q=1}^{NB_q} \int_{\mathbf{B}(b_q)} \mathbf{w}\ q_s''\, ds + \sum_{b_h=1}^{NB_h} \int_{\mathbf{B}(b_h)} \mathbf{w}\ h\, T_\infty\, ds - \left[\sum_{b_h=1}^{NB_h} \int_{\mathbf{B}(b_h)} \mathbf{w}\ h\ \mathbf{w}^T\, ds \right] \mathbf{T} \quad \text{(A.74)}$$

In Eq. A.74, q_s'' is the specified heat flux at boundaries with a heat flux, while at convection boundaries, the energy into boundary segments from outside the region is given by $q_o'' = h\,(T_\infty - T)$. Myers (1989) defined a *boundary-segment heat flow vector* $\mathbf{q}^{(b_q)}$, a *boundary-segment convection vector* $\mathbf{h}^{(b_h)}$, and a *boundary-segment convection matrix* $\mathbf{H}^{(b_h)}$ as

$$\mathbf{q}^{(b_q)} = \int_{\mathbf{B}(b_q)} \mathbf{w}\ q_s''\, ds \qquad \mathbf{h}^{(b_h)} = \int_{\mathbf{B}(b_h)} \mathbf{w} h\, T_\infty\, ds \qquad \mathbf{H}^{(b_h)} = \int_{\mathbf{B}(b_h)} \mathbf{w} h\ \mathbf{w}^T\, ds$$

With these relations for $\mathbf{q}^{(b_q)}$, $\mathbf{h}^{(b_h)}$ and $\mathbf{H}^{(b_h)}$, Eq. A.74 becomes

$$\mathbf{q}_o = \sum_{b_q=1}^{NB_q} \mathbf{q}^{(b_q)} + \sum_{b_h=1}^{NB_h} \mathbf{h}^{(b_h)} - \left[\sum_{b_h=1}^{NB_h} \mathbf{H}^{(b_h)} \right] \mathbf{T} = \mathbf{q} + \mathbf{h} - \mathbf{HT} \qquad \text{(A.75)}$$

In Eq. A.75, the summation of $\mathbf{q}^{(b_q)}$, $\mathbf{h}^{(b_h)}$, and $\mathbf{H}^{(b_h)}$ over all appropriate boundary segments are given by **q**, **h** and **H**, respectively.

A.2.2.2.1 Uniform Properties along Boundary Segment

Specified heat flux

The value of the heat flux q_s'' will be assumed uniform along a boundary segment. Myers (1989) has shown that the integration of *boundary-segment heat flow vector* $\mathbf{q}^{(b_q)}$

$$\mathbf{q}^{(b_q)} = \int_{\mathbf{B}^{(b_q)}} \mathbf{w}\, q_s''\, ds$$

gives

$$\mathbf{q}^{(b_q)} = \frac{q_s''^{(b_q)}\, s_{ij}^{(b_q)}}{2} \begin{bmatrix} 1 \\ 1 \end{bmatrix} \begin{matrix} \text{Row } i \\ \text{Row } j \end{matrix} \qquad \text{(A.76)}$$

In Eq. A.76, s_{ij} is the distance from node i to node j.

Convection

The value of the convective heat transfer coefficient h and the fluid temperature at a large distance from the surface T_∞ will be assumed constant along the boundary. Myers (1989) has shown that the *boundary-segment convection vector* in Eq. A.75 is given by

$$\mathbf{h}^{(b_k)} = \frac{h^{(b_k)} t_{\infty}^{(b_k)} s_{ij}^{(b_k)}}{2} \begin{bmatrix} 1 & \text{Row } i \\ 1 & \text{Row } j \end{bmatrix} \tag{A.77}$$

Also, Myers (1989) has shown that the *boundary-segment convection matrix* is given by

$$\mathbf{H}^{(b_k)} = \frac{h^{(b_k)} s_{ij}^{(b_k)}}{6} \begin{bmatrix} 2 & 1 & \text{Row } i \\ 1 & 2 & \text{Row } j \\ \text{Column } i & \text{Column } j & \end{bmatrix} \tag{A.78}$$

A.2.2.2.2 Variable Properties along Boundary Segment

The values of the specified heat flux q_s'', the convective heat transfer coefficient h, and the temperature at a large distance from the outer boundary T_∞ will be variable along a boundary. The values of q_s'', h and T_∞ are scalar values that are functions of x and y along a boundary.

Specified heat flux

The *boundary-segment heat flow vector* $\mathbf{q}^{(b_q)}$ is given by (Myers 1987)

$$\mathbf{q}^{(b_q)} = \int_{\mathbf{B}^{(b_q)}} \mathbf{w}\ q_s''\, ds \tag{A.79}$$

This will be integrated along the boundary segment b_q. The boundary segment is the distance from node i to node j. Let the heat flux q_s'' along the boundary segment be a linear function as defined by

$$q_s'' = \begin{bmatrix} q_{s_i}'' & q_{s_j}'' \end{bmatrix} \begin{bmatrix} \delta_i \\ \delta_j \end{bmatrix} = \delta_i q_{s_i}'' + \delta_j q_{s_j}'' \tag{A.80}$$

In Eq. A.80, q_{s_i}'' and q_{s_j}'' are the heat fluxes at nodes i and j. As in Sec. A.2.2.1.2, $\delta_i(x,y) = \xi_i$, $\delta_j(x,y) = \xi_j$, $\delta_k(x,y) = \xi_k$, and so Eq. A.80 becomes

$$q_s'' = \xi_i q_{s_i}'' + \xi_j q_{s_j}'' \tag{A.81}$$

Substituting Eq. A.81 into Eq. A.79 gives

$$\mathbf{q}^{(b_q)} = \int_{\mathbf{B}^{(b_q)}} \begin{bmatrix} \xi_i^2 q_{s_i}'' + \xi_i \xi_j q_{s_j}'' \\ \xi_i \xi_j q_{s_i}'' + \xi_j^2 q_{s_j}'' \end{bmatrix} ds \tag{A.82}$$

Notice that $\xi_j = 0$ at node i and $\xi_j = 1$ at node j. Therefore,

$$\int_{s=s_i}^{s=s_j} ds = \int_{\xi_j=0}^{1} s_{ij}\, d\xi_j = s_{ij} \int_{\xi_j=0}^{1} d\xi_j = s_{ij} \tag{A.83}$$

Changing the limits of integration in Eq. A.82 with the use of Eq. A.83 gives

$$\mathbf{q}^{(b_q)} = s_{ij} \int_{\xi_j = 0}^{1} \begin{bmatrix} \xi_i^2 \, q''_{s_i} + \xi_i \, \xi_j \, q''_{s_j} \\ \xi_i \, \xi_j \, q''_{s_i} + \xi_j^2 \, q''_{s_j} \end{bmatrix} d\xi_j \tag{A.84}$$

Since $\xi_i + \xi_j = 1$, ξ_i can be substituted for in Eq. A.84 to give

$$\mathbf{q}^{(b_q)} = s_{ij} \int_{\xi_j = 0}^{1} \begin{bmatrix} (1 - \xi_j)^2 \, q''_{s_i} + (1 - \xi_j) \, \xi_j \, q''_{s_j} \\ (1 - \xi_j) \, \xi_j \, q''_{s_i} + \xi_j^2 \, q''_{s_j} \end{bmatrix} d\xi_j \tag{A.85}$$

The integration of Eq. A.85 with respect to ξ_j gives

$$\mathbf{q}^{(b_q)} = \frac{s_{ij}}{6} \begin{bmatrix} 2 \, q''_{s_i} + q''_{s_j} \\ q''_{s_i} + 2 \, q''_{s_j} \end{bmatrix} \tag{A.86}$$

Convection

The *boundary-segment convection matrix* $\mathbf{H}^{(b_h)}$ is given by (Myers 1987)

$$\mathbf{H}^{(b_h)} = \int_{\mathbf{B}^{(b_h)}} \mathbf{w} h \, \mathbf{w}^T \, ds \tag{A.87}$$

Equation A.87 will be integrated along the boundary segment b_h. Let the heat transfer coefficient h along the boundary segment be a linear function as defined by

$$h = [h_i \quad h_j]\begin{bmatrix}\delta_i \\ \delta_j\end{bmatrix} = \delta_i h_i + \delta_j h_j \tag{A.88}$$

In Eq. A.88, h_i and h_j are the heat transfer coefficients at nodes i and j. As earlier, $\delta_i\,(x,y) = \xi_i$ and $\delta_j\,(x,y) = \xi_j$, and so Eq. A.88 becomes

$$h = \xi_i h_i + \xi_j h_j \tag{A.89}$$

Substituting Eq. A.89 into Eq. A.87 gives

$$\mathbf{H}^{(b_k)} = \int_{s=s_i}^{s_j} \begin{bmatrix} \left(\xi_i^3 h_i + \xi_i^2 \xi_j h_j\right) & \left(\xi_i^2 \xi_j h_i + \xi_i \xi_j^2 h_j\right) \\ \left(\xi_i^2 \xi_j h_i + \xi_i \xi_j^2 h_j\right) & \left(\xi_i \xi_j^2 h_i + \xi_j^3 h_j\right) \end{bmatrix} ds \tag{A.90}$$

Applying the relation given in Eq. A.83 to Eq. A.90 and then integrating gives

$$\mathbf{H}^{(b_k)} = \frac{s_{ij}}{12}\begin{bmatrix} (3h_i + h_j) & (h_i + h_j) \\ (h_i + h_j) & (h_i + 3h_j) \end{bmatrix} \tag{A.91}$$

The *boundary-segment convection vector* $\mathbf{h}^{(b_k)}$ is given by

$$\mathbf{h}^{(b_k)} = \int_{\mathbf{B}^{(b_k)}} \mathbf{w} h\, T_\infty\, ds \tag{A.92}$$

The ambient temperature T_∞ is not a function of the boundary segment length and can be brought outside the integral. In general, though, T_∞ can be a function of time. The heat transfer coefficient will be integrated along the boundary length and can be defined by Eq.

A.89. Substituting Eq. A.89 into Eq. A.92 and then applying the relation given in Eq. A.83 gives

$$\mathbf{h}^{(b_k)} = T_\infty \, s_{ij} \int_{\xi_j = 0}^{1} \begin{bmatrix} \xi_i{}^2 h_i + \xi_i \xi_j h_j \\ \xi_i \xi_j h_i + \xi_j{}^2 h_j \end{bmatrix} d\xi_j \tag{A.93}$$

Since the integration of Eq. A.93 is identical to the integration of Eq. A.84, the result is obtained directly

$$\mathbf{h}^{(b_k)} = \frac{T_\infty \, s_{ij}}{6} \begin{bmatrix} 2h_i + h_j \\ h_i + 2h_j \end{bmatrix} \tag{A.94}$$

A.2.2.3 Specified Temperature

By combining all of the contributions from each interior element (Sec. A.2.2.1) and each boundary segment (Sec. A.2.2.2), Eq. A.7 may be written as a system of ordinary differential equations

$$\mathbf{C}\dot{\mathbf{T}} + (\mathbf{K} + \mathbf{B} + \mathbf{H})\mathbf{T} = \mathbf{g} + \mathbf{b} + \mathbf{q} + \mathbf{h} \tag{A.95}$$

In expanded form Eq. A.95 looks like

$$\begin{bmatrix} c_{ii} & & \\ & \ddots & \\ & & c_{li} \end{bmatrix} \begin{bmatrix} \dot{T}_i \\ \\ \end{bmatrix} + \begin{bmatrix} \kappa_{ii} & & \\ & \ddots & \\ & & \kappa_{li} \end{bmatrix} \begin{bmatrix} T_i \\ \\ \end{bmatrix} = \begin{bmatrix} g_i \\ \\ g_l \end{bmatrix}$$

where κ is an entry in **(K + B + H)** rather than **(K + B)** and g is an entry in **(g + b + q + h)** rather than **(g + b)**.

Myers (1989) has shown that if the temperature at node i is specified to be $T_{i,\,sp}$, the differential equation in row i will be

$$c_{ii}\dot{T}_i + \kappa_{ii} T_i = \kappa_{ii} T_{i,\,sp}$$

With a specified temperature at node i, the global set of differential equations is now given by

$$\begin{bmatrix} c_{ii} & & \\ & \ddots & \\ & & c_{li} \end{bmatrix} \begin{bmatrix} \dot{T}_i \\ \\ \end{bmatrix} + \begin{bmatrix} \kappa_{ii} & & \\ & \ddots & \\ & & \kappa_{li} \end{bmatrix} \begin{bmatrix} T_i \\ \\ \end{bmatrix} = \begin{bmatrix} \kappa_{ii} T_{i,\,sp} \\ \\ g_l \end{bmatrix}$$

where the off-diagonal terms in row i are now 0. To maintain the symmetry of (**K** + **B** + **H**), the off-diagonal entries in column i in (**K** + **B** + **H**) are set to zero. This is done by transferring the off-diagonal entries in (**K** + **B** + **H**) to the right-hand side of the system of equations and replacing c_{li} by 0 in **C**. After making this modification, the system of differential equations becomes

$$\begin{bmatrix} & & \\ & c_{ii} & \\ & & \\ 0 & & \end{bmatrix} \begin{bmatrix} \\ \dot{T}_i \\ \\ \end{bmatrix} + \begin{bmatrix} & & \\ & \kappa_{ii} & \\ & & \\ 0 & & \end{bmatrix} \begin{bmatrix} \\ T_i \\ \\ \end{bmatrix} = \begin{bmatrix} \kappa_{ii} T_{i,\,sp} \\ \\ g_l - \kappa_{li} T_{i,\,sp} \end{bmatrix}$$

The modified system of equations is now given by

$$\mathbb{C}\dot{\mathbf{T}} + \mathbf{ST} = \mathbf{r} \tag{A.96}$$

In Eq. A.96, $\mathbb{C}$, **S** (= **K** + **B** + **H**) and **r** (= **g** + **b** + **q** + **h**) are as modified for specified temperatures.

A.2.3 Temperature Determination

A.2.3.1 Uniform Properties

For steady-state problems, the time derivative of temperature is zero and Eq. A.96 reduces to

$$\mathbf{ST} = \mathbf{r} \tag{A.97}$$

Equation A.96 is no longer a system of ordinary differential equations but is now a system of algebraic equations given by Eq. A.97. The equation solving routine in FEHT (FEM2D) determines **T** in Eq. A.97 by inverting **S** using the *Cholesky square-root decomposition* method (Myers 1989).

Solutions to time-dependent problems are obtained by solving the system of ordinary differential equations given by Eq. A.96. FEHT solves this system of equations with given initial conditions using either the Euler or Crank-Nicolson methods (Myers 1989).

A.2.3.2 Variable Properties

The solution of Eq. A.97 to determine the steady-state temperature distribution for tissues with uniform properties requires only one matrix inversion of **S**. However, for properties that are dependent on temperature, an iterative solution process is necessary. (Recall that **S** and **r** can contain material, thermal, tissue perfusion, generation and boundary conditions that depend on temperature.) Initially, the properties that vary with temperature are specified with guessed values and then **S** and **r** are formed. Next the temperatures in **T** are determined using the method described in Sec. A.2.3.1. Then the properties that vary with temperature are recomputed with the known temperatures. If the newly computed properties differ from the guessed values, **S** and **r** are reformed using the average of the old and new temperatures to evaluate the properties. Again the temperatures in **T** are redetermined. This iterative process continues until all properties that vary with temperature converge.

The solution of the system of ordinary differential equations given by Eq. A.96 to determine the transient temperature distribution for tissues with uniform properties required only one inversion of **S** at each time step. For properties that depend on temperature, the temperatures from the last time step are used for evaluation of properties at the next time step.

A.2.4 Heat-flow and Nodal Energy Balance

Once Eq. A.96 has been solved for the nodal temperatures, the heat fluxes within the tissue, the heat flows at the boundary of the tissue, and the nodal energy balances can be determined.

Myers (1989) gives an energy interpretation of Eq. A.95 without the perfusion terms **B** and **b**. The form of Eq. A.95 considered here is given by

$$\mathbf{g} + (\mathbf{b} - \mathbf{BT}) + \mathbf{q} + (\mathbf{h} - \mathbf{HT}) = \mathbf{C}\dot{\mathbf{T}} + \mathbf{KT} \qquad \text{(A.98)}$$

The left-hand-side of Eq. A.98 gives the sum of the energy generation plus the perfusion inflow plus the specified heat inflow plus the convection inflow to each of the finite element nodal systems. The vector $(\mathbf{b} - \mathbf{BT})$ will contain zeros for all nodes if there is no tissue perfusion. The vector $(\mathbf{h} - \mathbf{HT})$ will contain zeros for all of the interior nodes and for all of the boundary nodes not along a convective boundary. The right-hand-side of Eq. A.98 gives the energy-storage rate in each nodal system plus the conduction out of each nodal system into the surrounding nodal systems. Thus Eq. A.98 represents an energy balance on each of the finite-nodal systems.

The boundary-heat inflow may be computed from

$$\mathbf{q_o = C\dot{T} + (K + B)T - g - b} \qquad \text{(A.99)}$$

The entries in $\mathbf{q_o}$ will be 0 (within numerical precision of the device used to compute it) for internal nodes that are not specified-temperature nodes. For internal nodes with a specified temperature, $\mathbf{q_o} \neq 0$, rather $\mathbf{q_o}$ provides an energy balance on the finite-sized tissue system surrounding the specified temperature node (Myers 1989).

Appendix B

Accuracy of Numerically Computed Temperatures

As with any software program, numerically predicted solutions should be compared with analytical solutions which are exact. The analytical temperature distribution in a square tissue model is derived in Sec. B.1. A comparison of the analytically-derived temperature distribution with the solution predicted by FEHT is shown in Sec. B.2. An error analysis of the temperature distribution predicted by FEHT is provided in Sec. B.3.

B.1 Analytical Temperature Distribution

The analytical steady-state temperature distribution was determined in the two-dimensional, square homogeneous tissue system with length a (Fig. B.1). In Fig. B.1 there are three constant temperature boundaries at $x = 0$, $x = a$ and $y = a$ and the temperature at the $y = 0$ boundary varies sinusoidally with position. Equation 2.2 was the energy equation used to determine the temperature distribution. Recalling that the parameter n equals $\sqrt{w_b c_b / k_t}$ (Eq. 3.1) and setting $\theta(x,y) = T(x,y) - T_b$, Eq. 2.2 becomes

$$\frac{\partial^2 \theta}{\partial x^2} + \frac{\partial^2 \theta}{\partial y^2} - n^2 \theta = 0 \qquad \text{(B.1)}$$

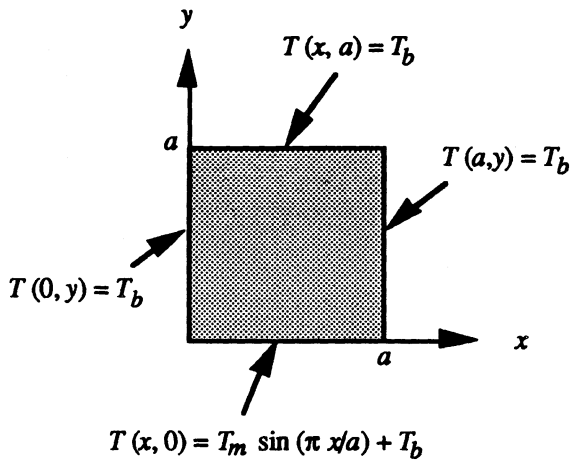

Figure B.1 Boundary conditions of tissue model. There are three constant temperature boundaries at $x = 0$, $x = a$ and $y = a$. The temperature at $y = 0$ varies sinusoidally with position along x.

The boundary conditions of Eq. B.1 are shown in Fig. B.2. The objective is to solve Eq. B.1 for the boundary conditions shown in Fig. B.2.

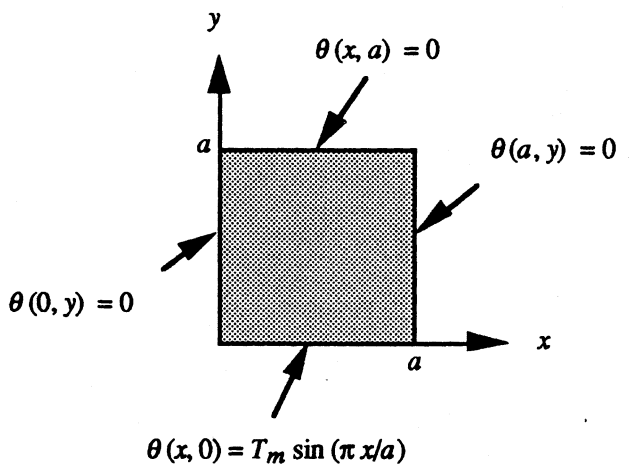

Figure B.2 Boundary conditions for Eq. B.1.

Equation B.1 is linear since it contains no products of the dependent variable or its derivatives (e.g., $(\theta')^2$ or $\theta'\theta$). Equation B.1 is also homogeneous since it is also satisfied by cq where c is an arbitrary constant ($c = 0$ is a special case). The boundary conditions given in Fig. B.2 are linear since they contain no products of the dependent variable or its derivatives. The boundary condition at $y = 0$, however, is nonhomogeneous since that boundary condition is *not* satisfied by $c\theta$.

The classical method of the *separation of variables* (Myers 1987) was used to solve Eq. B.1. Since Eq. B.1 is a linear, homogeneous partial-differential equation, it can be integrated assuming a product solution for $\theta(x, y)$ of the form

$$\theta(x, y) = X(x)\, Y(y) \tag{B.2}$$

where $X(x)$ is a function of x only, and $Y(y)$ is a function of y alone. After some effort the analytical temperature distribution was found to be

$$T(x, y) = T_m \frac{\sin\left(\frac{\pi x}{a}\right) \sinh\left[\left(n^2 + \frac{\pi^2}{a^2}\right)^{1/2} (a - y)\right]}{\sinh\left[\left(n^2 + \frac{\pi^2}{a^2}\right)^{1/2} a\right]} + T_b \tag{B.3}$$

B.2 Comparison of Analytical and Numerical Temperatures

The analytically-derived temperature distribution given by Eq. B.3 was compared to the temperature distribution computed by FEHT. The comparison was performed on a square tissue model with $a = 0.1$ m and with an n^2 value of 10,000. (An n^2 value of 3130 is typical for blood flow through normal muscle tissue at body temperature.) Arterial blood temperature T_b was 37 C and the amplitude of the sinusoidally-varying

surface (at $y = 0$) temperature T_m was 23 C. This gave a maximum temperature of 60 C at the midpoint along the x-axis. A temperature of 60 C is near the upper limit of the operating temperature of thermoseeds used in hyperthermia treatments. The temperature distribution calculated with FEHT was performed with a mesh of 1024 finite elements. Figure B.3 is a plot of several analytically- and numerically-computed isotherms between 38 and 58 C.

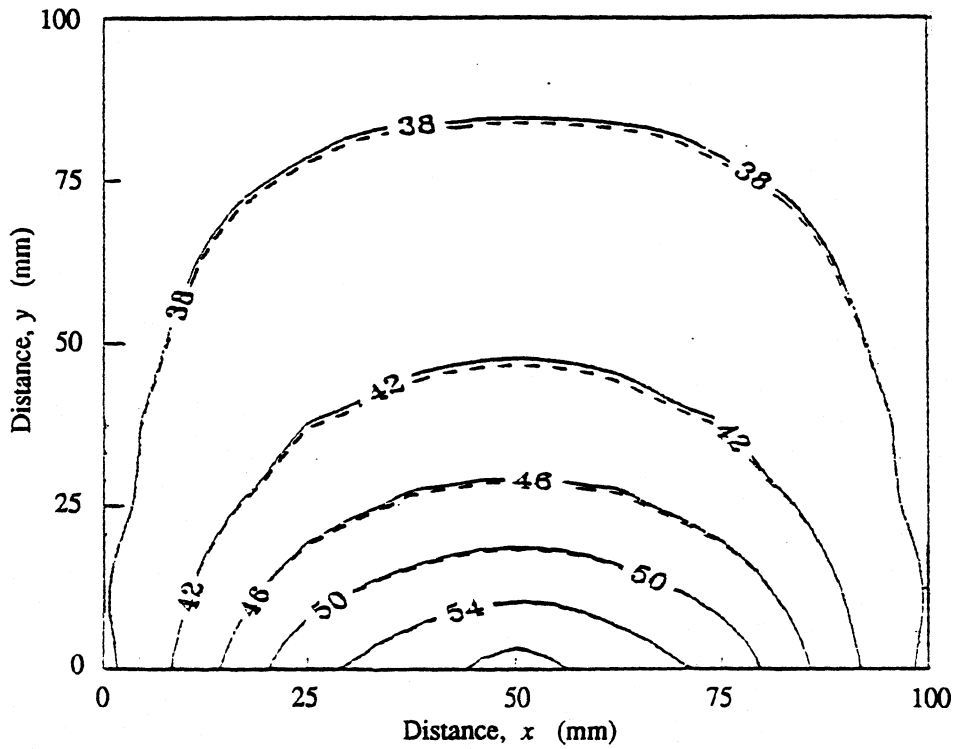

Figure B.3 The 38, 42, 46, 50, 54 and 58 C isotherms as predicted analytically (dashed lines) and numerically with FEHT (solid lines). The analytical solution was computed using Eq. B.3 with boundary conditions given in Fig. B.2. The solution predicted with FEHT was determined using a mesh of 1024 finite elements.

B.3 Error Analysis of Numerically Computed Temperature Distribution

An error analysis of the temperature distribution predicted with FEHT was performed. The error was based on the difference in temperature between the analytical solution and the FEHT solution at 25 locations within the square, simulated tissue system. The 25 locations coincide with the interior nodal points of the finite element mesh in Fig. B.4. Since the accuracy of the numerical solution will depend on the number of finite elements, discretizations of 64, 256 and 1024 finite elements were evaluated. The mesh of 256 elements was created by reducing uniformly the mesh of 64 elements. The mesh of 1024 elements was created by reducing uniformly the mesh of 256 elements. The errors were determined for n^2 values of 0, 1, 10, 100, 1000, and 10,000.

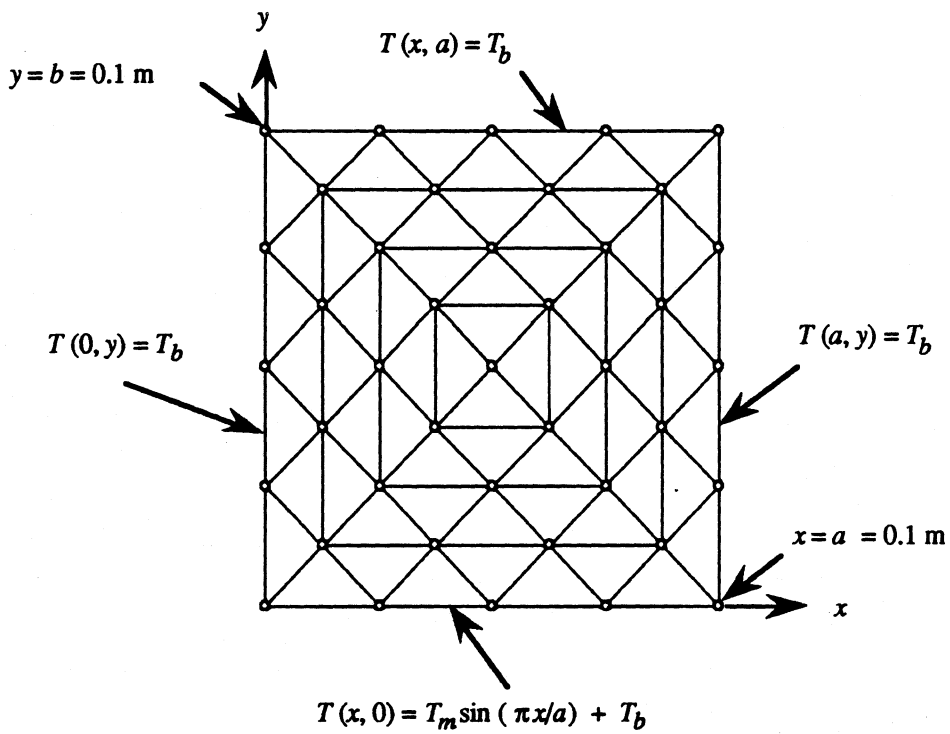

Figure B.4 Finite element mesh with 64 triangular elements and 41 nodes (open circles). This is a mesh of the simulated tissue system shown in Fig. B.2.

An estimate of the error was computed using several norms (Strikwerda 1989). The l^∞ (or maximum) norm is given by

$$|T|^\infty = \max_{1 \le i \le 25} |\widetilde{T}_i - T_i| \tag{B.4}$$

where i is one of the 25 interior nodal locations in Fig. B.4. The l^∞ norm gives the largest temperature difference between the analytical $\widetilde{T}_i$ and the numerical T_i solutions. The error in the l^∞ norm is shown in Fig. B.5. For values of n^2 studied, the l^∞ norm decreased by approximately 77% as the number of finite elements increased from 64 to 256. As the number of elements increased from 256 to 1024, the l^∞ norm decreased by 73%. Error in the l^∞ norm decreased by 72%, 70% and 67% with 64, 256 and 1024 finite element, respectively, when n^2 decreased from 10,000 to 1000.

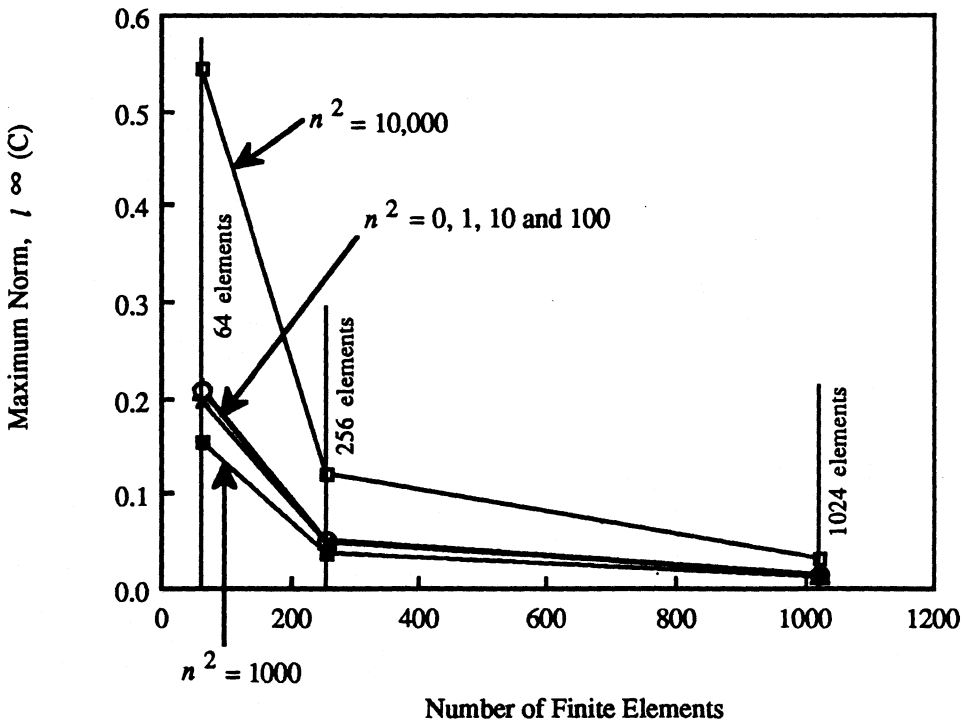

Figure B.5 Error in the l^∞ (or maximum) norm. The l^∞ norm was computed with Eq. B.4.

The l^2 (or Euclidean) norm is a summation of the error over all 25 interior locations and is given by

$$|T|^2 = \left[h_{max} \sum_{i=1}^{25} (\tilde{T}_i - T_i)^2\right]^{1/2} \tag{B.5}$$

In Eq. B.5, the diameter of the largest circle inscribed within any finite element in the mesh is h_{max}. The error in the l^2 norm is shown in Fig. B.6. The error in the l^2 norm decreased by approximately 84% as the number of finite elements increased from 64 to 256. As the number of elements increased from 256 to 1024, the error decreased by 80%. The error in the l^2 norm decreased by 55, 55 and 50% with 64, 256 and 1024

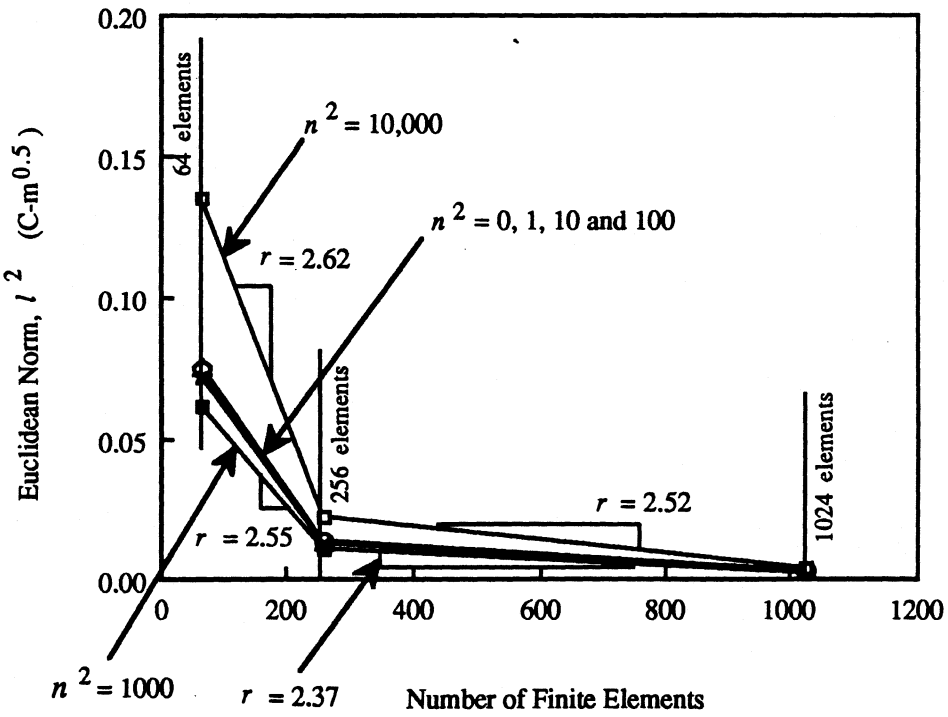

Figure B.6 Error in the l^2 norm. The error in the l^2 norm was computed with Eq. B.5.

elements, respectively, when n^2 decreased from 10,000 to 1000.

Theoretically, as h_{max} approaches zero, the finite element solution will converge to the exact solution (Burnett 1987). This form of convergence is known as *h-convergence* since it is achieved by letting the size of the elements become progressively smaller. For linear finite elements, the theoretical rate of convergence for ordinary function points such as nodal temperatures is $O(h^2)$. Therefore as h-refinement is performed on the mesh shown in Fig. B.4, the rate of convergence should approach 2. The rate of convergence, r, is computed using

$$\frac{Error_{l2}(h_1)}{Error_{l2}(h_2)} = \frac{C\,(h_1)^r}{C\,(h_2)^r} \tag{B.7}$$

In Eq. B.7, $Error_{l2}$ is the error in the Euclidean norm; h_1 and h_2 are the diameters of the largest circles inscribed within finite elements in meshes 1 and 2, respectively; and C is a constant. The constant C vanishes when the computation to determine r is performed. In Fig. B.6, the rate of convergence between meshes 1 and 2 is 2.62 and 2.55 for n^2 values of 10,000 and 1000, respectively. The convergence rate between meshes 2 and 3 is 2.52 and 2.37 for similar n^2 values. Thus r began to approach 2 for decreasing h_{max}.

Appendix C

Cell Survival Determination

Appendix C contains input and output of the Mathematica software program (Wolfram *et al.* 1988) which was used to evaluate several integrations in Chapter 5.

C.1 Solution to Eqs. 5.6 and 5.9

The following is the input and output from Mathematica that were used to solve for Eqs. 5.6 and 5.9:

```
kt    = 0.642;   {Thermal conductivity of tissue, W/m-C}
wbcb  = 3720;    {Tissue perfusion * Specific heat of tissue, W/m^3-C}
tb    = 37;      {Blood temperature, C}
n     = Sqrt[wbcb/kt]; {Nondimensional term in Eq. 3.4}
ri    = 0.00045;      {Inner radius of cylindrical tissue system, Fig. 3.1}
rseed = 0.00045;      {Radius of thermoseed, m}
ro    = 0.1;          {Outer radius of cylindrical tissue system, Fig. 3.1}
r42   = 0.008072;     {Radius of the 42 C isotherm in Fig. 3.1, m}
r     = r42;
SeedPower= 26.513;          {Power per unit length of thermoseed, W/m, for 60 C
Thermoseed}
Aseed = Pi*rseed^2;   {Area of thermoseed, m^2}
I1    = BesselI[1, n ri]; {Bessel function}
K0    = BesselK[0, n ro]; {Bessel function}
I0    = BesselI[0, n ro]; {Bessel function}
K1    = BesselK[1, n ri]; {Bessel function}
Denom = I1*K0 + I0*K1;    {Numerical constant}
```

```
C1    = ( SeedPower*ri / (2*Aseed*n*kt*Denom) ) * BesselI[0, n ro];  {Numerical
constant}
C2    = ( SeedPower*ri / (2*Aseed*n*kt*Denom) ) * BesselK[0, n ro];  {Numerical
constant}
Delt  = C1*BesselK[0, n r] - C2*BesselI[0, n r];  {Temperature given by Eq. 3.4}
TissueTempAtr = Delt + tb;  {Tissue temperature at 42 C isotherm}
N[TissueTempAtr,8]
42.000394
r =.
Delt  = C1*BesselK[0, n r] - C2*BesselI[0, n r];  {Temperature given by Eq. 3.4}
Tumora  = 86;      {Coefficient in Eq. 5.2 for survival of tumor tissue}
Tumorb  = -2;      {Coefficient in Eq. 5.2 for survival of tumor tissue}
Normala = 44;      {Coefficient in Eq. 5.2 for survival of normal tissue}
Normalb = -1;      {Coefficient in Eq. 5.2 for survival of normal tissue}
rtumor  = 0.005;       {Radius of tumor, m}
TumorTissueArea          = Pi*(rtumor^2 - rseed^2) / 3; {Tumor area}
IntegratedTumorAreaAbove42  = Pi*(rtumor^2 - rseed^2) / 3; {Tumor area above 42 C}
NormalTissueArea         = Pi*(ro^2 - rtumor^2) / 3;   {Normal area}
IntegratedNormalAreaAbove42 = Pi*(r42^2 - rtumor^2) / 3;   {Normal area above 42 C}
TumorIntegral =
        NIntegrate[r 10^(Tumora + Tumorb*(tb + Delt) ),
                                    {r, rseed, rtumor},
                    MinRecursion    -> 2,
                    WorkingPrecision -> 20,
                    AccuracyGoal     -> 10]; {Numerical integration of integral in
numerator of Eq 5.7}
NormalIntegral =
        NIntegrate[r 10^(Normala + Normalb*(tb + Delt) ),
                                    {r, rtumor, r42},
                    MinRecursion    -> 2,
                    WorkingPrecision -> 20,
                    AccuracyGoal     -> 10]; {Numerical integration of integral in
numerator of Eq. 5.7}
TumorTissueAreaBelow42              = 0;
TumorTissueAreaAbove42      = TumorTissueArea - TumorTissueAreaBelow42;
PercentTumorTissueAreaAbove42                                    =
(TumorTissueAreaAbove42/TumorTissueArea)*100;
NormalTissueAreaBelow42     = Pi * (ro^2 - r42^2) / 3;
NormalTissueAreaAbove42     = NormalTissueArea - NormalTissueAreaBelow42;
```

```
PercentNormalTissueAreaAbove42                    =
(NormalTissueAreaAbove42/NormalTissueArea)*100;
PercentNormalSurvival                    = (2*Pi/3) * NormalIntegral /
IntegratedNormalAreaAbove42;
            {Calculation of Eq. 5.8 for normal tissue}
PercentTumorSurvival                     = (2*Pi/3) * TumorIntegral   /
IntegratedTumorAreaAbove42;
            {Calculation of Eq. 5.8 for tumor tissue}
PsiTumorKill                        = ( (1 - PercentTumorSurvival/100)  *
IntegratedTumorAreaAbove42 )/TumorTissueArea;
            {Calculation of Eq. 5.9}
PsiNormalKill                       = ( (1 - PercentNormalSurvival/100) *
IntegratedNormalAreaAbove42 )/TumorTissueArea;
            {Calculation of Eq. 5.9}
WF                  = 0.8;  {Weighting function for tumor tissue}
F = WF*PsiTumorKill - (1-WF)*PsiNormalKill
0.5508493017385405299
PercentTumorTissueAreaAbove42
100.
PercentNormalTissueAreaAbove42
0.402578285714285706
PercentTumorSurvival
0.00003825884731179527651
PercentNormalSurvival
23.07345492218264737
PsiTumorKill
0.9999996174115268822
PsiNormalKill
1.245751960953404879
```

C.2 Symbolic form of Solution to Eqs. 5.6 and 5.14

The following is the input and output from Mathematica that were used to solve for the symbolic form of the solutions to Eqs. 5.6 and 5.14:

```
xi = 1
yi = 9
xj = 9
yj = 1
xk = 11.9282032
yk = 11.9282032

ti = .
tj = .
tk = .

a = .
b = .

xij = xj - xi
xik = xk - xi
xjk = xk - xj
yij = yj - yi
yik = yk - yi
yjk = yk - yj
bijk = xij*yjk - xjk*yij
Areaelem = 0.5 * bijk


a1 = (1/bijk) * ((xj*yk - xk*yj)*ti + (xk*yi - xi*yk)*tj + (xi*yj - xj*yi)*tk )
a2 = (1/bijk) * (-yjk*ti + yik*tj - yij*tk)
a3 = (1/bijk) * (xjk*ti - xik*tj + xij*tk)

m1 = (yk-yi)/(xk-xi)
b1 = yk - (m1*xk)
m2 = (yj-yi)/(xj-xi)
b2 = yj - (m2*xj)
m3 = (yk-yj)/(xk-xj)
```

```
b3 = yk - (m3*xk)

F1 = Integrate [ 10.^(a - b a1 - b a2 x - b a3 y),{x,xi,xj},{y,m2 x + b2, m1 x +  b1}]
F2 = Integrate [ 10.^(a - b a1 - b a2 x - b a3 y),{x,xj,xk},{y,m3 x + b3, m1 x +  b1}]
PerSurvival = (F1 + F2)/Areaelem

0.018042195991018277 29*(0. +
  (20.907842604692704 98*E^
    (2.302585092994045684*
     (a - 0.009021097995509138647*b*
       (95.42562560000000001*ti + 95.42562560000000001*tj -
        80*tk) - 0.1076054899775456932*b*
       (2.9282032*ti - 10.9282032*tj + 8*tk) -
      0.1076054899775456932*b*
       (-10.9282032*ti + 2.9282032*tj + 8*tk))))/
   (b*(2.9282032*ti - 10.9282032*tj + 8*tk)*
    (-0.0336671963141207395*b*
      (2.9282032*ti - 10.9282032*tj + 8*tk) -
     0.009021097995509138647*b*
      (-10.9282032*ti + 2.9282032*tj + 8*tk))) -
  (20.907842604692704 98*E^
    (2.302585092994045684*
     (a - 0.009021097995509138647*b*
       (95.42562560000000001*ti + 95.42562560000000001*tj -
        80*tk) - 0.009021097995509138647*b*
       (2.9282032*ti - 10.9282032*tj + 8*tk) -
      0.081189881959582247 83*b*
       (-10.9282032*ti + 2.9282032*tj + 8*tk))))/
   (b*(2.9282032*ti - 10.9282032*tj + 8*tk)*
    (-0.0336671963141207395*b*
      (2.9282032*ti - 10.9282032*tj + 8*tk) -
     0.009021097995509138647*b*
      (-10.9282032*ti + 2.9282032*tj + 8*tk))) -
  (20.907842604692704 98*E^
    (2.302585092994045684*
     (a - 0.009021097995509138647*b*
       (95.42562560000000001*ti + 95.42562560000000001*tj -
        80*tk) - 0.1076054899775456932*b*
       (2.9282032*ti - 10.9282032*tj + 8*tk) -
      0.1076054899775456932*b*
```

```
      (-10.9282032*ti + 2.9282032*tj + 8*tk))))/
 (b*(2.9282032*ti - 10.9282032*tj + 8*tk)*
  (-0.0024171959044432341 28*b*
    (2.9282032*ti - 10.9282032*tj + 8*tk) -
   0.009021097995509138647*b*
    (-10.9282032*ti + 2.9282032*tj + 8*tk))) +
(20.907842604692704 98*E^
   (2.3025850929940456 84*
    (a - 0.009021097995509138647*b*
      (95.425625600000000 01*ti + 95.425625600000000 01*tj -
        80*tk) - 0.081189881959582247 83*b*
      (2.9282032*ti - 10.9282032*tj + 8*tk) -
     0.009021097995509138647*b*
      (-10.9282032*ti + 2.9282032*tj + 8*tk))))/
 (b*(2.9282032*ti - 10.9282032*tj + 8*tk)*
  (-0.0024171959044432341 28*b*
    (2.9282032*ti - 10.9282032*tj + 8*tk) -
   0.009021097995509138647*b*
    (-10.9282032*ti + 2.9282032*tj + 8*tk))) +
(20.907842604692704 98*E^
   (2.3025850929940456 84*
    (a - 0.009021097995509138647*b*
      (95.425625600000000 01*ti + 95.425625600000000 01*tj -
        80*tk) - 0.009021097995509138647*b*
      (2.9282032*ti - 10.9282032*tj + 8*tk) -
     0.081189881959582247 83*b*
      (-10.9282032*ti + 2.9282032*tj + 8*tk))))/
 (b*(2.9282032*ti - 10.9282032*tj + 8*tk)*
  (0.009021097995509138647*b*
    (2.9282032*ti - 10.9282032*tj + 8*tk) -
   0.009021097995509138647*b*
    (-10.9282032*ti + 2.9282032*tj + 8*tk))) -
(20.907842604692704 98*E^
   (2.3025850929940456 84*
    (a - 0.009021097995509138647*b*
      (95.425625600000000 01*ti + 95.425625600000000 01*tj -
        80*tk) - 0.081189881959582247 83*b*
      (2.9282032*ti - 10.9282032*tj + 8*tk) -
     0.009021097995509138647*b*
      (-10.9282032*ti + 2.9282032*tj + 8*tk))))/
```

```
(b*(2.9282032*ti - 10.9282032*tj + 8*tk)*
 (0.009021097995509138647*b*
   (2.9282032*ti - 10.9282032*tj + 8*tk) -
  0.009021097995509138647*b*
   (-10.9282032*ti + 2.9282032*tj + 8*tk))))
```

C.3 Particular Solutions to Eqs. 5.6 and 5.14

The following is the input and output from Mathematica that were used to solve for particular solutions of Eqs. 5.6 and 5.14:

```
xi = 1
yi = .
xj = 9
yj = 1
xk = 11.9282032
yk = 11.9282032

ti = 43.00001
tj = 43.000001
tk = 43.0000001

a = 44
b = 1

xij = xj - xi
xik = xk - xi
xjk = xk - xj
yij = yj - yi
yik = yk - yi
yjk = yk - yj
bijk = xij*yjk - xjk*yij
Areaelem = 0.5 * bijk

a1 = (1/bijk) * ((xj*yk - xk*yj)*ti + (xk*yi - xi*yk)*tj + (xi*yj - xj*yi)*tk )
a2 = (1/bijk) * (-yjk*ti + yik*tj - yij*tk)
a3 = (1/bijk) * (xjk*ti - xik*tj + xij*tk)

m1 = (yk-yi)/(xk-xi)
b1 = yk - (m1*xk)
m2 = (yj-yi)/(xj-xi)
b2 = yj - (m2*xj)
m3 = (yk-yj)/(xk-xj)
b3 = yk - (m3*xk)
```

```
F1 = Integrate [ 10.^(a - b a1 - b a2 x - b a3 y),{x,xi,xj},{y,m2 x + b2, m1 x +  b1}]
F2 = Integrate [ 10.^(a - b a1 - b a2 x - b a3 y),{x,xj,xk},{y,m3 x + b3, m1 x +  b1}]
PerSurvival = (F1 + F2)/Areaelem
PerSurvivalTable = Table[{yi,N[PerSurvival, 20]},{yi,9,69,10}]


PerSurvivalTable = Table[{yi,N[PerSurvival,20]},{yi,9,69,10}]

ListPlot [{{xi, 9},{xj,yj},{xk,yk},{xi,9},
        {xj,yj},{xk,yk},{xi,39},
        {xj,yj},{xk,yk},{xi,69},
       {xj,yj}},
  AxesLabel->{" x coordinate","y coordinate      " },
  PlotLabel->"    Finite Element",
  AspectRatio->0.75,
  PlotJoined->True,
   PlotRange->{{0,12},{0,80}}]


ListPlot[PerSurvivalTable,
  AxesLabel->{"  y coordinate","Survival      " },
  PlotLabel->"    Percent Survival",
  Framed->False,
  PlotColor->True,
  PlotJoined->True,
  AspectRatio->1,
   PlotRange->{{0,100},{9,11}}]


ListPlot[PerSurvivalTable,
  AxesLabel->{"  y coordinate","Survival      " },
  PlotLabel->"    Percent Survival",
  Framed->False,
  PlotColor->True,
  PlotJoined->True,
  AspectRatio->1,
   PlotRange->{{0,100},{9.9999110,9.9999180}}]
```

```
DerPerSurvival = D[PerSurvival,yi]
DerPerSurvivalTable = Table[{yi,N[DerPerSurvival,20]},
                {yi, 9,69,10}]

ListPlot[DerPerSurvivalTable,
  AxesLabel->{"  y coordinate","Survival      " },
  PlotLabel->"    Percent Survival Derivative",
  Framed->False,
  PlotColor->True,
  PlotJoined->True,
  AspectRatio->1,
  PlotLabel -> "Percent Survival Derivative",
   PlotRange->{{0,100},{-1*10^(-8),7*10^(-8)}}]


xi = 1
yi = .
xj = 9
yj = 1
xk = 11.9282032
yk = 11.9282032

ti = 42.
tj = 44.
tk = 46.

a = 44
b = 1

xij = xj - xi
xik = xk - xi
xjk = xk - xj
yij = yj - yi
yik = yk - yi
yjk = yk - yj
bijk = xij*yjk - xjk*yij
Areaelem = 0.5 * bijk

a1 = (1/bijk) * ((xj*yk - xk*yj)*ti + (xk*yi - xi*yk)*tj + (xi*yj - xj*yi)*tk )
```

```
a2 = (1/bijk) * (-yjk*ti + yik*tj - yij*tk)
a3 = (1/bijk) * (xjk*ti - xik*tj + xij*tk)

m1 = (yk-yi)/(xk-xi)
b1 = yk - (m1*xk)
m2 = (yj-yi)/(xj-xi)
b2 = yj - (m2*xj)
m3 = (yk-yj)/(xk-xj)
b3 = yk - (m3*xk)

F1 = Integrate [ 10.^(a - b a1 - b a2 x - b a3 y),{x,xi,xj},{y,m2 x + b2, m1 x +  b1}]
F2 = Integrate [ 10.^(a - b a1 - b a2 x - b a3 y),{x,xj,xk},{y,m3 x + b3, m1 x +  b1}]
PerSurvival = (F1 + F2)/Areaelem
PerSurvivalTable = Table[{yi,N[PerSurvival, 20]},{yi,9,69,10}]


ListPlot[PerSurvivalTable,
   AxesLabel->{"  y coordinate","Survival      " },
   PlotLabel->"     Percent Survival",
   Framed->False,
   PlotColor->True,
   PlotJoined->True,
   AspectRatio->0.75,
    PlotRange->{{0,100},{4,5}}]


ListPlot[PerSurvivalTable,
   AxesLabel->{"  y coordinate","Survival      " },
   PlotLabel->"     Percent Survival",
   Framed->False,
   PlotColor->True,
   PlotJoined->True,
   AspectRatio->1,
    PlotRange->{{0,100},{4.62145810602707020,
                4.62145810602707042}}]


DerPerSurvival = D[PerSurvival,yi]
DerPerSurvivalTable = Table[{yi,N[DerPerSurvival,20]},
                {yi, 9,69,10}]
```

```
ListPlot[DerPerSurvivalTable,
   AxesLabel->{"   y coordinate","        " },
   PlotLabel->"     Percent Survival Derivative",
   Framed->False,
   PlotColor->True,
   PlotJoined->True,
   AspectRatio->1,
   PlotLabel -> "           Percent Survival Derivative",
    PlotRange->{{0,100},{-1*10^(-18),1*10^(-18)}}]


xi = 1
yi = 1
xj = 10
yj = 1.000001
xk = 10.0000001
yk = 5

ti = 42.
tj = 44.
tk = 46.

a = 44
b = 1

xij = xj - xi
xik = xk - xi
xjk = xk - xj
yij = yj - yi
yik = yk - yi
yjk = yk - yj
bijk = xij*yjk - xjk*yij
Areaelem = 0.5 * bijk

a1 = (1/bijk) * ((xj*yk - xk*yj)*ti + (xk*yi - xi*yk)*tj + (xi*yj - xj*yi)*tk )
a2 = (1/bijk) * (-yjk*ti + yik*tj - yij*tk)
a3 = (1/bijk) * (xjk*ti - xik*tj + xij*tk)

m1 = (yk-yi)/(xk-xi)
```

```
b1 = yk - (m1*xk)
m2 = (yj-yi)/(xj-xi)
b2 = yj - (m2*xj)
m3 = (yk-yj)/(xk-xj)
b3 = yk - (m3*xk)

F1 = Integrate [ 10.^(a - b a1 - b a2 x - b a3 y),{x,xi,xj},{y,m2 x + b2, m1 x +  b1}]
F2 = Integrate [ 10.^(a - b a1 - b a2 x - b a3 y),{x,xj,xk},{y,m3 x + b3, m1 x +  b1}]
PerSurvival = (F1 + F2)/Areaelem


ListPlot [{{xi, yi},{xj,yj},{xk,yk},{xi,yi}},
  AxesLabel->{" x coordinate","y coordinate      " },
  PlotLabel->"         Finite Element",
  AspectRatio->.5,
  PlotJoined->True,
   PlotRange->{{0,12},{0,6}}]
```

Node	x - coordinate	y - coordinate	Temperature
i	1	1	42
j	10	1.000001	44
k	10.0000001	5.	46

Elemental Area = 18 units

Percent Survival - 4.62 %

```
xi = 1
yi = 1
xj = 5
yj = 1.00001
xk = 1.000001
yk = 10

ti = 42.
tj = 44.
tk = 46.
```

```
a = 44
b = 1

xij = xj - xi
xik = xk - xi
xjk = xk - xj
yij = yj - yi
yik = yk - yi
yjk = yk - yj
bijk = xij*yjk - xjk*yij
Areaelem = 0.5 * bijk

a1 = (1/bijk) * ((xj*yk - xk*yj)*ti + (xk*yi - xi*yk)*tj + (xi*yj - xj*yi)*tk )
a2 = (1/bijk) * (-yjk*ti + yik*tj - yij*tk)
a3 = (1/bijk) * (xjk*ti - xik*tj + xij*tk)

m1 = (yk-yi)/(xk-xi)
b1 = yk - (m1*xk)
m2 = (yj-yi)/(xj-xi)
b2 = yj - (m2*xj)
m3 = (yk-yj)/(xk-xj)
b3 = yk - (m3*xk)

F1 = Integrate [ 10.^(a - b a1 - b a2 x - b a3 y),{x,xi,xj},{y,m2 x + b2, m1 x +  b1}]
F2 = Integrate [ 10.^(a - b a1 - b a2 x - b a3 y),{x,xj,xk},{y,m3 x + b3, m1 x +  b1}]
PerSurvival = (F1 + F2)/Areaelem


ListPlot [{{xi, yi},{xj,yj},{xk,yk},{xi,yi}},
  AxesLabel->{" x coordinate","y coordinate      " },
  PlotLabel->"          Finite Element",
  AspectRatio->1.0,
  PlotJoined->True,
   PlotRange->{{0,6},{0,12}}]
```

Node	x - coordinate	y - coordinate	Temperature
i	1	1	42
j	5	1.00001	44
k	1.000001	10.	46

Elemental Area = 18 units

Percent Survival - 4.62 %

```
xi = 1
yi = 1
xj = 5
yj = 1.00001
xk = 1.000001
yk = 10

ti = 42.
tj = 46.
tk = 44.

a = 44
b = 1

xij = xj - xi
xik = xk - xi
xjk = xk - xj
yij = yj - yi
yik = yk - yi
yjk = yk - yj
bijk = xij*yjk - xjk*yij
Areaelem = 0.5 * bijk

a1 = (1/bijk) * ((xj*yk - xk*yj)*ti + (xk*yi - xi*yk)*tj + (xi*yj - xj*yi)*tk )
a2 = (1/bijk) * (-yjk*ti + yik*tj - yij*tk)
a3 = (1/bijk) * (xjk*ti - xik*tj + xij*tk)

m1 = (yk-yi)/(xk-xi)
b1 = yk - (m1*xk)
m2 = (yj-yi)/(xj-xi)
b2 = yj - (m2*xj)
m3 = (yk-yj)/(xk-xj)
b3 = yk - (m3*xk)

F1 = Integrate [ 10.^(a - b a1 - b a2 x - b a3 y),{x,xi,xj},{y,m2 x + b2, m1 x +  b1}]
```

```
F2 = Integrate [ 10.^(a - b a1 - b a2 x - b a3 y),{x,xj,xk},{y,m3 x + b3, m1 x +  b1}]
PerSurvival = (F1 + F2)/Areaelem


ListPlot [{{xi, yi},{xj,yj},{xk,yk},{xi,yi}},
   AxesLabel->{" x coordinate","y coordinate      " },
   PlotLabel->"         Finite Element",
   AspectRatio->1,
   PlotJoined->True,
    PlotRange->{{0,6},{0,12}}]
```

Purpose - Transpose the temperatures of nodes i and j

Node	x - coordinate	y - coordinate	Temperature
i	1	1	42
j	5	1.00001	46
k	1.000001	10.	44

Elemental Area = 18 units

Result - Percent Survival is unchanged

Percent Survival - 4.62 %

```
ListPlot [{{1, 9},{9, 1},{11.9282032, 11.9282032},{1, 9}},
  AxesLabel->{" x coordinate","y coordinate      " },
  PlotLabel->"         Finite Element",
  AspectRatio->1,
  PlotJoined->True,
   PlotRange->{{0,15},{0,15}}]
```